

Comparison of the Thermal Performance of Several Tip Cooling Designs for a Turbine Blade

Jesse R. Christophel

Thesis submitted to the Faculty
of Virginia Polytechnic Institute and State University
in partial fulfillment of the requirements for the degree of

Master of Science
in
Mechanical Engineering

Dr. Karen Thole, Chair
Dr. Wing Ng
Dr. Brian Vick

September 19, 2003
Blacksburg, VA

Keywords: gas turbines, film-cooling, blade tip,
blade heat transfer

© 2003, Jesse R. Christophel

Comparison of the Thermal Performance of Several Tip Cooling Designs for a Turbine Blade

Jesse R. Christophel

Abstract

Gas turbine blades are subject to harsh operating conditions that require innovative cooling techniques to insure reliable operation of parts. Film-cooling and internal cooling techniques can prolong blade life and allow for higher engine temperatures. This study examines several unique methods of cooling the turbine blade tip. The first method employs holes placed directly in the tip which inject coolant onto the blade tip. The second and third methods used holes placed on the pressure side of a blade near the tip representative of two different manufacturing techniques. The fourth method is a novel cooling technique called a microcircuit, which combines internal convection and injection from the pressure side near a turbine blade tip. Wind tunnel tests are used to observe how effectively these designs cool the tip through adiabatic effectiveness measurements and convective heat transfer measurements. Tip gap size and blowing ratio are varied for the different tip cooling configurations.

Results from these studies show that coolant injection from either the tip surface or from the pressure side near the tip are viable cooling methods. All of these studies showed better cooling could be achieved at small tip gaps than large tip gaps. The results in which the two different manufacturing techniques were compared indicated that the technique producing more of a diffused hole provided better cooling on the tip.

When comparing the thermal performance of all the cooling schemes investigated, the added benefit of the internal convective cooling shows that the microcircuit outperforms the other designs.

Preface

To improve turbine engine designs, new methods are needed to reduce heat transfer to turbine airfoils. In particular, one region of the airfoil having high heat transfer rates, resulting in component failures, is the tip region of a turbine blade. Research on blade tip heat transfer is a relatively new area when considering cooling schemes such as injection from or near the blade tip. Because of the complex interaction between the coolant and mainstream gases as flow enters the tip gap, it is important to understand how different coolant injection schemes affect both the film-cooling and heat transfer along the blade tip surface. This thesis consists of four journal articles that summarize four unique experimental studies with film-cooling injection in or near the tip of a turbine blade.

The first paper in this thesis presents the benefits of coolant injection from holes placed directly in the tip of a turbine blade. The second paper presents adiabatic effectiveness results for two separate pressure-side injection designs, representing two different hole geometries representative of two different manufacturing techniques. The third paper presents a companion paper to the second paper in which the heat transfer on the blade tip that is associated with blowing from each of the two hole designs. The fourth paper presents yet a third cooling design in which a microcircuit is evaluated in terms of the external heat transfer and internal heat transfer.

Additional results for each of the studies as well as analysis techniques, benchmarking, and recommendations for future work are included in the appendices.

Acknowledgements

I would like to acknowledge all of the people who have provided support, love, and teaching to me during my life. I would like to thank God for blessing my life so richly and providing me with the strength and abilities to finish this degree. I also would like to thank my family, including my mother, father, and brother, and especially my wonderful wife, Kim. Thank you for supporting me during the rough times and celebrating with me during the good times. You mean the world to me and I couldn't have done this without you!

To my advisor, Karen Thole, thank you for providing me with the opportunity to work and learn with you and for your guidance and patience over the last 21 months. I am also grateful to Pratt & Whitney for sponsoring this project and for the many people at P&W who helped me along the way, including Frank Cunha, Brett Teller, Keith Santeler, and Barry Kleinfeld. Thank you to the many professors here at Virginia Tech who have provided such a wonderful learning environment, especially Dr. Vick and Dr. Ng for being part of my committee.

Thanks to all of the students whom I have worked with here at VTeXCCL: Andy, Andrew, Angela, Chris, Daniel, Erin, Evan, Jeff, Joe, Mike, Paul, Sachin, Scott, Sundar (adopted), Will, and William, for providing friendship and entertainment both in and out of the lab. Special recognition is also due to my fellow Pratt Team members, Eric and Erik; there can never be a team like us!

Finally, I would like to thank Blacksburg and the Virginia Tech Hokies. I have enjoyed the mountains and streams of the New River Valley as much as any other place that I have been. Also, I hope that I can visit here in the future and see a national championship banner waiving in Lane Stadium.

Table of Contents

Abstract.....	ii
Preface.....	iii
Acknowledgements.....	iv
List of Tables	vii
List of Figures.....	viii
Paper 1: Measured Adiabatic Effectiveness and Heat Transfer for Blowing from the Tip of a Turbine Blade	1
Abstract.....	1
Introduction.....	2
Relevant Past Studies.....	3
Experimental Facility and Methodology	5
Experimental Test Cases.....	8
Adiabatic Effectiveness Results for the Blade Tip.....	9
Heat Transfer Measurements for the Blade Tip.....	11
Conclusions.....	15
Nomenclature.....	16
References.....	17
Paper 2: Comparison of Exit Hole Shapes for Cooling the Tip of a Turbine Blade – Part 1: Film Effectiveness Measurements	31
Abstract.....	31
Introduction.....	32
Relevant Past Studies.....	32
Description of Cooling Hole Geometries	34
Experimental Facilities	35
Experimental Results for Blowing Cases	41
Conclusions.....	45
Nomenclature.....	46
References.....	47
Paper 3: Comparison of Exit Hole Shapes for Cooling the Tip of a Turbine Blade – Part 2: Heat Transfer Measurements	64
Abstract.....	64
Introduction.....	65
Relevant Past Studies.....	65
Experimental Facility and Instrumentation.....	67
Measurement of Tip Heat Transfer Coefficients	70
Conclusions.....	78
Nomenclature.....	78
References.....	79

Paper 4: Using a Microcircuit Design for Cooling the Tip of a Turbine Blade –	
Part 2: Internal and External Heat Transfer Measurements.....	94
Abstract.....	94
Introduction.....	95
Relevant Past Studies.....	96
Experimental Facility and Instrumentation.....	97
Measurement of External Tip Heat Transfer Coefficients.....	101
Measurement of Internal Heat Transfer Coefficients.....	106
Conclusions.....	108
Nomenclature.....	108
References.....	109
Appendix A: Introduction.....	126
A.1 Thesis Overview.....	126
A. References.....	127
Appendix B: Data Analysis Methods.....	129
B.1 Description of Infrared Image Analysis.....	129
B.2 Benchmarking and Repeatability of Experimental Results.....	130
B.3 Uncertainty Calculations.....	131
B.4 Nomenclature.....	134
B.5 References.....	134
Appendix C: Additional Analysis for Dirt Purge Results.....	144
C.1 Discussion of Additional Data.....	144
C.2 Nomenclature.....	146
C.3 References.....	146
Appendix D: Additional Analysis for EDM and Laser Hole Shapes.....	156
D.1 Discussion of Additional Data.....	156
D.2 Nomenclature.....	157
Appendix E: Additional Analysis for Microcircuit Results.....	163
E.1 Discussion of Additional Data.....	163
E.2 Nomenclature.....	164
E.3 References.....	164
Appendix F: Comparison Between EDM, Laser, and Microcircuit Designs.....	176
F.1 Discussion of Comparison.....	176
F.2 Nomenclature.....	177
F.3 References.....	177
Appendix G: Summary and Recommendations for Future Work.....	188
G.1 Overview of Results.....	188
G.2 Recommendations for Future Work.....	190
G.3 References.....	191

List of Tables

Table 1.1	Geometry for the Blade Tip Model.....	20
Table 1.2	Matrix of Experiments and Resulting Blowing Ratios	20
Table 2.1	Description of Hole Models.....	49
Table 2.2	Blade Geometry and Flow Conditions.....	49
Table 2.3	Matrix of Experiments	49
Table 2.4	Location of Path Line Data for Each Geometry	50
Table 3.1	Testing Conditions and Blade Parameters	82
Table 3.2	Line Positions Used to Make Path Line Plots.....	82
Table 4.1.	Testing Conditions and Blade Parameters	112
Table 4.2.	Line Positions Used to Make Path Line Plots.....	112
Table 4.3.	Reynolds numbers and geometric properties of several microcircuit channels.....	112
Table E.1	Microcircuit Channel Convective Effectiveness Values	165
Table E.2	Geometric Properties of Microcircuit Channels	166

List of Figures

Figure 1.1	Schematic of the wind tunnel facility used for the testing of the blade tips.	21
Figure 1.2	The corner test section of the wind tunnel housed three blades that formed two full passages.	21
Figure 1.3	The blade tip included a plenum that supplied coolant to the dirt purge holes.	21
Figure 1.4	Main tip heat transfer surface showing serpentine passages (a) and detail of main tip heater as placed on the blade surface (b).	22
Figure 1.5	Measured and predicted static pressures at the blade mid-span.	22
Figure 1.6	Adiabatic effectiveness contours taken along the tip with dirt purge blowing of 0.10%, 0.19%, 0.29%, 0.38% flow for the small tip gap.	23
Figure 1.7	Adiabatic effectiveness contours taken along the tip with dirt purge blowing of 0.10%, 0.19%, 0.29%, 0.38% flow for the large tip gap.	23
Figure 1.8	Definition of the blade camber line and associated axis.	23
Figure 1.9	Effectiveness measurements taken along the blade camber line for the small (a) and large (b) tip gaps.	24
Figure 1.10	Area-averaged adiabatic effectiveness along the tip plotted against dirt purge flow at various coolant blowing levels.	25
Figure 1.11	Comparison of experimental data to a fully-developed correlation.	25
Figure 1.12	Baseline Nusselt number contour plots for the small (a) and large (b) tip gap heights.	26
Figure 1.13	Camber line data for h_f/h_0 for the small (a) and large (b) tip gap.	27
Figure 1.14	CFD predictions of dirt purge streamlines for the large tip gap (Hohlfeld [21]).	28
Figure 1.15	Area-averaged heat transfer augmentation for the small and large tip gaps.	28
Figure 1.16	Contour plots of NHFR for the small (top) and large (bottom) gap heights at all blowing ratios tested.	29
Figure 1.17	NHFR taken along the Camber line for the small (a) and large (b) gap heights.	30

Figure 1.18	Area-averaged NHFR for both gap heights and all blowing ratios tested.	30
Figure 2.1	Schematics showing the hole geometry for the EDM drilled holes.....	50
Figure 2.2	Schematics showing the hole geometry for the laser drilled holes.....	51
Figure 2.3	Images of SLA model for the EDM holes (a) and laser holes (b) placed within the foam blade.....	51
Figure 2.4	Schematic of wind tunnel facility for the tip tests	51
Figure 2.5	Top view of the test section for the blade tip tests.....	52
Figure 2.6	Predicted and measured static pressure distributions for the large and small tip gap cases for the EDM (a) and laser drilled (b) holes for the tip study. Also indicated are the hole locations along the pressure side of the airfoil and the pressure distribution at the 95% span location near the tip.....	53
Figure 2.7	Discharge coefficients that were measured for the EDM hole model (a) and laser hole model (b) including the discharge coefficients for the dirt purge holes and TEF.	54
Figure 2.8	Local mass flux ratios for each of the EDM (a) and laser (b) holes placed on the pressure side of the blade	54
Figure 2.9	Coolant flow split for the EDM (a) and laser (b) holes at a total coolant of 0.68%. Note hole 1 is closest to the stagnation location.....	55
Figure 2.10	Comparison of computational and experimental flow rates for the EDM holes with 0.68% coolant flow.....	55
Figure 2.11	Measured adiabatic effectiveness levels on the tip for the EDM (left) and laser (right) drilled hole cases for the small tip gap.....	56
Figure 2.12	Predicted path lines for the EDM geometry (left) and laser geometry (right).	57
Figure 2.13	Data taken along the camber line for the small tip gap with EDM holes (a) and laser holes (b).	58
Figure 2.14	Measured adiabatic effectiveness levels on the tip for the EDM (left) and laser (right) drilled hole cases for the large tip gap.	59
Figure 2.15	Data taken along the camber line for the large tip gap with EDM holes (a) and laser holes (b).	60

Figure 2.16	Camber lines of effectiveness for the small (a) and large (b) tip gaps for the two cooling hole geometries.	61
Figure 2.17	Path line data for the EDM (a – c) and laser (d – f) cases.	62
Figure 2.18	Area-averaged effectiveness for the entire tip (a) and for downstream 70% portion of the blade tip (b).	63
Figure 2.19	Effectiveness contours with no dirt purge blowing for the front plenum only with the EDM holes (a) and laser holes (b).	63
Figure 3.1	Test section viewed from top showing flow adjustment capabilities and infrared (IR) window segments.	83
Figure 3.2	Pressure distribution around the center blade mid-span compared to inviscid CFD prediction. Also indicated are the hole locations placed on the pressure side of the tip.	83
Figure 3.3	The three tip geometries tested were the baseline geometry (a), EDM hole geometry (b, d), and laser hole geometry (c, e).	84
Figure 3.4	Main tip heat transfer surface showing serpentine passages (a) and detail of main tip heater as placed on the blade surface (b).	84
Figure 3.5	Comparison of experimental data to a fully-developed correlation.	85
Figure 3.6	Comparison of experimental data to the proposed augmentation factor. ...	85
Figure 3.7	Baseline Nusselt number contour plots for the small (a) and large (b) tip gap heights.	86
Figure 3.8	Camber line and pressure side line plots for the baseline cases.	86
Figure 3.9	Normal line plots at lines 0 and 3 for baseline cases at the large and small tip gaps.	87
Figure 3.10	Heat transfer augmentation shown on path line plots for the laser and EDM hole shapes for both tip gaps at lines 1, 2, and 3.	88
Figure 3.11	Heat transfer augmentation taken at the camber line for the small tip gap (a) and large tip gap (b).	89
Figure 3.12	Area-averaged heat transfer augmentation with blowing for the small and large tip gaps for both hole geometries.	89

Figure 3.13	Pressure side line plots for the laser hole showing areas of negative NHFR for the small tip gap.	90
Figure 3.14	NHFR for the EDM and laser holes for both tip gaps at 0.58% and 1% coolant flow.	91
Figure 3.15	NHFR shown on path line plots for the laser and EDM hole shapes for both tip gaps at lines 1, 2, and 3.....	92
Figure 3.16	NHFR Camber lines for the EDM and laser holes for the small and large tip gap.....	93
Figure 3.17	Area-averaged NHFR using the total tip area (a) and area-averaged NHFR over the downstream 70% of blade (b).	93
Figure 4.1.	Detail of microcircuit design and internal cooling.	113
Figure 4.2.	Test section viewed from top showing flow adjustment capabilities and infrared (IR) window segments.	113
Figure 4.3.	Pressure distribution around the center blade mid-span compared to inviscid CFD prediction. Also indicated are the hole locations placed on the pressure side of the tip.	114
Figure 4.4.	Microcircuit tip geometry passage layout (a) and hole locations on blade tip (b).....	115
Figure 4.5.	Relative coolant flow through each of the microcircuit holes (1-16) and the dirt purge holes (17-18) for typical cases	115
Figure 4.6.	Main tip heat transfer surface showing serpentine passages (a) and detail of main tip heater as placed on the blade surface (b).....	116
Figure 4.7.	Baseline Nusselt number contour plots for the small (a) and large (b) tip gap heights.	116
Figure 4.8.	Heat transfer augmentation shown on path line plots for both tip gaps at all blowing ratios tested at lines 1, 2, and 3.	117
Figure 4.9.	Heat transfer augmentation shown on path line 4 for both tip gaps.	118
Figure 4.10.	Adiabatic effectiveness and heat transfer augmentation taken at the pressure-side line showing the difference in peak locations.....	118
Figure 4.11	Heat transfer augmentation taken at the camber line for the small tip gap (a) and large tip gap (b).....	119

Figure 4.12.	Area-averaged heat transfer augmentation with blowing for the small and large tip gaps for the entire blade surface (a) and the last 70% (b).	119
Figure 4.13.	Lines showing areas of low NHFR.	120
Figure 4.14.	NHFR for both tip gaps at all coolant flows tested.....	121
Figure 4.15	NHFR shown on path line plots for both tip gaps at all blowing ratios tested at lines 1 and 2.	122
Figure 4.16.	NHFR along the camber lines for the small (a) and large (b) tip gaps. ...	123
Figure 4.17.	Area-averaged NHFR for the blade for the large and small tip gap over the entire blade surface (a) and the last 70% (b).....	123
Figure 4.18.	Example of methodology for finding microcircuit internal efficiency, shown here for the large tip gap, 0.5% coolant flow case.	124
Figure 4.19.	Microcircuit efficiency for all blowing ratios tested and both tip gaps. ...	124
Figure 4.20.	Internal heat transfer augmentation with microcircuit design shown for channels 8, 10, 15, and 16.....	125
Figure 4.21.	Internal heat transfer augmentation with microcircuit design plotted as a function of channel Reynolds number based on hydraulic diameter.	125
Figure A.1	Pratt & Whitney's F-119 turbo fan engine used to power the F-22 fighter.	128

Figure B.1	Image numbering scheme used in MATLAB contouring program.	135
Figure B.2	Location of calibration thermocouples and markers on the test tips.	135
Figure B.3	Visualization of mapping sequence. Infrared images are loaded into MATLAB (a) and mapped to the blade co-ordinate system (b). User interaction corrects the imperfections and the blade contour is mapped correctly (c).	136
Figure B.4	Benchmarking tests for blowing from the dirt purge holes at the large tip gap at four coolant flow conditions.	136
Figure B.5	Repeatability test for the laser hole geometry at the small tip gap with 0.47% total coolant flow.	137
Figure B.6	Heat transfer augmentation for the dirt purge small tip gap at 0.19% total coolant flow with a heat flux of 2500 W/m ² (a) and 3700 W/m ² (b).	137
Figure B.7.	Heat transfer augmentation along the camber line for the low ($q'' = 2500$ W/m ²) and high ($q'' = 3700$ W/m ²) dirt purge cases with 0.19% coolant flow.	138
Figure B.8	Description of test performed to verify uniform thermal field within microcircuit passages and repeatability of internal heat transfer measurements.	138
Figure B.9	Repeatability test for internal channel efficiency also verified uniform thermal field. The microcircuit numbers in bold (6, 11, 15) had the thermocouples moved as shown in Figure B.8.	139
Figure C.1	Contours of heat transfer augmentation for all dirt purge cases at the small tip gap (left) and large tip gap (right).	147
Figure C.2	Adiabatic effectiveness along the pressure-side line for the small tip gap (a) and large tip gap (b).	148
Figure C.3	Heat transfer augmentation taken along the pressure side line for all dirt purge cases at the small tip gap (a) and large tip gap (b).	149
Figure C.4	NHFR along the pressure-side line for the small tip gap (a) and large tip gap (b).	150
Figure C.5	Line positions used for dirt purge analysis. All lines taken normal to the blade pressure-side curve.	151

Figure C.6	Adiabatic effectiveness, heat transfer augmentation, and NHFR at line position 1 for the small (left) and large (right) tip gaps.....	152
Figure C.7	Adiabatic effectiveness, heat transfer augmentation, and NHFR at line position 2 for the small (left) and large (right) tip gaps.....	153
Figure C.8	Adiabatic effectiveness, heat transfer augmentation, and NHFR at line position 3 for the small (left) and large (right) tip gaps.....	154
Figure C.9	Adiabatic effectiveness, heat transfer augmentation, and NHFR at line position 4 for the small (left) and large (right) tip gaps.....	155
Figure D.1	Heat transfer augmentation contours for the EDM and laser holes at both tip gaps and blowing ratios tested.....	158
Figure D.2	Nu/Nu_0 for path lines 2, 3, and 4 as described in the third paper.	159
Figure D.3	Adiabatic effectiveness along the pressure-side line for the EDM and laser holes at both tip gaps and blowing ratios tested.	160
Figure D.4	Heat transfer augmentation along the pressure-side line for the EDM and laser holes at both tip gaps and blowing ratios tested.....	161
Figure D.5	NHFR along the pressure-side line for the EDM and laser holes at both tip gaps and blowing ratios tested.	162
Figure E.1	Contours of heat transfer augmentation for all microcircuit cases at the small tip gap (left) and large tip gap (right).....	167
Figure E.2	Adiabatic effectiveness (η) data taken along the pressure-side line for the microcircuit small tip gap tests at all blowing ratios.	168
Figure E.3	Adiabatic effectiveness (η) data taken along the pressure-side line for the microcircuit large tip gap tests at all blowing ratios.	168
Figure E.4	Cooling effectiveness (ϕ) data taken along the pressure-side line for the microcircuit small tip gap tests at all blowing ratios.	169
Figure E.5	Cooling effectiveness (ϕ) data taken along the pressure-side line for the microcircuit large tip gap tests at all blowing ratios.	169
Figure E.6	Heat transfer (h_f/h_0) data taken along the pressure-side line for the microcircuit small tip gap tests at all blowing ratios.	170

Figure E.7	Heat transfer (h_f/h_0) data taken along the pressure-side line for the microcircuit large tip gap tests at all blowing ratios.	170
Figure E.8	NHFR data taken along the pressure-side line for the microcircuit small tip gap tests at all blowing ratios.....	171
Figure E.9	NHFR data taken along the pressure-side line for the microcircuit large tip gap tests at all blowing ratios.....	171
Figure E.10	Comparison of adiabatic effectiveness and heat transfer augmentation for the 0.5% coolant flow taken along the pressure-side line.....	172
Figure E.11	Comparison of adiabatic effectiveness and heat transfer augmentation for the 1.0% coolant flow taken along the pressure-side line.....	172
Figure E.12	Comparison of adiabatic effectiveness and heat transfer augmentation for the 1.5% coolant flow taken along the pressure-side line.....	173
Figure E.13	Comparison of adiabatic effectiveness and heat transfer augmentation for the 2.0% coolant flow taken along the pressure-side line.....	173
Figure E.14	Comparison of adiabatic effectiveness and heat transfer augmentation for the 0.5% coolant flow taken along the blade camber line.	174
Figure E.15	Comparison of adiabatic effectiveness and heat transfer augmentation for the 1.0% coolant flow taken along the blade camber line.	174
Figure E.16	Comparison of adiabatic effectiveness and heat transfer augmentation for the 1.5% coolant flow taken along the blade camber line.	175
Figure E.17	Comparison of adiabatic effectiveness and heat transfer augmentation for the 2.0% coolant flow taken along the blade camber line.	175
Figure F.1	Comparison between hole shapes for 1.0% coolant flow at the small tip gap.....	178
Figure F.2	Comparison between hole shapes for 1.0% coolant flow at the large tip gap.....	179
Figure F.3	Adiabatic effectiveness (η) taken along the camber line for the 1.0% coolant flow comparison at the small tip gap.	180
Figure F.4	Adiabatic effectiveness (η) taken along the camber line for the 1.0% coolant flow comparison at the large tip gap.	180

Figure F.5	Heat transfer augmentation (h_f/h_0) taken along the camber line for the 1.0% coolant flow comparison at the small tip gap.	181
Figure F.6	Heat transfer augmentation (h_f/h_0) taken along the camber line for the 1.0% coolant flow comparison at the large tip gap.	181
Figure F.7	NHFR along the camber line for the 1.0% coolant flow comparison at the small tip gap.	182
Figure F.8	NHFR along the camber line for the 1.0% coolant flow comparison at the large tip gap.	182
Figure F.9	Adiabatic effectiveness (η) taken along the pressure-side line for the 1.0% coolant flow comparison at the small tip gap.	183
Figure F.10	Adiabatic effectiveness (η) taken along the camber line for the 1.0% coolant flow comparison at the large tip gap.	183
Figure F.11	Heat transfer augmentation (h_f/h_0) taken along the camber line for the 1.0% coolant flow comparison at the small tip gap.	184
Figure F.12	Heat transfer augmentation (h_f/h_0) taken along the camber line for the 1.0% coolant flow comparison at the large tip gap.	184
Figure F.13	NHFR along the camber line for the 1.0% coolant flow comparison at the small tip gap.	185
Figure F.14	NHFR along the camber line for the 1.0% coolant flow comparison at the large tip gap.	185
Figure F.15	Area-averaged adiabatic effectiveness levels over the entire tip (a) and the last 70% (b) for all geometries and tip gaps tested.	186
Figure F.16	Area-averaged heat transfer augmentation over the entire tip (a) and the last 70% (b) for all geometries and tip gaps tested.	186
Figure F.17	Area-averaged NHFR over the entire tip (a) and the last 70% (b) for all geometries and tip gaps tested.	187
Figure F.18	Area-averaged cooling effectiveness over the entire tip (a) and the last 70% (b) for the microcircuit holes.	187

Paper 1:
**Measured Adiabatic Effectiveness and Heat Transfer
for Blowing from the Tip of a Turbine Blade**

To be submitted to the *Journal of Turbomachinery**

Abstract

The clearance gap between the tip of a turbine blade and the shroud has an inherent leakage flow from the pressure side to the suction side of the blade. This leakage flow of combustion gas and air mixtures leads to severe heat transfer rates on the blade tip of the high pressure turbine. As the thermal load to the blade increases, blade alloy oxidation and erosion rates increase thereby adversely affecting component life. The subject of this paper is the cooling effectiveness levels and heat transfer coefficients that result from blowing through two holes placed in the forward region of a blade tip. These holes are referred to as dirt purge holes and are generally required for manufacturing purposes and expelling dirt from the coolant flow when, for example, operating in sandy environments.

Experiments were performed at two tip gap heights over a range of blowing ratios. Results indicate that the cooling effectiveness is highly dependent upon the tip gap clearance with better cooling achieved for the smaller clearances. Also, heat transfer is found to increase with blowing. In considering an overall benefit of cooling from the dirt purge blowing, a large benefit can be realized for a smaller tip gap as compared with a large tip gap.

*Co-authors: Dr. Karen A. Thole, Mechanical Engineering Department, Virginia Tech
Dr. Frank J. Cunha, Turbine Durability, Pratt & Whitney

Introduction

The performance of a turbine engine is a strong function of the maximum gas temperature at rotor inlet. Because turbine airfoils are exposed to hot gas exiting the combustion chamber(s), the materials and cooling methods are of critical importance. Turbine blade designers concentrate heavily on finding better cooling schemes to increase the overall operation life of all turbine airfoils, namely the high pressure turbine blades. The clearance between the blade tip and the associated shroud, also known as the blade outer air seal, provides a flow path across the tip that leads to aerodynamic losses and high heat transfer rates along the blade tip. The flow within this clearance gap is driven by a pressure differential between the pressure and suction side of the blade, but is also affected by the viscous forces as the fluid comes into contact with the walls of the gap.

From an operational point-of-view, engine removals from service are primarily dictated by the spent exhaust gas temperature (EGT) margin caused by deterioration of the high pressure turbine components. Increased clearance gaps accelerate effects of low cycle thermal-mechanical fatigue, oxidation, and erosion as a result of increased temperatures in the turbine and decreased EGT margin. In general, tip clearance reductions for large commercial engines are of the order of 0.25 mm, which can reduce the specific fuel consumption by 1% and EGT by 10°C as stated by Lattime and Steinetz, [1]. Improving the blade tip durability can, therefore, produce fuel and maintenance savings over hundreds of millions of dollars per year (Lattime and Steinetz, [1]).

The work presented in this paper is on a realistic design for a turbine blade tip consisting of a flat tip with the exception of a small cavity in which two dirt holes are placed. The location of these holes is a direct consequence of the internal cooling passages within the blade. The purge hole cavity extends only over a small area in the front portion of the blade tip. The function of the dirt purge holes includes the following: (1) purge holes allow centrifugal forces to expel any dirt ingested by the compressor into the turbine rather than clogging the smaller diameter film cooling holes; and (2) purge holes provide a way to support the ceramic core during the lost-wax investment casting of the blade manufacturing process. The dirt purge cavity is present to insure that the purge holes remain open during eventual blade rubbing.

This paper details the film-cooling and heat transfer associated with blowing from the dirt purge holes along the tip of a turbine blade. Measurements of adiabatic effectiveness and heat transfer coefficients are studied while varying the tip clearance and mass flux (blowing) ratios.

Past Relevant Studies

The work presented in this paper is concerned with the effects of injecting coolant from the tip of a turbine blade whereby the experiments were completed for a stationary, linear cascade. As such, it is important to consider the relevance of past studies to evaluate the effects of the relative motion between the blade tip and outer shroud. While there have been no studies reported in the open literature with a geometry such as that presented in this paper, it is also relevant to consider tests whereby tip blowing has been investigated.

Regarding the effects of blade rotation, the first work to address the flow field effects was that by Morphis and Bindon [2] who found that their static pressure measurements across the blade tip in an annular turbine cascade were not affected by the relative motion at the tip. They concluded that the basic nature of the flow structures remained unchanged with and without relative motion. In contrast, the studies by Tallman and Lakshminarayana [3] and Yaras and Sjölander [4] showed that the leakage flow through the gap was reduced along with the leakage vortex in the case of a moving wall relative to a fixed wall. They attributed this difference to the passage vortex being convected towards the suction surface by the moving wall and postulated that the passage vortex position can alter the driving pressure through the tip gap.

Although there are apparent effects of a moving wall on some of the reported flow field studies, tip heat transfer studies generally indicate relatively minor to non-existent effects of a moving wall. The reason for this relatively minor effect was first hypothesized by Mayle and Metzger [5], who evaluated the effects of relative motion on the heat transfer in a simple pressure-driven duct flow. They derived and also showed experimentally that for a flow path length with less than 20 times the clearance gap, the flow can be considered as developing duct flow. As such, the boundary layers on each surface do not merge and therefore the effect of the relative wall (shroud) movement is inconsequential. This range is relevant to the assessment given that the length of the flow path along the blade tip relative to the clearance gap ranges between 2.5 near the trailing edge for the smallest gap to 25 near the leading edge (thickest part of the airfoil) for the largest gap. Lending further credibility to the hypothesis of Mayle and Metzger are the works of Chyu et al. [6] with a shroud surface moving over a simple rectangular cavity and Srinivasan and Goldstein [7] with a moving wall over a turbine blade. In particular, the work of Srinivasan and Goldstein showed only small effects of the wall motion on their measured Sherwood numbers (heat-mass transfer analogy) in the leading edge region where the

path length to clearance gap was larger (30) than the criterion stated by Mayle and Metzger (20) for the smallest clearance gap that they studied. At the largest clearance gap in their study, they saw no noticeable effect of the wall motion.

The only reported tip blowing studies were those completed by Kim and Metzger [8] and Kim et al.[9], who used a two-dimensional channel with a number of different injection geometries, and by Kwak and Han [10,11], Acharya, et al. [12], and Hohlfeld, et al.[13], who all used blade geometries. Four tip blowing geometries were investigated by Kim et al. that included the following: discrete slots located along the blade tip, round holes located along the blade tip, angled slots positioned along the pressure side, and round holes located within a cavity of a squealer tip. For a given coolant flow, the best cooling performance was obtained using the discrete slot configuration whereby an optimum blowing ratio was discerned. In general, Kim et al. reported higher effectiveness accompanied by higher heat transfer coefficients with higher injection rates. Kwak and Han [10,11] reported measurements for varying tip gaps with cooling holes placed along the pressure surface at a 30° breakout angle and on the tip surface for an unshrouded [10] and shrouded [11] tip. For the unshrouded (flat) tip, Kwak and Han found increases in the heat transfer coefficients and adiabatic effectiveness occurred with increased coolant injection and increased gap heights. This is in contrast to the work presented by Kim et al., who identified an optimum blowing ratio. For the shrouded tip, Kwak and Han indicated a benefit of having a shroud in that there was a reduction of the heat transfer coefficients and an increase in adiabatic effectiveness levels when compared to the flat tip.

Heat transfer measurements on flat tips with no cooling have been presented by many authors, including Bunker et al. [14], Kwak and Han [10], and Jin and Goldstein [15]. These studies have shown there to be a region of low heat transfer located near the thickest portion of the blade. Morphis and Bindon [2] and Bindon [16] have also shown there to be a separation region that others have shown to have a very high heat transfer along the pressure side of the blade tip in the entry region (Bunker et al. [14]).

There have also been only a relatively few computational predictions for a tip gap with blowing including those by Acharya et al. [12] and Hohlfeld et al. [13]. Acharya et al. found that film coolant injection lowered the local pressure ratio and altered the nature of the leakage vortex. High film cooling effectiveness and low heat transfer coefficients were predicted along the coolant trajectory. Both studies indicated that for the smallest tip gap, the coolant impinged

directly on the shroud, but as the gap size increased, predictions indicated that the coolant jets were unable to impinge upon the shroud.

In summary, only a handful of studies have addressed blowing in the tip gap region with none of these studies detailing a geometry similar to the one presented in this paper.

Experimental Facilities and Methodology

The experiments were conducted in a large-scale, low-speed, closed-loop wind tunnel that provided matched engine Reynolds number conditions. The flow conditions and relevant geometry are summarized in Table 1.1 with a diagram of the wind tunnel and test section shown in Figure 1.1 and Figure 1.2. Results reported in this paper include adiabatic wall temperature measurements and heat transfer coefficients along the tip.

The wind tunnel, shown in Figure 1.1, includes a 50 Hp fan that drives the flow through a primary heat exchanger to obtain a uniform temperature profile. The flow is divided into three passages. The main passage, located in the center, has a heater used to achieve a hot mainstream gas, while the flow in the two outer passages provided a single row of normal jets used to generate an inlet turbulence level to the cascade of 10% and a length scale of 11 cm. These jets were unheated (due to a facility constraint) and were injected one chord upstream of the blade. The mass flow of the injected jets represented 4.3% of the core mass flow and had a momentum flux ratio of 8. Because of the high turbulence generated, the thermal field entering the cascade was quite uniform.

The main features of the linear cascade test section, shown in Figure 1.2, were an instrumented center blade, two outer blades, sidewall bleeds, and adjustable tailboards. These components were required to insure periodic flow conditions. Coolant flow for the blade tip was provided to a plenum inside the center blade from an independent pressurized air supply. The pressure drop across a venturi meter was used to quantify the coolant flowrate while the incoming velocity to the test section was measured with a pitot probe at several locations across the blade pitch.

Figure 1.3 shows the details of the plenum for the blade tip, the dirt purge cavity and the dirt purge holes. The removable portion of the tip was 28% of the span and was specifically molded to allow for a number of different tip geometries to be studied. A two-part foam mixture that exothermically expanded was used to mold the tip. The thermal conductivity of this foam

was quite low at 0.036-0.043 W/mK dependent upon the foam properties after expansion; thereby allowing for an adiabatic surface on the blade tip.

For the adiabatic effectiveness tests, the experiments were conducted such that the coolant was nominally 25°C lower than the mainstream. This thermal equilibrium required about 4 hours for each test. For the heat transfer measurements, separate experiments were performed with a constant heat flux surface installed on the tip surface. For these tests, the coolant and mainstream temperatures were typically kept to within 0.15°C of one another. Two separate heaters were necessary because of the dirt purge cavity on the tip. The dirt purge cavity was heated with one strip of Inconel that was 0.051 mm thick and had a surface area of 17.3 cm². The main heater covered an area of 261.2 cm² and consisted of a serpentine Inconel circuit. As shown in Figure 1.4, the circuit consisted of the Inconel sandwiched between insulating Kapton and then covered with a very thin (0.013 mm) layer of copper on both sides. Both heaters were attached to a foam blade tip using double-sided tape that was 0.64 mm thick. The nominal heat flux for both heaters was set to 3700 W/m² which provided a maximum temperature difference between the mainstream and blade surface of 28°C. The two heaters were controlled independently with a variac to within 0.67% of one another during all tests. The current supplied to each heater was known by placing a precision resistor ($R = 1\Omega \pm 0.1\%$) in each circuit and measuring the voltage drop across each resistor with a digital multimeter. The heater power was then determined from the supplied current and known heater resistance.

Equation 1 was used when calculating the heat transfer coefficients.

$$h = \frac{q_{\text{tot}}'' - q_r''}{T_w - T_\infty} \quad (1)$$

In this equation, q_{tot}'' represents the total heat flux output from the resistive heaters and q_r'' represents the energy lost to radiation. Typically, radiation losses were less than 2% with the maximum for all cases being 3.4%. Conduction losses were found to be negligible since the heaters were placed on the low thermal conductivity foam.

For the surface temperature measurements along the tip, an infrared (IR) camera was used to take four separate images that were then assembled to provide the entire surface temperatures of the tip. The image locations are shown in Figure 1.2. The IR camera was positioned to look directly at the blade tip and required the use of a zinc selenide window placed along the outer shroud that permitted 8-12 micron wavelengths to pass through. Each of the four

IR camera images covered an area that was 21.3 cm by 16 cm with the area being divided into 320 by 240 pixel locations. The camera was located approximately 55 cm from the tip, resulting in a spatial resolution of 0.63 mm, which is over 16 times smaller than the dirt purge diameter. At each viewing location five images were acquired and averaged at each pixel location to give an overall image of the tip.

The calibration process for the camera involved direct comparisons of the infrared radiation collected by the camera with measured surface temperatures using either thermocouple strips placed on the tip surface (for the adiabatic effectiveness measurements) or thermocouple beads placed underneath the heater (for the heat transfer measurements). For both experiments, thermocouples were placed on the blade surface using a bonding agent with a high thermal conductivity of 1.6 W/m K. For the thermocouples placed underneath the main tip heater, a 2°C temperature adjustment was applied during calibration to account for the thermal resistivity of the heater at the nominal $q'' = 3700 \text{ W/m}^2$. The thermal resistance of the Inconel heater in the dirt purge cavity was found to be negligible and no correction was needed for this area of the blade tip. After the experiments were completed, the infrared images were processed whereby adjustments of the surface emissivity and background temperature (irradiation) were made until the image and thermocouple temperatures matched. This process resulted in an agreement between all of the thermocouples and infrared temperatures to within $\pm 1.0\text{C}$ ($\Delta\eta = \pm 0.04$). A check on the calibration process is that the four individual images matched up well to form one entire blade contour without any jumps in measured values between images.

Static pressure taps were located near the mid-span of the central blade and tufts were located near the stagnation locations of all the blades to insure periodic flow through the passages was achieved. The measured static pressure distribution around the center blade was compared with an inviscid CFD simulation using periodic boundary conditions indicating good agreement, as shown in Figure 1.5.

Overall uncertainties were calculated for non-dimensional temperature and heat transfer (η and Nu values) according to the partial derivative method described in Moffat [17]. The total uncertainty of all measurements was calculated as the root of the sum of the squares of the precision uncertainty and the bias uncertainty.

The precision uncertainty for measurements made with the infrared camera was determined through an analysis of five calibrated images taken in succession on one portion of

the tip at constant conditions. The precision uncertainty was calculated to be 0.31°C , which is the standard deviation of the five readings based on a 95% confidence interval. The camera manufacturer reported the bias uncertainty as 2.0% of the full scale. The largest scale used in this study was 20°C though some images could be captured on a 10°C range. The thermocouples measuring the freestream and coolant temperatures were reported by the manufacturer to read within $\pm 0.2^{\circ}\text{C}$. The total uncertainty in effectiveness was found to be $\partial\eta = \pm 0.026$ at $\eta = 1$ and $\partial\eta = \pm 0.026$ at $\eta = 0.2$. The total uncertainty in heat transfer measurements was 6% at $\text{Nu}_{\text{Dh}} = 45$ and 10.5% at $\text{Nu}_{\text{Dh}} = 55.7$.

Experimental Test Cases

This series of experiments focused on investigating the effect of tip gap height and blowing ratio as indicated in Table 1.2. With regards to the tip gap height, two different gaps relative to the span were investigated including gaps that were 0.54% (h) and 1.63% (H) of the span. Through the remainder of this paper these two tip gaps will be referred to as small and large tip gaps. With regards to the blowing from the dirt purge holes, cases at each tip gap height were measured with a coolant flow rate that ranged from 0.10% to 0.38% of the primary core flow. Note that these flow rate ranges were chosen to simulate engine conditions. A baseline case was also considered for heat transfer measurements that had the dirt purge cavity present, but no holes. Measurements were performed at both gap heights for the baseline case.

The global and local ratios of mass and momentum fluxes were calculated for the blowing cases and are also given in Table 1.2. The global mass and momentum flux ratios were based on the incident inlet velocity to the blade passage while the local mass and momentum flux ratios were based on the local tip flow conditions for each of the two dirt purge holes. To compute the local external velocity for the dirt purge hole exits, the local static pressure for the dirt purge holes was taken as the average of the predicted static pressures for the pressure and suction surfaces at the 95% blade span location. The blade locations of these pressures were at 2% and 5% of the total surface distance measured from the stagnation location for dirt purge holes 1 and 2, respectively. The coolant velocity was calculated directly from measured coolant flow rates and was assumed to be equally split among the two dirt purge holes. As seen in Table 1.2, the local blowing (and momentum) ratio for hole 1, which is the hole closest to the leading

edge, is significantly higher than hole 2, due to the lower local velocity present at the hole 1 location.

Adiabatic Effectiveness Results for the Blade Tip

The dirt purge holes serve the functional purpose of expelling dirt from the blade that might otherwise block smaller film cooling holes. Any cooling from the dirt purge holes is of potential benefit for cooling the leading edge region. The cooling effects of the dirt purge jets are presented as adiabatic effectiveness levels that were measured only in the leading edge half of the blade. No coolant from the dirt purge holes was measured along the downstream portion of the blade tip, and as such, only the front portions of the tip were measured and are presented in this paper.

Figure 1.6 presents the measured adiabatic effectiveness contours for the small tip gap case at four different blowing ratios, ranging from 0.10% to 0.38%. At the lowest blowing ratio, the dirt purge holes cool only a portion of the tip downstream of the holes. There is very little cooling measured within the dirt purge cavity. There is a dramatic increase in the measured adiabatic effectiveness levels as the coolant flow is increased for the small tip gap. The maximum effectiveness for the lowest blowing ratio was 0.86 while the 0.19%, 0.29%, and 0.38% blowing ratios reached the maximum value of $\eta = 1.0$. For coolant injection greater than the 0.19% case, a completely cooled region was measured to extend from the pressure side of the tip to the suction side. Interestingly, the coolant is also present upstream of the dirt purge holes such that at the highest blowing ratio, the coolant extended to the leading edge of the tip. This is because the coolant exiting the dirt purge holes impacted the shroud and then propagated outward in all directions. These very high effectiveness levels in the leading edge region indicate a saturation of the coolant within the tip gap. In general, this is consistent with field run hardware where this portion of the airfoil has little evidence of tip oxidation.

Figure 1.7 presents the measurements of adiabatic effectiveness contours for the large tip gap. Results indicate a significantly reduced benefit of the coolant exiting the dirt purge holes as compared with the small tip gap. As the coolant is increased, the experiments show a much broader cool region downstream of the cavity. This spreading of the coolant for the higher blowing ratio cases is caused by an impingement of the jets onto the shroud. At the 0.38%

coolant injection there is coolant present with the dirt purge cavity and upstream of the cavity. This is more similar to the small tip gap where coolant is filling the entire gap.

The camber line of the blade is used to compare data and is defined in Figure 1.8. This line extends through the mid-section of the blade. Effectiveness data was taken along the camber line of the blade, shown in Figure 1.9, to further illustrate the differences between the cases tested. The vertical lines on both plots indicate the location of the dirt purge holes. For the small tip gap shown in Figure 1.9a, the 0.10% case has significantly lower effectiveness values than the other coolant levels. For the 0.19%, 0.29%, and 0.38% cases, there is hardly any difference in peak values between the cases, but there is increased spreading in the leading edge region with increased blowing. Also, at the higher blowing ratios, the camber line shows that the effectiveness does reach a value of one almost all the way to the stagnation point ($x/C = 0$). For the large tip gap shown in Figure 1.9b the effectiveness steadily increases with each blowing case as was discussed for the contour levels. Both the peak values and spreading in the leading edge are increased with each increase in blowing rate. However, there appears to be no benefit of nearly doubling the coolant flow from 0.10% to 0.19% at the large tip gap until downstream of the second hole after which there is more spreading of the coolant for the higher coolant flow. Also, the overall effectiveness levels are lower at the large tip gap relative to the small tip gap.

For all cases shown in Figures 9a and 9b, the results indicate η values that are above zero outside of the region affected by the dirt purge blowing. The reason for this non-zero effectiveness level is due to a thermal boundary layer effect. As was discussed in the experimental section of this paper, the heaters for the main gas path are located significantly upstream of the test section. As the flow progresses through the contraction of just upstream of the test section, the flow near the wall is slightly cooler than the mid-span temperature resulting in non-zero effectiveness levels.

All of the effectiveness measurements for dirt purge cases are summarized by considering an area average of the effectiveness levels over the forward 30% of the tip, as shown in Figure 1.10. Only the front portion of the blade is considered to emphasize the dirt purge region. Overall there is a dramatic difference between the small tip gap and the large tip gap at each blowing ratio. The small tip gap shows the average effectiveness increases with blowing ratio, but is leveling off at the higher injection levels. The area averages for the large tip gap case show

that the effectiveness only slightly increases when the blowing ratio is increased from 0.10% to 0.19% with larger increases being measured beyond 0.19% injection levels.

Heat Transfer Measurements for the Blade Tip

As discussed, separate experiments were performed to measure heat transfer for baseline cases with no blowing and for the blowing cases at both tip gap heights. These measurements were completed using a constant heat flux boundary conditions on the tip surface. Baseline studies with no blowing were used to validate the current experiments with previous ones by comparing with a fully developed channel flow correlation. The heat transfer for the blowing cases was normalized by the baseline cases to provide the heat transfer augmentation associated with each blowing case considered. Also, the results from the adiabatic effectiveness experiments were combined with these heat transfer measurements to quantify the overall blade thermal loading for each of the blowing cases.

Baseline Cases – No blowing

Previous studies have compared flow in a turbine blade tip gap region to that of a fully developed channel flow correlation for turbulent flow in a duct. The correlation that was used for comparison in our paper was developed by Gnielinski [18]. Gnielinski's correlation is given in equation 2 and has been reported in the literature to provide accuracy to within 6% as reported by Kakaç [19] for a large Reynolds number range ($10^4 < Re < 10^6$).

$$Nu_{fd} = 0.0214(Re^{0.8} - 100) Pr^{0.4} \quad (2)$$

Mayle and Metzger [5] furthered this correlation for a tip gap by adding an augmentation factor to account for the overwhelming entry region effects of thin blade tips. This augmentation factor, which was taken from Kays and Crawford [20], allows blade designers to relate overall blade tip heat transfer (for a given blade thickness and tip gap) to an overall heat transfer expected in a fully developed channel.

Comparisons have been made to the data of Jin and Goldstein [15] and Bunker et al. [14] that confirm this augmentation factor approach. Although Mayle and Metzger [5] first noted the augmentation factor, their data has not been included in this comparison because only experiments performed on airfoil shapes were considered. This is because the plotting variables were based on blade exit velocity, of which there is no equivalent in the Mayle and Metzger

tests. Figure 1.11 shows Nusselt number values based on the hydraulic diameter of the tip gap ($2h$ or $2H$) plotted as a function of the blade Reynolds number based on the exit velocity and hydraulic diameter. The Gnielinski correlation has been plotted for several L_T/D_h ratios as shown on the plot. Note that L_T represents the maximum thickness of the blade. As known for turbulent channel flow, fully developed conditions generally occur for $L/D_h > 20$ (Kays and Crawford [20]). There is fairly good agreement between experimental data and the appropriate correlations. It should be noted that the L_T/D_h ratios are based on the maximum blade thickness and the Nusselt numbers are the average values calculated for the tip surface. Therefore, this ratio is not a perfect representation of a blade profile, but works reasonably well for the area-averaged values shown here. More experiments should be performed to further verify this trend.

The baseline results are presented as contour plots of Nusselt number (based on chord) in Figure 1.12. Note that the chord rather than hydraulic diameter was used for these contour plots to illustrate the differences in the heat transfer coefficients along the blade tip for both tip gaps. Results at both gap heights show similar trends, however, the large tip gap shows higher Nusselt numbers at the blade trailing edge relative to the small tip gap. This increase in heat transfer at the larger tip gap trailing edge is a result of the increased entry region effect relative to the small tip gap. With smaller L/D_h values (for the large tip gap), the entry region is expected to have a greater effect, as mentioned at the beginning of this section. For the large tip gap, the L/D_h is as low as 1 across the trailing edge of the tip surface, whereas for the small tip gap the L/D_h is 3.5.

The area-averaged Nusselt numbers are given for each case to quantify the increase in heat transfer with gap height. For these cases, the Nusselt number at the large tip gap is 3.2 times that of the small tip gap when based on the exit velocity and hydraulic diameter. By using Reynolds number scaling for a turbulent channel flow, the large tip gap is expected to have 2.4 times the heat transfer of the small tip gap. This larger than expected increase results from the overwhelming entry region effects, which serve to greatly increase the tip heat transfer.

As shown in Figure 1.12, there are regions of low heat transfer immediately downstream of the dirt purge cavity for both tip gap heights. This is near the thickest portion of the blade and represents the area of lowest heat transfer on the blade tip. This region was first pointed out by Bunker et al. [14] and has been confirmed by other authors. Within the dirt purge cavity, there are high heat transfer coefficients resulting from low velocity flow re-circulation in the cavity.

Overall, the leading edge region experiences relatively low heat transfer outside of the dirt purge cavity in comparison to the trailing edge.

Also seen on these contour plots are regions of high heat transfer along the pressure side that begin around $S/S_{\max} = 0.1$ and extend until the trailing edge. These regions of high heat transfer have been noted by Morphis and Bindon [2] and Bindon [16] to be the separation region that forms along the pressure side due to mainstream and leakage flow interaction. This region occurs within the entry region and is more dominant at the large tip gap than at the small tip gap, and extends over a large region of the tip for the large tip gap.

Heat Transfer Augmentation with Blowing

By first comparing the heat transfer with blowing to that of the baseline cases, the augmentation associated with tip blowing can be studied. The camber line plots for the dirt purge blowing are shown in Figure 1.13 a and b for the small and large tip gaps, respectively. For both tip gaps, the heat transfer is increased with blowing for the region of $0 < x/C < 0.25$. Beyond $x/C = 0.3$, there is no difference between any of the cases because the dirt purge blowing does not affect heat transfer in this area. In comparing Figure 1.13 with Figure 1.9, there are striking differences between the two data sets. The film cooling effectiveness (Figure 1.9) extends further down the blade than does the heat transfer augmentation. For the small tip gap, the film-cooling remains near $\eta = 1$ out to $x/C = 0.25$ for the highest blowing ratio whereas the heat transfer augmentation is at a value of one at that location. This shows that for the small tip gap, the dirt purge holes are impinging upon the shroud and effectively spreading coolant flow while the heat transfer increase is localized around the hole exits. For the large tip gap, there are localized peaks of film-effectiveness for each of the three highest blowing ratios located at $x/C = 0.15$ for the 0.19% case, and near $x/C = 0.2$ for the 0.29% and 0.38% cases. These peaks of film-effectiveness correspond to peaks of heat transfer. At the 0.29% and 0.38% cases, the peaks are located at the same position, suggesting that the coolant flow has impinged upon the shroud and bounced back down to the tip. At the 0.19% case, however, the peaks are not co-located. Instead, the peak in heat transfer is located downstream of the peak in film-effectiveness. This suggests that at this particular blowing ratio, the dirt purge jet is causing flow vortices to form near the jet which do not cause high film-effectiveness but do increase the heat transfer.

CFD results by Hohlfeld [21] predicted these vortices. Coolant flow stream lines for the large tip gap are shown in Figure 1.14. At the highest blowing ratio (0.38%), the coolant is spread in all directions after hitting the shroud. At the 0.19% case, the first dirt purge hole is split by the second hole, such that part of the flow rolls into a vortex around the right side of the second hole jet. This vortex extends the full gap height and is what causes the peak in heat transfer to be located further downstream than the peak in film-effectiveness for this case. The 0.10% case is shown to verify that there are no vortices at this case, but rather calm flow exiting the holes and immediately flowing out of the gap region.

Peaks of heat transfer are seen immediately around both of the dirt purge holes in Figure 1.13. The reason for this is because the holes cut-out of the foil heater had high current gradients very near to the holes resulting in high heat transfer coefficients.

Area-averages of the heat transfer augmentation for both tip gaps are shown in Figure 1.15. Again, these averages are over the forward 30% of the blade, so than only the area affected by the blowing is considered. These results show there to be the same heat transfer augmentation for the lowest blowing ratios at both tip gaps. As the blowing ratio increases, however, the small tip gap shows increasingly higher augmentation than the large tip gap. As was discussed in the adiabatic results section, flow from the dirt purge holes for the small tip gap can flood the leading edge gap region, causing very good cooling over most of the leading edge. At the large tip gap, the flow is blowing off the tip surface and impinging on the shroud. Because of this, the augmentation is higher at the small tip gap than the large tip gap for the same blowing ratio.

Net Heat Flux Reduction

Combining the heat transfer measurements with the film effectiveness measurements can give the overall cooling benefit in the form of a net heat flux reduction (NHFR). Shown in equation 3, NHFR is an established method of evaluating the overall effect of a cooling scheme on a surface (Sen et al. [22]).

$$\text{NHFR} = 1 - \frac{h_r}{h_0} \left(1 - \frac{\eta}{\theta} \right) \quad (3)$$

In this equation, all variables have been measured experimentally except for θ . A constant value for θ of 1.6 was used for this paper based on the previous literature (Sen et al. [22]). This value

corresponds to a cooling effectiveness of 62.5%, or the inverse of 1.6. As this equation shows, when high heat transfer augmentation is not accompanied by high film cooling, the NHFR can become negative. A negative NHFR means that an increased heat load to the blade surface, which is totally undesirable.

The NHFR values were calculated locally for each case and are shown in Figure 1.16. The NHFR is always higher at the small tip gap relative to the large tip gap. This can be attributed to the much higher film cooling effectiveness and only slightly higher heat transfer augmentation of the small tip gap relative to the large tip gap. At the small tip gap, the NHFR always increases with blowing. For the large tip gap, the area downstream of the dirt purge cavity shows increased NHFR values with increased blowing, however, for the entire leading edge region, the 0.19% case appears to be lower than the 0.10% case. This is because of the slightly negative areas downstream of the second dirt purge hole. This region is caused by the vortices created by the dirt purge blowing that are not seen in any of the other cases, as was discussed in the previous section.

NHFR values along the camber line are shown in Figure 1.17 for the small and large tip gaps. For the small tip gap (Figure 1.17 a), there is increased spreading of the NHFR in the region $0 < x/C < 0.3$ as blowing increases. The highest blowing case (0.38%) shows a large spike at the first dirt purge hole. This is caused by high heat transfer immediately surrounding the dirt purge hole, where the uncertainty is higher due to non-uniform heat flux, as discussed previously. For the large tip gap, there is generally increased NHFR with increased blowing with the exception of the region around $x/C = 0.2$. Around this area, the 0.19% case actually shows lower NHFR than the 0.10% case due to the decreased film effectiveness.

Area-averages of the NHFR values were also calculated for the forward 30% of the blade. The results, shown in Figure 1.18, indicate that the NHFR is always higher for the small tip gap at all blowing ratios tested. Also, at the small tip gap, the NHFR levels increase with blowing ratio in a nearly linear fashion. For the large tip gap, however, the lowest blowing ratio shows higher NHFR values than the 0.19% case, although subsequent increases in blowing ratio result in increased NHFR, which also responds in a near linear fashion.

Conclusions

Intended to prevent dirt and dust particles from clogging smaller film cooling holes, dirt purge holes can provide significant cooling to the leading edge of a blade tip. The dirt purge jets provided a significant amount of cooling for the leading edge area particularly for the small tip gap. From the contours and profiles on the tip for the small gap case, it was apparent that there was an overcooling of the leading edge area for coolant injections that were greater than 0.19% of the main passage flow. Increased blowing resulted in a larger cooling benefit for the large tip gap as compared with the small tip gap, although the small tip gap always showed higher overall effectiveness for the same blowing ratio. For the large tip gap at the lower coolant injection rates of 0.10% and 0.19% of the passage flow, the coolant was effective within the dirt purge cavity and just downstream of the cavity. As the coolant injection was increased to 0.29% and 0.38% at this large gap height, cooling was evident within, upstream, and downstream of the dirt purge cavity.

Heat transfer measurements indicate that heat transfer augmentation with blowing is increased with higher blowing ratios for both gap heights tested. Also, the augmentation seen for the small tip gap tends to be higher than that of the large tip gap. By combining the adiabatic effectiveness and heat transfer measurements, the small tip gap was shown to outperformed the large tip gap. The NHFR levels steadily increased with increased blowing for the small tip gap. For the large tip gap, the NHFR decreased from the 0.10% case to the 0.19% case, but increased with subsequent blowing ratios. Overall, the measurements indicate that better NHFR from the dirt purge holes can be achieved for a small tip gap as compared with a large tip gap.

Acknowledgments

The authors gratefully acknowledge United Technologies – Pratt and Whitney for their support of this work.

Nomenclature

B_x	= axial chord
C	= true chord of blade
C_p	= pressure coefficient, $C_p = (p - p_{in}) / (\rho U_{in}^2 / 2)$
d	= hole diameter of the dirt purge
D_h	= hydraulic diameter, always used as $2h$ or $2H$
h	= small tip gap height
H	= large tip gap height

h_f	= film heat transfer coefficient
h_0	= blade heat transfer coefficient with no blowing
k	= thermal conductivity
I	= local $(\rho_c U_c^2 / \rho_\infty U_\infty^2)$ or global $(\rho_c U_c^2 / \rho_{in} U_{in}^2)$ momentum flux ratio
L	= local thickness of blade
L_{max}	= max local thickness of blade
L_T	= max thickness of blade overall
\dot{m}	= mass flowrate
M	= local $(\rho_c U_c / \rho_\infty U_\infty)$ or global $(\rho_c U_c / \rho_{in} U_{in})$ mass flux ratio
NHFR	= net heat flux reduction, see equation 4
Nu_{Dh}	= Nusselt number based on hydraulic diameter, $h(D_h)/k$
Nu_{fd}	= Nusselt number at fully developed condition based on hydraulic diameter, $h(D_h)/k$, see equation 2.
$Nu_{0,C}$	= baseline Nusselt number based on chord, $h(C)/K$
$Nu_{0,Dh}$	= baseline Nusselt number based on hydraulic diameter, $h(D_h)/k$
P	= blade pitch
P_o, p	= total and static pressures
Pr	= Prandtl number
q''_{tot}	= heat flux supplied to tip surface heater
q''_r	= heat flux loss due to radiation
R	= resistance in Ω .
Re_{in}	= inlet Reynolds number, $U_{in}(C)/\nu$
Re_{Dh}	= Reynolds number based on local velocity and hydraulic diameter, $U_{local}(D_h)/\nu$
$Re_{ex,Dh}$	= Reynolds number based on exit velocity and hydraulic diameter, $U_{ex}(D_h)/\nu$
Re	= Reynolds number
S	= surface distance along blade
T	= temperature
U_{local}	= local velocity on tip gap
U_{ex}	= exit velocity (at blade trailing edge)
U_{in}	= inlet velocity (1 chord upstream)
x	= distance along blade chord

Greek

η	= adiabatic effectiveness, $\eta = (T_{in} - T_{aw}) / (T_{in} - T_c)$
Δ	= denotes a difference in value
ρ	= density
ν	= kinematic viscosity
ε	= emissivity of tip heater surface, always set to 0.93.
θ	= dimensionless temperature ration, $(T_\infty - T_c) / (T_\infty - T_w)$, always set to 1.6.

Subscripts

ave, $\overline{\quad}$	= pitchwise average at a given axial location
ave, $\overline{\overline{\quad}}$	= area average
aw	= adiabatic wall
c	= coolant conditions
in	= inlet value at 1C upstream of blade
ms	= value at blade midspan
∞	= local inviscid value

w = wall temperature with heat transfer surface
b = background temperature for surface radiation

References

- [1] Lattime, S. B. and Steinetz, B. M., 2002, "Turbine Engine Clearance Control Systems: Current Practices and Future Directions," NASA TM 2002-211794.
- [2] Morphis, G. and Bindon, J. P., "The Effects of Relative Motion, Blade Edge Radius and Gap Size on the Blade Tip Pressure Distribution in an Annular Turbine Cascade with Clearance," ASME 88-GT-256.
- [3] Tallman, J. and Lakshmiarayana, B., 2001, "Numerical Simulation of Tip Leakage Flows in Axial Flow Turbines, With Emphasis on Flow Physics: Part II—Effect of Outer Casing Relative Motion," *J of Turbomachinery*, vol. 123, pp. 324-333.
- [4] Yaras, M.I., and Sjölander, S. A., "Effects of Simulated Rotation on Tip Leakage in a Planar Cascade of Turbine Blades: Part I Tip Gap Flow," *J of Turbomachinery*, vol. 114, pp. 652-659, 1992.
- [5] Mayle, R. E. and Metzger, D. E., "Heat Transfer at the Tip of an Unshrouded Turbine Blade," Proceedings 7th International Heat Transfer Conference, vol. 3, pp. 87-92, 1982.
- [6] Chyu, M. K., Moon, H. H., and Metzger, D. E., "Heat Transfer in the Tip Region of Grooved Turbine Blades," *J of Turbomachinery*, vol. 111, pp. 131-138, 1989.
- [7] Srinivasan, V. and Goldstein, R.J., "Effect of Endwall Motion on Blade Tip Heat Transfer," *J of Turbomachinery*, vol. 125, pp. 267-273, 2003.
- [8] Kim, Y. W. and Metzger, D. E., "Heat Transfer and Effectiveness on Film Cooled Turbine Blade Tip Models," *J of Turbomachinery*, vol. 117, pp. 12-21, 1995.
- [9] Kim, Y. W., Downs, J. P., Soechting, F. O., Abdel-Messeh, W., Steuber, G., and Tanrikut, S., "A Summary of the Cooled Turbine Blade Tip Heat Transfer and Film Effectiveness Investigations Performed by Dr. D. E. Metzger," *J of Turbomachinery*, vol. 117, pp. 1-11, 1995.
- [10] Kwak, J. S. and Han, J. C., "Heat Transfer Coefficient and Film-Cooling Effectiveness on a Gas Turbine Blade Tip," GT-2002-30194.

- [11] Kwak, J. S. and Han, J. C., "Heat Transfer Coefficient and Film-Cooling Effectiveness on a Squealer Tip of a Gas Turbine Blade Tip," GT-2002-30555.
- [12] Acharya, S., Yang, H., Ekkad, S.V., Prakash, C., Bunker, R., "Numerical Simulation of Film Cooling Holes On the Tip of a Gas Turbine Blade," GT-2002-30553.
- [13] Hohlfeld, E. M., Christophel., J. R., Couch, E. L., and Thole, K. A., 2003, "Predictions of Cooling from Dirt Purge Holes Along the Tip of a Turbine Blade," GT2003-38251.
- [14] Bunker, R.S., Bailey, J.C., and Ameri, A.A., "Heat Transfer and Flow on the First-Stage Blade Tip of a Power Generation Gas Turbine: Part 1 – Experimental Results," *J of Turbomachinery*, **122**, pp. 263-271, 2000.
- [15] Jin, P. and Goldstein, R.J., "Local Mass/Heat Transfer on a Turbine Blade Tip," *J of Rotating Machinery*, **9**, No. 2, pp 981-995, 2003
- [16] Bindon, J.P., "The Measurement and Formation of Tip Clearance Loss," *J of Turbomachinery*, **111**, pp. 257-263, 1989.
- [17] Moffat, R. J., 1988, "Describing the Uncertainties in Experimental Results," *Experimental Thermal and Fluid Science*, Vol. 1, pp. 3-17.
- [18] Gnielinski, V., "New Equations for Heat and Mass Transfer in Turbulent Pipe and Channel Flow," *Int. Chem. Eng.*, **16**, pp. 359-368, 1976.
- [19] Kakaç, S., Shah, R.K., and Aung, W., *Handbook of Single-Phase Convective Heat Transfer*, John Wiley & Sons, pp. 34-35, 1987.
- [20] Kays, W.M. and Crawford, M.E., *Convective Heat and Mass Transfer*, 2nd ed., McGraw-Hill, pp. 269-270, 1980.
- [21] Hohlfeld, E.H., *Film Cooling Predictions Along the Tip and Platform of a Turbine Blade*, Master's Thesis, Virginia Polytechnic Institute and State University, Blacksburg, VA, 2003
- [22] Sen, B., Schmidt, D.L., and Bogard, D.G., "Film Cooling with Compound Angle Holes: Heat Transfer," 94-GT-311.

Table 1.1 Geometry for the Blade Tip Model

Parameter	Scaled Model
Scaling Factor	12X
Axial chord, B_x (% Span)	63
True Chord, C (% Span)	96.3
Pitch, P (% Span)	78
Re	2.1×10^5
Inlet Angle, θ	16.5°
Coolant to Mainstream ΔT	25°
Small tip gap, h (% Span)	0.545
Large tip gap, H (% Span)	1.635

Table 1.2 Matrix of Experiments and Resulting Blowing Ratios

Coolant Flow (% Total Flow)	Tip Gap	Holes 1 and 2		Hole 1		Hole 2	
		Global M	Global I	Local M	Local I	Local M	Local I
0.10	Small, Large	1.4	3.6	1.9	6.6	1.1	2.1
0.19	Small, Large	2.7	13.0	3.6	23.7	2.0	7.5
0.29	Small, Large	4.1	30.3	5.5	55.3	3.1	17.4
0.38	Small, Large	5.3	52.0	7.2	94.9	4.1	29.9

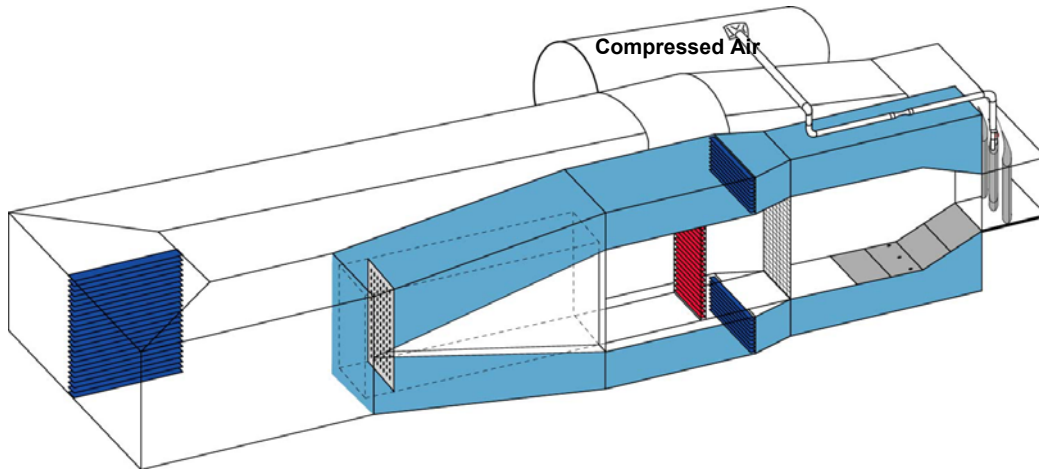


Figure 1.1 Schematic of the wind tunnel facility used for the testing of the blade tips.

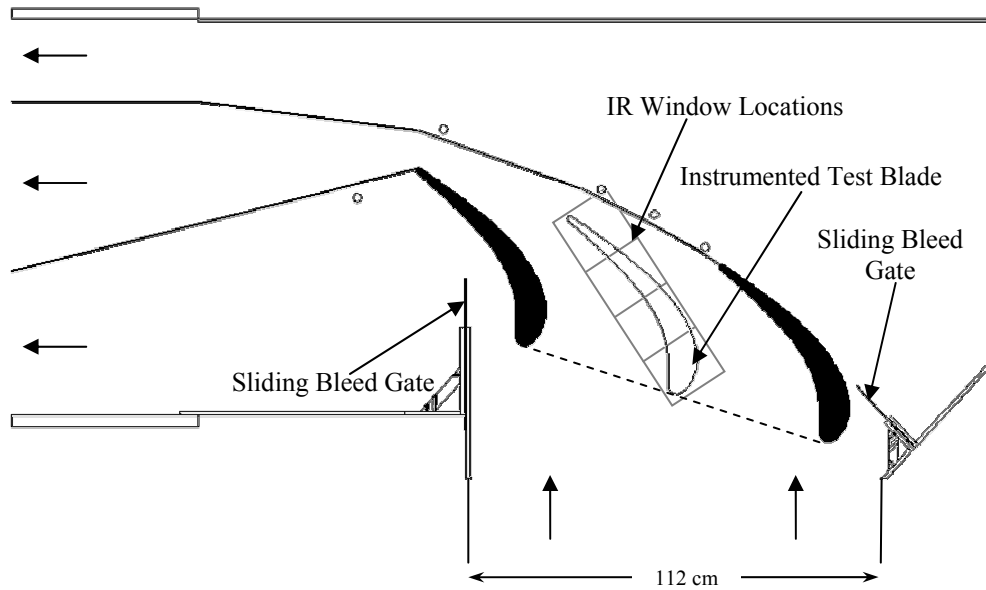


Figure 1.2 The corner test section of the wind tunnel housed three blades that formed two full passages.

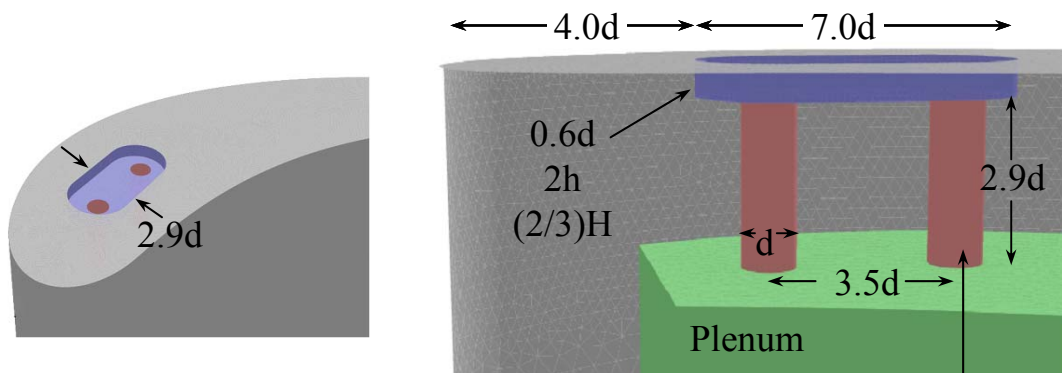


Figure 1.3 The blade tip included a plenum that supplied coolant to the dirt purge holes.

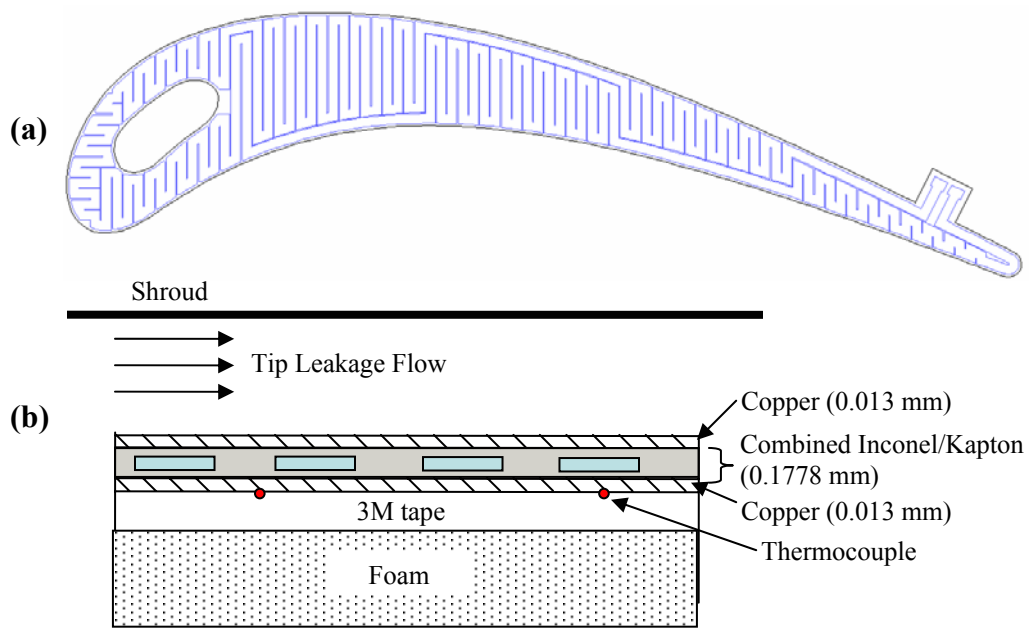


Figure 1.4 Main tip heat transfer surface showing serpentine passages (a) and detail of main tip heater as placed on the blade surface (b).

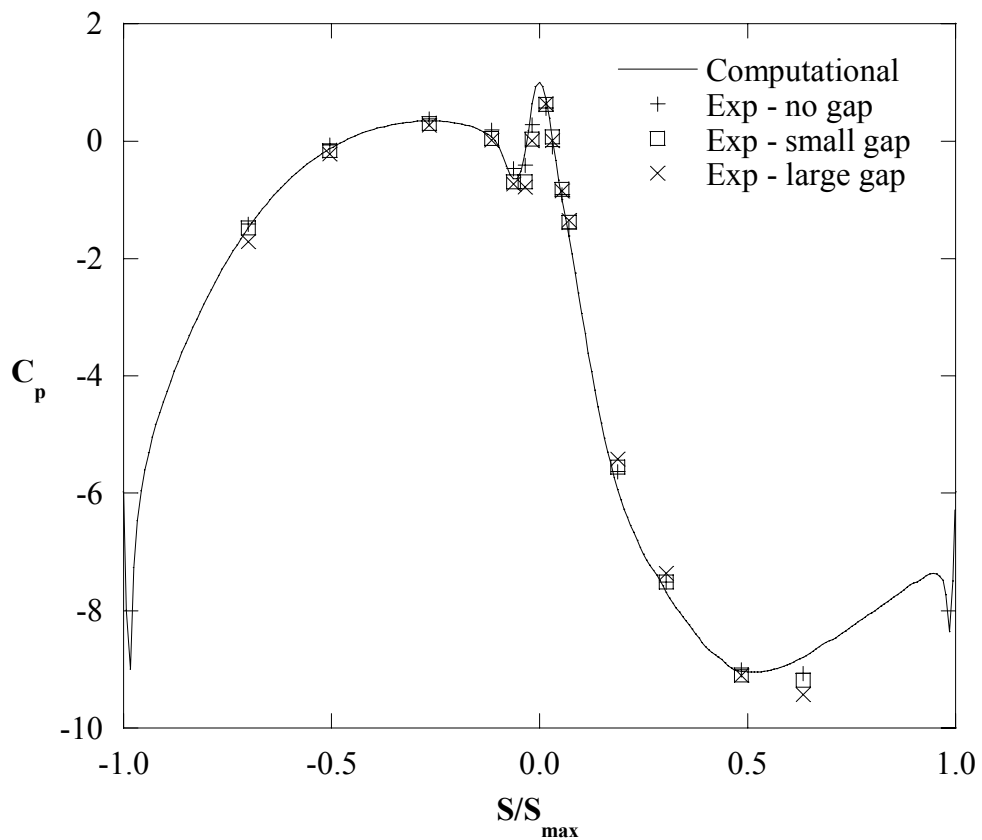


Figure 1.5 Measured and predicted static pressures at the blade mid-span.

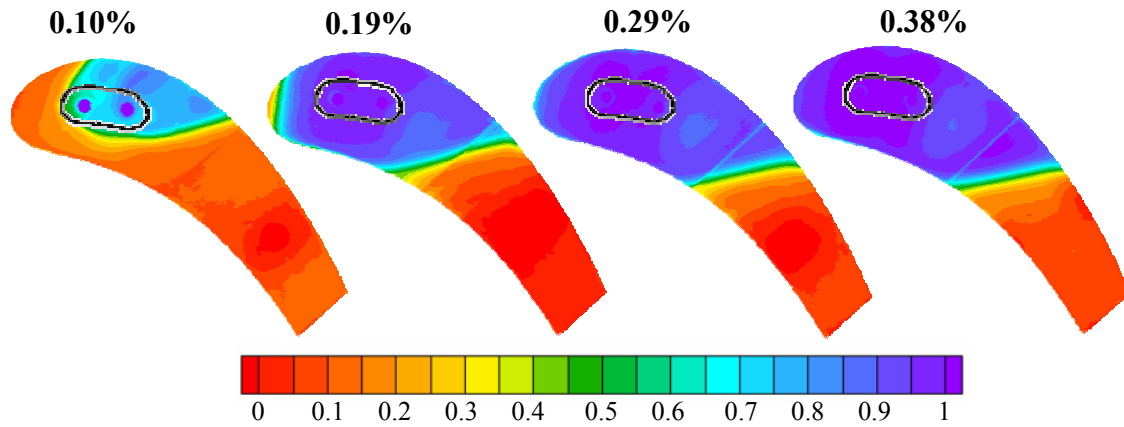


Figure 1.6 Adiabatic effectiveness contours taken along the tip with dirt purge blowing of 0.10%, 0.19%, 0.29%, 0.38% flow for the small tip gap.

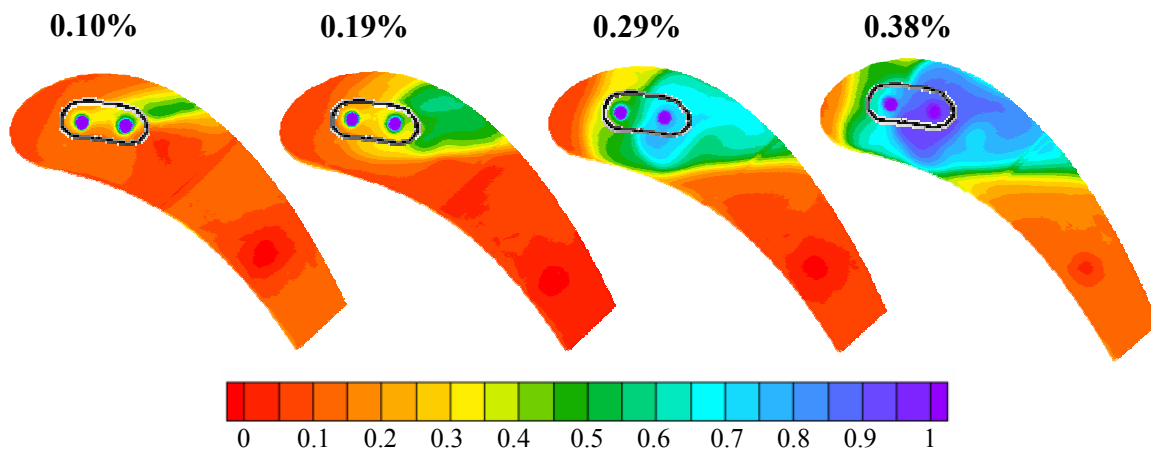


Figure 1.7 Adiabatic effectiveness contours taken along the tip with dirt purge blowing of 0.10%, 0.19%, 0.29%, 0.38% flow for the large tip gap.

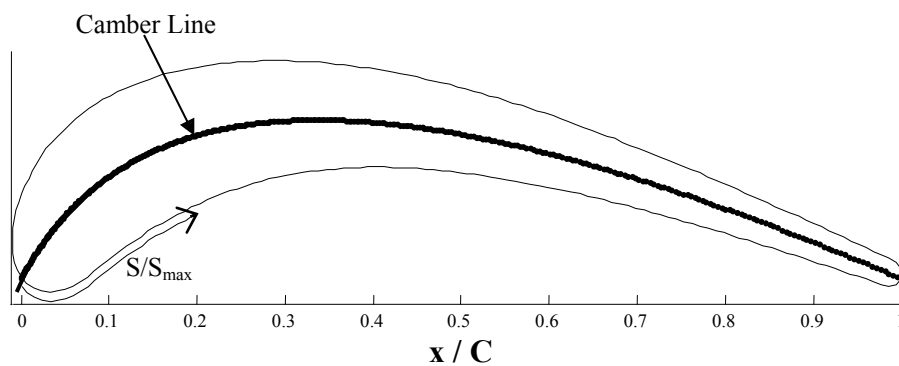


Figure 1.8 Definition of the blade camber line and associated axis.

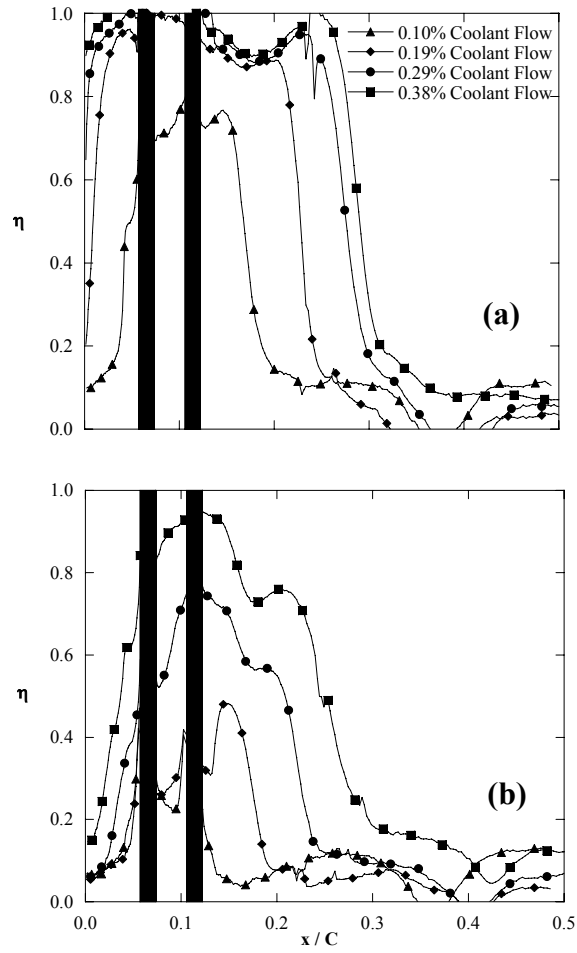


Figure 1.9 Effectiveness measurements taken along the blade camber line for the small (a) and large (b) tip gaps.

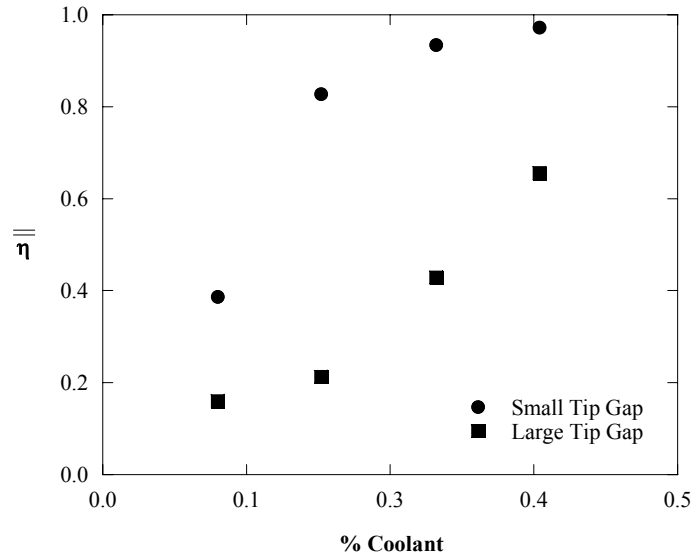


Figure 1.10 Area-averaged adiabatic effectiveness along the tip plotted against dirt purge flow at various coolant blowing levels.

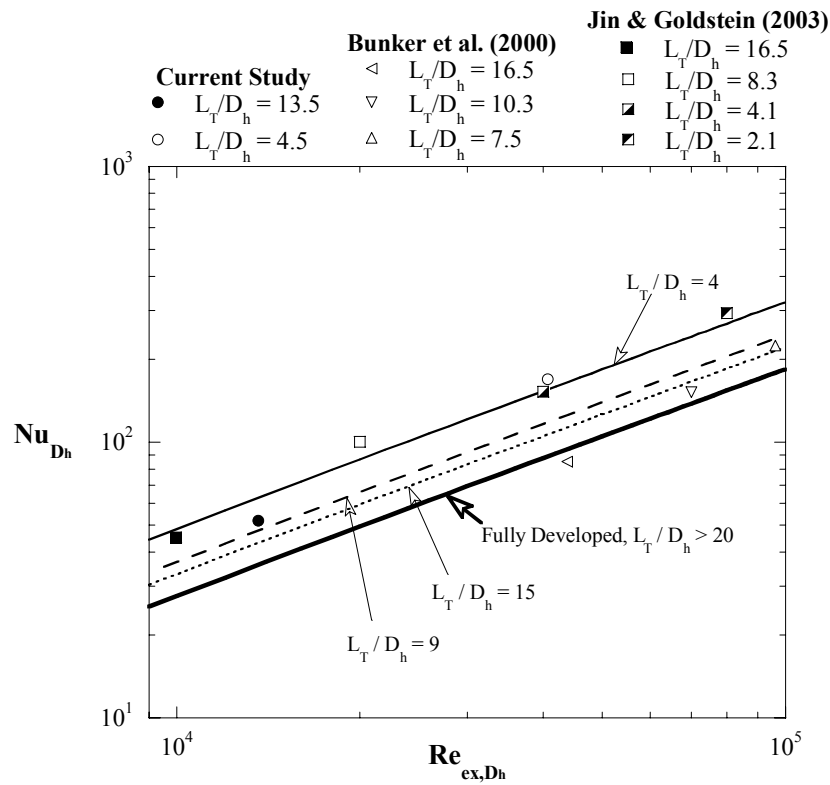


Figure 1.11 Comparison of experimental data to a fully-developed correlation.

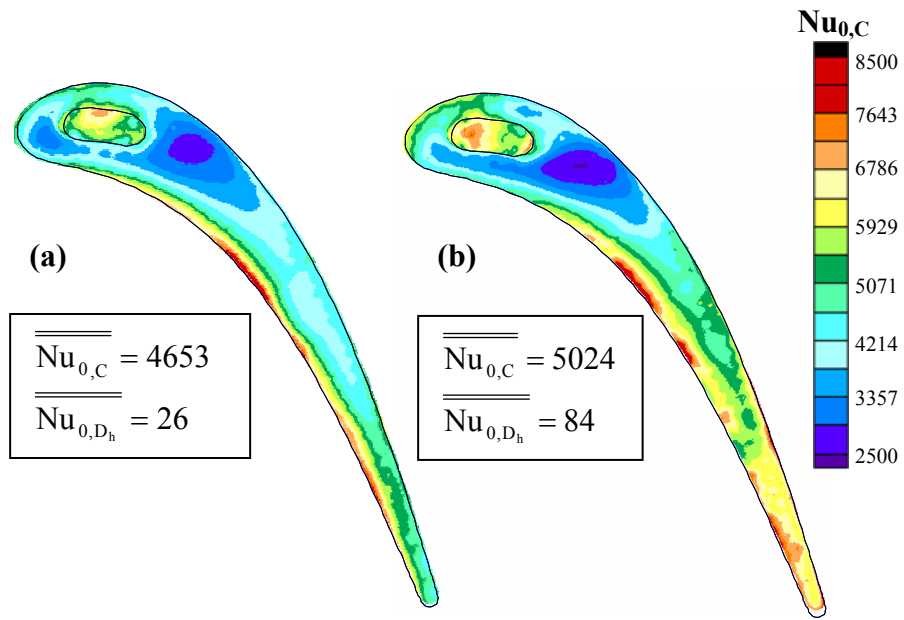


Figure 1.12 Baseline Nusselt number contour plots for the small (a) and large (b) tip gap heights.

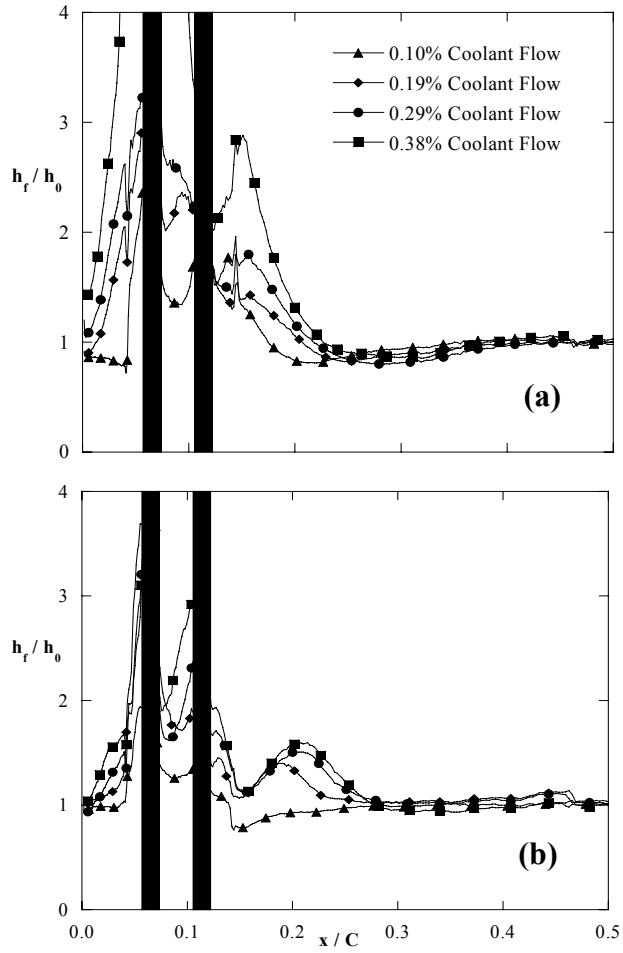


Figure 1.13 Camber line data for h_r/h_0 for the small (a) and large (b) tip gap

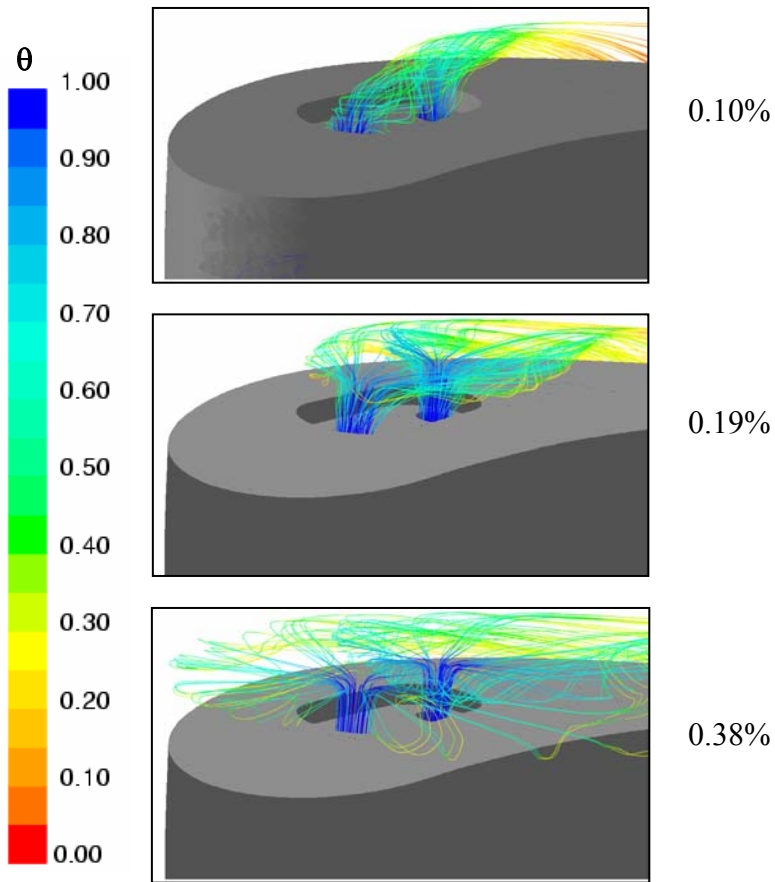


Figure 1.14 CFD predictions of dirt purge streamlines for the large tip gap (Hohlfeld [21]).

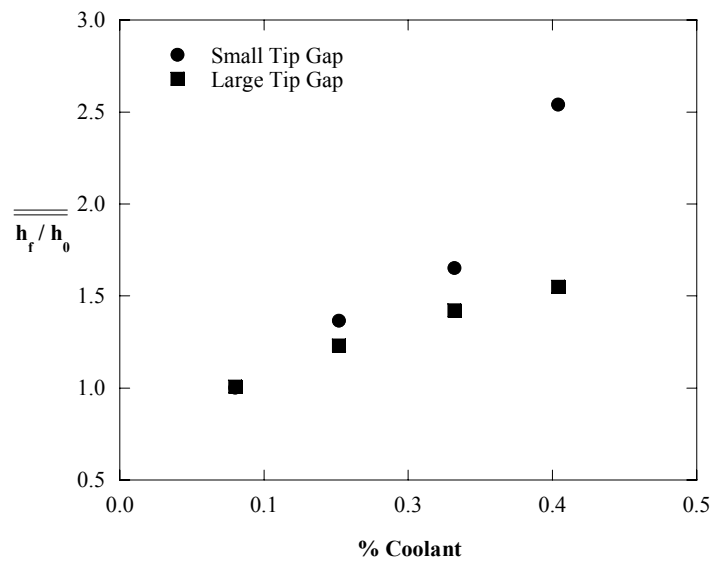


Figure 1.15 Area-averaged heat transfer augmentation for the small and large tip gaps.

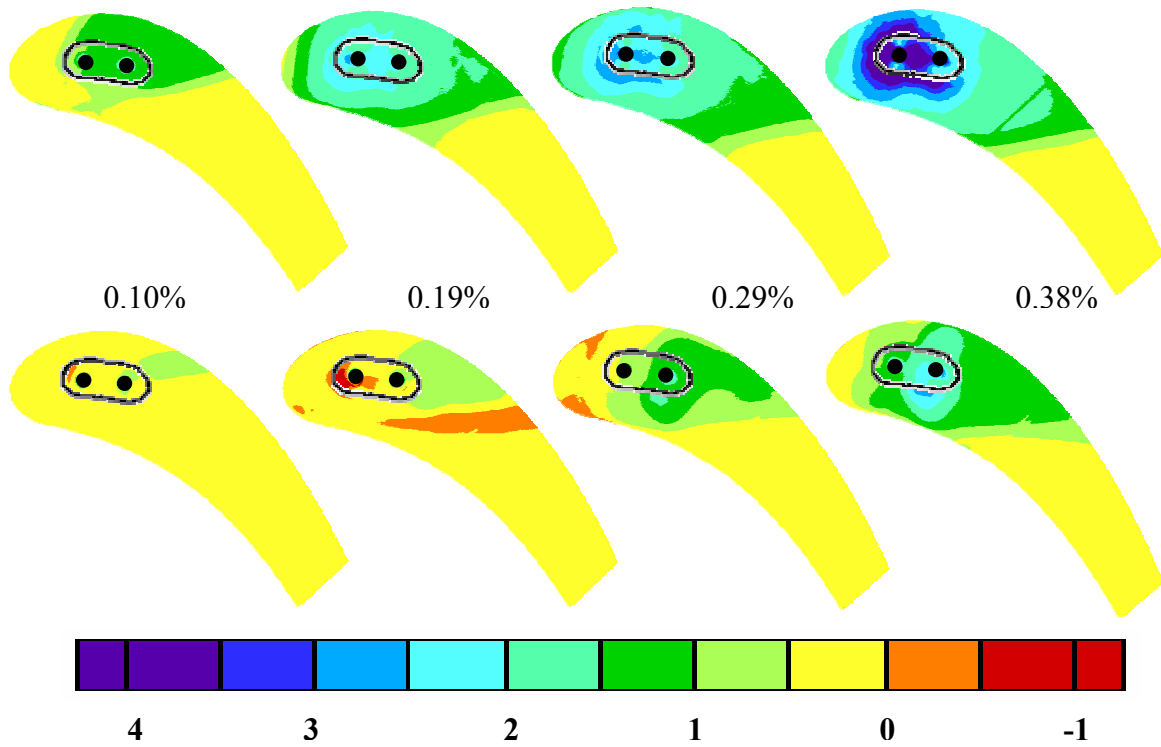


Figure 1.16 Contour plots of NHFR for the small (top) and large (bottom) gap heights at all blowing ratios tested.

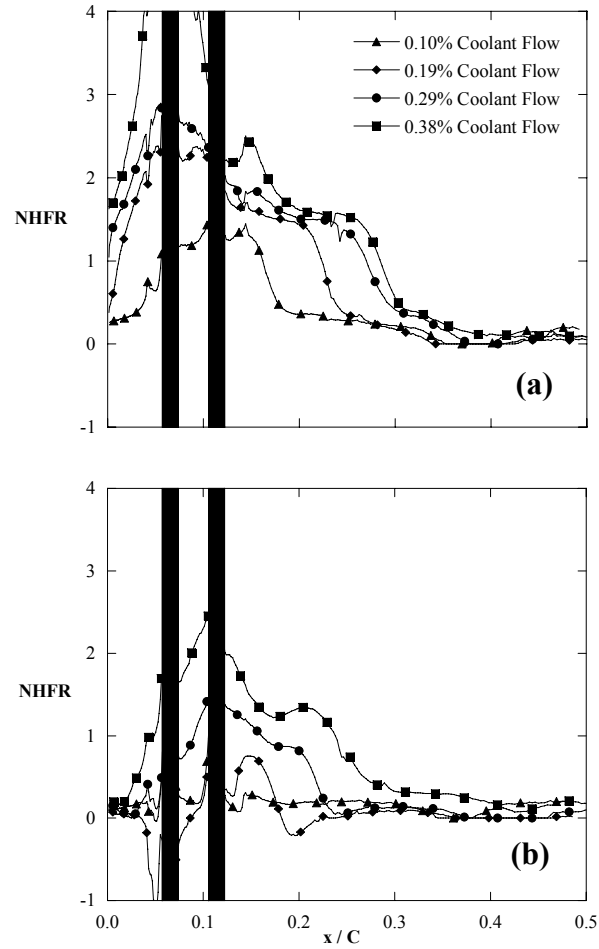


Figure 1.17 NHFR taken along the Camber line for the small (a) and large (b) gap heights.

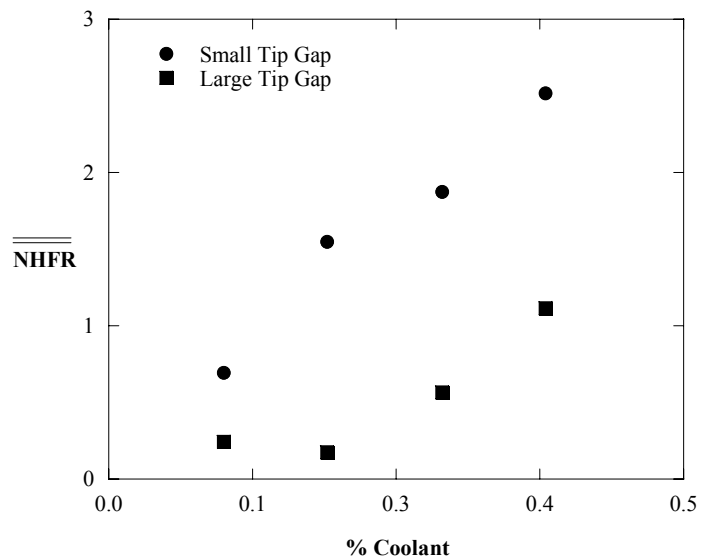


Figure 1.18 Area-averaged NHFR for both gap heights and all blowing ratios tested.

Paper 2:
**Comparison of Exit Hole Shapes for Cooling the Tip of a Turbine
Blade—Part 1: Film Effectiveness Measurements**

To be submitted to the *Journal of Turbomachinery**

Abstract

High pressure turbine blade tip sealing and durability have been challenging problems since the development of gas turbine engines. Blade tip designs are extremely important in terms of sealing and overall engine performance. In general, increasing overall engine performance can be accomplished by increasing turbine inlet temperatures. This must be done, however, without sacrifice of part life. As a result, cooling methods along the blade tip need to be devised and applied effectively. Film-cooling is typically used as a blade tip cooling method, whereby coolant is supplied through holes placed along the pressure side of a blade. As the leakage flow convects across the tip, so does the coolant injected from the pressure side film-cooling holes.

This paper is the first of a two part series that compares two film-cooling hole shapes, representative of two differing manufacturing techniques used in blade tip cooling designs. These manufacturing techniques consist of Electrical Discharge Machining (EDM) and Light Amplification by Stimulated Emission of Radiation (laser) drilling processes. Part 1 compares the two manufacturing hole shapes based on adiabatic effectiveness levels measured along a blade tip while Part 2 combines measured heat transfer coefficients with the adiabatic effectiveness levels to assess the overall cooling benefit of pressure side blowing near a blade tip. The results indicate that for two different tip clearances and all of the blowing ratios considered, the diffusion of the jet through the EDM holes provided better cooling on the blade tip than that for the laser drilled holes. Results from both hole geometries also show better cooling can be achieved for a small tip gap compared with a large tip gap.

*Co-authors: Dr. Karen A. Thole, Mechanical Engineering Department, Virginia Tech
Dr. Frank J. Cunha, Turbine Durability, Pratt & Whitney

Introduction

Using different manufacturing methods for film-cooling holes placed in a turbine blade, such as Electrical Discharge Machining (EDM) or Light Amplification by Stimulated Emission of Radiation (laser) drilling, can result in a variety of hole shapes in a turbine blade. The shape of a film-cooling hole affects the mixing characteristics between the coolant and hot gas that in turn affect the overall cooling benefit of the film. While there have been several studies comparing the cooling benefits for different shaped film-cooling holes placed in a simple flat plate, there have been no studies documenting the effect of a shaped film-cooling hole injection near the tip of an airfoil.

Airfoil tips experience high heat transfer rates and there is relatively little known about flow within the tip of an airfoil. The goal of the work presented in this paper is to assess the effects of different hole manufacturing techniques on the cooling performance of high pressure turbine blade tip designs. Two different hole shapes were considered. Both cooling hole arrangements were placed near the tip of a blade along the pressure side. These two hole shapes represent geometries of a standard EDM manufacturing technique and a laser drilling manufacturing technique. Comparisons were made for these two hole geometries with the same blowing conditions and relatively similar hole placement along the pressure side of a blade. The comparisons made in this paper (Part 1) have been made through measurements of the adiabatic effectiveness along the turbine blade tip. A companion paper, Part 2 [1], provides a full heat transfer analysis including the overall benefit of film-cooling on the tip.

Relevant Past Studies

One method for improving the thermal environment along the blade tip is to inject coolant into the tip region. In a review paper on tip heat transfer, Bunker [2] states that for a blade tip there has been very little film-cooling research reported in the literature even though film-cooling is widely used. Blowing from the tip has been considered by Kim and Metzger [3], Kim et al. [4], Kwak and Han [5, 6], Acharya et al. [7] and Hohlfeld et al. [8].

Kim et al. [4] present a summary of the experimental work that D. Metzger performed on tip blowing. In addition to concluding that there is only a weak effect of the relative motion between a simulated blade and shroud on tip heat transfer coefficient,

they stated that there is a strong dependency of cooling effectiveness for a tip on the shape of the hole and injection locations. Note that a more recent study by Srinivasan and Goldstein [9], who used an actual airfoil, also indicated a negligible effect of the relative motion between the tip and shroud on tip heat transfer with the exception being near the leading edge region. Four hole configurations were discussed by Kim et al. that included the following: discrete slots located along the blade tip, round holes located along the blade tip, angled slots positioned along the pressure side, and round holes located within the cavity of a squealer tip. The studies reported by Kim et al. were performed in a channel that simulated a tip gap, whereby no blade with its associated flow field was simulated. In comparing the discrete slots to the holes, their data indicated a substantial increase in cooling effectiveness using the discrete slots for all blowing ratios tested. Injection from the pressure side holes provided cooling levels of similar magnitude to the holes placed on the tip with better spreading occurring in the case of the pressure side injection. Kim et al. also reported that an increase in coolant mass flow generally yielded improved cooling with tip surface holes, but for pressure side holes, increased coolant flow yielded decreased cooling effectiveness.

In another study, Kim and Metzger [3] examined heat transfer coefficients from cooling slots located on the pressure side of the tip of the same channel geometry that simulated a tip gap. They concluded that film-cooling along the pressure side corner of the blade tip provides adequate effectiveness levels, and that the film effectiveness increases with increased blowing rates.

Kwak and Han [5, 6] reported measurements for varying tip gaps with cooling holes placed along the pressure surface at a 30° breakout angle and on the tip surface at a 90° angle for a flat and a squealer tip geometry. Contrary to the work summarized by Kim et al., they found a substantial improvement in effectiveness with the addition of a squealer tip. The coolant circulated within the squealer tip providing a better distribution of the coolant along much of the tip compared with no squealer cases. Only along parts of the suction side was the cooling effectiveness poor. They found that for the flat tip, good cooling was provided to the trailing edge due to the accumulation of coolant that exited in this area. Their results also indicated that more coolant resulted in improved effectiveness.

Predictions for varying tip gap sizes by Acharya et al. [7] indicated that film cooling injection lowered the local pressure ratio and altered the nature of the leakage vortex. High film-cooling effectiveness and low heat transfer coefficients were predicted along the coolant trajectory with the lateral spreading of the coolant jets being quite small for all cases. With an increased tip gap the coolant was able to provide better downstream effectiveness through increased mixing. For the smallest tip gap, the coolant was shown to impinge directly on the surface of the shroud leading to high film effectiveness at the impingement point. As the gap size increased, their predictions indicated that the coolant jets were unable to penetrate to the shroud. Computational results by Hohlfeld et al. [8] indicated that the cooling achieved through injection from dirt purge holes placed in the blade tip is dependent on the gap size as well as the blowing ratio. They found, in particular, that as the blowing ratio is increased for a large tip gap the cooling only increased slightly while the cooling to the shroud increased significantly.

In summary, there are only a very limited number of studies that have addressed blowing in the tip gap region with none of these studies comparing different hole shapes for blowing into the tip gap for an actual blade geometry.

Description of Cooling Hole Geometries

As was stated in the introduction, the focus of this work is to compare two different hole shapes representing EDM and laser drilled holes as shown in Figure 2.1 and 2, respectively. Both geometries had a dirt purge cavity that was recessed two small gap heights ($2h$) and 0.67 large gap heights ($0.67H$) from the tip surface. Within this cavity were two dirt purge holes, which have been described in detail by Hohlfeld et al. [8]. In addition to the dirt purge holes, the EDM tip had 10 pressure side holes placed near the tip surface while the laser tip had 15 pressure side holes placed slightly closer to the tip surface.

All of the EDM holes had expansions in both the axial and span directions and had a metering hole diameter of $0.56D$, where D is the diameter of the dirt purge holes. The hole centerlines at the hole exit breakout for the EDM holes ranged from 94% to 96% of the blade span, which is between $6.7h$ and $10h$ ($2.2H$ or $3.3H$) from the blade tip. The hole centerlines at the hole breakout for the laser holes was at 98.5% of the blade span, which is $3h$ ($1H$) down from the blade tip.

The four film cooling holes just downstream of the stagnation for the laser tip were expanded in the axial direction and had a metering hole diameter of $0.56D$ whereas the remainder of the holes had no expansion and a metering hole diameter of $0.4D$. For both the laser and EDM tip models, there is a slot at the trailing edge called the trailing edge flag (TEF). The two TEFs were designed differently in that the TEF for the EDM tip was larger than for the laser tip. Table 2.1 further summarizes the two different hole designs that were used in this study.

The blade models were made from stereo lithography (SLA) to allow for a good replication of the hole shapes and sizes. To insure good control on the blowing ratios through the holes, which will be further discussed in the next section, a dividing wall was placed within the blade cavity to allow for two different supplies inside the blade. These two different supply cavities are illustrated in Figure 2.1 and 2 for each of the two hole geometries. Each cavity was supplied by a separate coolant flow source such that independent control of the coolant flow rates could be achieved. Note that the EDM hole model had the separating wall of the two cavities placed after the third cooling hole (measured from the stagnation location) while the laser hole model had the separating wall placed after the second cooling hole. The placements of these two supply cavities were based on insuring that the local blowing ratios could be best matched to that of the engine.

Because the SLA material does not have a sufficiently low thermal conductivity, the models were designed to have foam molded around the holes and supply chambers. After SLA models of the hole outlines were made, the SLA models were then placed inside a mold of the blade geometry. A polyurethane foam compound, with a thermal conductivity of $0.04 \text{ W/m}^2\text{K}$, was poured in the blade mold and then allowed to expand and harden. The combined SLA holes and foam blade were then removed from the mold, attached as the tip to an SLA blade, and then placed in the wind tunnel for testing. The molded tip model extended 28% of the blade span. Pictures of the combined SLA hole model and foam blade for the EDM and laser drilled holes are shown in Figure 2.3.

Experimental Facilities

The experimental facility for this work consisted of a large-scale, low-speed, closed-loop wind tunnel providing an inlet velocity to the test section of 12 m/s to match

engine Reynolds number conditions for a 12X blade model. The blade geometry and flow conditions are summarized in Table 2.2 with a diagram of the wind tunnel shown in Figure 2.4. Starting at the fan, flow passed through a primary heat exchanger to obtain a uniform temperature profile before being divided into three passages. The main passage, located in the center, has a heater that was used to achieve hot mainstream gas, while flow to the two auxiliary passages was used to supply a single row of high momentum jets used to generate a high turbulence level to the cascade. The inlet turbulence level, measured one chord upstream, was 10% and the length scale was 11cm. Flow entered the experimental test section, consisting of the blade model as shown in Figure 2.5. An independent compressed air supply provided the coolant flow to the two cavities, which was ultimately injected through the film-cooling holes placed in the blade tip.

The blade test section consisted of a two passage linear cascade as shown in Figure 2.5. Velocity measurements were taken approximately one chord upstream at a number of pitch-wise locations to verify a uniform incoming velocity field. Static pressure taps were located near the mid-span of the central blade to insure the pressure distribution around the blade was matched. Matching the pressure distribution around the blade insured equal flow distribution between each of the respective flow passages, and insured the correct driving pressures across the tip gap. The non-dimensional pressure distributions for the central blade are shown in Figure 2.6 for representative EDM and laser tip tests. Also shown on these two graphs is the placement of the film-cooling holes along the pressure side of the airfoil for the EDM and laser drilled holes. The vertical lines in Figure 2.6 indicate the placement of the supply chambers separating the front and back set of holes as well as the stagnation location ($S/S_{\max} = 0$). The front plenum supplies the first three cooling holes and the two dirt purge holes for the EDM model while the back plenum supplies the remaining seven holes and the TEF. For the laser hole model, the front plenum supplies the first two cooling holes along with the dirt purge holes while the remaining thirteen cooling holes and TEF are supplied by the back plenum.

Because coolant was supplied to two independently controlled plenums, which also included the supplies for the dirt purge holes and TEF, a number of experiments were conducted to deduce a discharge coefficient for each cooling component to insure correct cooling flows were ultimately set. Each tip had four cooling components: (i)

front plenum film-cooling holes, (ii) dirt purge holes, (iii) back plenum film-cooling holes, and (iv) TEF. The discharge coefficients were found by isolating each component while all other three components were sealed. By measuring the supply chamber pressure, the calculated flow rate could be compared to that of the measured flow rate using a venturi flow meter. All four components were tested at various flow rates to create discharge coefficient curves for both hole geometries.

The measured discharge coefficients for each of the components are shown in Figure 2.7 for the EDM and laser models. Because dirt purge holes were present for both geometries, the discharge coefficients only needed to be measured once and are shown only on Figure 2.7 a for simplicity. The discharge coefficients for the TEF, however, are different between the two tip models because the laser TEF has a much smaller area than the EDM TEF (see Table 2.1). The front and back holes of the laser tip model approach nominally the same value ($C_d = 0.64$), which is expected because the hole geometries are very similar. This same trend is not present for the EDM tip model, which has differing hole shapes for the front and back. The EDM holes in the first supply chamber have a very strong dependence on pressure ratios below 10. This may be due to large expansion angle of those holes, which causes the flow to become separated within the hole exit at very low flow rates.

As a check on the accuracy of using the previously described method for setting the coolant flows, a comparison was made between the total coolant flow to the entire tip measured using the venturi flow meter and that calculated using the measured pressures combined with the discharge coefficients. The coolant mass balance for typical cases considered was within 2.8%.

Several parameters were considered when comparing the low speed wind tunnel tests to that of an actual engine. A matrix of tests was designed to assess the effects of the blowing ratio, momentum flux ratio, tip gap height, and hole shape. The split of flow for each of the cases is given in Table 2.3. To compute the local external velocity at each hole exit, the predicted static pressure at the 95% span location of the blade (also shown on Figure 2.6) was used at each hole location. The coolant velocity through the holes was based on the velocity at the metering area of the hole. The local blowing ratios that were tested are shown in Figure 2.8a for the EDM holes and in Figure 2.8b for the laser

holes. Because the density ratio used during testing was one, the momentum flux ratios show the same relative levels only as squared values.

There were three nominal total coolant flow rates that were tested, which were 0.58%, 0.68%, and 1.0%. The reason that the laser holes had the additional 0.47% coolant flow test was because this lower flow rate better represented engine conditions. In Figure 2.8a, the blowing ratios are shown at both the large and small tip gaps for one case to show the typical variation for the measurements. Nominally, there was no difference in the blowing ratio with gap height. Also, in these figures, only the blowing ratios for the film cooling holes are shown.

Figure 2.9 provides the distribution of coolant for the 0.68% cooling flow case through each of the film holes, the dirt purge holes, and tip flag for the EDM and laser holes. Note that the 0.68% refers to the total coolant flow relative to the total blade passage flow. As would be expected, much of the coolant flow passes through the dirt purge holes and tip flags relative to the cooling holes as a result of the larger cross-sectional area. For both the EDM and laser hole geometries, most of the holes in the mid-section have approximately the same coolant flow exiting the holes. Because the EDM model had a large TEF, more coolant flow passed through the TEF for the EDM than for the laser holes. Also as a result of this difference, more coolant passed through the dirt purge holes for the laser hole model than for the EDM hole model. As such the flow distribution (the local mass flux and momentum flux ratios) for both the EDM and laser holes were nearly the same. Also, a comparison was made between experimental and computational coolant flow distributions. Shown in Figure 2.10, there was relatively good agreement between the individual flow rates for each hole as predicted by CFD and as calculated experimentally using the discharge coefficients and measured pressures.

Experimental Methodology

Investigation of the hole geometries required obtaining surface temperatures on the foam model, representing the adiabatic surface temperatures along the tip. Typical operating conditions consisted of a temperature differential between the coolant flow and hot mainstream by approximately 25°C. The mainstream and coolant supply chamber temperatures were measured during the experiments with type E thermocouples. Each test required the wind tunnel and tip models to reach a thermal equilibrium, which

required approximately four hours. Temperatures and flows are monitored during this time to insure equilibrium conditions.

The tip surface temperatures were obtained using an Inframetrics P20 infrared (IR) camera. The images were processed with Thermacam Researcher 2002[®] and an in-house MATLAB code. Four IR images were acquired through the zinc selenide windows placed in the shroud surface to cover the entire blade, as shown in Figure 2.5. Each image covered an area that was 21.3 cm by 16 cm and contained 320 by 240 pixels. The camera was located approximately 55 cm from the tip and resulted in a spatial resolution of 0.63 mm. For every test, each of the four images was taken five times and the average of these five images was used.

The calibration process for the camera required direct comparisons of measured surface temperatures, using thermocouple strips placed on the tip surface, with the infrared radiation collected by the camera. Thermocouple strips were used to insure accurate surface temperatures were measured. These strips were placed on the blade tip using a thermally conducting bonding agent. After the experiments were completed, the infrared image was processed whereby the emissivity and background temperature of the infrared pixels nearby the surface thermocouple were adjusted to insure agreement between the measured temperatures. Each of the four images was processed in a similar manner whereby six thermocouples were ultimately used to insure all four images were accurately calibrated. An emissivity of 0.83 was used for all the images while the background temperatures were adjusted to insure a calibrated image. This process resulted in an agreement between all of the thermocouples and infrared temperatures to within 1.0°C, thereby giving a difference in effectiveness of η of ± 0.04 .

Overall uncertainties were calculated for non-dimensional adiabatic effectiveness levels (η) according to the partial derivative method described in Moffat [10]. The total uncertainty of all measurements was calculated as the root of the sum of the squares of the precision uncertainty and the bias uncertainty. The precision uncertainty for measurements made with the infrared camera was determined through an analysis of five calibrated images taken in succession on one portion of the tip at constant conditions. The precision uncertainty was calculated to be 0.31°C, which is the standard deviation of the five readings based on a 95% confidence interval. The camera manufacturer reported the bias uncertainty as 2.0% of the full scale. The largest scale used in this study was

20°C though some images could be captured on a 10°C range. The thermocouples measuring the free-stream and coolant temperatures were reported by the manufacturer to read within $\pm 0.2^\circ\text{C}$. The total uncertainty in effectiveness was found to be $\partial\eta = \pm 0.026$ at $\eta = 1$ and $\partial\eta = \pm 0.026$ at $\eta = 0.2$.

Computational Methodology

To better understand the effects of these hole shapes, a computational fluid dynamics (CFD) simulation was also performed. A commercially available CFD code, Fluent 6.0 [11] was used to perform all simulations. Fluent is a pressure-based, incompressible flow solver that can be used with structured or unstructured grids. An unstructured grid was used for the study presented in this paper. Solutions were obtained by numerically solving the Navier-Stokes and energy equation through a control volume technique. All geometric construction and meshing were performed with GAMBIT. To ensure a high quality mesh, the flow passage was divided into multiple volumes, which allowed for more control during meshing. The tip gap region was of primary concern and was composed entirely of hexahedral cells with an aspect ratio smaller than three.

Computations were performed on a single turbine blade exposed to periodic conditions along all boundaries in the pitch direction. Inlet conditions to the model were set as a uniform inlet velocity at approximately one chord upstream of the blade. Flow angles were set to match those conditions of the experiments as well as the scaled values for the engine while the turbulence levels and mixing length were set to 1% and 0.1 m, respectively. Computations were also performed with an inlet turbulence level of 10%, but no noticeable differences were predicted between the 1% and 10% inlet turbulence cases. All other experimental conditions were matched in the simulations including the temperature levels and flow rates.

To allow for reasonable computational times, all computations were performed using the RNG k- ϵ turbulence model with non-equilibrium wall functions whereby the near-wall region was resolved to y^+ values ranging between 30 and 60. Mesh insensitivity was confirmed through several grid adaptations based on viscous wall values, velocity gradients, and temperature gradients. Typical mesh sizes were composed of 1.8 million cells with 50% of the cells in and around the tip gap region. After adapting from

a mesh of 1.7×10^6 to 2.2×10^6 , the pitchwise-averaged effectiveness predictions on the tip were found to vary by only $\delta\eta = \pm 0.007$ at a level of $\eta = 0.40$. Typical computations required 1200 iterations for convergence to be met.

Experimental Results for Blowing Cases

Contour plots of local film cooling effectiveness levels are given in this section to show the cooling trends for both geometries. To quantify the differences between the two geometries, data have been compared along various lines across the tip. One of these comparisons was made along two different lines along the trajectory of the cooling jets near the middle of the blade tip. Because the two geometries do not have holes in exactly the same positions and because the jet trajectories differed, these data lines have been taken at locations along the jet trajectory, identified as the location having the maximum effectiveness levels, in relatively the same blade tip area. These lines, referred to as path line data, are given in Table 2.4. A third comparison was made along the blade camber line. The camber line is the mid-way line of the blade tip, and is shown in the illustration of Table 2.4.

Comparisons for the Small Tip Gap

Figure 2.11 shows the measured adiabatic effectiveness levels along the blade tip for the EDM and laser holes for the small tip gap. Note that the exits of the hole locations are indicated by the black dots along the pressure side. For all cases, the entire leading edge region is nearly completely cooled by the dirt purge holes. This leading edge area shows essentially no change in effectiveness with increased blowing. For the mid-chord region and trailing edge, the EDM holes significantly outperform the laser holes for all blowing ratios tested. Both the spreading and overall levels are much better for the EDM hole design relative to the laser hole design. As the blowing ratio is increased for the small tip gap, there is nearly no improvement in effectiveness for either hole geometry. The streaky nature of the coolant flow for the laser holes is likely caused by the characteristics of the high momentum jets exiting the cooling holes as compared with diffused shaped EDM holes, which provide more coolant spreading for the lower momentum jets.

For the lowest coolant flow (0.47%) case, the laser holes showed that the trailing edge is actually cooler than for the higher coolant flow cases. The higher effectiveness for the lower coolant flow is because the momentum flux ratios of the jets exiting the trailing edge are low, as shown in Figure 2.8b for the 0.47% cooling flow case, resulting in a cooler gap flow along the tip of the blade.

The nature of the coolant flow can be better understood by comparing the hole exit location to the jet trajectory. For the EDM holes, the peak effectiveness level on the pressure side of the tip is located far downstream of the hole. This shows that the EDM holes are diffused such that the exiting flow remains attached to the blade pressure side and is drawn along the pressure surface towards the trailing edge before being swept over the tip. Near the trailing edge, this sweeping motion becomes more severe as the mainstream flow gradients are stronger in this region. For the laser holes, the peak effectiveness levels are also swept downstream, although not as severely as the EDM holes. This is because the laser jets have a higher momentum such that the coolant is injected with enough momentum to separate from the pressure side. Because of the injection angle, the coolant jets are forced both downstream and towards the tip.

Computations were performed for the small tip gap for a total coolant flow of 0.58% for the EDM and laser hole models to verify these flow patterns. Path lines exiting the holes are given in Figure 2.12 for the two cases to help understand how the flow out of the holes behaves. In the mid-chord region, both the EDM and laser holes appear to be swept downstream before being carried over the tip. The predictions also indicate several jet trajectories for both hole geometries where the coolant remains along the pressure side of the blade for most of the blade before entering into the gap region. This phenomenon is more prevalent for the laser holes than the EDM holes. The holes in the leading edge have the highest blowing ratio, relative to the rest of the blade, so the prediction is somewhat expected.

Camber line comparisons for the small tip gap are shown in Figure 2.13. Note that the distance x is shown as the ordinate of the graph illustrated in Table 2.4. For the same total coolant flow rate, the dirt purge flow dominates to $x/C = 0.2$ for the EDM holes whereas for the laser holes the dirt purge flow dominates to $x/C = 0.3$. The reason for this difference is because there is more flow from the dirt purge holes with the laser cases than with the EDM holes for the same total coolant flow rate (shown in Figure 2.9).

For $x/C > 0.4$, the EDM holes show higher effectiveness levels than the laser holes for the same overall flow rate.

Comparisons for the Large Tip Gap

For the large tip gap results, shown in Figure 2.14, the effectiveness levels for both hole designs are much lower than for the small tip gap. Consistent with those results of the small tip gap, the effectiveness levels are higher for the EDM holes as compared with that for the laser drilled holes. For both hole geometries, the largest difference in the effectiveness contours as a function of the coolant flows occurs near the dirt purge holes. The results for the laser holes actually indicate a worse performance as the coolant flow is increased from 0.47% to 1% in the mid-portion of the tip. This is not true for the EDM holes, which shows nearly the same if not slightly better performance with increased coolant flow. The reason for the worse performance of the laser holes at high blowing ratios is because of the high momentum cooling jets whereby most of the coolant is impinging upon the shroud. The hole locations given on these contour plots show the same results as seen with the small tip gap. Both the EDM and laser holes show the peak effectiveness levels located downstream of the injection location.

The camber line data for the large tip gap, shown in Figure 2.15, shows an increase in effectiveness with increased blowing for the EDM geometry. Downstream of $x/C = 0.3$, the 1% case has slightly higher effectiveness values, but the trends for both blowing cases are similar. The laser holes show no apparent cooling benefit beyond $x/C = 0.3$ as the coolant is increased from 0.58% to 1%. In fact, the average appears to be similar for the two blowing cases with the laser holes, except the 0.58% case has higher peaks and valleys than the 1% case.

Direct Comparison of Hole Shapes

Figure 2.16 does a direct comparison of the two hole geometries at one coolant flow condition. Because more coolant exits the dirt purge holes for the laser model, it is not surprising that Figure 2.16 indicates higher effectiveness in the leading edge region for the laser holes than for the EDM holes. In most of the mid-portion of the airfoil, however, the EDM holes out perform the laser holes with higher effectiveness levels even though blowing ratios between the two geometries were similar.

In comparing the region between $0.4 < x/C < 0.8$, there is an interesting trend. The typical difference between the peaks and valleys associated with the EDM holes remains at about $\eta = 0.15$ for both the large and small tip gaps. The typical difference between the peaks and valleys associated with the laser holes is about $\eta = 0.25$ for the small tip gap and $\eta = 0.15$ for the large tip gap. This suggests that the jets exiting the laser holes tend to blow off the tip surface and onto the shroud. When this occurs for the small tip gap, the gap is small enough that the jets are still effective on the tip surface. When blow-off occurs for the large tip gap, however, the cooling does not significantly affect the tip surface, but rather remains along the shroud surface.

Figure 2.17 shows path line data for the laser and EDM cases at blowing ratios of 0.58% and 1.0%. Note that the distance along the tip (L) was normalized with the maximum distance along the tip (L_{\max}). At positions 1 and 2, which follow the path lines of maximum effectiveness, the film cooling always increases with blowing for the small tip gap. For the large tip gap, the same trend is true for the EDM holes, but not for the laser holes. The laser holes have some segments of the blade where the effectiveness is higher with a lower blowing ratio, especially near the pressure side ($L/L_{\max} < 0.2$). The reason for this is because at the lower blowing ratio the coolant trajectories from the laser holes remain attached to the blade surface. At higher blowing ratios, the coolant becomes separated from the blade surface. In general, for the same gap height and blowing ratio the EDM holes have higher effectiveness than the laser holes.

Figure 2.17c and 17f show data taken in between two coolant trajectories. For the EDM holes, there is essentially no difference with increased blowing, suggesting that the spreading in between holes is not greatly affected by blowing rate. For the laser holes, the same is true at the large tip gap. The reason for this is because the coolant flow is attached to the shroud. At the small tip gap, however, there is increased effectiveness with increased blowing for the laser holes. As mentioned before, the flow fills the gap at this height and with increased blowing there is increased spreading of the laser jets onto the blade tip.

Area-averaged film effectiveness results were calculated to make overall conclusions about the testing performed, as shown in Figure 2.18a. This Figure 2. shows the overall trend that the effectiveness increases with increased blowing. Also, the effectiveness is significantly higher for the small tip gap for both hole geometries. These

results show that the laser geometry has a higher area-averaged value than the EDM geometry for the same coolant flow. Because this data is greatly affected by the dirt purge cooling and as such does not allow a one-to-one comparison of the hole shapes, a second area-average was calculated. The area-averages for the downstream portion representing 70% of the blade tip are shown in Figure 2.18b. These results show that the EDM significantly outperforms the laser hole flows at all cooling flow conditions indicating a better performance.

Leading Edge Blowing with no Dirt Purge Blowing

Because the dirt purge blowing overwhelms a large portion of the leading edge region, an additional test was conducted for both hole geometries whereby coolant from only the film-cooling holes was exhausted in the leading edge (no dirt purge blowing). The coolant flows for these two cases were set to be the coolant exhaust that resulted for the 0.68% case subtracting out the dirt purge, tip flag, and back supply chamber cooling. This resulted in a total coolant flow of 0.09% being injected from the first three EDM holes and an equivalent 0.07% being injected from the first two laser holes.

Figure 2.19 shows the measured results of these tests for a large tip gap. Note that while the dirt purge holes were not flowing, the cavity was still present. These results indicate the better performance of the EDM holes over that of the laser holes. It is interesting to note that the total coolant flow for the EDM test results in 0.03% per hole, whereas the laser has 0.035% per hole. So, even though the laser holes have more mass flowing through each hole, the separation of the jet away causes lower effectiveness levels on the tip. The results for the laser holes also indicate that the coolant is actually being brought into the dirt purge cavity and then mixed with hot mainstream fluid before exiting at a much higher temperature. The hole locations are also shown and indicate that in the leading edge region, without dirt purge blowing, the laser holes are significantly further swept downstream of their respective hole exit.

Conclusions

The conclusions reached from these tests indicate that the EDM holes outperformed the laser holes for all of the cases considered. The performance of cooling holes placed at the pressure side tip was better for a small tip gap than for a large tip gap.

Also, for the small tip gap there was not a large increase of effectiveness for increases in coolant flow. At a small tip gap, the EDM holes provide good coverage ($\eta \sim 0.4$) with a local blowing ratio as low 2, whereas a blowing ratio of 4 is needed to provide the same effectiveness for a large tip gap. For the laser holes, a blowing ratio of about 4 is needed to provide good coverage ($\eta \sim 0.4$) at a small tip gap, and no blowing ratio tested provided good coverage of the blade tip with laser holes for a large tip gap.

Computational predictions showed trends that agreed with the experimental results. These trends included the trajectory of the jets. More importantly, the CFD results indicated some of the coolant was blowing into the passage and in the case of the laser holes never entered the gap region.

In general, the laser holes provided a much streakier effectiveness pattern as compared with the EDM holes in which the coolant was more evenly spread across the tip. This spreading resulted from the diffused hole exits for the EDM holes relative to the laser holes. The low exiting momentum of the EDM jets allows the coolant to remain attached to the blade pressure-side surface and be swept across the blade tip. The laser holes were found to become separated from the pressure side surface as a result of the higher exit momentum compared with the EDM holes.

Acknowledgements

The authors gratefully acknowledge United Technologies – Pratt and Whitney for their support of this work.

Nomenclature

C	= true chord of blade
C_d	= discharge coefficient
C_p	= pressure coefficient, $C_p = (p - p_{in}) / (\rho U_{in}^2 / 2)$
D	= dirt purge hole diameter
D_h	= hydraulic diameter, always set as twice the gap height
h, H	= small and large gap distances
I	= momentum flux ratio
L	= distance along the path line across the tip
M	= mass flux ratio

P_o, p = total and static pressures
 Re_{in} = Reynolds number defined as $Re_{in} = C U_{in} / \nu$
 S = surface distance along blade pressure side from stagnation
 T = temperature
 U = measured air velocity
 x = distance along the blade chord

Greek

α = angle relative to blade pressure side curve
 δ, Δ = denotes a differential
 η = adiabatic effectiveness, $\eta = (T_{in} - T_{aw}) / (T_{in} - T_c)$
 ρ = density
 θ = blade inlet angle
 ν = kinematic viscosity

Subscripts

aw = adiabatic wall
b = blade
c = coolant conditions
dyn = dynamic
in = value at 1C upstream of blade
max = denotes maximum value

References

- [1] Christophel, J., Thole, K.A., and Cunha, F., "Comparison of Exit Hole Shapes for Cooling the Tip of a Turbine Blade – Part 2: Heat Transfer Measurements," GT2004-53254.
- [2] Bunker, R.S., "A Review of Turbine Blade Tip Heat Transfer," Turbine 2000 Symposium on Heat Transfer in Gas Turbine Systems, Cesme, Turkey, 2000.
- [3] Kim, Y.W. and Metzger, D.E., "Heat Transfer and Effectiveness on Film Cooled Turbine Blade Tip Models," *J of Turbomachinery*, **117**, 1995.
- [4] Kim, Y.W., Downs, J.P., Soechting, F.O., Abdel-Messeh, W., Steuber, G., and Tanrikut, S., "A Summary of the Cooled Turbine Blade Tip Heat Transfer and Film

Effectiveness Investigations Performed by Dr. D. E. Metzger,” *J of Turbomachinery*, **117**, pp. 1-11, 1995.

[5] Kwak, J.S. and Han, J.C., “Heat Transfer Coefficient and Film-Cooling Effectiveness on a Gas Turbine Blade Tip,” GT2002-30194.

[6] Kwak, J.S. and Han, J.C., 2002b, “Heat Transfer Coefficient and Film-Cooling Effectiveness on the Squealer Tip of a Gas Turbine Blade,” GT2002-30555

[7] Acharya, S., Yang, H., Ekkad, S.V., Prakash, C., and Bunker, R., 2002, “Numerical Simulation of Film Cooling Holes On the Tip of a Gas Turbine Blade,” GT-2002-30553.

[8] Hohlfeld, E.M., Christophel, J.R., Couch, E.L., and Thole, K.A., “Predictions of Cooling from Dirt Purge Holes Along the Tip of a Turbine Blade,” GT2003-38251.

[9] Srinivasan, V. and Goldstein, R.J., “Effect of Endwall Motion on Blade Tip Heat Transfer,” *Journal of Turbomachinery*, **125**, pp. 267-273, 2003.

[10] Moffat, R.J., “Describing the Uncertainties in Experimental Results,” *Experimental Thermal and Fluid Science*, **1**, pp. 3-17, 1988.

[11] Fluent Inc., Fluent User’s Guide, Version 6.0, 2002 (Fluent Inc. New Hampshire).

Table 2.1 Description of Hole Models

Parameter	Laser Hole Model	EDM Hole Model
Total Number of Cooling Holes	15	10
Total Coolant Flow Area (dirt purge, cooling holes, and TEF), cm ²	5.15	5.71
Hole Metering Area / Total Coolant Flow Area	0.51	0.46
Dirt Purge Flow Area / Total Coolant Flow Area	0.33	0.30
TEF Flow Area / Total Coolant Flow Area	0.16	0.24
Pressure side hole placement below tip (H = large tip gap; h = small tip gap)	3h 1H	6.7h – 10h 2.2H – 3.3H

Table 2.2 Blade Geometry and Flow Conditions

Parameter	Wind Tunnel Settings
Scaling Factor	12X
Axial chord / True Chord	0.66
Pitch / True Chord	0.81
Span / True Chord	1.03
Re _m	2.1 x 10 ⁵
Inlet Angle, θ	16.5°
Coolant to Mainstream ΔT	25°
Small tip gap / Span (%)	0.54
Large tip gap / Span (%)	1.63

Table 2.3 Matrix of Experiments

Gap Setting	Holes Tested	Total Coolant Flow (% passage)	Flow Split Plenums 1 / 2 (% coolant)
Small, Large	EDM	0.58	53 / 47
Small, Large	EDM	0.68	52 / 48
Small, Large	EDM	1.0	51 / 49
Small, Large	Laser	0.47	58 / 42
Small, Large	Laser	0.58	59 / 41
Small, Large	Laser	0.68	59 / 41
Small, Large	Laser	1.0	51 / 49
Small no dirt purge flow	EDM	0.09	100 / 0
Small no dirt purge flow	Laser	0.07	100 / 0

Table 2.4 Location of Path Line Data for Each Geometry

		Laser		EDM	
		Large Tip Gap	Small Tip Gap	Large Tip Gap	Small Tip Gap
Pathline 1	S/S_{max}	0.42	0.41	0.38	0.38
	α	74°	70°	67°	67°
Pathline 2	S/S_{max}	0.54	0.54	0.54	0.54
	α	68°	72°	72°	60°
Pathline 3	S/S_{max}	0.61	0.61	0.58	0.59
	α	63°	68°	65°	60°

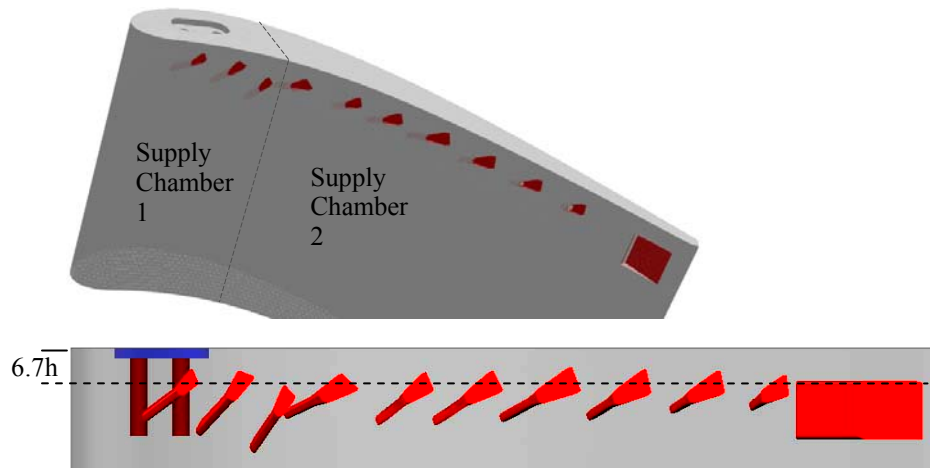
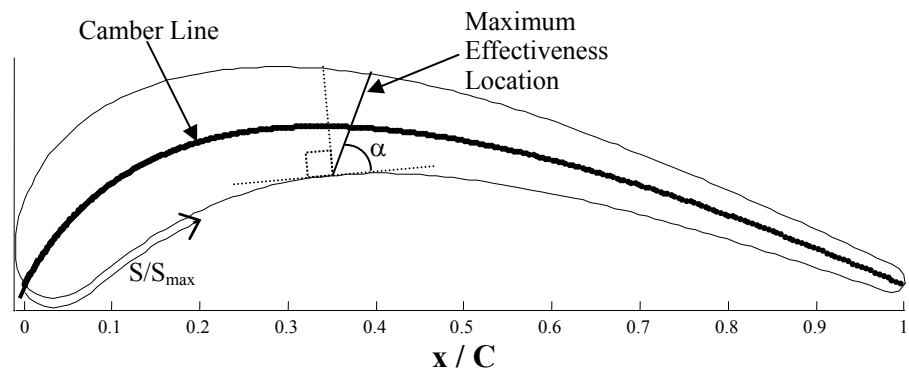


Figure 2.1 Schematics showing the hole geometry for the EDM drilled holes

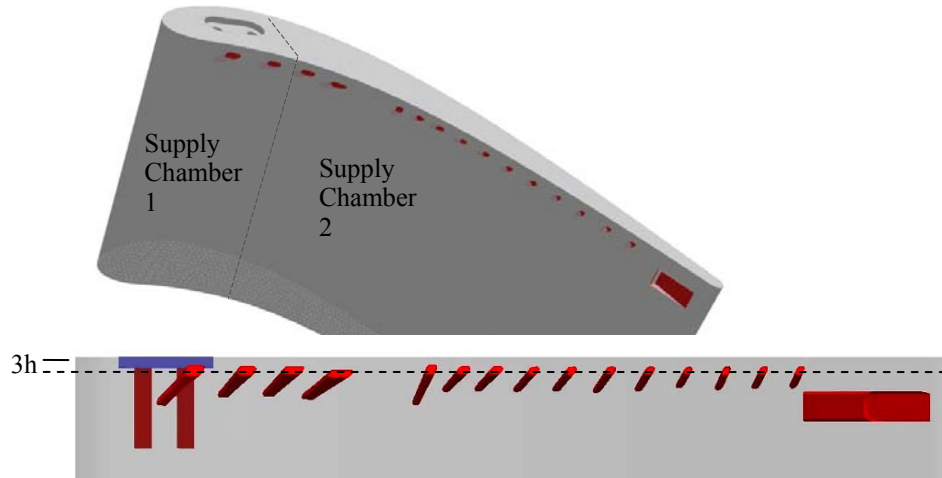


Figure 2.2 Schematics showing the hole geometry for the laser drilled holes

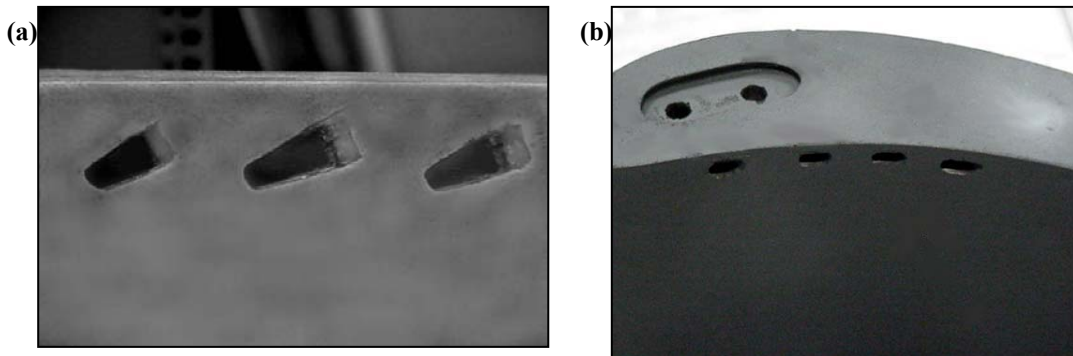


Figure 2.3 Images of SLA model for the EDM holes (a) and laser holes (b) placed within the foam blade

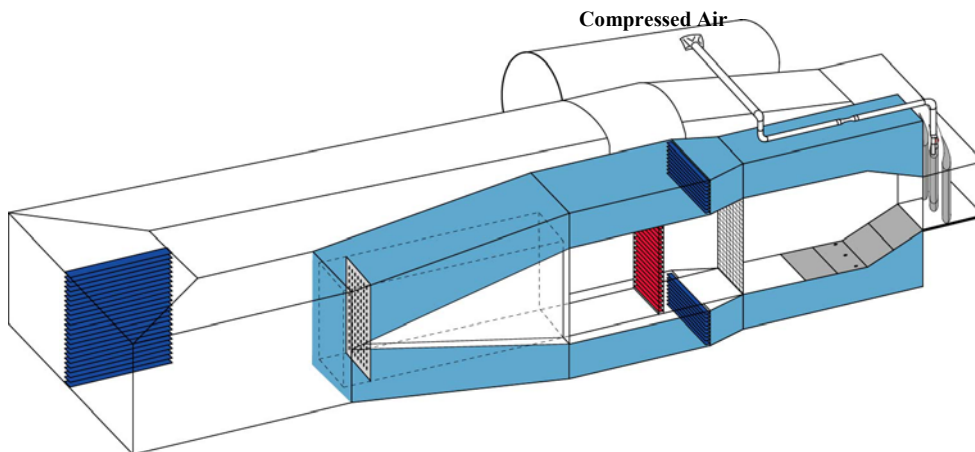


Figure 2.4 Schematic of wind tunnel facility for the tip tests

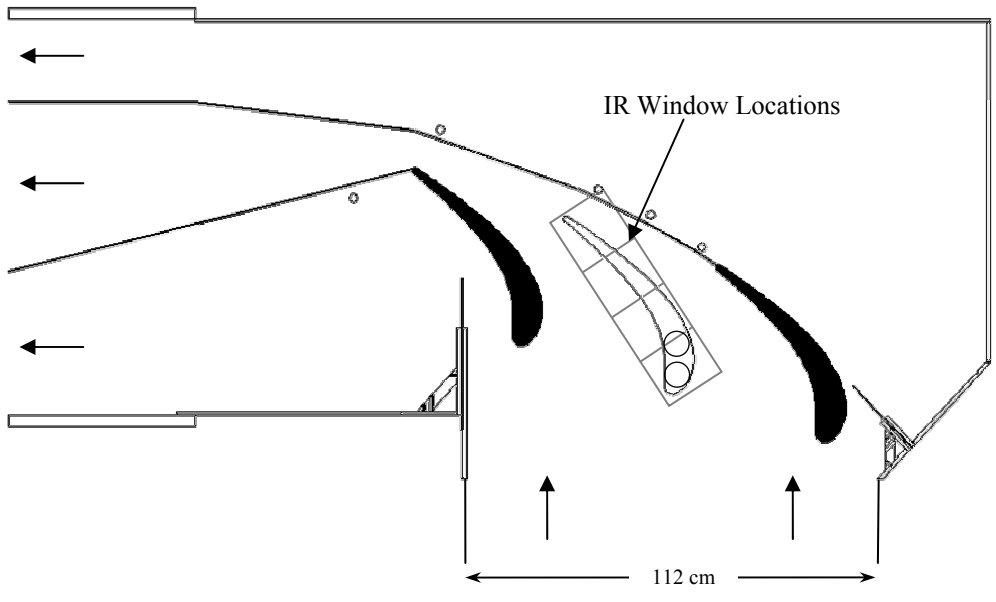


Figure 2.5 Top view of the test section for the blade tip tests

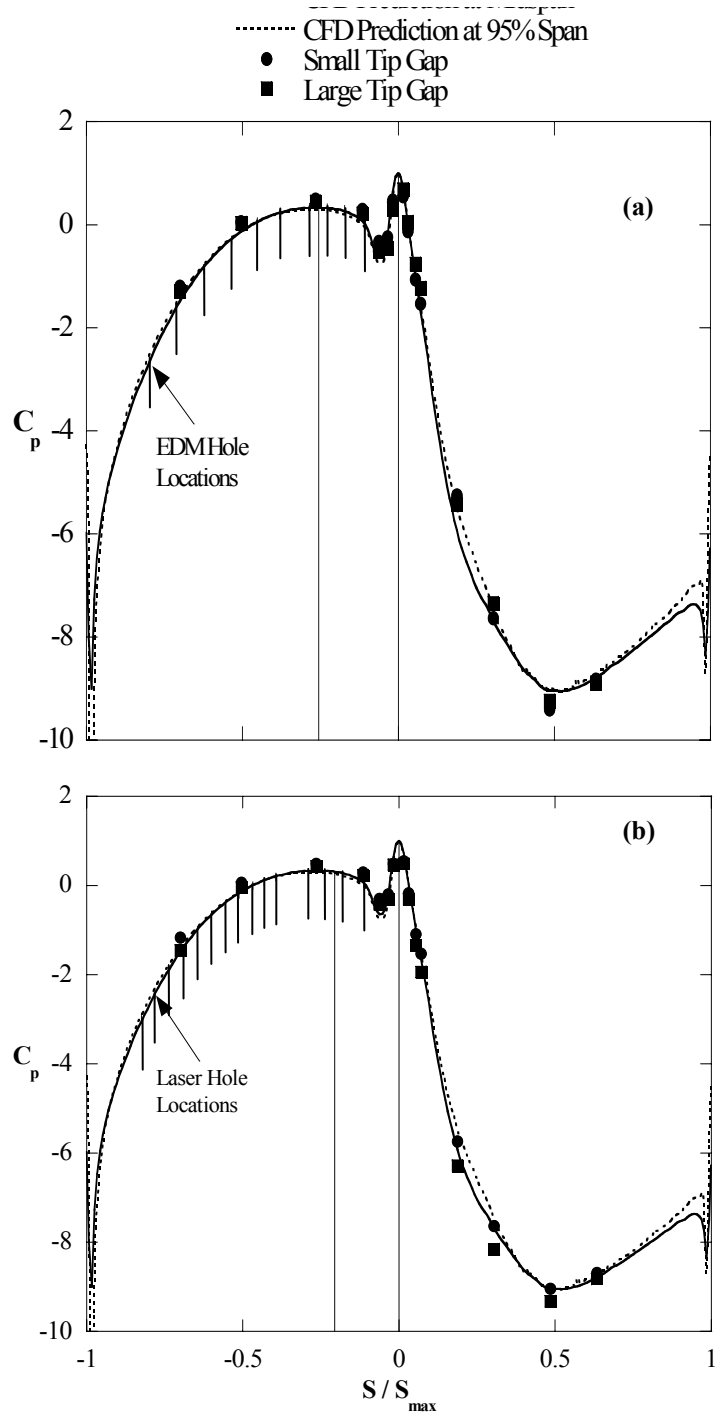


Figure 2.6 Predicted and measured static pressure distributions for the large and small tip gap cases for the EDM (a) and laser drilled (b) holes for the tip study. Also indicated are the hole locations along the pressure side of the airfoil and the pressure distribution at the 95% span location near the tip.

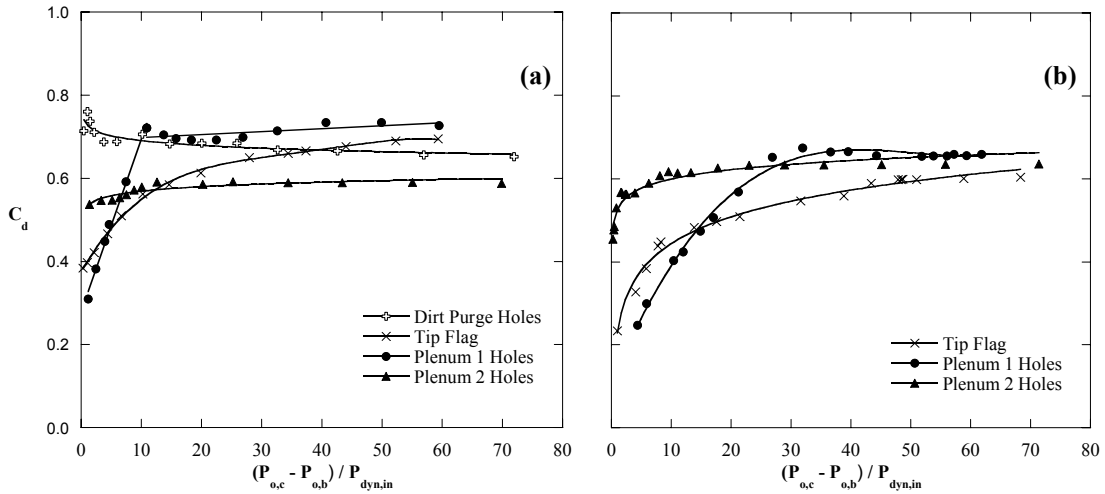


Figure 2.7 Discharge coefficients that were measured for the EDM hole model (a) and laser hole model (b) including the discharge coefficients for the dirt purge holes and TEF.

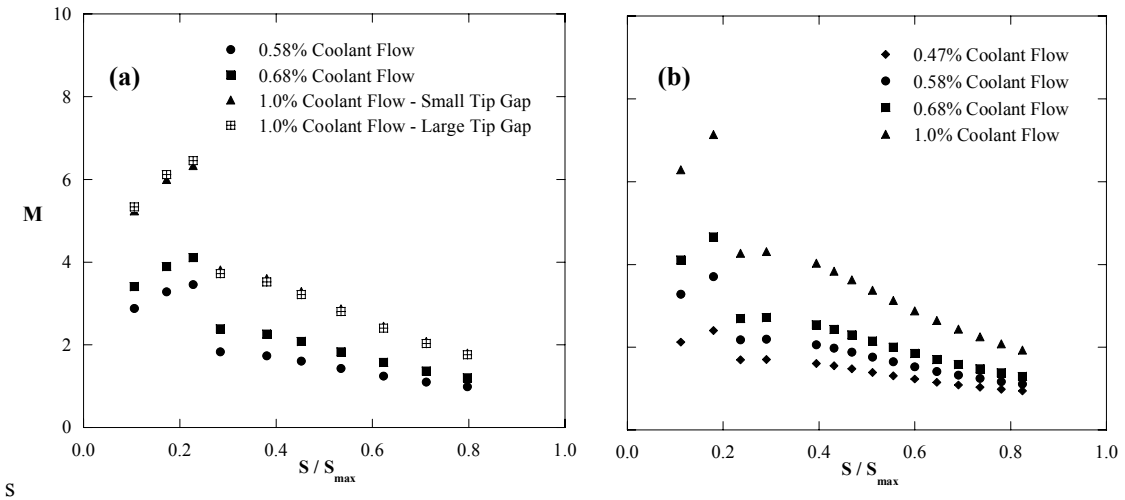


Figure 2.8 Local mass flux ratios for each of the EDM (a) and laser (b) holes placed on the pressure side of the blade

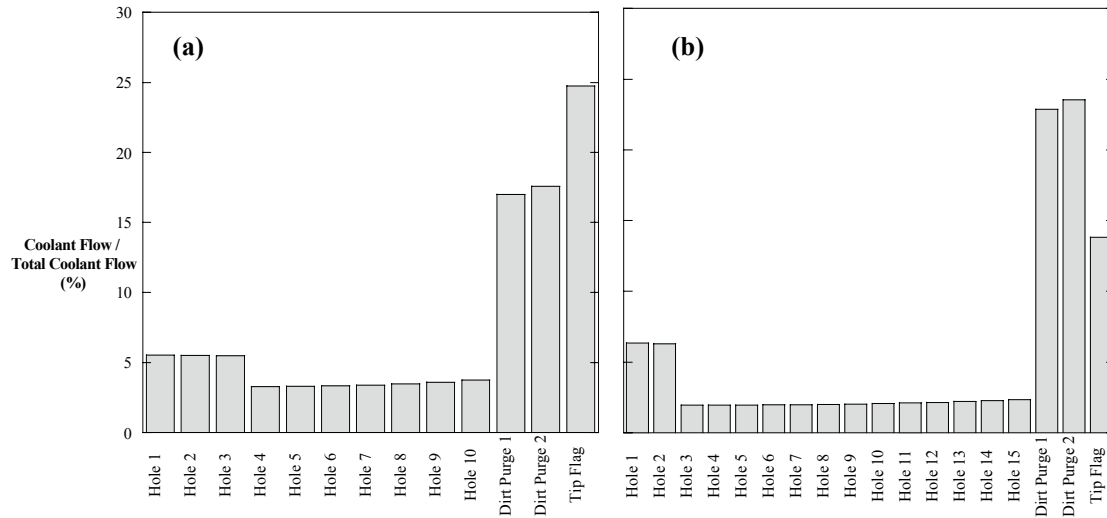


Figure 2.9 Coolant flow split for the EDM (a) and laser (b) holes at a total coolant of 0.68%. Note hole 1 is closest to the stagnation location.

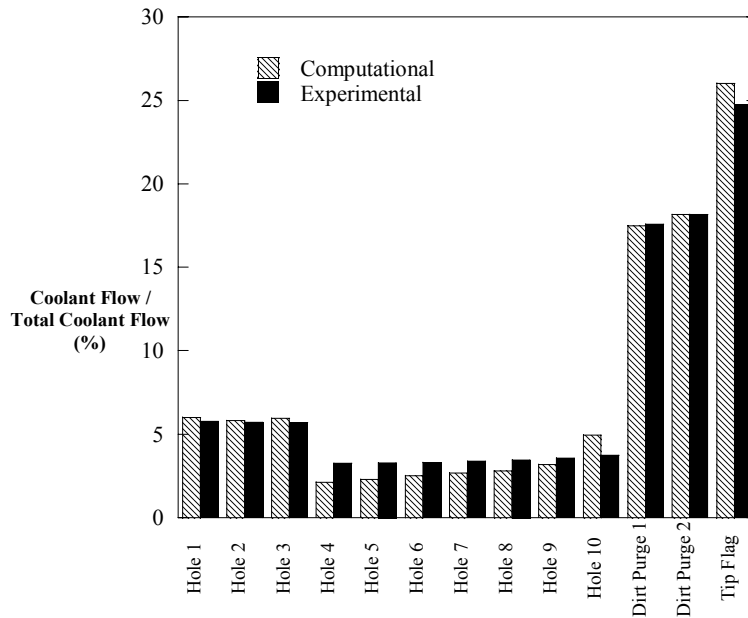


Figure 2.10 Comparison of computational and experimental flow rates for the EDM holes with 0.68% coolant flow.

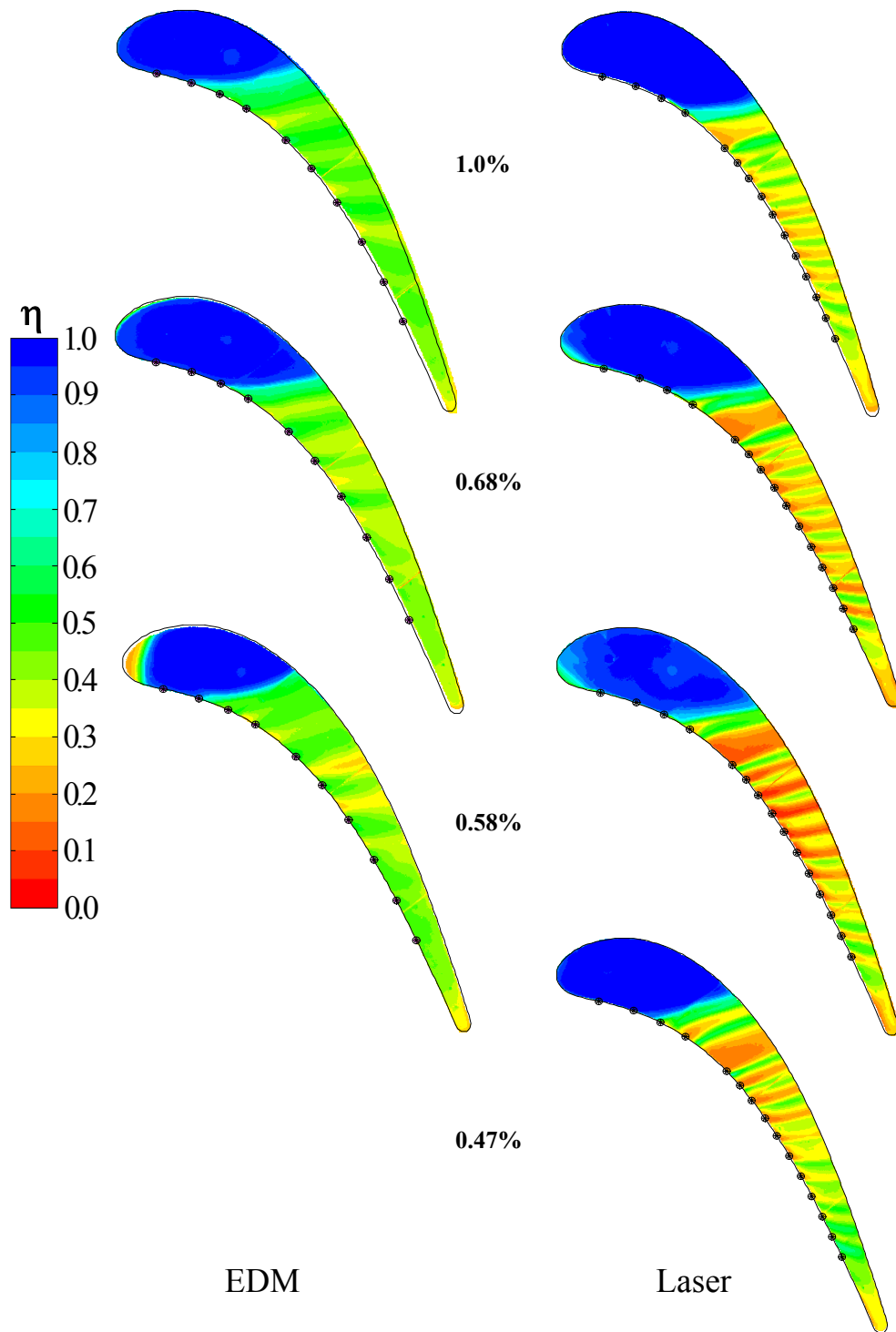


Figure 2.11 Measured adiabatic effectiveness levels on the tip for the EDM (left) and laser (right) drilled hole cases for the small tip gap.

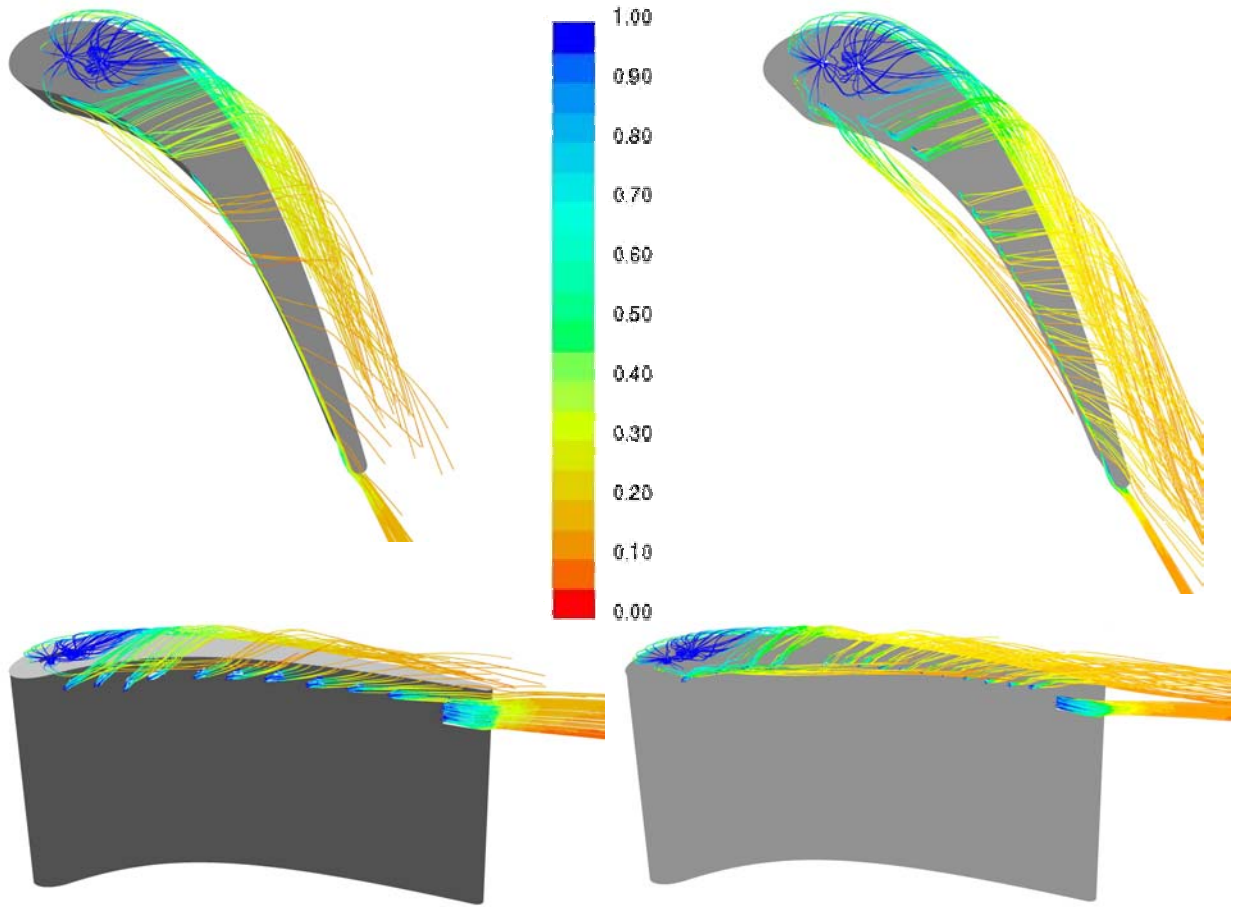


Figure 2.12 Predicted path lines for the EDM geometry (left) and laser geometry (right).

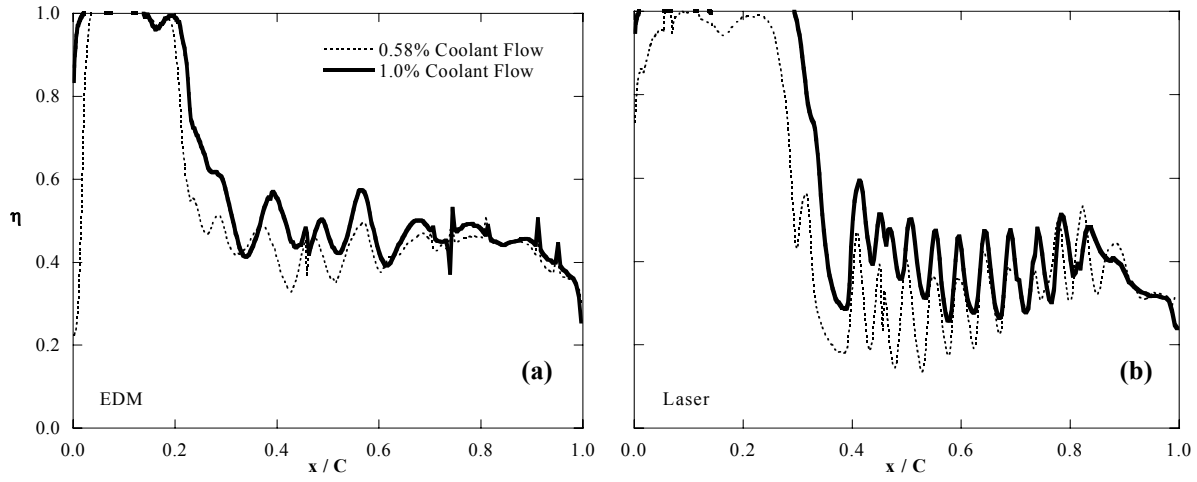


Figure 2.13 Data taken along the camber line for the small tip gap with EDM holes (a) and laser holes (b).

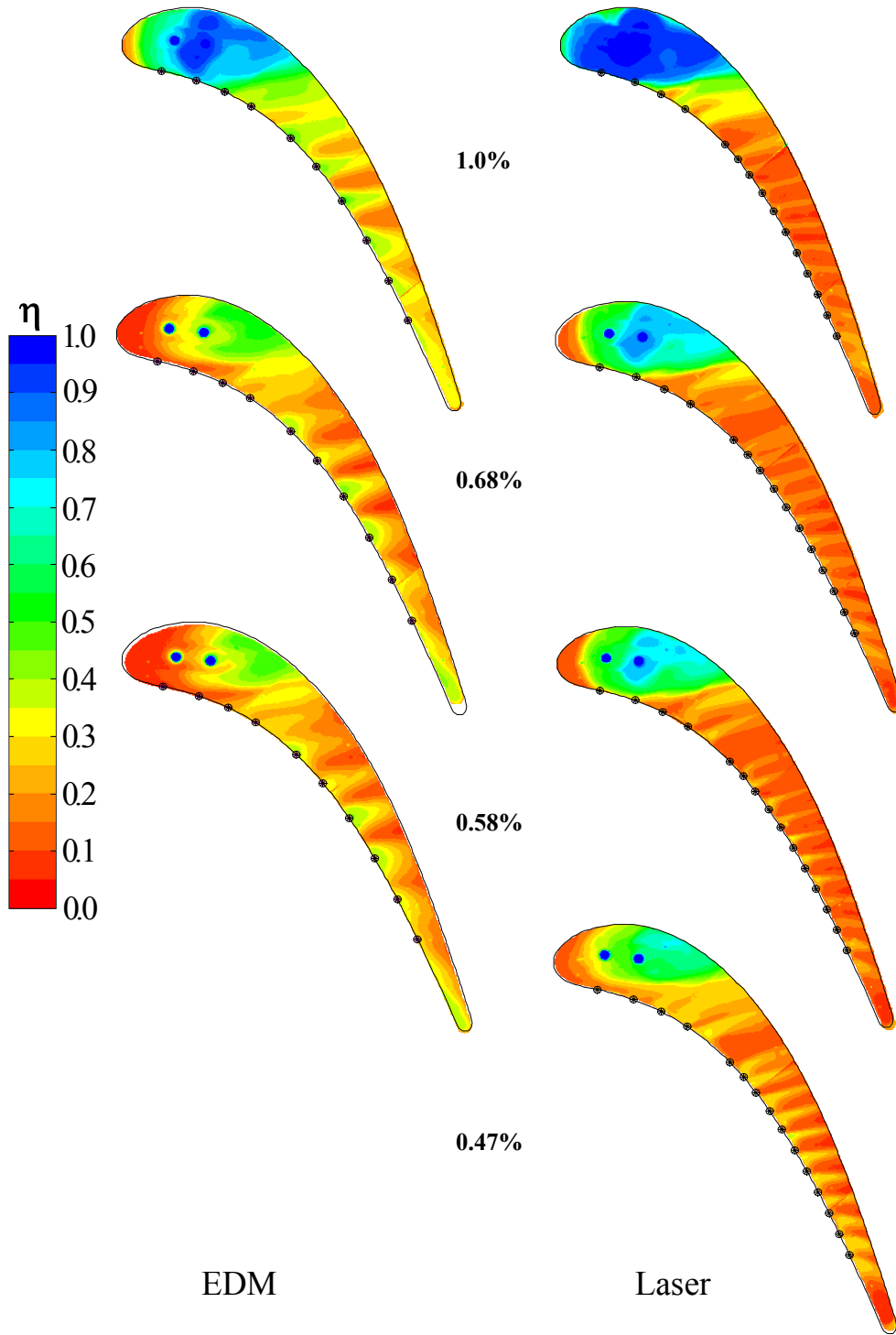


Figure 2.14 Measured adiabatic effectiveness levels on the tip for the EDM (left) and laser (right) drilled hole cases for the large tip gap.

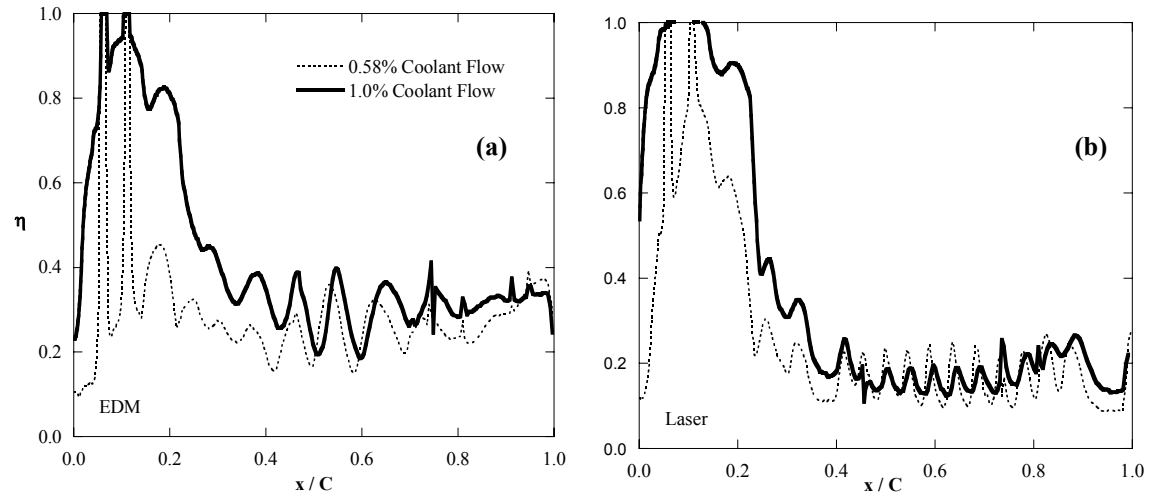


Figure 2.15 Data taken along the camber line for the large tip gap with EDM holes (a) and laser holes (b).

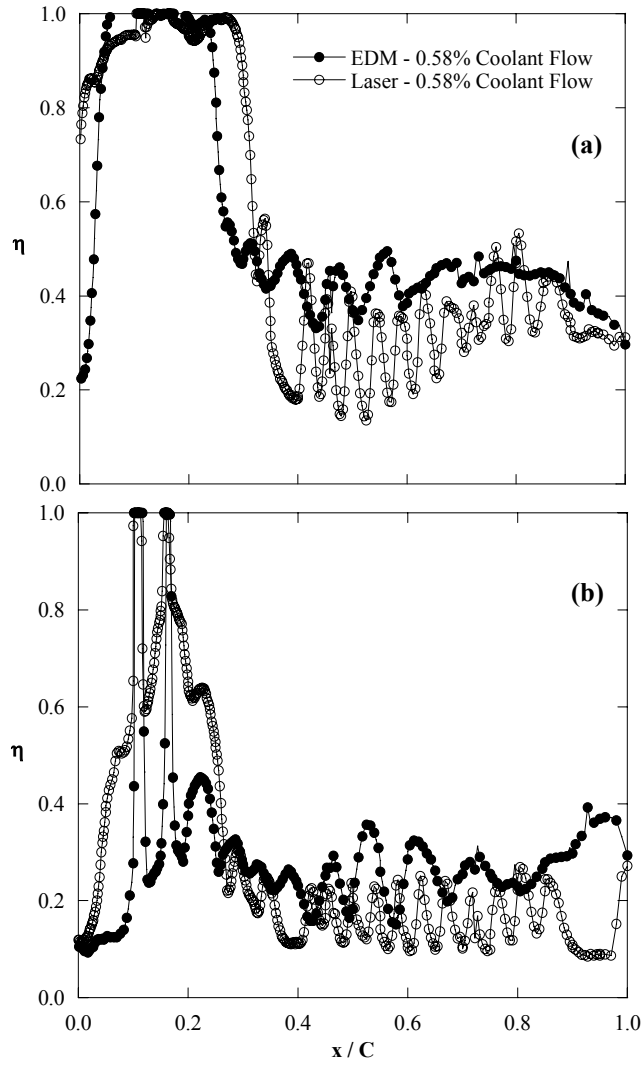


Figure 2.16 Camber lines of effectiveness for the small (a) and large (b) tip gaps for the two cooling hole geometries.

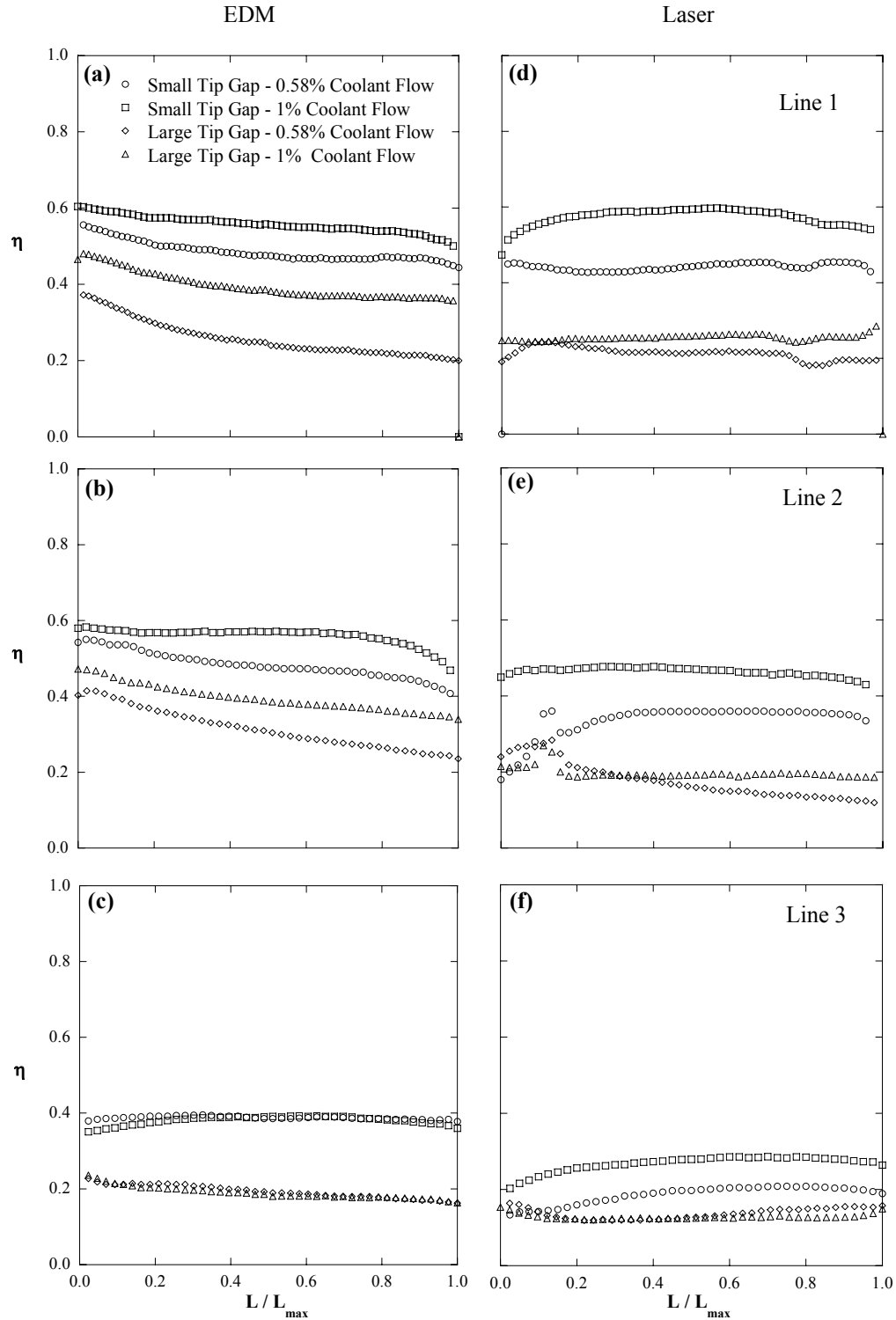


Figure 2.17 Path line data for the EDM (a – c) and laser (d – f) cases.

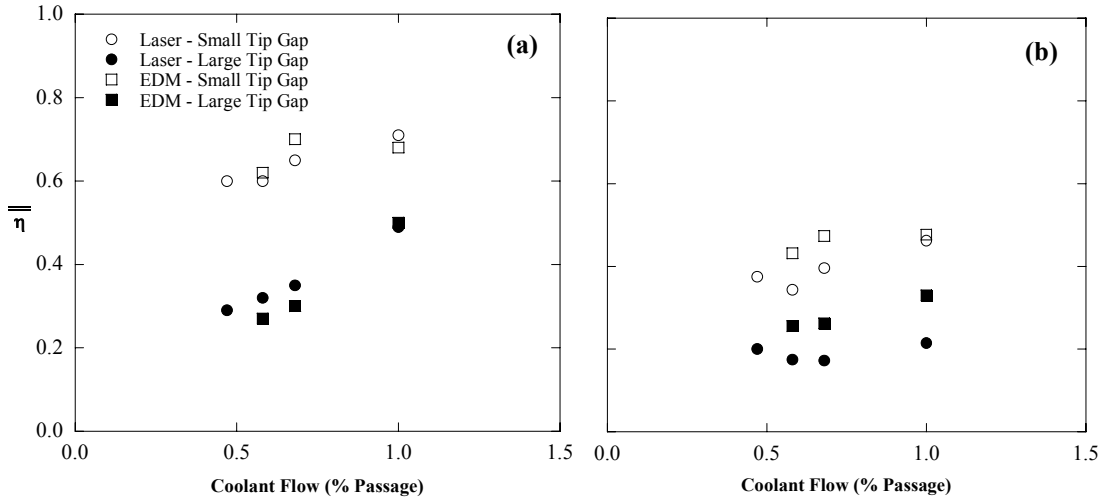


Figure 2.18 Area-averaged effectiveness for the entire tip (a) and for downstream 70% portion of the blade tip (b).

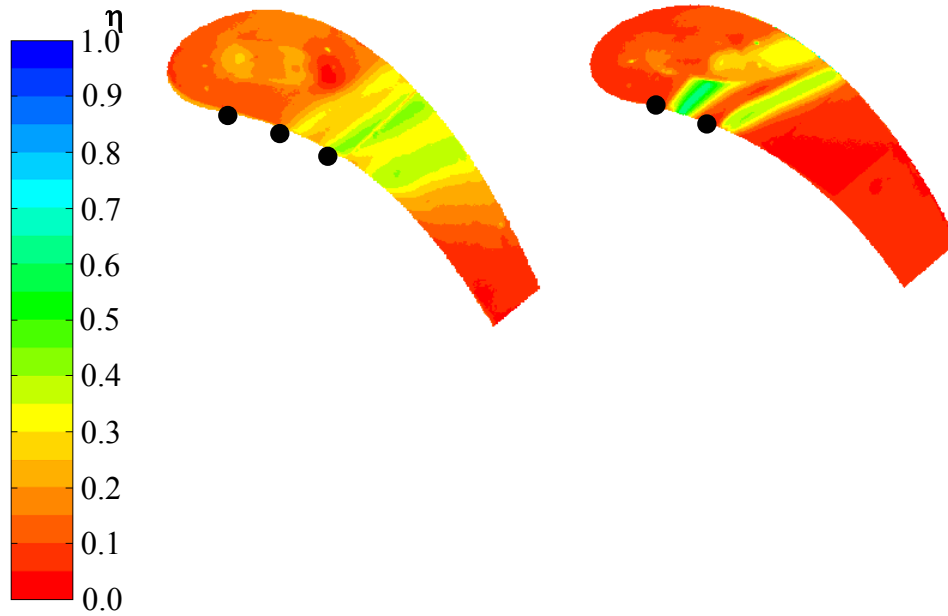


Figure 2.19 Effectiveness contours with no dirt purge blowing for the front plenum only with the EDM holes (a) and laser holes (b).

Paper 3:
**Comparison of Exit Hole Shapes for Cooling the Tip of a
Turbine Blade—Part 2: Heat Transfer Measurements**

To be submitted to the *Journal of Turbomachinery**

Abstract

The clearance gap between a turbine blade tip and its associated shroud allows leakage flow across the tip gap from the pressure side to the suction side of the blade. Understanding how this leakage flow affects heat transfer is critical in extending blade tip durability in terms of oxidation, erosion, clearance, and overall turbine performance. This paper is the second of a two part series that discusses the augmentation of tip heat transfer as a result of blowing from the pressure side of the tip through two different types of pressure side film hole shapes. One of the film hole shapes represents those that would occur from Electro-Discharge Machining (EDM) while the other represents that of a Light Amplification Stimulation with Emission Radiation (laser) drilling process.

For the experimental investigation, three scaled-up blades were used to form a two-passage linear cascade in a low speed wind tunnel. The rig was designed to simulate different tip gap sizes and coolant flow rates. Heat transfer coefficients were quantified by measuring the total power supplied to a constant heat flux surface placed on the tip of the blade and measuring the tip temperatures. Results indicate that for both hole shapes, increased blowing leads to increased augmentations in tip heat transfer, particularly at the entrance region to the gap. When combined with adiabatic effectiveness measurements, the EDM holes provide coolant that results in a higher overall net heat flux reduction as compared with the laser holes.

*Co-authors: Dr. Karen A. Thole, Mechanical Engineering Department, Virginia Tech
Dr. Frank J. Cunha, Turbine Durability, Pratt & Whitney

Introduction

Technical advancements in the gas turbine industry require higher turbine rotor inlet temperatures (RIT) to allow for more efficient operation and engine performance. RIT is, however, the limiting design criteria since as these temperatures increase component life decreases for the same material and cooling technology. Gas turbine airfoils are typically cooled using both convective and film cooling. Film cooling is a method whereby cooler compressor fluid is injected through film holes in the blade surface that can be manufactured a number of different ways. This type of protection is most important for high pressure turbine blade tip where the heat transfer coefficients can be as much as two and a half times higher than on the pressure and suction side of the blade airfoil (Kwak and Han [1]). As such, film cooling holes can be placed on the pressure side of a turbine blade near the tip region. Because of the pressure driven flow over the tip, the coolant from these holes can sweep over the tip through the gap clearance, providing film cooling along the blade tip. The manufacturing methods for these film-cooling holes can be of the following two types: Electro-Discharge Machining (EDM) or Light Amplification Stimulation with Emission Radiation (laser) drilling process. Laser drilling provides a sharp hole exit whereas EDM generally provides hole exits that are diffused or shaped.

The purpose of this study was twofold. The first part examines the heat transfer on a flat blade tip without cooling to verify fundamental trends. The second part examines the heat transfer coefficients for two different blade tip representative film hole shapes (EDM and laser) placed on the pressure side near the tip region in terms of blade tip heat thermal load. The affect of pressure side blowing for different tip gaps and different blowing ratios are also presented in this paper. The results from this overall study will also be to combine adiabatic effectiveness results from Part 1 [2] with heat transfer coefficients from this paper, Part 2, to evaluate the overall benefit of the tip cooling. This work will assess the differences in these two primary methods of hole drilling and will aid in the turbine blade future design process.

Past Relevant Studies

As early as 1982, Mayle and Metzger [3] showed that the tip leakage flow is comprised primarily of mainstream passage fluid. Other researchers showed a separation bubble formation along the tip pressure side, which was confirmed by Morphis and Bindon [4]. Bindon [5] went

on to show that this separation bubble dominates the gap flow characteristics and associated pressure losses. In his recent review of turbine blade tip heat transfer, Bunker [6], noted that this separation bubble causes a heat transfer enhancement factor of two to three times above that occurring at the tip camber line of an airfoil.

In an effort to reduce the tip leakage flow, many studies have been performed on blade tips with a squealer geometry. This has been shown to significantly reduce the blade tip heat transfer, however, the trends seen on a flat tip are much different than a tip with a squealer cavity. Bunker et al. [7], using a recessed shroud, showed the first experimental heat transfer results on a flat blade tip. His research showed there to be a small area of low heat transfer located near the thickest part of the blade. This low region has been confirmed by many authors including Kwak and Han [1] and Jin and Goldstein [8]. Kwak and Han [1] also noted that the area of low heat transfer tends to be smaller and pushed downstream at increased tip gap heights.

Azad and Han [9], Kwak and Han [1], and Jin and Goldstein [8] have all shown that the blade tip heat transfer increases with increasing tip gap height. For a flat tip with no blowing, Jin and Goldstein [8] showed that the average heat transfer increases along the blade towards the trailing edge. This was confirmed by Saxena et al. [10] who showed that the heat transfer along the blade camber line increased towards the trailing edge.

There have been relatively few studies with blowing over a blade tip surface. Kim and Metzger [11] measured the heat transfer coefficients along a channel representing a blade tip with injection directly into the tip region. They showed that coolant injection always led to higher heat transfer over a case with no injection. Kim et al. [12] found this same trend with tip surface injection, but noted that injection from the pressure side showed reduced heat transfer on the tip surface. Kwak and Han [13] used an actual airfoil shape with both tip and pressure side injection. Their results, in contrast to Kim et al. [12], indicated that increased coolant injection resulted in reduced heat transfer coefficients.

Other studies have focused on the differences between hole shapes but have not been performed on a blade tip. Studies by Sen et al. [14] and Gritsch et al. [15] have shown that expanded holes provide lower heat transfer coefficients relative to blowing through cylindrical holes. These same studies have also shown that increases in the blowing ratio will increase the heat transfer. When compared to a surface without injection, Gritsch et al. [15] and Yu et al. [16] have reported that expanded holes can actually reduce the heat transfer coefficients when

blowing is present compared with no blowing, whereas cylindrical holes increase heat transfer coefficients.

Generally, tip heat transfer studies without injection have all shown that increasing the tip gap increases heat transfer. Also, regions of low heat transfer are expected near the thickest portions of the blade. When coolant injection is introduced; however, the results are still unclear. Some researchers show that the injection will cause an increase in the heat transfer from the baseline case, whereas others show a decrease. The difference between hole shapes has been well established for flat plate tests, but have not been performed on an airfoil geometry at the tip surface. This study will assess the differences in hole shapes when blowing is present near the pressure side tip surface.

Experimental Facility and Instrumentation

The experiments in this study were performed in a large-scale, low-speed, closed-loop wind-tunnel facility that provided matched engine Reynolds number conditions, as described in Part 1 [2] of this paper. The test section was attached downstream of a contraction section which used a row of high momentum normal jets to provide a turbulence level of 10% and length scale of 11 cm at the blade entrance. The linear cascade test section, shown in Figure 3.1, consisted of an instrumented center blade and two outer blades with tailboards. The tailboards along with the bleed gates allowed for flow control around the center blade, insuring flow periodicity. Velocity measurements were taken approximately one chord upstream at several pitch-wise locations to verify a uniform incoming velocity field. Static pressure measurements were taken around the blade mid-span to insure flow periodicity. This measured pressure distribution was compared with a 2-D, inviscid prediction and is shown in Figure 3.2. Figure 3.2 also presents the hole locations for both tip models.

Coolant flow used for the tip blowing experiments was supplied by an in-house compressor and was controlled by using a series of valves before exiting through the blade tip cooling holes. The overall coolant flow rate was known by measuring the pressure drop across a venturi nozzle. Discharge coefficients, which had previously been measured for the hole geometries, allowed for the estimation of flow rate through each individual hole by way of pressure measurements [2]. The total coolant flow could then be calculated by summing each of

the individual hole flow rates. This was compared to the total coolant flow measured by the venturi nozzle. In general, the two flow rates were within 2.8% of each other.

The three tips that were tested, shown in **Figure 3.3**, are referred to as the baseline (3a), EDM holes (3b), and laser holes (3c). The EDM and laser holes were designed to be representative of the EDM and laser manufacturing, respectively. All blades had a dirt purge cavity that was recessed $2h$ ($0.67H$) from the tip surface. The baseline geometry had no holes present on the pressure side or within the dirt purge cavity and therefore no film cooling. The EDM and laser geometries had tip holes placed in the pressure side surface of the blade in addition to two holes within the dirt purge cavity, which have been described in detail by Hohlfeld et al. [17]. The purpose of the dirt purge holes is to allow for blade manufacturing and to expel dirt particles so as not to plug smaller diameter film cooling holes.

In addition to the dirt purge holes, the EDM tip model had 10 pressure side holes placed near the tip surface while the laser tip model had 15 pressure side holes placed slightly closer to the tip surface as shown in Figure 3.3. All of the EDM holes had expansions in both the axial and span directions and had a metering hole diameter of $0.56 D$, where D is the diameter of the dirt purge holes. The centerline at the hole breakout for the EDM holes ranged from 94% to 96% of the blade span, which is between $6.7h$ and $10h$ ($2.2H$ or $3.3H$) from the blade tip. The centerline at the hole breakout for the laser holes is at 98.5% of the blade span, which is $3h$ ($1H$) below the blade tip. The four film cooling holes just downstream of the stagnation for the laser tip were expanded in the axial direction and had a metering hole diameter of $0.56 D$ whereas the remainder of the holes had no expansion and a metering hole diameter of $0.41 D$. For both the laser and EDM tip models, there is a slot at the trailing edge denoted as the trailing edge flag (TEF).

Testing conditions and blade parameters are given in Table 3.1. The small (h) and large (H) tip gap settings considered were 0.54% and 1.63% of full blade span, respectively. All tests were conducted at a density ratio of one, such that the coolant and mainstream temperatures were typically kept to within 0.15°C . For the baseline geometry, experiments were conducted at both the small and large tip gap settings with no blowing present. For the laser geometry, experiments were conducted at both tip gap settings and at overall coolant flow rates of 0.58% and 1% of the total passage flow. For the EDM geometry, experiments were again conducted at both tip gap

settings and at coolant flow rates of 0.58% and 1% of the total passage flow. The total passage flow was calculated based on the inlet mainstream velocity, blade span, and pitch.

For making the heat transfer measurements, foil heaters were used to supply a constant heat flux at the tip surface. Two separate heaters were necessary as shown in Figure 3.4, one for the blade tip surface and the other for the dirt purge cavity on the tip. The dirt purge cavity was heated with one strip of Inconel that was 0.051 mm thick and had a surface area of 17.3 cm². The main heater covered an area of 261.2 cm² and consisted of a serpentine Inconel circuit. The circuit shown in Figure 3.4 used Inconel sandwiched between insulating Kapton and then covered with a very thin (0.013 mm) layer of copper on both sides. Both heaters were attached to a foam blade tip using double-sided tape that was 0.64 mm thick. The nominal heat flux for both heaters was set to 3700 W/m² which provided a maximum temperature difference between the mainstream and blade surface of 28°C. The two heaters were controlled independently with a variac to within 0.67% of one another during all tests. The current supplied to each heater was known by placing a precision resistor ($R = 1\Omega \pm 0.1\%$) in each circuit and measuring the voltage drop across each resistor with a digital multimeter. The heater power was then determined from the supplied current and known heater resistance.

Equation 1 was used when calculating the heat transfer results to account for radiation losses.

$$h = \frac{q_{\text{tot}}'' - q_r''}{T_w - T_\infty} \quad (1)$$

In this equation, q_{tot}'' represents the total heat flux output from the resistive heaters and q_r'' represents the energy lost to radiation. Typically, radiation losses were less than 2% with the maximum for all cases being 3.4%. Conduction losses were found to be negligible since the heaters were placed on low thermal conductivity foam.

The surface temperatures on the tip (T_w) were obtained using an Inframetrics P20 infrared (IR) camera. The images were processed with Thermacam Researcher 2002[®] and using an in-house MATLAB code. Four IR images were acquired through the zinc selenide windows placed in the shroud surface to cover the entire blade, as shown in Figure 3.1. Each image covered an area that was 21.3 cm by 16 cm and contained 320 by 240 pixels. The camera was located approximately 55 cm from the tip, resulting in a spatial resolution of 0.63 mm. For every test, each of the four images was taken five times and the average of these five images was used.

Each image was calibrated using thermocouples placed underneath the heater. These thermocouples were held in place with a highly thermal conductive adhesive ($k = 1.6 \text{ W/mK}$). This insured that the thermocouple would read the surface temperature of the heater. This surface temperature was calculated to be 2°C less than the outer test copper surface for $q'' = 3700 \text{ W/m}^2$ due to the Kapton thermal resistance. This temperature difference was accounted for in the calibration process. The thermal resistance of the Inconel heater in the dirt purge cavity was found to be negligible and no correction was needed for this area of the blade tip. The IR images were calibrated to a total of six thermocouples by adjusting the background temperature (T_b) and surface emissivity (ϵ). The emissivity is a surface property, which was set to 0.93 for all cases as a result of the heaters being painted with flat black paint. During the calibration process, all IR images were matched to the thermocouples to within 1.0°C . A check on the calibration process is that the four individual images matched up well to form one entire blade contour without any jumps in measured values between images.

Overall uncertainties were calculated for high and low values of heat transfer coefficients and Nusselt numbers according to the partial derivative method described in Moffat [18]. The total uncertainty of any measurement was calculated as the root of the sum of the squares of the precision and bias uncertainties. Based on a 95% confidence interval, the IR camera precision uncertainty was calculated to be 0.06°C . The manufacturers reported bias uncertainty is 2.0% full scale, where typical ranges were set to 20°C . The thermocouples used to determine mainstream and coolant temperatures had a reported bias uncertainty of $\pm 0.2^\circ\text{C}$ and the precision uncertainty was determined to be $\pm 0.1^\circ\text{C}$ from repeated measurements. The total uncertainty in heat transfer measurements was 6% at $Nu_{Dh} = 45$ and 10.5% at $Nu_{Dh} = 55.7$.

Measurement of Tip Heat Transfer Coefficients

Previous studies have compared flow in a turbine blade tip gap region to that of a fully developed channel flow correlation for turbulent flow in a duct. The correlation that was used for comparison in our paper was developed by Gnielinski [19]. Gnielinski's correlation is given in equation 2 and has been reported in the literature to provide accuracy to within 6% as reported by Kakaç [20] for a large Reynolds number range ($10^4 < Re < 10^6$).

$$Nu_{fd} = 0.0214(Re^{0.8} - 100)Pr^{0.4} \quad (2)$$

Mayle and Metzger [3] furthered this correlation for a tip gap by adding an augmentation factor to account for the overwhelming entry region effects of thin blade tips. This augmentation factor, which was taken from Kays and Crawford [21], allows blade designers to relate overall blade tip heat transfer (for a given blade thickness and tip gap) to an overall heat transfer expected in a fully developed channel.

Using data collected in this study, comparisons have been made to the data of Jin and Goldstein [8] and Bunker et al. [7] that confirm this augmentation factor approach. Although Mayle and Metzger [3] first noted the augmentation factor, their data has not been included in this comparison because only experiments performed on airfoil shapes were considered. This is because the plotting variables were based on blade exit velocity, of which there is no equivalent in the Mayle and Metzger tests.

Figure 3.5 shows Nusselt number values based on the hydraulic diameter of the tip gap ($2h$ or $2H$) plotted as a function of the blade Reynolds number based on the exit velocity and hydraulic diameter. The Gnielinski correlation has been plotted for several L_T/D_h ratios as shown on the plot. Note that L_T represents the maximum thickness of the blade. As known for the turbulent channel flow, fully developed conditions generally occur for $L/D_h > 20$ (Kays and Crawford [21]). There is fairly good agreement between experimental data and the appropriate correlations. It should be noted that the L_T/D_h ratios are based on the maximum blade thickness and the Nusselt numbers are the average values calculated for the tip surface. Therefore, this ratio is not a perfect representation of a blade profile, but works reasonably well for the area-averaged values shown here.

Figure 3.6 shows the same experimental data points, plotted as a ratio of the Nusselt number normalized by the fully developed correlation. The solid line represents the augmentation factor given by Kays and Crawford [21]. Most of the data points fall close to the line, with the exception of two Jin and Goldstein points: $Re = 1.0 \times 10^4$ and $Re = 2.0 \times 10^4$. These data points, however, are at low Reynolds numbers, which has been shown to greatly affect the heat transfer. Mayle and Metzger [3] showed that low Reynolds numbers can cause an increase of 20-30% above of the expected augmentation factors used in Figure 3.6. More experiments should be performed to further verify this trend.

Baseline Results (No Blowing)

The baseline results are presented as contour plots of Nusselt number in Figure 3.7. Note that the chord rather than hydraulic diameter can be used for these contour plots to illustrate the differences in the heat transfer coefficients along the blade tip for both tip gaps. Results at both gap heights show similar trends, however, the large tip gap shows higher Nusselt numbers at the blade trailing edge relative to the small tip gap. This increase in heat transfer at the larger tip gap trailing edge is a result of the increased entry region effect relative to the small tip gap. With smaller L/D_h values (for the large tip gap), the entry region is expected to have a greater effect, as mentioned at the beginning of this section. For the large tip gap, the L/D_h is as low as 1 across the trailing edge of the tip surface, whereas for the small tip gap the L/D_h is 3.5.

The area-averaged Nusselt numbers are given for each case to quantify the increase in heat transfer with gap height. For these cases, the Nusselt number at the large tip gap is 3.2 times that of the small tip gap when based on the exit velocity and hydraulic diameter. By using Reynolds number scaling, the large tip gap is expected to have 2.4 times the heat transfer of the small tip gap. This larger than expected increase results from the overwhelming entry region effects, which serve to greatly increase the tip heat transfer.

As shown in Figure 3.7, there are regions of low heat transfer immediately downstream of the dirt purge cavity for both tip gap heights. This is near the thickest portion of the blade and represents the area of lowest heat transfer on the blade tip. This region was first pointed out by Bunker [6] and has been confirmed by other authors. Within the dirt purge cavity, there are high heat transfer coefficients resulting from low velocity flow re-circulation in the cavity. Overall, the leading edge region experiences relatively low heat transfer outside of the dirt purge cavity in comparison to the trailing edge.

Also seen on these contour plots are regions of high heat transfer along the pressure side that begin around the leading edge at $S/S_{max} = 0.1$ and extend until the trailing edge. These regions of high heat transfer have been noted by Morphis and Bindon [4] and Bindon [5] to be the separation region that forms along the pressure side due to mainstream and leakage flow interaction. This region occurs within the entry region and is more dominant at the large tip gap than at the small tip gap, and extends over a large region of the tip for the large tip gap.

To further study the effect of this entry region, line plots have been made which compare the Nusselt numbers at the pressure side of the tip with that of the blade camber line in Figure

3.8. These line plots are defined in Table 3.2. Note that Nusselt numbers displayed from this point forward in the paper are given based on the hydraulic diameter (D_h). Shown in Figure 3.8, these line plots show similar trends at both tip gaps. For the blade camber line, there are very low values for both tip gaps immediately downstream of the dirt purge cavity. Downstream of this area of low heat transfer, the camber line data increases as the blade becomes thinner. The pressure side data begins to increase at about $x/C = 0.15$ as the separation bubble begins to form. Nusselt numbers increase until $x/C = 0.4$, where the maximum Nusselt numbers are reached for both tip gaps. Downstream of this location, the pressure side data remains relatively constant with oscillating levels. These oscillations, seen especially at the large tip gap, suggest localized effects in the separation bubble most likely due to the sensitivity of the separation region to any imperfections at the corner of the blade tip. This separation region was also computationally predicted by Hohlfeld et al. [17]. At the very trailing edge of the blade, the camber and pressure side lines become equal for the same gap height. This is because the tip is so thin that the entry region covers the entire tip passage. In general, the pressure side of the blade tip experiences relatively high heat transfer and, as such, justifies the idea of adding pressure side film cooling holes.

To compare the baseline results to Gnielinski's turbulent channel flow correlation, data has been taken along various lines across the tip. For each line to be compared to channel flow, the local inviscid velocity was used to calculate the Reynolds number. This velocity was found from the local pressure difference as predicted at 95% span. The Reynolds number based on local velocity and D_h are given in Table 3.2 along with the L/D_h at each position. Also shown are the exact line positions, which will be discussed in more detail in the next section.

Line 0 is only of interest to the baseline cases because when blowing is present, this area is affected by the dirt purge holes and can alter the results of the pressure side blowing. Figure 3.9 shows lines 0, at $S/S_{max}=0.28$, and 3, at $S/S_{max}=0.59$, for the baseline cases. Note that for this plot, L_{max} is the maximum local blade thickness at each line location, and L is the distance along that line. This plot shows that within the range of uncertainty, flow at both gap heights becomes fully developed at line 0. At line 3, the measured heat transfer is higher than the correlation. Once again, this is due to $L/D_h \ll 20$ at the trailing edge of the blade reflecting the influence of the entry region.

Film Cooling Hole Results

The heat transfer measurements on the blade tip with blowing from pressure side holes were compared to the baseline with no blowing. The correlation of the non-blowing case with the Gnielinski's correlation was presented in the previous section. For this comparison, a h_f/h_0 ratio greater than one means that there is increased heat transfer with blowing and a ratio less than one means that the heat transfer is reduced when blowing is present. Two lines were chosen to follow the peak effectiveness locations of separate film cooling holes (lines 1 and 2) and a third line was chosen to follow in between two film cooling holes (line 3) as shown in the illustration of Table 3.2. Because the two geometries do not have holes in exactly the same positions, these data lines have been taken at locations specific to each hole in relatively the same area. The differences in the line locations are also given in Table 3.2.

Figure 3.10 shows the comparison lines for the tip results with blowing. For both geometries, blowing causes severe increases in heat transfer up to one hydraulic diameter into the large tip gap and up to five hydraulic diameters into the small tip gap. For the remainder of the gap length, the EDM holes can sometimes increase heat transfer, have no effect, or even decrease heat transfer, whereas the laser holes generally increase heat transfer.

Based on the results shown in Figure 3.10, flow models can be described for each of the hole geometries. For the EDM holes at a large tip gap, the flow remains attached to the surface until the tip is reached. At the tip-pressure side corner, a small separation bubble occurs. Because of the uniform flow structure (due to the low exiting momentum), the coolant trajectory quickly re-attaches to the tip surface. The lower momentum coolant causes the decrease in heat transfer in some areas. At the small tip gap, the coolant flow remains attached to blade, but because of the small gap size, it becomes disturbed by the separation bubble and fills the entire gap.

For the laser holes at a large tip gap, the flow separates from the blade pressure side and impinges upon the shroud. The separation bubble is augmented by the high momentum flow from the laser holes. At the small tip gap, the coolant jet separates from the surface and acts similar to the EDM flow in that the coolant is caught up in the separation bubble and fills the entire gap.

Data taken along the camber line for the laser and EDM cases are shown in Figure 3.11a and 11b for the small and large tip gaps, respectively. Heat transfer augmentation within the dirt

purge cavity (the hashed area) is very high. Immediately after the dirt purge cavity, the large tip gap has a higher h_f/h_0 than the small tip gap. This is most likely due to vortices that are created by the dirt purge holes. Higher heat transfer occurs on the downstream side of the second dirt purge hole, which is where the lowest heat transfer occurs at the baseline case. This combination results in high augmentation values at this location for the large tip gap.

At the small tip gap (Figure 3.11a), augmentations decrease to below one around $x/C = 0.2$. From $x/C = 0.3$ to 1, the laser holes show a continued increase along the blade tip at the small tip gap. The increased heat transfer augmentation for the laser holes may likely be due to an increase in the size of the separation bubble along the pressure side of the tip. The EDM cases remain below one from $x/C = 0.2$ to 0.5 and have generally lower augmentations relative to the laser cases. For both the laser and EDM geometries there is always an increase in the heat transfer augmentation with increased blowing. Kim et al. [12] showed that with a shaped hole, the heat transfer increases as much as 13% with a 60% increase in coolant flow. Results from this test show about an 8% increase in heat transfer for a 75% increase in coolant flow. The lower augmentations may be attributed to the compound injection angle of these tests as compared with Kim et al.

For the large tip gap (Figure 3.11b), the heat transfer ratio plot for the EDM geometry has significant parts of the camber line that are below 1 for $x/C = 0.5$ to 1. Also, for both the EDM and laser geometries, increased blowing results in increased heat transfer augmentation as with the small tip gap. At both tip gaps, the heat transfer augmentation with the EDM lower flow rate case of 0.58% is generally lowest, which is also shown by the area-averages in Figure 3.12. The percentage of the blade surface area that has decreased heat transfer ($h_f/h_0 < 1$) with blowing ranges from 2% to 29% for the laser cases, whereas for the EDM cases, it ranges from 22% to 57%. This shows that the EDM cases have significant areas on the blade that have reduced heat transfer when compared to the heat transfer without blowing.

Net Heat Flux Reduction

Combining the heat transfer measurements of this paper with the film effectiveness measurements of Part I, the overall cooling benefit can be summarized in the form of net heat flux reduction (NHFR). Shown in equation 2, NHFR is an established method of evaluating the overall effect of a cooling scheme on a surface (Sen et al. [14]).

$$\text{NHFR} = 1 - \frac{h_f}{h_0} \left(1 - \frac{\eta}{\theta} \right) \quad (2)$$

In this equation, all variables have been measured experimentally except for θ . A constant value of 1.6, which corresponds to a cooling effectiveness of 62.5% or the inverse of 1.6, was used for this paper based on the previous literature (Sen et al. [14]). As this equation shows, when high heat transfer augmentation is not accompanied by high film cooling, the NHFR can become negative. A negative NHFR means that the cooling scheme is actually causing an increased heat load to the blade surface. Thus, NHFR is a measure of heat load to the part in terms of heat transfer ratio, film effectiveness, and cooling effectiveness. Figure 3.13 shows two examples of this for the laser holes at the small tip gap at 0.58% and 1% coolant flow. Line plots along the pressure side of the tip are shown for two of the laser cases for η , h_f/h_0 , and NHFR. The vertical lines show the locations where NHFR is negative. For the negative values relating to the small tip gap case, the negative NHFR comes from localized minimum values in η along with high heat transfer. These two locations are in between film cooling holes where the cooling effectiveness is low (because the laser holes have relatively poor spreading) and the heat transfer is high.

The NHFR values were calculated locally for each case and are shown in Figure 3.14. Generally the entire blade tip surface has positive values. Also, the leading edge tends to have high NHFR due to the dirt purge blowing. There are noticeable streaks along the blade that are aligned with the film cooling trajectories. To further study the NHFR along a cooling path, the data was taken along the path line plots described in Table 3.2. These results are shown in Figure 3.15. Once again, lines 1 and 2 follow the direct path of coolant over the tip, and line 3 lies in between two coolant paths

For the EDM holes, the NHFR starts high at the pressure side ($L/L_{\max} = 0$) and steadily drops until the suction side is reached. This is because the film effectiveness steadily drops along the coolant path as spreading and mixing occurs within the tip gap. Also, for the EDM holes, at both gap heights, the NHFR increases for each hole path as blowing increases, and the small tip gap always has higher NHFR. At line 3 for the EDM holes, the lower blowing rate

actually has a higher NHFR for both tip gaps. Because this line is in between two coolant paths, this suggests that there is more mixing and spreading at lower blowing ratios for the EDM holes.

For the laser holes, increased blowing results in increased NHFR at the small tip gap but not always at the large tip gap. As has been mentioned in Part I, the lower coolant flow rates actually allow the jet paths of the laser to remain attached to the blade at the large tip gap. This is made evident at line 2. The 0.58% case starts off near $\text{NHFR} = 0.5$ and quickly drops as the low coolant flow is diffused with the main gap flow. The 1% case, however, is constant at $\text{NHFR} \sim 0.2$ across the entire gap width. This agrees with previous suggestions that the jets for the large tip gap separate from the blade and attaches to the shroud at higher blowing rates. For line 3, which is in between two hole paths, similar results are seen as on the hole paths such that at the small tip gap, increased blowing increases the NHFR whereas at the large tip gap, the opposite is true.

NHFR results taken at the camber line are shown in Figure 3.16. At the small tip gap (Figure 3.16a and c), the NHFR tends to decrease between $x/C = 0.3$ to 1. This is because for that same section of the blade, the heat transfer increases along the blade whereas the film effectiveness remains relatively constant. There is very little difference between the two different cooling flow levels for the EDM holes at the small tip gap. The laser cases, however, show much higher variation between hole locations at the lower blowing ratio. On average, the EDM camber line shows higher NHFR than the laser cases.

At the large tip gap (Figure 3.16b and d) similar trends are seen for the laser holes, such that the lower blowing ratio exhibits higher variation between holes. For the EDM geometry, the 0.58% case is relatively low after the dirt purge cavity, but then increases to a similar level of the 1% case at $x/C = 0.45$. In general, the large tip gap has lower NHFR than the small tip gap because the film cooling effectiveness is lower while the heat transfer is higher for the large tip gap. Overall, the EDM cases have higher NHFR values downstream of the dirt purge cavity. Also, increasing the tip gap tends to decrease the NHFR whereas increasing blowing ratio has no noticeable affect on the NHFR.

Area-averaged results of the NHFR are shown in Figure 3.17a. These results show increasing NHFR with increased blowing. Also, the small tip gap has significantly higher NHFR values than the large tip gap. Based on these values, there is no apparent benefit of one geometry over another. Because the dirt purge holes dominate the area-average results, the NHFR was

averaged over the downstream 70% portion of the blade to illustrate the effects of the holes alone, shown in Figure 3.17b. By discounting the dirt purge flow, both blowing ratios indicate that the EDM outperforms the laser holes. Also, there is nearly no dependence upon blowing ratio for these results.

Conclusion

Baseline cases with no blowing at two tip gaps have confirmed that tip heat transfer increases with gap height. Also, a separation region along the pressure side of the tip surface has been indicated by the tip heat transfer measurements. The baseline results also showed that there is a small region of low heat transfer that occurs near the thickest portion of the blade, and tip heat transfer tends to increase towards the trailing edge.

When injecting coolant through pressure side film cooling holes, tip heat transfer also increases with increased gap height. Cooling holes representative of laser drilling tends to cause increased heat transfer when compared to the baseline cases whereas the diffused or shaped holes, representative of EDM. Increasing the blowing ratio leads to increase heat transfer on the tip surface for both geometries.

By evaluating the overall cooling benefit through a net heat flux reduction, the results indicate an overall benefit to the tip for both hole geometries. The results also indicated that the EDM holes provide better protection than the laser holes. The cooling benefit for the small tip gap provides better results than for the large tip gap.

Acknowledgments

The authors gratefully acknowledge United Technologies – Pratt and Whitney for their support of this work.

Nomenclature

C	= true blade chord
D	= dirt purge hole diameter
D_h	= hydraulic diameter, always used as $2h$ or $2H$
F	= augmentation factor for fully developed correlation, see Figure 3.6.
h, H	= small or large tip gap
h_f	= film heat transfer coefficient
h_0	= blade heat transfer coefficient with no blowing
k	= thermal conductivity
L	= local thickness of blade
L_{max}	= max local thickness of blade

L_T = max thickness of blade overall

NHFR = net heat flux reduction, see equation 4

Nu_{Dh} = Nusselt number based on hydraulic diameter, $\frac{h(D_h)}{k}$

Nu_{fd} = Nusselt number at fully developed condition based on hydraulic diameter, $\frac{h(D_h)}{k}$, see equation 2.

$Nu_{0,C}$ = baseline Nusselt number based on chord, $\frac{h(C)}{k}$

$Nu_{0,Dh}$ = baseline Nusselt number based on hydraulic diameter, $\frac{h(D_h)}{k}$

Pr = Prandtl number

q''_{tot} = heat flux supplied to tip surface heater

q''_r = heat flux loss due to radiation

R = resistance in Ω .

Re_{in} = inlet Reynolds number, $\frac{U_{in} C}{\nu}$

Re_{Dh} = Reynolds number based on local velocity and hydraulic diameter, $\frac{U_{local}(D_h)}{\nu}$

$Re_{ex,Dh}$ = Reynolds number based on exit velocity and hydraulic diameter, $\frac{U_{ex}(D_h)}{\nu}$

Re = Reynolds number

S = Distance along the airfoil from leading to trailing edge

Smax = Maximum distance along the airfoil from leading to trailing edge

T_w = blade wall temperature

T_∞ = freestream temperature

T_b = background temperature of radiation surface

T_c = coolant temperature

U_{local} = local velocity on tip gap

U_{ex} = exit velocity (at blade trailing edge)

U_{in} = inlet velocity (1 chord upstream)

x = distance along blade chord

Greek

α = angle taken from blade pressure side curve normal line, shown in Table 3.2.

η = Film cooling effectiveness, $(T_{aw} - T_c)/(T_\infty - T_c)$.

ν = Fluid dynamic viscosity

ρ = Fluid density

ϵ = emissivity of tip heater surface, always set to 0.93.

θ = dimensionless temperature ration, $(T_\infty - T_c)/(T_\infty - T_w)$, always set to 1.6.

Superscripts

 Area-averaged value

References

- [1] Kwak, J.S. and Han, J.C., "Heat Transfer Coefficient on the Squealer Tip and Near Squealer Tip Regions of a Gas Turbine Blade," GT2002-32109.
- [2] Christophel, J., Thole, K.A., and Cunha, F., "Comparison of Exit Hole Shapes for Cooling the Tip of a Turbine Blade – Part 1: Adiabatic Effectiveness Measurements," GT2004-53251.
- [3] Mayle, R.E. and Metzger, D.E., "Heat Transfer at the Tip of an Unshrouded Turbine Blade," *Proceedings of the 7th International Heat Transfer Conference*, **3**, pp. 87-92, 1982.
- [4] Morphis, G. and Bindon, J.P., "The Effects of Relative Motion, Blade Edge Radius and Gap Size on the Blade Tip Pressure Distribution in an Annular Turbine Cascade With Clearance," 88-GT-256.
- [5] Bindon, J.P., "The Measurement and Formation of Tip Clearance Loss," *J of Turbomachinery*, **111**, pp. 257-263, 1989.
- [6] Bunker, R.S., "A Review of Turbine Blade Tip Heat Transfer," Turbine 2000 Symposium on Heat Transfer in Gas Turbine Systems, Cesme, Turkey, 2000.
- [7] Bunker, R.S., Bailey, J.C., and Ameri, A.A., "Heat Transfer and Flow on the First-Stage Blade Tip of a Power Generation Gas Turbine: Part 1 – Experimental Results," *J of Turbomachinery*, **122**, pp. 263-271, 2000.
- [8] Jin, P. and Goldstein, R.J., "Local Mass/Heat Transfer on a Turbine Blade Tip," *J of Rotating Machinery*, **9**, No. 2, pp 981-995, 2003
- [9] Azad, G.S., Han, J.C., and Boyle, R.J., "Heat Transfer and Flow on the Squealer Tip of a Gas Turbine Blade," 2000-GT-195.
- [10] Saxena V., Nasir, H., Ekkad, S.V., "Effect of Blade Tip Geometry on Tip Flow and Heat Transfer For a Blade in a Low Speed Cascade," GT2003-38176.
- [11] Kim, Y.W. and Metzger, D.E., "Heat Transfer and Effectiveness on Film Cooled Turbine Blade Tip Models," *J of Turbomachinery*, **117**, pp. 12-21, 1995.
- [12] Kim, Y.W., Downs, J.P., Soechting, F.O., Abdel-Messeh, W., Steuber, G., and Tanrikut, S., "A Summary of the Cooled Turbine Blade Tip Heat Transfer and Film Effectiveness Investigations Performed by Dr. D. E. Metzger," *J of Turbomachinery*, **117**, pp. 1-11, 1995.
- [13] Kwak, J.S. and Han, J.C., "Heat Transfer Coefficient and Film-Cooling Effectiveness on the Squealer Tip of a Gas Turbine Blade," GT2002-30555

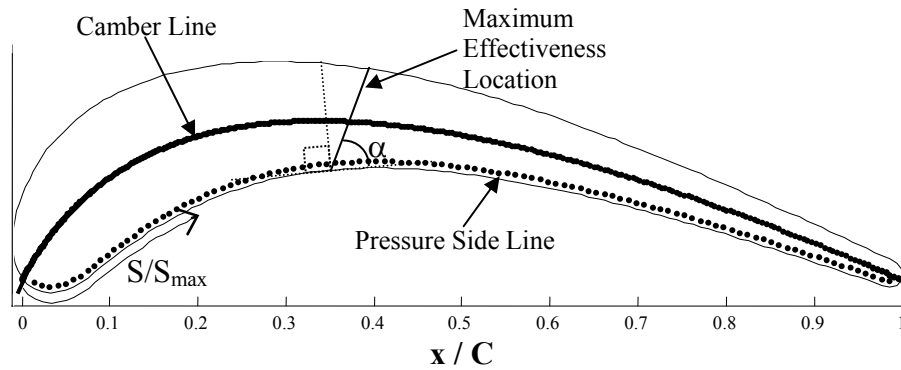
- [14] Sen, B., Schmidt, D.L., and Bogard, D.G., "Film Cooling with Compound Angle Holes: Heat Transfer," 94-GT-311.
- [15] Gritsch, M., Schulz, A., and Wittig, S., "Heat Transfer Coefficient Measurements of Film-Cooling Holes with Expanded Exits," 98-GT-28.
- [16] Yu, Y., Yen, C.H., Shih, I.P., and Chyu, M.K., "Film Cooling Effectiveness and Heat Transfer Coefficient Distribution Around Diffusion Shaped Holes," 99-GT-34.
- [17] Hohlfeld, E.M., Christophel, J.R., Couch, E.L., and Thole, K.A., "Predictions of Cooling from Dirt Purge Holes Along the Tip of a Turbine Blade," GT2003-38251.
- [18] Moffat, R.J., "Describing the Uncertainties in Experimental Results," *Experimental Thermal and Fluid Science*, **1**, pp. 3-17, 1988.
- [19] Gnielinski, V., "New Equations for Heat and Mass Transfer in Turbulent Pipe and Channel Flow," *Int. Chem. Eng.*, **16**, pp. 359-368, 1976.
- [20] Kakaç, S., Shah, R.K., and Aung, W., *Handbook of Single-Phase Convective Heat Transfer*, John Wiley & Sons, pp. 34-35, 1987.
- [21] Kays, W.M. and Crawford, M.E., *Convective Heat and Mass Transfer*, 2nd ed., McGraw-Hill, pp. 269-270, 1980.

Table 3.1 Testing Conditions and Blade Parameters

Parameter	Value
Scaling Factor	12X
Axial Chord / True Chord	0.66
Pitch / True Chord	0.81
Span / True Chord	1.03
Blade Inlet Angle	16°
Re_{in}	2.1×10^5
U_{∞}	12.4 (m/s)
T_{∞}	21 (°C)

Table 3.2 Line Positions Used to Make Path Line Plots

	Large Tip Gap		Small Tip Gap			Baseline	Laser		EDM	
	Re_{Dh}	L/D_h	Re_{Dh}	L/D_h		Large and Small Tip Gap	Large Tip Gap	Small Tip Gap	Large Tip Gap	Small Tip Gap
Pathline 0	4.4×10^4	4.0	1.5×10^4	11.9	S/S_{max}	0.28				
					α	90°				
Pathline 1	4.7×10^4	4.0	1.6×10^4	12.1	S/S_{max}	0.40	0.42	0.41	0.38	0.38
					α	70°	74°	70°	67°	67°
Pathline 2	4.5×10^4	2.9	1.5×10^4	8.7	S/S_{max}	0.54	0.54	0.54	0.54	0.54
					α	70°	68°	72°	72°	60°
Pathline 3	4.4×10^4	2.7	1.5×10^4	8.1	S/S_{max}	0.59	0.61	0.61	0.58	0.59
					α	65°	63°	68°	65°	60°



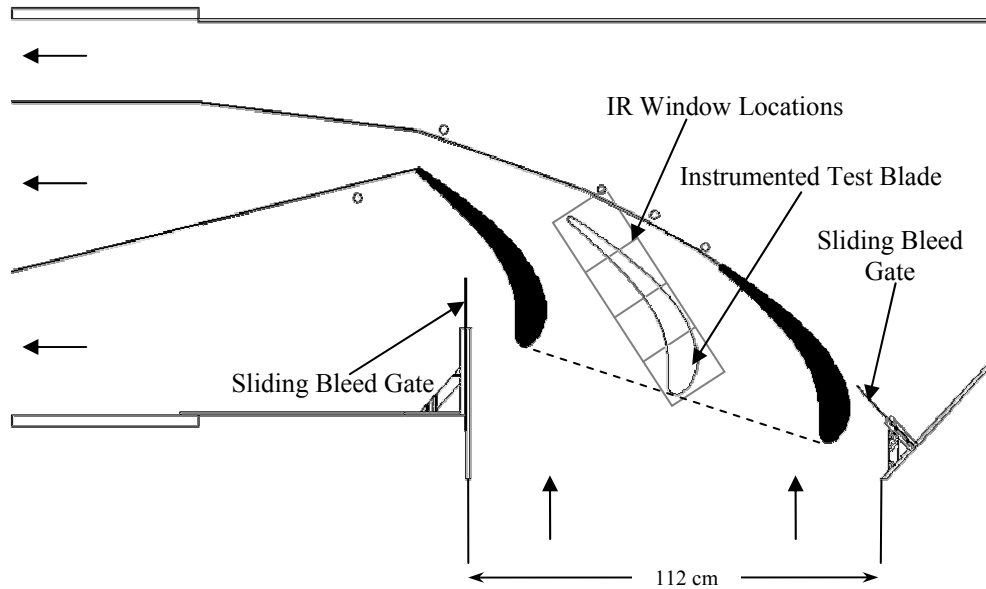


Figure 3.1 Test section viewed from top showing flow adjustment capabilities and infrared (IR) window segments.

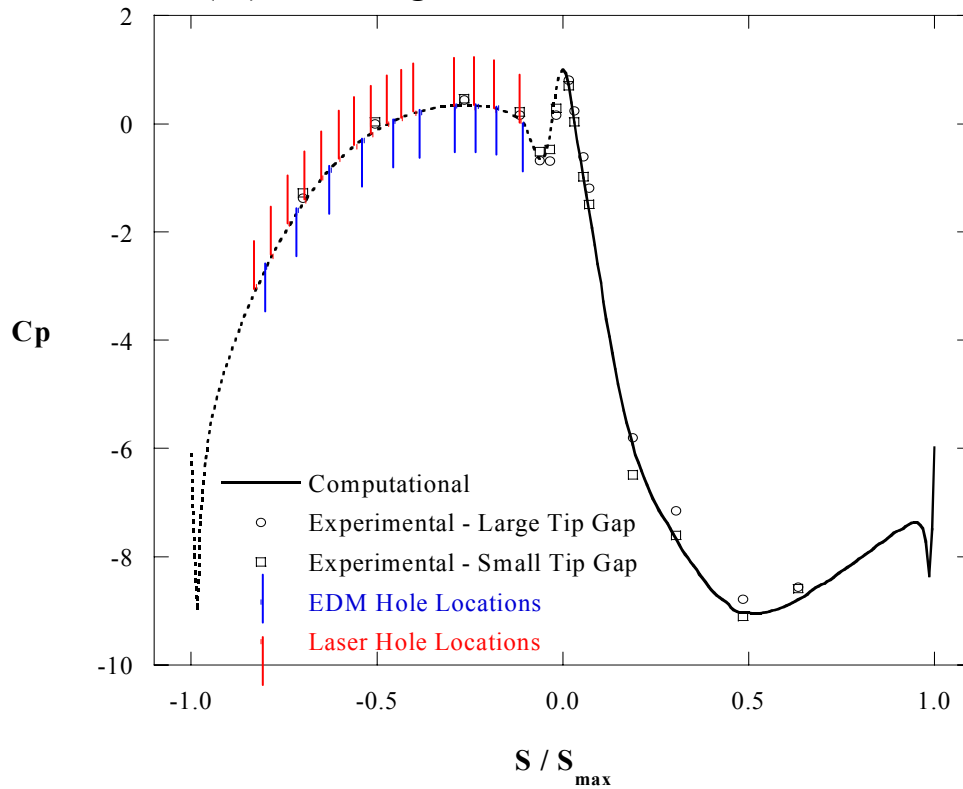


Figure 3.2 Pressure distribution around the center blade mid-span compared to inviscid CFD prediction. Also indicated are the hole locations placed on the pressure side of the tip.

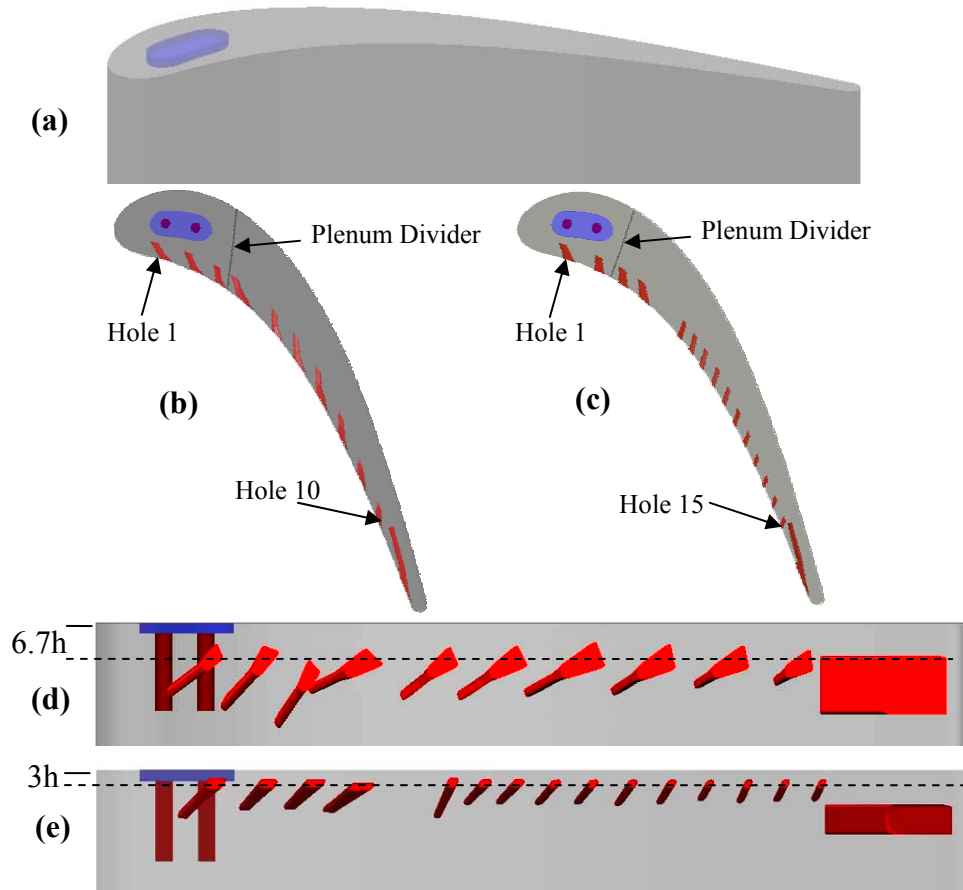


Figure 3.3 The three tip geometries tested were the baseline geometry (a), EDM hole geometry (b, d), and laser hole geometry (c, e).

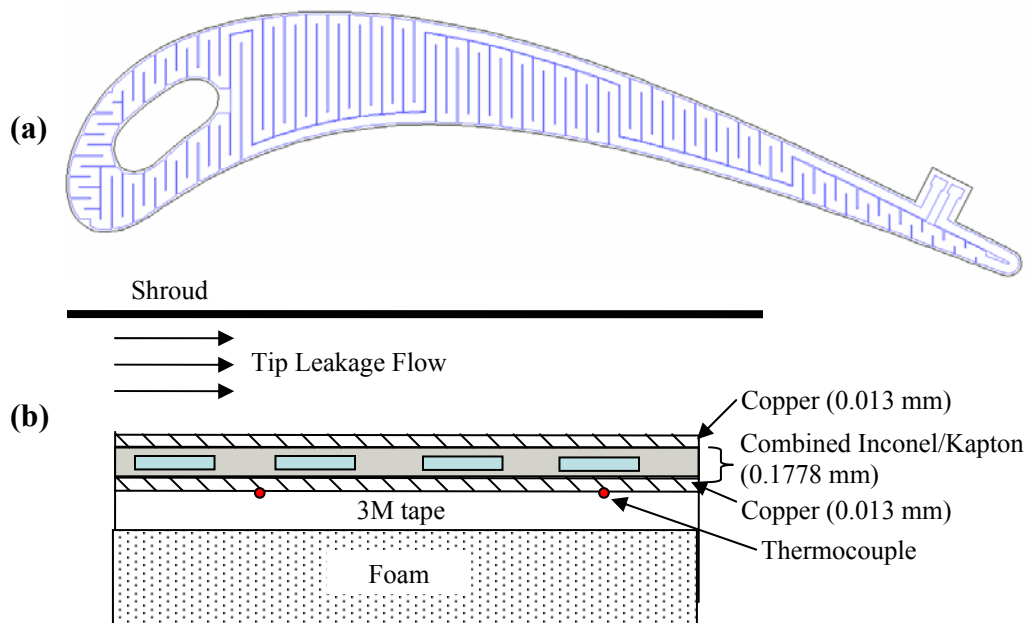


Figure 3.4 Main tip heat transfer surface showing serpentine passages (a) and detail of main tip heater as placed on the blade surface (b).

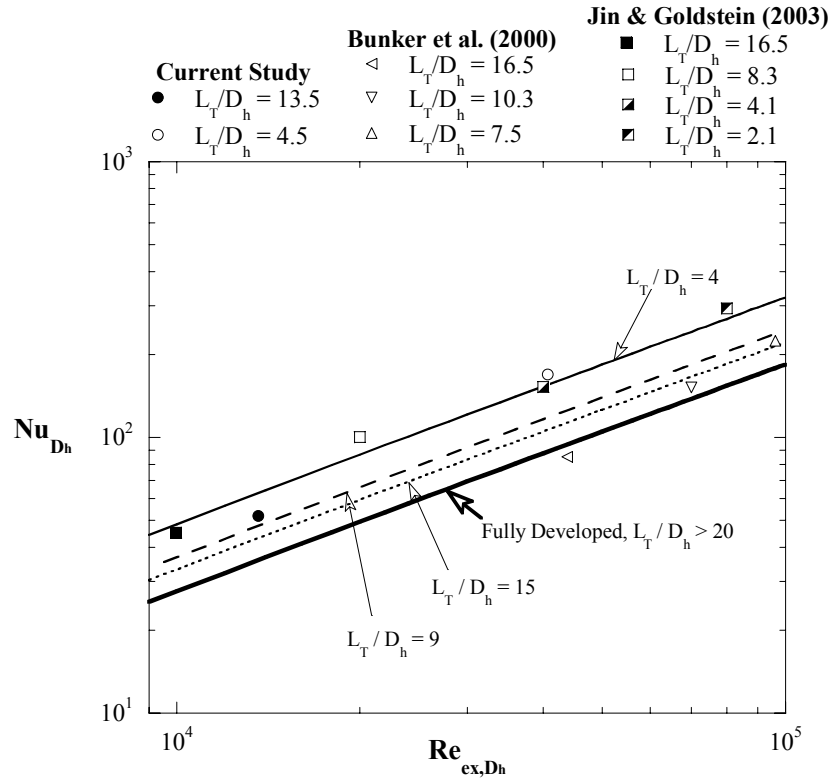


Figure 3.5 Comparison of experimental data to a fully-developed correlation.

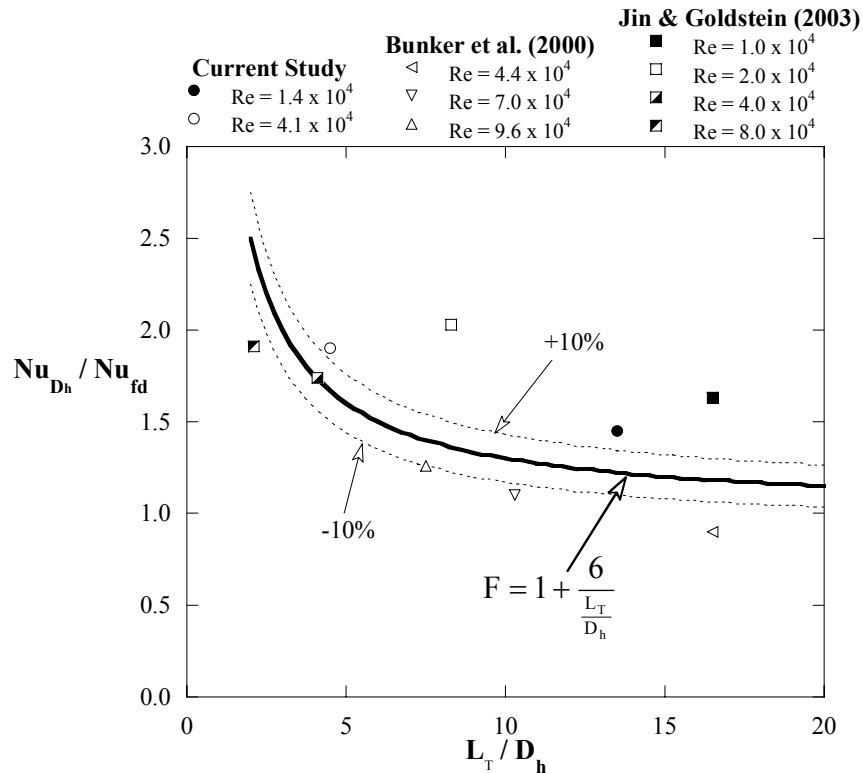


Figure 3.6 Comparison of experimental data to the proposed augmentation factor.

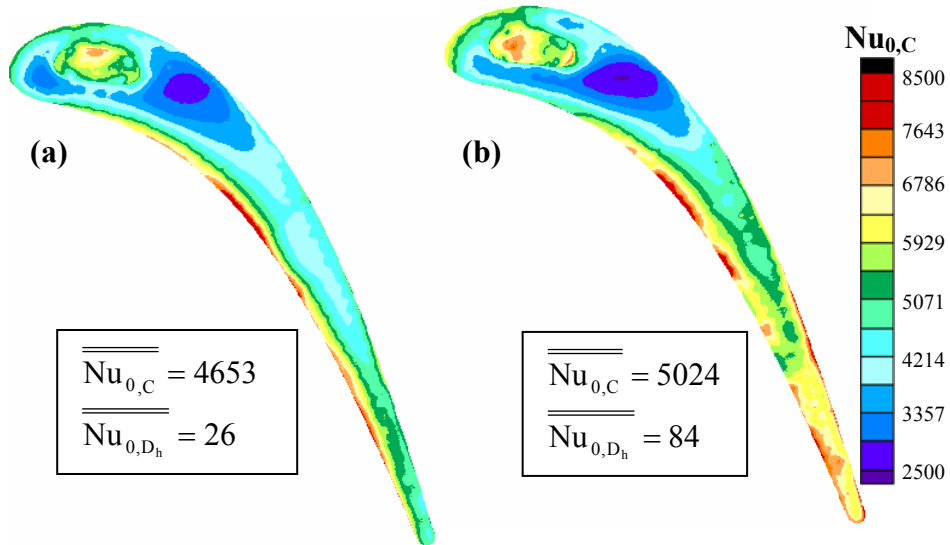


Figure 3.7 Baseline Nusselt number contour plots for the small (a) and large (b) tip gap heights.

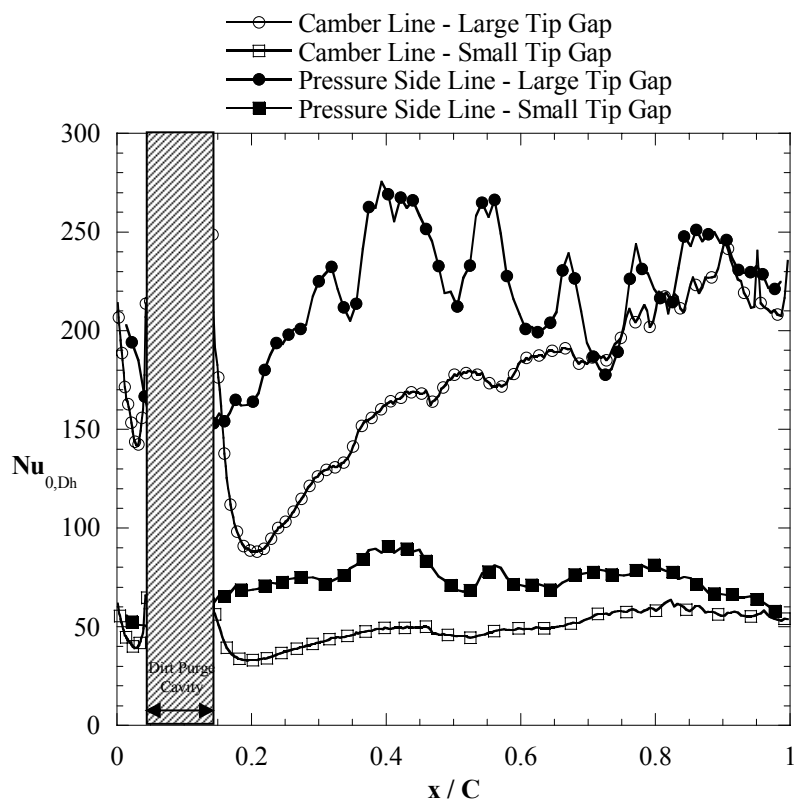


Figure 3.8 Camber line and pressure side line plots for the baseline cases.

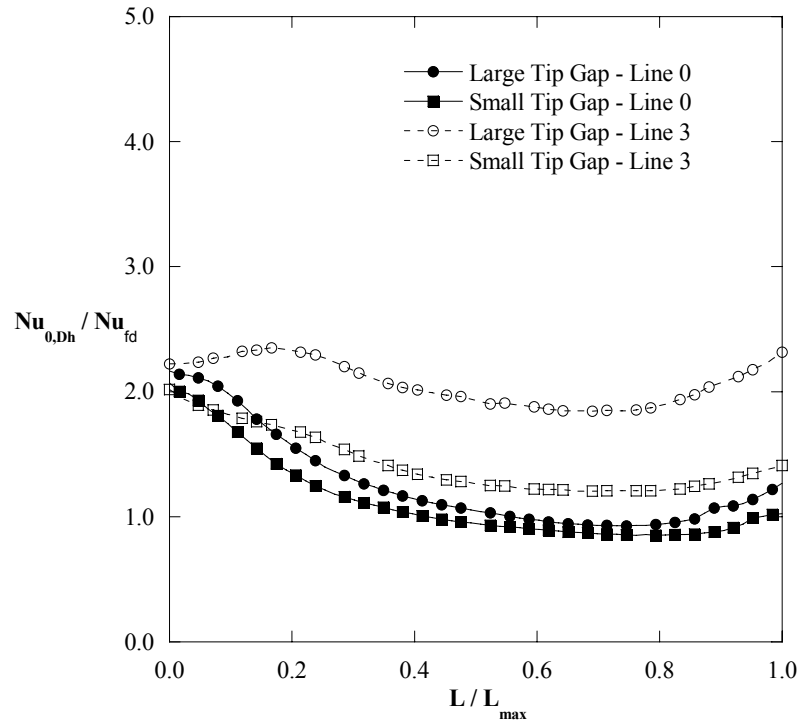


Figure 3.9 Normal line plots at lines 0 and 3 for baseline cases at the large and small tip gaps.

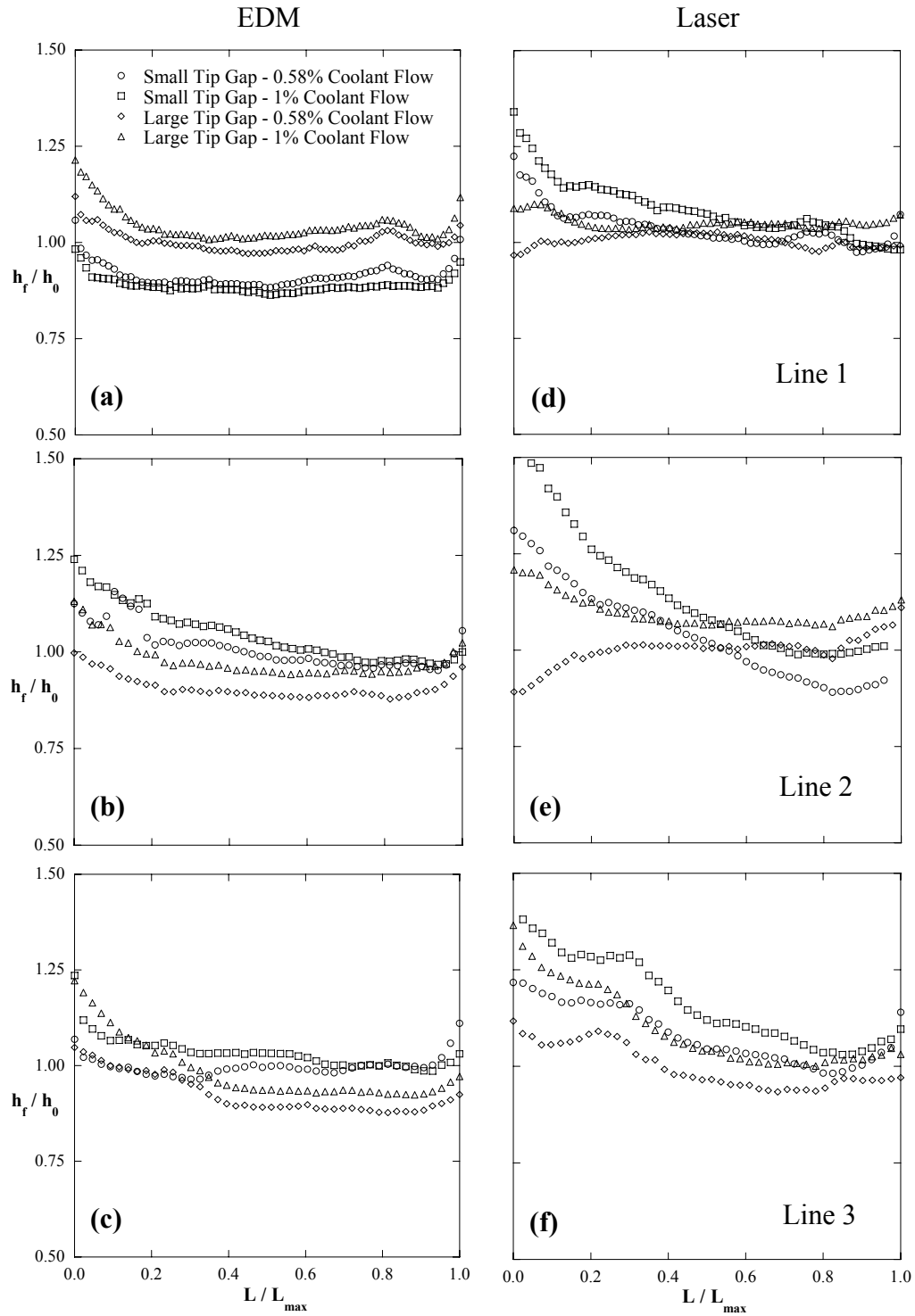


Figure 3.10 Heat transfer augmentation shown on path line plots for the laser and EDM hole shapes for both tip gaps at lines 1, 2, and 3.

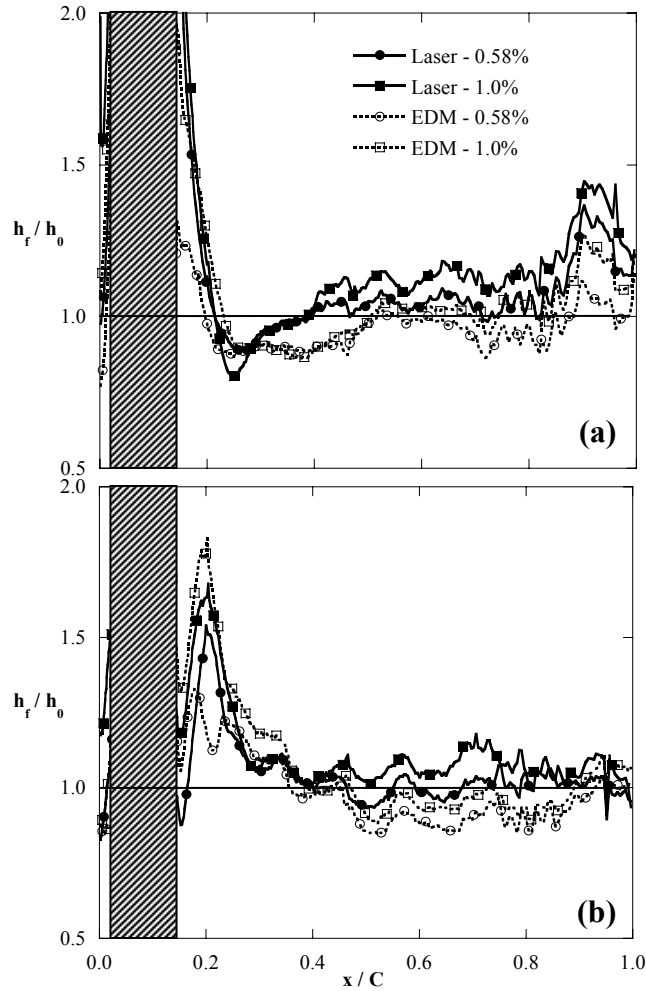


Figure 3.11 Heat transfer augmentation taken at the camber line for the small tip gap (a) and large tip gap (b).

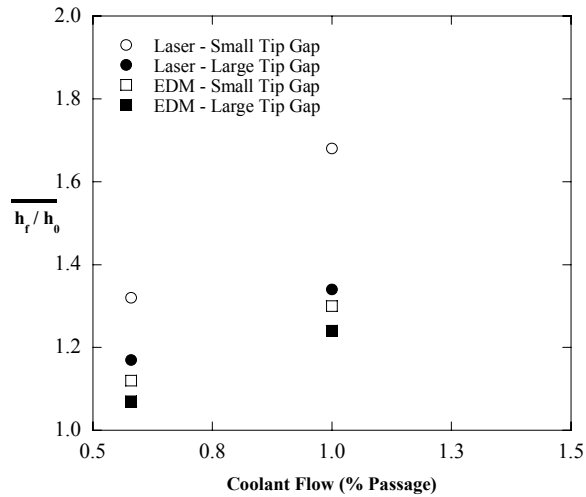


Figure 3.12 Area-averaged heat transfer augmentation with blowing for the small and large tip gaps for both hole geometries.

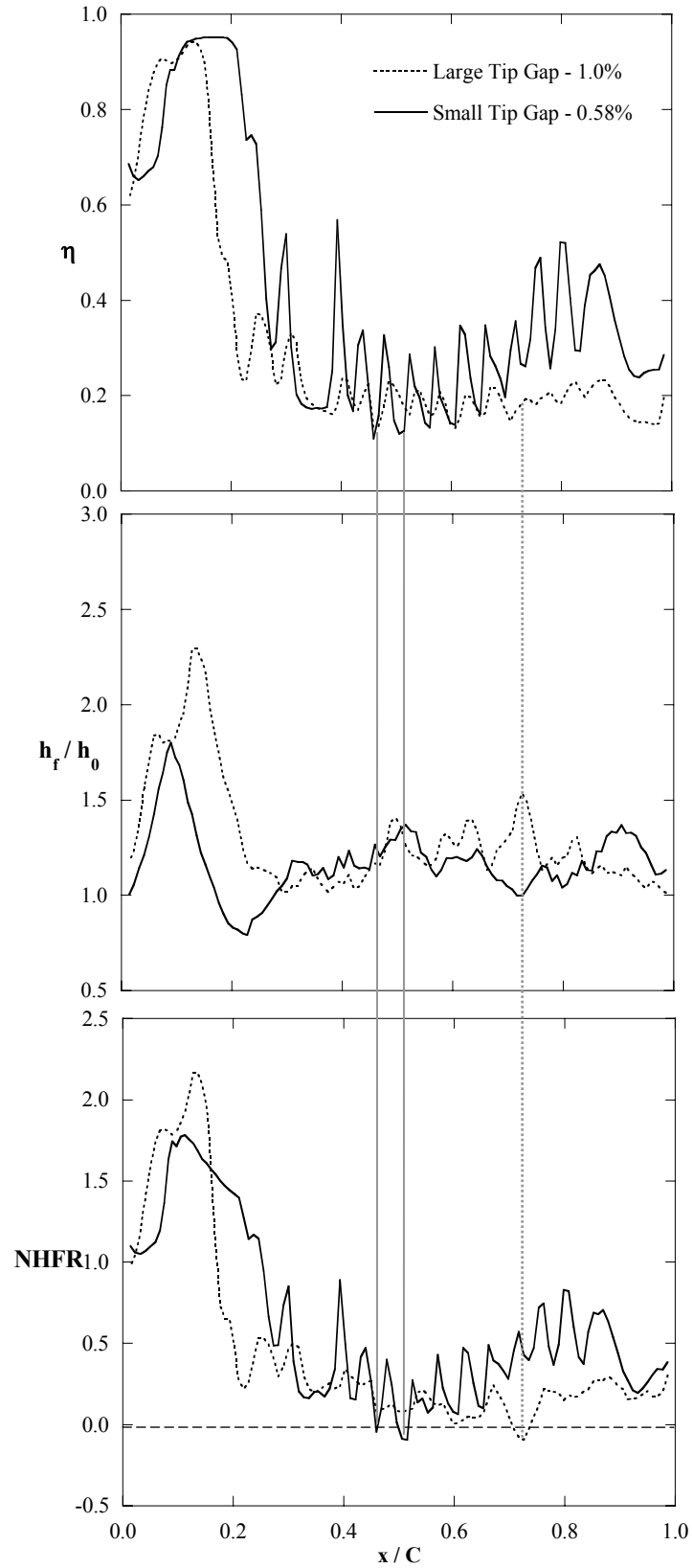


Figure 3.13 Pressure side line plots for the laser hole showing areas of negative NHFR for the small tip gap.

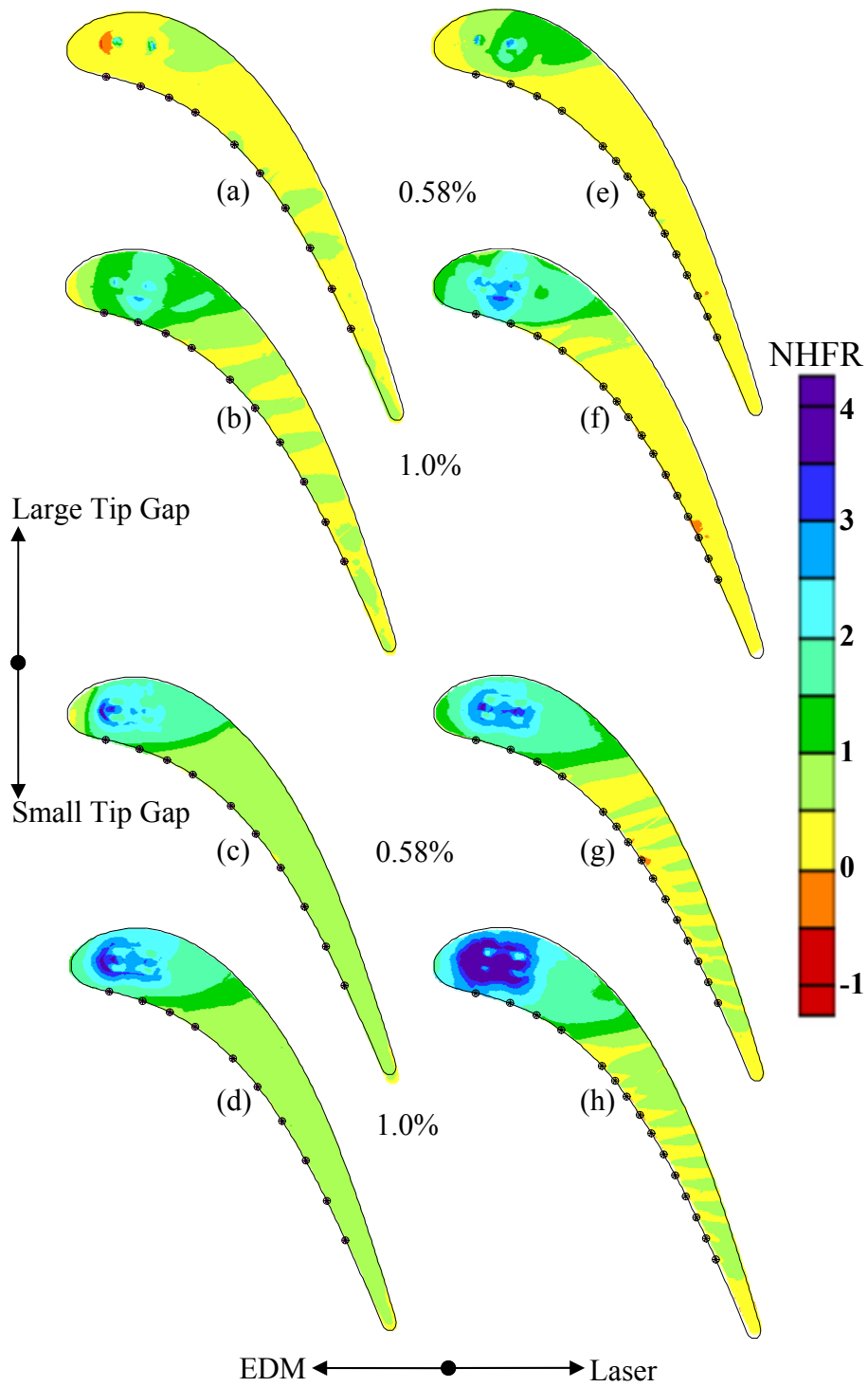


Figure 3.14 NHFR for the EDM and laser holes for both tip gaps at 0.58% and 1% coolant flow.

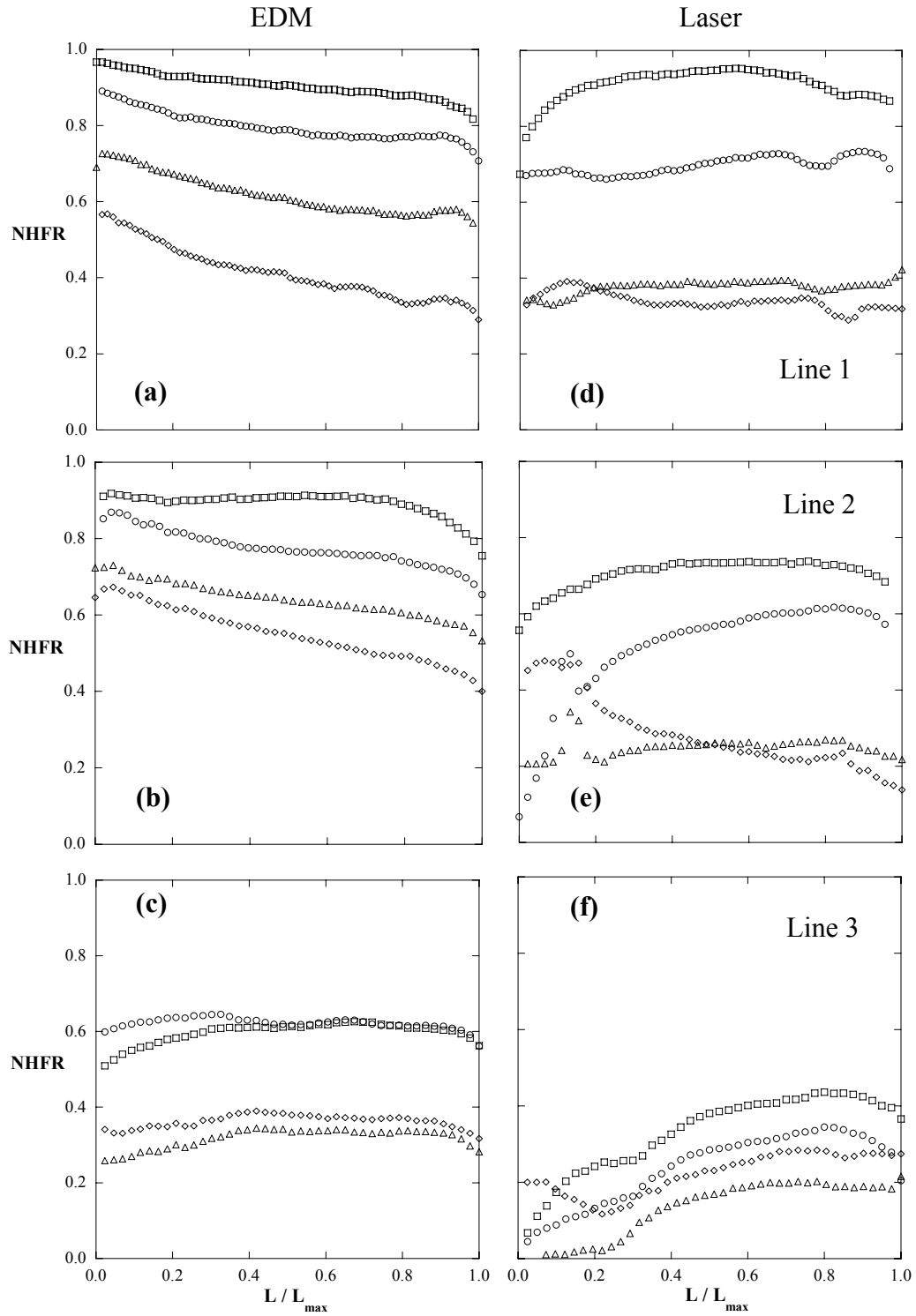


Figure 3.15 NHFR shown on path line plots for the laser and EDM hole shapes for both tip gaps at lines 1, 2, and 3.

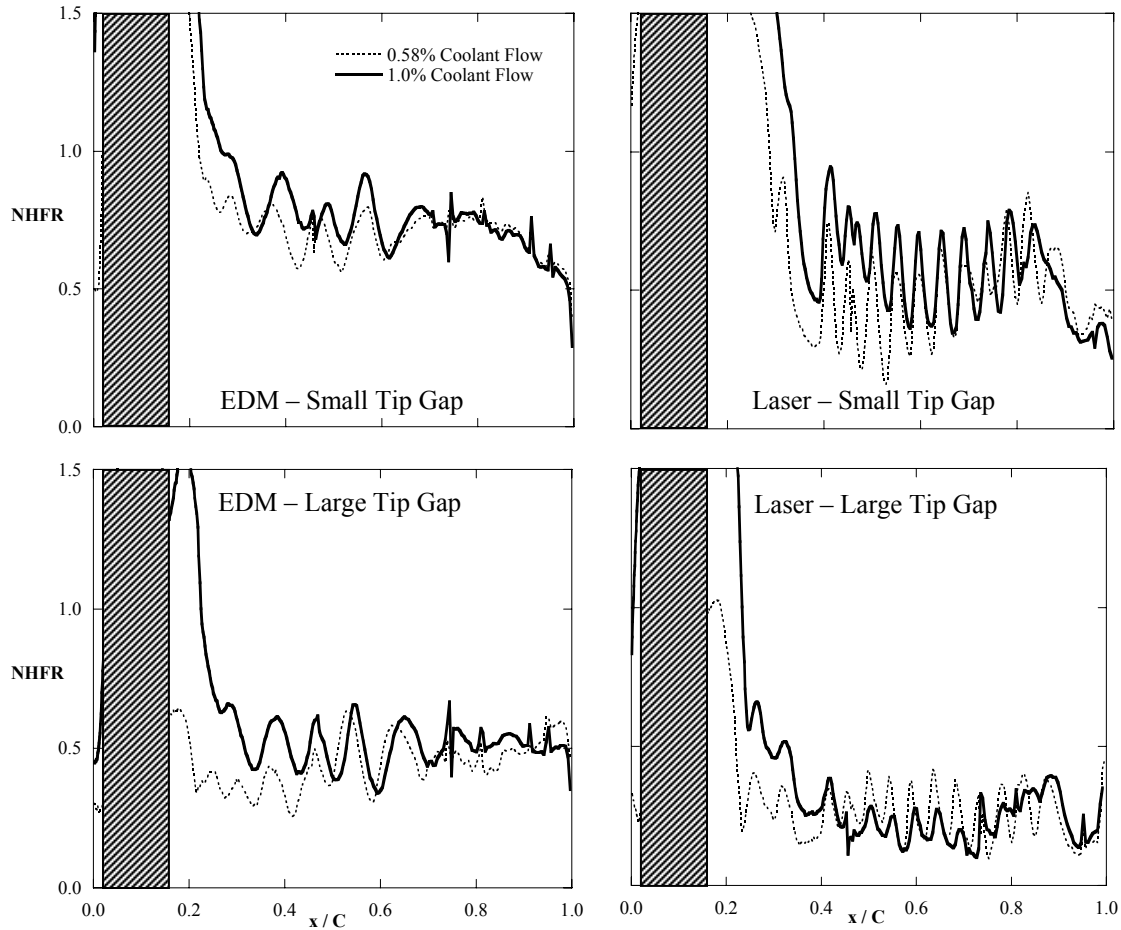


Figure 3.16 NHFR Camber lines for the EDM and laser holes for the small and large tip gap.

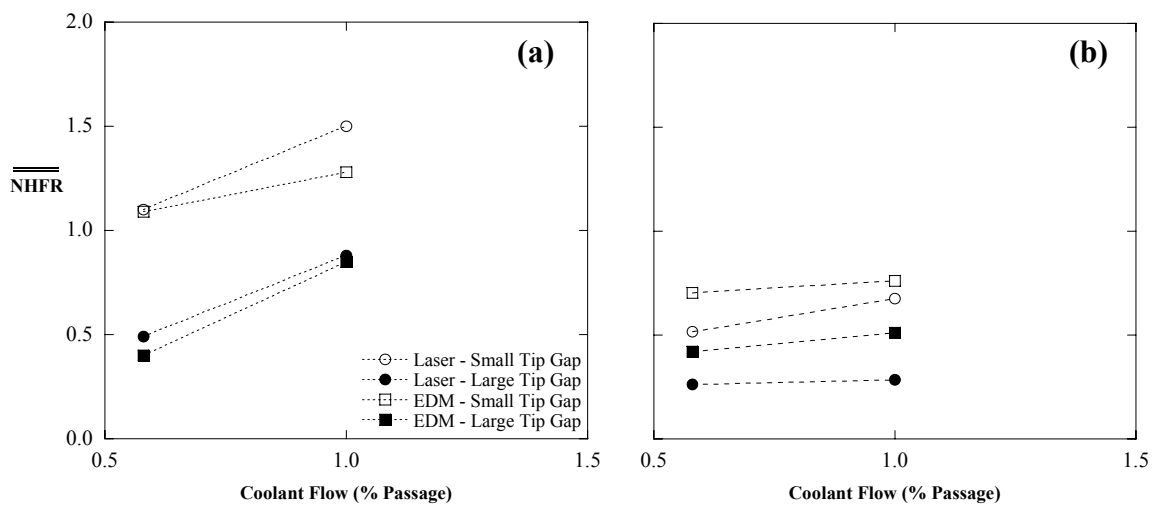


Figure 3.17 Area-averaged NHFR using the total tip area (a) and area-averaged NHFR over the downstream 70% of blade (b).

Paper 4:
**Using a Microcircuit Design for Cooling the Tip of a Turbine Blade—
Part 2: Internal and External Heat Transfer Measurements**

To be submitted to the *Journal of Turbomachinery**

Abstract

The clearance gap between a turbine blade tip and its associated shroud allows leakage flow across the tip from the pressure side to the suction side of the blade. Traditionally, film cooling has been the primary method of protecting the blade tip surface from hot gases. In this paper, a new design has been studied which attempts to cool the tip surface through both external film-cooling and internal convection cooling. This paper is the second of a two part series that discusses the heat transfer associated with this novel technique, known as the microcircuit. Both the external and internal results are presented.

For the experimental investigation, three scaled-up blades were used to form a two-passage linear cascade in a low speed wind tunnel. The rig was designed to simulate different tip gap sizes and coolant flow rates. Heat transfer coefficients along the tip surface (external) were quantified by measuring the total power supplied to a constant heat flux surface placed on the tip of the blade and measuring the tip temperatures. Microcircuit channel (internal) heat transfer coefficients were quantified by measuring the inlet and exit temperatures of air passing through a tip model made from alumina. Alumina was used to construct the tip because it correctly matches the Biot number of an actual turbine blade.

Results indicate increased blowing leads to increased augmentations in tip heat transfer, particularly at the entrance region to the gap. When combined with adiabatic and cooling effectiveness measurements, the tests show that overall blade performance is enhanced with increased blowing. Also, the internal heat transfer coefficients are shown to be higher than a fully developed duct, but decreases as the flow rate increases.

*Co-authors: Dr. Karen A. Thole, Mechanical Engineering Department, Virginia Tech
Dr. Frank J. Cunha, Turbine Durability, Pratt & Whitney

Introduction

The three methods commonly used to cool turbine airfoils are film-cooling, internal convection, and impingement cooling. Of these three methods, film-cooling is the most commonly used at the tip of a blade. The film coolant fluid is compressor bleed air that has been directed through internal blade passages to convectively cool the internal blade surface. Because of the high heat transfer coefficients on the tip (up to 250 times that of the blade pressure and suction sides, Han et al. [1]) and the required blade thickness at the tip, the thermal resistance is such that convectively cooling the tip alone is not sufficient. Thicker blade material is required because of the strains due to centrifugal forces.

Because of recent improvements in manufacturing technology, there now exists a method to realistically use internal convective cooling at the blade tip. This technology, known as microcircuits, uses small passages within the blade material thereby reducing the thermal resistance while maintaining the blade integrity and supporting the blade loading constraints. The heat transfer across the blade tip is described by equation 1, and is shown in Figure 4.1.

$$Q = h_g A_g (T_{aw} - T_{s1}) = \frac{kA_k}{t} (T_{s1} - T_{s2}) = h_c A_c (T_{s2} - T_c) \quad (1)$$

Equation 1 is the energy balance across the blade tip and explains the relative contributions from internal convective cooling and external film cooling. Typically, only film-cooling provides heat reduction at the blade tip. However, because the film-cooling is injected into the mainstream, it mixes and cannot perfectly cool the blade. By carefully using internal convective cooling at the tip, the microcircuit aims to remove heat from the blade surface internally, while still providing ample film-cooling. The energy balance is such that if the microcircuit passages removed all of the heat through internal convective cooling, the coolant air would be ejected at the gas temperature, thereby eliminating any film-cooling effectiveness.

The purpose of this study was twofold. First, this study examined the external heat transfer coefficients on a blade tip as a result of film cooling from hole exits placed on the pressure and suction side near the tip region. Second, the internal convective heat transfer associated with the microcircuit channels was analyzed. The effects of different tip gaps and blowing ratios will be discussed in this paper. The results from this study will also be combined

with adiabatic and cooling effectiveness results from Part 1 [2] to evaluate the overall benefit of the tip cooling. This work will assess the ability of a microcircuit design to effectively cool the blade tip through both internal and external cooling.

Past Relevant Studies

Because turbine blade tips are such an important part in the engine, yet are subject to the harshest conditions, they have been the subject of numerous experimental and computational studies. As early as 1982, Mayle and Metzger [3] showed that the tip leakage flow is comprised primarily of mainstream passage fluid. Other researchers showed a separation bubble formation along the tip pressure side, which was confirmed by Morphis and Bindon [4]. Bindon [5] went on to show that this separation bubble dominates the gap flow characteristics and associated pressure losses. In his recent review of turbine blade tip heat transfer, Bunker [6], noted that this separation region causes a heat transfer enhancement factor of two to three times above that occurring at the tip camber line of an airfoil.

In an effort to reduce the tip leakage flow, many studies have been performed on blade tips with a squealer geometry. This has been shown to significantly reduce the blade tip heat transfer, however, the trends seen on a flat tip are much different than a tip with a squealer cavity. Bunker et al. [7], using a recessed shroud, showed the first experimental heat transfer results on a flat blade tip. His research showed there to be a small area of low heat transfer located near the thickest part of the blade. This low region has been confirmed by many authors including Kwak and Han [1] and Jin and Goldstein [8]. Kwak and Han [1] also noted that the area of low heat transfer tends to be smaller and pushed downstream at increased tip gap heights.

Azad and Han [9], Kwak and Han [1], and Jin and Goldstein [8] have all shown that the blade tip heat transfer increases with increasing tip gap height. For a flat tip with no blowing, Jin and Goldstein [8] showed that the average heat transfer increases along the blade towards the trailing edge. This was confirmed by Saxena et al. [10] who showed that the heat transfer along the blade camber line increased towards the trailing edge.

There have been relatively few studies with blowing over a blade tip surface. Kim and Metzger [11] measured the heat transfer coefficients along a channel representing a blade tip with injection directly into the tip region. They showed that coolant injection always led to higher heat transfer over a case with no injection. Kim et al. [12] found this same trend with tip

surface injection, but noted that injection from the pressure side showed reduced heat transfer on the tip surface. Kwak and Han [13] used an actual airfoil shape with both tip and pressure side injection. Their results, in contrast to Kim et al. [12], indicated that increased coolant injection resulted in reduced heat transfer coefficients.

Generally, tip heat transfer studies without injection have all shown that increasing the tip gap increases heat transfer. Also, regions of low heat transfer are expected near the thickest portions of the blade. When coolant injection is introduced; however, the results are unclear. Some researchers show that the injection will cause an increase in the heat transfer from the baseline case, whereas others show a decrease. Also, no study to date has included an internal microcircuit design for cooling the tip of a turbine blade.

Experimental Facility and Instrumentation

The experiments in this study were performed in a large-scale, low-speed, closed-loop wind-tunnel facility that provided matched engine Reynolds number conditions, as described in Part 1 [2] of this paper. The test section was attached downstream of a contraction section which used a row of high momentum normal jets to provide a turbulence level of 10% and length scale of 11 cm at the blade entrance. The linear cascade test section, shown in Figure 4.2, consisted of an instrumented center blade and two outer blades with tailboards. The tailboards along with the bleed gates allowed for flow control around the center blade, insuring flow periodicity. Velocity measurements were taken approximately one chord upstream at several pitch-wise locations to verify a uniform incoming velocity field. Static pressure measurements were taken around the blade mid-span to insure flow periodicity. This measured pressure distribution was compared with a 2-D, inviscid prediction and is shown in Figure 4.3. Figure 4.3 also presents the hole locations of the microcircuit passage exits.

Coolant flow used for the tip blowing experiments was supplied by an in-house compressor and was controlled by using a series of valves before exiting through the blade tip microcircuit passages. The overall coolant flow rate was known by measuring the pressure drop across a venturi nozzle.

The tip contained the microcircuit geometry and is shown in Figure 4.4. This geometry consisted of multiple serpentine passages that effectively exchanged heat with the coolant and mainstream gases. The passages then exited the blade through 16 film cooling holes placed near

the tip surface. The holes were evenly spaced over the leading edge and most of the pressure side. Towards the trailing edge, due to blade thickness constraints, only one passage was feasible.

There were three separate tip models used to complete all of the testing for these two papers. The first tip had an adiabatic surface and used a microcircuit model that was made from stereo lithography (SLA) to allow for a good replication of the passages and hole shapes. Because the SLA material does not have a sufficiently low thermal conductivity, this model was designed to have foam molded around the microcircuit and supply chamber. A polyurethane foam compound, with a thermal conductivity of $0.04 \text{ W/m}^2\text{K}$, was poured in the blade mold and then allowed to expand and harden, thereby providing the adiabatic surface. The combined SLA microcircuit and foam blade were then removed from the mold, attached as the tip to an SLA blade, and then placed in the wind tunnel for testing. The molded tip model extended 28% of the blade span. This model was used for the η tests in Part I.

The second tip model built upon the first tip model by applying a constant heat flux surface to the adiabatic tip. This model was used for measuring the external heat transfer coefficients and will be discussed later in this section.

The third tip model was constructed from alumina, which provided a matched Biot number to the engine blade material and allowed for conduction through the blade. This model was used in Part I for the ϕ tests, which measured the metal surface temperatures (T_{s1} from Figure 4.1), and in this paper to measure the inlet and exit temperatures of each microcircuit passage. A Biot number matched to that of the engine was used so that the combination of these experimental measurements would allow the properly scaled blade surface temperatures to be known. This is done by re-arranging equation 1 to get equation 2, as shown by Alahyari and Bogard [2].

$$\theta = \frac{T_{aw} - T_{s1}}{T_{aw} - T_c} = \frac{\Psi A}{h_g A_g} = \frac{1}{1 + Bi + h_{gc}} \quad (2)$$

Because the Biot number of an airfoil the engine is low, it can be dropped from this equation, so that by measuring the external and internal heat transfer coefficients, the non-dimensional blade temperature, θ , is calculated directly. This methodology has been documented by Couch [1].

In addition to the microcircuit channels and exits, the blade tip geometry included a dirt purge cavity that was recessed $2h$ ($0.67H$) from the tip surface and contained two dirt purge holes. Each of these dirt purge holes had a diameter of 10.4 mm, and have been described in detail by Hohlfeld et al. [17]. The purpose of the dirt purge holes is to allow for blade manufacturing and to expel dirt particles so as not to clog smaller diameter film cooling holes.

In addition to the dirt purge holes, the microcircuit had 15 exits along the pressure side and one exit along the suction side near the blade tip, as discussed above. All holes were rectangular and had no expansion, with holes 1-5 and 16 having an area of 1 cm^2 and a height to width ratio of 0.6. Holes 6-15 had an area of 0.65 cm^2 and a height to width ratio of 0.8. The centerline of the holes was at 99% of the blade span, which is $3h$ ($1H$) below the blade tip.

Testing conditions and blade parameters are given in Table 4.1. The small (h) and large (H) tip gap settings considered were 0.54% and 1.63% of full blade span, respectively. All tests were conducted nominally at a density ratio of one, with coolant flow rates ranging from 0.5% to 2% of the total passage flow. The total passage flow was calculated based on the inlet mainstream velocity, blade span, and pitch. The split of flow between each of the microcircuit passages and dirt purge holes for a typical case is shown in Figure 4.5.

Separate tests were required for measuring the external and internal heat transfer coefficients. For making the external heat transfer measurements, a constant heat flux surface was put on the foam blade, as discussed above, and experiments were conducted such that the coolant and mainstream were kept to within 0.15°C . For the internal heat transfer measurements, an alumina model containing the microcircuit tip, as described above, was instrumented with thermocouples at each of the passage exits to record the exiting coolant temperature. For these alumina tests, the mainstream was nominally 30°C above the coolant temperature.

Two separate heaters were necessary to provide the constant heat flux surface on the tip because of the dirt purge cavity. The dirt purge cavity was heated with one strip of Inconel that was 0.051 mm thick and had a surface area of 17.3 cm^2 . The main heater covered an area of 261.2 cm^2 and consisted of a serpentine Inconel circuit. As shown in Figure 4.6, the circuit consisted of the Inconel sandwiched between insulating Kapton and then covered with a very thin (0.013 mm) layer of copper on both sides. Both heaters were attached to a foam blade tip using double-sided tape that was 0.64 mm thick. The nominal heat flux for both heaters was set to 3700 W/m^2 which provided a maximum temperature difference between the mainstream and

blade surface of 28°C. The two heaters were controlled independently with a variac to within 0.67% of one another during all tests. The current supplied to each heater was known by placing a precision resistor ($R = 1\Omega \pm 0.1\%$) in each circuit and measuring the voltage drop across each resistor with a digital multimeter. The heater power was then determined from the supplied current and known heater resistance.

Equation 3 was used when calculating the external heat transfer results.

$$h = \frac{q''_{\text{tot}} - q''_r}{T_w - T_\infty} \quad (3)$$

In this equation, q''_{tot} represents the total heat flux output from the resistive heaters and q''_r represents the energy lost to radiation. Typically, radiation losses were less than 2% with the maximum for all cases being 3.4%. Conduction losses were found to be negligible since the heaters were placed on low thermal conductivity foam.

The surface temperatures on the tip (T_w) were obtained using an Inframetrics P20 infrared (IR) camera. The images were processed with Thermacam Researcher 2002[®] and using an in-house MATLAB code. Four IR images were acquired through the zinc selenide windows placed in the shroud surface to cover the entire blade, as shown in Figure 4.2. Each image covered an area that was 21.3 cm by 16 cm and contained 320 by 240 pixels. The camera was located approximately 55 cm from the tip, resulting in a spatial resolution of 0.63 mm. For every test, each of the four images was taken five times and the average of these five images was used.

Each image was calibrated using thermocouples placed underneath the heater. These thermocouples were held in place with a highly thermal conductive adhesive ($k = 1.6 \text{ W/mK}$). This insured that the thermocouple would read the surface temperature of the heater. This surface temperature was calculated to be 2°C less than the outer test copper surface for $q'' = 3700 \text{ W/m}^2$ due to the Kapton thermal resistance. This temperature difference was accounted for in the calibration process. The thermal resistance of the Inconel heater in the dirt purge cavity was found to be negligible and no correction was needed for this area of the blade tip. The IR images were calibrated to a total of six thermocouples by adjusting the background temperature (T_b) and surface emissivity (ϵ). The emissivity is a surface property, which was set to 0.93 for all cases as a result of the heaters being painted with flat black paint. During the calibration process, all IR images were matched to the thermocouples to within 1.0°C. A check on the calibration process

is that the four individual images matched up well to form one entire blade contour without any jumps in measured values between images.

Overall uncertainties were calculated for high and low values of heat transfer coefficients and Nusselt numbers according to the partial derivative method described in Moffat [18]. The total uncertainty of any measurement was calculated as the root of the sum of the squares of the precision and bias uncertainties. Based on a 95% confidence interval, the IR camera precision uncertainty was calculated to be 0.06°C . The manufacturers reported bias uncertainty is 2.0% full scale, where typical ranges were set to 20°C . The thermocouples used to determine mainstream and coolant temperatures had a reported bias uncertainty of $\pm 0.2^{\circ}\text{C}$ and the precision uncertainty was determined to be $\pm 0.1^{\circ}\text{C}$ from repeated measurements. The total uncertainty in external heat transfer measurements was 6% at $\text{Nu}_e = 45$ and 10.5% at $\text{Nu}_e = 55.7$. For internal heat transfer coefficients, the total uncertainty was 2% at $\text{Nu}_i = 100$ and 9% at $\text{Nu}_i = 10$.

Measurement of External Tip Heat Transfer Coefficients

Experiments were first performed with the microcircuit passages closed to obtain baseline data with no blowing. The baseline results were first presented by Christophel and Thole [19] and are presented here for comparison purposes. The contour plots of external Nusselt number (based on chord) are shown in Figure 4.7. Note that the chord rather than hydraulic diameter was used for these contour plots to illustrate the differences in the heat transfer coefficients along the blade tip for both tip gaps. Results at both gap heights show similar trends, however, the large tip gap shows higher Nusselt numbers at the blade trailing edge relative to the small tip gap. This increase in heat transfer at the larger tip gap trailing edge is a result of the increased entry region effect relative to the small tip gap. With smaller $L/D_{h,e}$ values (for the large tip gap), the entry region is expected to have a greater effect, as mentioned at the beginning of this section. For the large tip gap, the $L/D_{h,e}$ is as low as 1 across the trailing edge of the tip surface, whereas for the small tip gap the $L/D_{h,e}$ is 3.5.

As shown in Figure 4.7, there are regions of low heat transfer immediately downstream of the dirt purge cavity for both tip gap heights. This is near the thickest portion of the blade and represents the area of lowest heat transfer on the blade tip. This region was first pointed out by Bunker [6] and has been confirmed by other authors. Within the dirt purge cavity, there are high heat transfer coefficients resulting from low velocity flow re-circulation in the cavity. Overall,

the leading edge region experiences relatively low heat transfer outside of the dirt purge cavity in comparison to the trailing edge.

Also seen on these contour plots are regions of high heat transfer along the pressure side that begin around $S/S_{\max} = 0.1$ and extend until the trailing edge. These regions of high heat transfer have been noted by Morphis and Bindon [4] and Bindon [5] to be the separation region that forms along the pressure side due to mainstream and leakage flow interaction. This region occurs within the entry region and is more dominant at the large tip gap than at the small tip gap, and extends over a large region of the tip for the large tip gap.

The heat transfer measurements on the blade tip with blowing from pressure side holes were normalized by the baseline with no blowing. For this comparison, a $h_f/h_{0,e}$ ratio greater than one means that there is increased heat transfer with blowing and a ratio less than one means that the heat transfer is reduced when blowing is present. Data was taken along the coolant path lines and were chosen to follow trajectories relative to specific microcircuit holes. Three lines were chosen to follow the peak effectiveness locations of separate microcircuit holes (lines 1, 2, and 3) and a fourth line was chosen to follow in between two microcircuit holes (line 4). The exact position for these lines is given in Table 4.2. Lines 1, 2, and 3 follow the coolant trajectory for microcircuits 8, 15, and 16, respectively, and line 4 follows in between the coolant paths of microcircuits 14 and 15.

Figure 4.8 shows the comparison lines for the tip results with blowing. At lines 1 and 2, there is generally little effect of the blowing on the heat transfer augmentation. Although the heat transfer augmentation tends to increase with blowing, the maximum difference in heat transfer augmentation between any blowing ratio for either gap at lines 1 and 2 is 14%. The only place where heat transfer augmentation does not increase with blowing is for line 1 at the small tip gap. Here, for the highest two blowing ratios, the heat transfer is actually less than the baseline. This suggests that coolant flow from the upstream microcircuit exit is interacting with the trajectory of the microcircuit exit being studied. At the higher blowing ratios, the flow is spreading more, causing the coolant flow from the upstream microcircuit exit to flow into the path of the downstream microcircuit. At line 3, there is a more pronounced effect of blowing ratio on heat transfer augmentation, especially at the small tip gap. For lines 1 and 2, the entry region is increased by the microcircuit blowing up to one hydraulic diameter into the large tip

gap and up to five hydraulic diameters into the small tip gap. At line 3, because the blade is so thin, the flow never becomes fully developed.

Figure 4.9 shows heat transfer augmentation for line 4, which takes data in between the coolant trajectories of microcircuit holes 14 and 15. For both tip gaps, the only difference seen with blowing is within the entry region. This is due to the increased spreading of the flow trajectories at higher blowing rates.

Because the path line positions used in Figure 4.8 were chosen to match the peak effectiveness levels, they do not necessarily coincide with the peak heat transfer augmentation levels. In order to understand how the film-effectiveness and heat transfer peaks compare, plots were made along the pressure side of the tip, shown in Figure 4.10 for two blowing cases at the large tip gap. These plots show that the peaks of heat transfer tend to be shifted downstream from the peaks of film-effectiveness. Arrows on the plots point out some of these areas. This trend suggests that at the entry region, the film trajectories cause high heat transfer on either side of the jet due to vortices.

Heat transfer augmentation data taken along the camber line for the microcircuit cases are shown in Figure 4.11a and Figure 4.11b for the small and large tip gaps, respectively. Heat transfer augmentation within the dirt purge cavity (the hashed area) is very high. Immediately after the dirt purge cavity, the large tip gap has a higher h_f/h_0 than the small tip gap. This is because of the vortices that are created by the dirt purge holes. High heat transfer augmentations occur downstream of the second dirt purge hole, which is where the lowest heat transfer occurs for the no blowing, baseline cases. This combination results in high augmentation values at this location for the large tip gap.

For the small tip gap (Figure 4.11a), augmentations along the camber line decrease below one at $x/C = 0.2$. From $x/C = 0.3$ to 1, the results show that the highest three blowing ratios have increased heat transfer from the lowest blowing ratio. This is consistent with the film-cooling results of Part I where the film-effectiveness at the highest three blowing ratios for the small tip gap show relatively no difference. The largest difference in heat transfer augmentation can be seen at $x/C = 0.9$ where the coolant path from hole 16 crosses the tip.

For the large tip gap (Figure 4.11b), there is a more uniform increase in heat transfer for each subsequent increase in blowing ratio. Also, within uncertainty, the entire camber line of the tip for the large tip gap remains at or above an augmentation value of one, suggesting that for the

large tip gap, at all blowing ratios, the heat transfer has either no change with blowing or is increased with blowing from microcircuit holes.

The area-averaged heat transfer augmentation for the entire tip surface is shown in Figure 4.12a. For both tip gaps, the heat transfer increases with blowing ratio. Also, the small tip gap always has higher heat transfer augmentation than the large tip gap. Averages taken over the last 70% of the blade are presented in Figure 4.12b. This was done to isolate the microcircuit holes. These results show that for both tip gaps, there is little variance in heat transfer augmentation with changing blowing ratios. Also, the small and large tip gaps show similar results and both are near to a value of one. These averages show that when considering the microcircuit holes alone, the heat transfer augmentation is still increased with blowing, although the results are less dependant on blowing.

Combining the heat transfer measurements of this paper with the adiabatic effectiveness and cooling effectiveness measurements of Part 1, the overall cooling benefit can be summarized in the form of a net heat flux reduction (NHFR). Shown in equation 4, NHFR is an established method of evaluating the overall effect of a cooling scheme on a surface (Sen et al. [14]).

$$\text{NHFR} = 1 - \frac{h_f}{h_{0,e}}(1 - \eta\phi) \quad (4)$$

In this equation, all variables have been measured experimentally. As this equation shows, when high heat transfer augmentation is not accompanied by high film cooling, the NHFR can become negative. A negative NHFR means that the cooling scheme is actually causing an increased heat load to the blade surface. Figure 4.13 shows two examples of low NHFR values for the large tip gap at 2% coolant flow. Line plots along the pressure side of the tip are shown for η , ϕ , $h_f/h_{0,e}$, and NHFR. The vertical lines show the locations where NHFR is low. These two locations are in between film cooling holes where the adiabatic effectiveness is low and the heat transfer is high.

The NHFR values were calculated locally for each case and are shown in Figure 4.14. Generally the entire blade tip surface has positive values. The only exception to this is near the trailing edge between holes 15 and 16. At this location, there was little or no film cooling present and the heat transfer is relatively high because of the small blade width. There are

noticeable streaks along the blade that are aligned with the microcircuit cooling trajectories. To further study the NHFR along a cooling path, the data was taken along some of the path lines described in Table 4.2. These results are shown in Figure 4.15.

At the small tip gap, the lowest blowing ratio has much higher NHFR values compared to the other blowing ratios tested. This is because at the lowest blowing ratio, the tip heat transfer is lower than all other blowing ratios while the film-effectiveness is at similar values to the higher blowing ratios. At higher blowing ratios, the coolant is thought to blow out into the pressure side and not increase the film-cooling on the tip. At the large tip gap for line 1, the 0.5% case has lower NHFR values than the other blowing ratio cases. This is because at the large tip gap, the film-effectiveness is significantly lower at the lowest blowing ratio. At line 2, for the large tip gap, there are only small differences between the blowing cases, suggesting that the increases in film-effectiveness and cooling effectiveness are equally matched by the increase in heat transfer with increased blowing, thereby causing similar NHFR values at all of the blowing ratios tested.

NHFR results taken at the camber line are shown in Figure 4.16. At the small tip gap (Figure 4.16a), the NHFR tends to be higher for the lowest blowing ratio, as discussed with Figure 4.15. In contrast, at the large tip gap (Figure 4.16b) the NHFR is generally lower for the lowest blowing ratio.

Area-averaged results of the NHFR for the entire tip surface are shown in Figure 4.17a. These results show that for both the large and small tip gaps, the NHFR is essentially the same for the highest three blowing ratios. For the lowest blowing ratio (0.5%), the large tip gap shows a lower value and the small tip gap shows a higher value. This is due to the relatively low heat transfer augmentation at this blowing ratio along with relatively low film cooling for large tip gap and relatively high film cooling for the small tip gap. Once again, an area-average over the last 70% of the blade was considered to view only the microcircuit effects, shown in Figure 4.17b. This shows very similar results to Figure 4.17a, which is because the adiabatic effectiveness and cooling effectiveness are high around the dirt purge, such that the NHFR values are less dependent on the heat transfer augmentation.

Measurement of Internal Heat Transfer Coefficients

Heat transfer coefficients for the microcircuit channels were calculated by combining the cooling effectiveness measurements from Part I with the thermocouple measurements made in these experiments. The microcircuit convective effectiveness, defined in equation 5, combines the entry and exit temperatures with the blade metal temperature for each microcircuit passage.

$$\eta_c = \frac{T_{c,o} - T_{c,i}}{T_m - T_{c,i}} = 1 - e^{\frac{-h_c A_c}{\dot{m} C_p}} \quad (5)$$

Effectiveness values were calculated for each microcircuit passage at each blowing ratio and tip gap tested. For each case, the inlet and exit temperatures of the passage were precisely known from direct thermocouple measurements. The tip surface temperatures on the alumina model (T_m), however, varied across a given passage, which produced varying convective effectiveness values along a given passage. This is demonstrated for one microcircuit passage in Figure 4.18. The average convective effectiveness value over the passage area was chosen to represent the overall passage effectiveness for each microcircuit.

Because many of the channels were geometrically similar, comparisons were made by averaging η_c values for a set of microcircuit passages. Figure 4.19 shows the average $\bar{\eta}_c$ values for microcircuits 8 – 15 (Avg. 1) and for microcircuit 16 as a function of total coolant flow. The first seven microcircuits are not shown because of the dirt purge interaction, which significantly alters the film cooling results. This Figure 4. shows that the microcircuit convective effectiveness decreases as the blowing ratio increases. This is because as the blowing ratio is increased, the mass flow rate through each of the passages is increased thereby causing the exit temperature to be closer to the inlet temperature, which drives the effectiveness value to zero. Also, the small tip gap results tend to be higher than the large tip gap results. For the same blowing ratio, it is expected that the exit and inlet temperatures be the same for both gap heights. The metal temperature, however, is lower at the smaller gap tests because of the increased film-cooling effectiveness. Because of this, the microcircuit convective effectiveness is increased at the small tip gap.

Equation 3 also allows the experimental results to be related to the average channel heat transfer coefficient. These results were compared to the expected trend for a straight turbulent channel in order to find the augmentation by the microcircuit to that of a simple duct flow. The

turbulent channel correlation, taken from Kays and Crawford [21] has been re-arranged to form equation 6.

$$\frac{h_{0,i} A_c}{\dot{m} C_p} = 0.084 \text{Re}^{-0.2} \text{Pr}^{-0.5} \frac{L}{D_h} \quad (6)$$

This correlation relates the channel Reynolds number and geometry to the mass flow rate and corresponding heat transfer coefficient. The Reynolds numbers and geometry for several microcircuit channels are given in Table 4.3. As shown, the Reynolds numbers are well into the turbulent range even at the lowest flow rate. Figure 4.20 shows the heat transfer augmentation relationship for four microcircuit holes at both gap heights and all blowing ratios tested. This shows that the small tip gap generally has higher heat transfer augmentations, which agrees with the higher convective effectiveness seen in Figure 4.19. This plot also shows a general decrease in heat transfer augmentation with increased blowing, similar to the decreasing convective effectiveness seen in Figure 4.19. This says that at the 2% blowing ratio, the heat transfer is actually less with the microcircuit channel than would be with a straight channel design. This may be due to large separation areas forming within the microcircuit where the main flow path does not interact with the passage walls, allowing for less heat exchange to occur. This data has also been plotted against the channel Reynolds number based on hydraulic diameter, in Figure 4.21. This data shows a definite trend of decreasing heat transfer augmentation as Reynolds number increases.

Some of the points have been removed from this plot because it was estimated that the channel heat transfer would result in a measured temperature drop across the channel that was within the thermocouple uncertainty. This is shown by equation 7.

$$h_c L_c P_c (T_m - T_{c,avg}) = \dot{m} C_p (T_{c,o} - T_{c,i}) \quad (7)$$

This equation relates the heat transfer through a given microcircuit passage as shown in Figure 4.1. Typically, these two sides of the equation balanced to within 10% for the data shown in Figure 4.20. At very high channel flow rates, as seen with the 1.5% and 2% coolant flow cases, the necessary ΔT to remove the heat for some microcircuit channels was less than 0.3°C.

Conclusions

Baseline cases with no blowing at two tip gaps have confirmed that tip heat transfer increases with gap height. Also, a separation region along the pressure side of the tip surface has been indicated by the tip heat transfer measurements. The baseline results also showed that there is a small region of low heat transfer that occurs near the thickest portion of the blade, and tip heat transfer tends to increase as the blade grows thinner towards the trailing edge.

When injecting coolant through pressure side film cooling holes, tip heat transfer increases with increased gap height. Also, increasing the coolant flow rate causes increased tip heat transfer. By evaluating the overall cooling benefit through a net heat flux reduction, the results indicate an overall benefit to the tip for all cases tested. The NHFR, however, is not a strong function of blowing ratio, especially at the higher blowing ratios tested.

The internal heat transfer coefficients are generally higher for the microcircuit than a straight channel at lower blowing ratios. At higher blowing ratios, however, the microcircuit performance decreases.

Acknowledgements

The authors gratefully acknowledge United Technologies – Pratt and Whitney for their support of this work.

Nomenclature

C	= true blade chord
D	= dirt purge hole diameter
D_h	= hydraulic diameter, always used as $2h$ or $2H$
F	= augmentation factor for fully developed correlation, see Figure 4.6.
h, H	= small or large tip gap
h_f	= film heat transfer coefficient
h_0	= blade heat transfer coefficient with no blowing
k	= thermal conductivity
L	= local thickness of blade
L_{max}	= max local thickness of blade
L_T	= max thickness of blade overall
NHFR	= net heat flux reduction, see equation 4
Nu_{D_h}	= Nusselt number based on hydraulic diameter, $h(D_h)/k$
Nu_{fd}	= Nusselt number at fully developed condition based on hydraulic diameter, $h(D_h)/k$, see equation 2.
$Nu_{0,C}$	= baseline Nusselt number based on chord, $h(C)/K$
Nu_{0,D_h}	= baseline Nusselt number based on hydraulic diameter, $h(D_h)/k$

Pr = Prandtl number
 q''_{tot} = heat flux supplied to tip surface heater
 q''_r = heat flux loss due to radiation
 R = resistance in Ω .
 Re_{in} = inlet Reynolds number, $U_{in}(C)/\nu$
 Re_{Dh} = Reynolds number based on local velocity and hydraulic diameter, $U_{local}(D_h)/\nu$
 $Re_{ex,Dh}$ = Reynolds number based on exit velocity and hydraulic diameter, $U_{ex}(D_h)/\nu$
 Re = Reynolds number
 T_w = blade wall temperature
 T_∞ = freestream temperature
 T_b = background temperature of radiation surface
 T_c = coolant temperature
 U_{local} = local velocity on tip gap
 U_{ex} = exit velocity (at blade trailing edge)
 U_{in} = inlet velocity (1 chord upstream)
 x = distance along blade chord

Greek

α = angle taken from blade pressure side curve normal line, shown in Table 4.2.
 η = film cooling effectiveness, $(T_{aw} - T_c)/(T_\infty - T_c)$.
 ν = fluid dynamic viscosity
 ρ = fluid density
 ε = emissivity of tip heater surface, always set to 0.93.
 θ = dimensionless temperature ration, $(T_\infty - T_c)/(T_\infty - T_w)$, always set to 1.6.

Superscripts

 = Area-averaged value

References

- [1] Kwak, J.S. and Han, J.C., "Heat Transfer Coefficient on the Squealer Tip and Near Squealer Tip Regions of a Gas Turbine Blade," GT2002-32109.
- [2] Christophel, J. and Thole, K.A., "Comparison of Exit Hole Shapes for Cooling the Tip of a Turbine Blade – Part 1: Adiabatic Effectiveness Measurements," GT2004-53251.
- [3] Mayle, R.E. and Metzger, D.E., "Heat Transfer at the Tip of an Unshrouded Turbine Blade," *Proceedings of the 7th International Heat Transfer Conference*, **3**, pp. 87-92, 1982.
- [4] Morphis, G. and Bindon, J.P., "The Effects of Relative Motion, Blade Edge Radius and Gap Size on the Blade Tip Pressure Distribution in an Annular Turbine Cascade With Clearance," 88-GT-256.

- [5] Bindon, J.P., "The Measurement and Formation of Tip Clearance Loss," *J of Turbomachinery*, **111**, pp. 257-263, 1989.
- [6] Bunker, R.S., "A Review of Turbine Blade Tip Heat Transfer," Turbine 2000 Symposium on Heat Transfer in Gas Turbine Systems, Cesme, Turkey, 2000.
- [7] Bunker, R.S., Bailey, J.C., and Ameri, A.A., "Heat Transfer and Flow on the First-Stage Blade Tip of a Power Generation Gas Turbine: Part 1 – Experimental Results," *J of Turbomachinery*, **122**, pp. 263-271, 2000.
- [8] Jin, P. and Goldstein, R.J., "Local Mass/Heat Transfer on a Turbine Blade Tip," *J of Rotating Machinery*, **9**, No. 2, pp 981-995, 2003
- [9] Azad, G.S., Han, J.C., and Boyle, R.J., "Heat Transfer and Flow on the Squealer Tip of a Gas Turbine Blade," 2000-GT-195.
- [10] Saxena V., Nasir, H., Ekkad, S.V., "Effect of Blade Tip Geometry on Tip Flow and Heat Transfer For a Blade in a Low Speed Cascade," GT2003-38176.
- [11] Kim, Y.W. and Metzger, D.E., "Heat Transfer and Effectiveness on Film Cooled Turbine Blade Tip Models," *J of Turbomachinery*, **117**, pp. 12-21, 1995.
- [12] Kim, Y.W., Downs, J.P., Soechting, F.O., Abdel-Messeh, W., Steuber, G., and Tanrikut, S., "A Summary of the Cooled Turbine Blade Tip Heat Transfer and Film Effectiveness Investigations Performed by Dr. D. E. Metzger," *J of Turbomachinery*, **117**, pp. 1-11, 1995.
- [13] Kwak, J.S. and Han, J.C., "Heat Transfer Coefficient and Film-Cooling Effectiveness on the Squealer Tip of a Gas Turbine Blade," GT2002-30555
- [14] Sen, B., Schmidt, D.L., and Bogard, D.G., "Film Cooling with Compound Angle Holes: Heat Transfer," 94-GT-311.
- [15] Gritsch, M., Schulz, A., and Wittig, S., "Heat Transfer Coefficient Measurements of Film-Cooling Holes with Expanded Exits," 98-GT-28.
- [16] Yu, Y., Yen, C.H., Shih, I.P., and Chyu, M.K., "Film Cooling Effectiveness and Heat Transfer Coefficient Distribution Around Diffusion Shaped Holes," 99-GT-34.
- [17] Hohlfeld, E.M., Christophel, J.R., Couch, E.L., and Thole, K.A., "Predictions of Cooling from Dirt Purge Holes Along the Tip of a Turbine Blade," GT2003-38251.
- [18] Moffat, R.J., "Describing the Uncertainties in Experimental Results," *Experimental Thermal and Fluid Science*, **1**, pp. 3-17, 1988.

- [19] Gnielinski, V., "New Equations for Heat and Mass Transfer in Turbulent Pipe and Channel Flow," *Int. Chem. Eng.*, **16**, pp. 359-368, 1976.
- [20] Kakaç, S., Shah, R.K., and Aung, W., *Handbook of Single-Phase Convective Heat Transfer*, John Wiley & Sons, pp. 34-35, 1987.
- [21] Kays, W.M. and Crawford, M.E., *Convective Heat and Mass Transfer*, 2nd ed., McGraw-Hill, pp. 269-270, 1980.

Table 4.1. Testing Conditions and Blade Parameters

Parameter	Value
Scaling Factor	12X
Axial Chord / True Chord	0.66
Pitch / True Chord	0.81
Span / True Chord	1.03
Blade Inlet Angle	16°
Re_{in}	2.1×10^5
U_∞	12.4 (m/s)
T_∞	21 (°C)

Table 4.2. Line Positions Used to Make Path Line Plots

	Pathline 1	Pathline 2	Pathline 3	Pathline 4
S/S_{max}	0.34	0.65	0.88	0.625
α	70	70	43	70

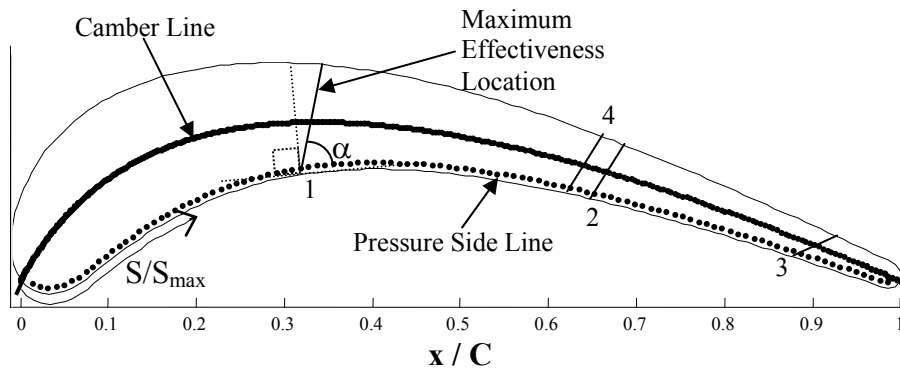


Table 4.3. Reynolds numbers and geometric properties of several microcircuit channels

Microcircuit Channel Number	Reynolds Number (at 0.5% Coolant Flow)	L/D_h	A_c (cm ²)
8	4500	13.8	0.65
10	4300	11.9	0.65
15	5600	11.3	0.65
16	4300	18.5	0.94

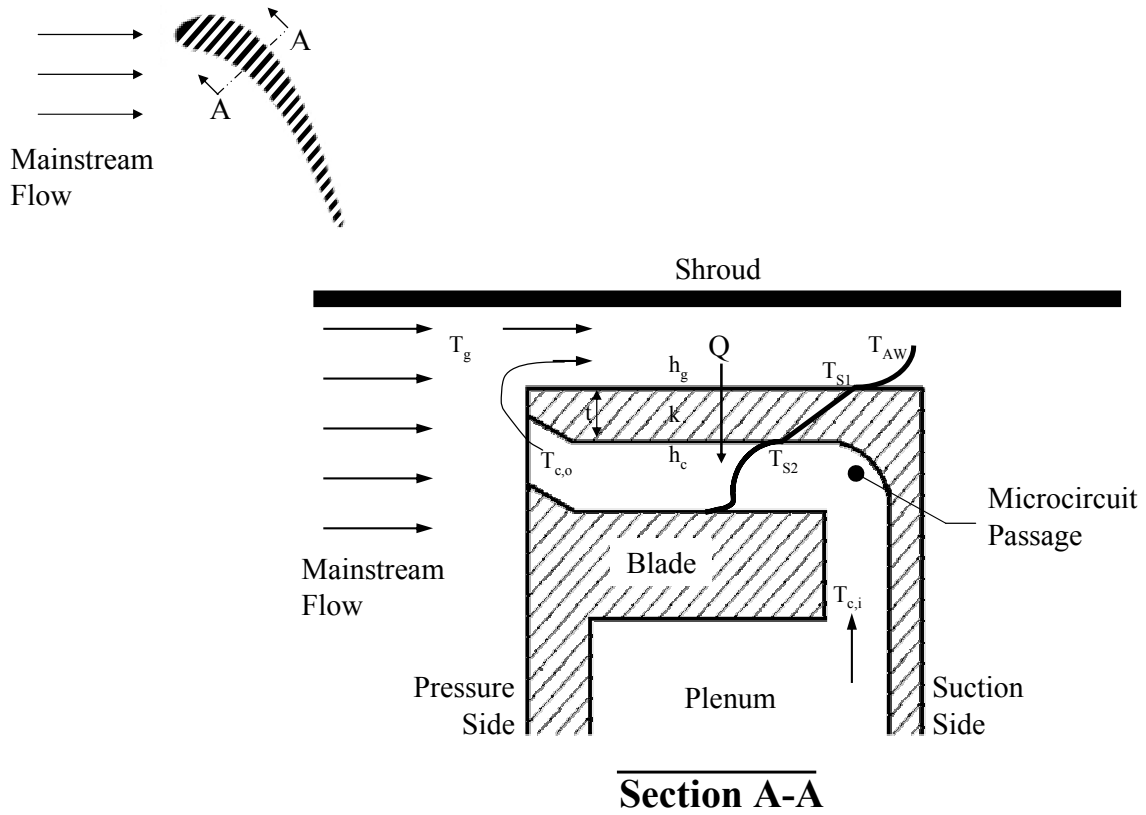


Figure 4.1. Detail of microcircuit design and internal cooling.

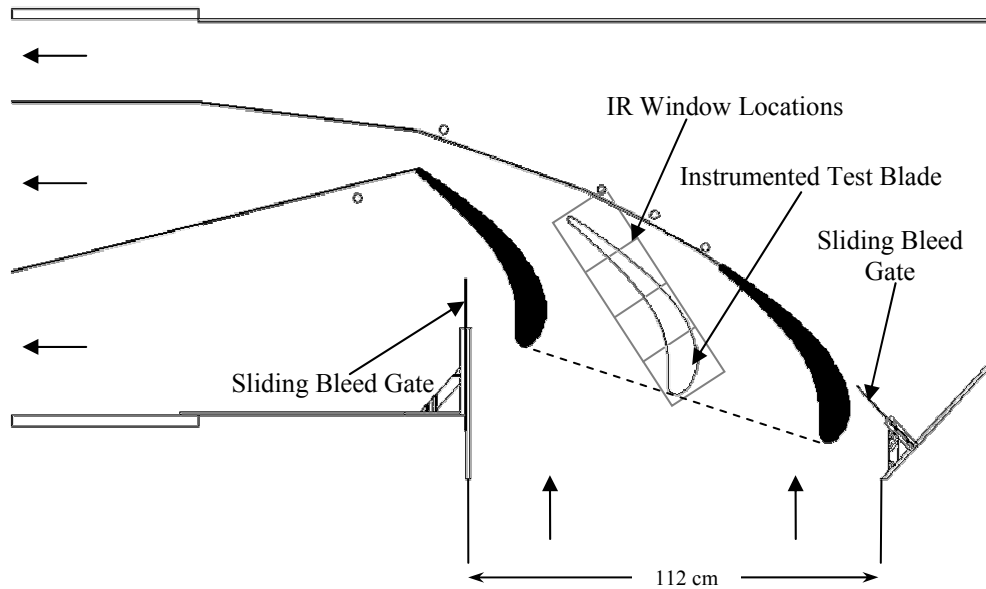


Figure 4.2. Test section viewed from top showing flow adjustment capabilities and infrared (IR) window segments.

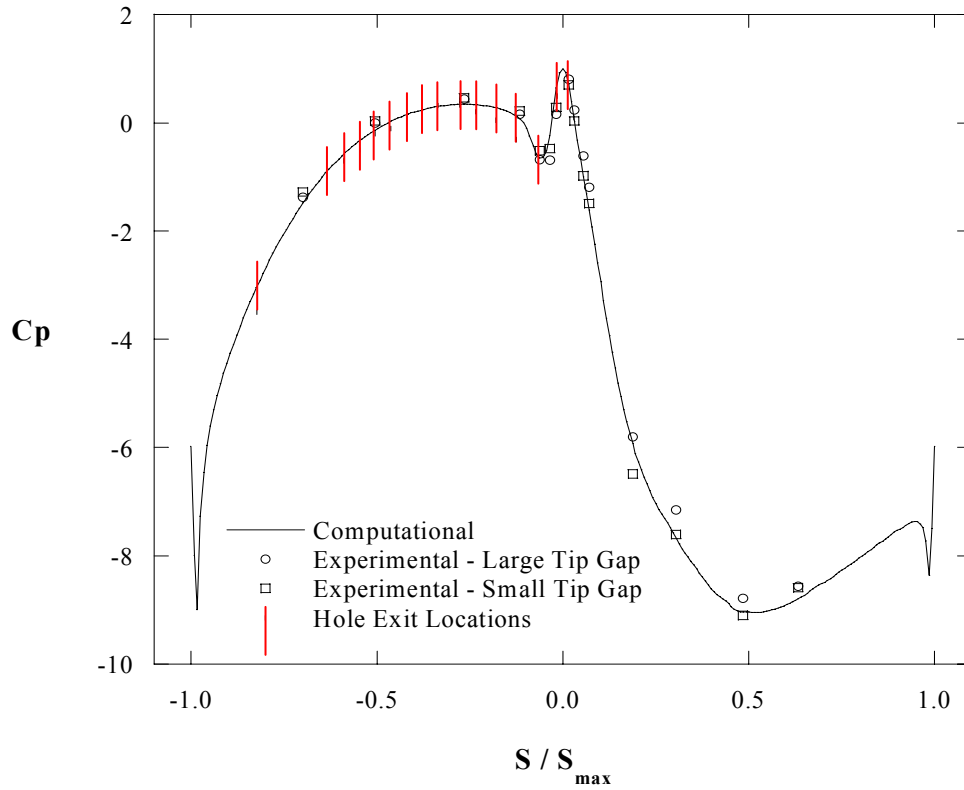


Figure 4.3. Pressure distribution around the center blade mid-span compared to inviscid CFD prediction. Also indicated are the hole locations placed on the pressure side of the tip.

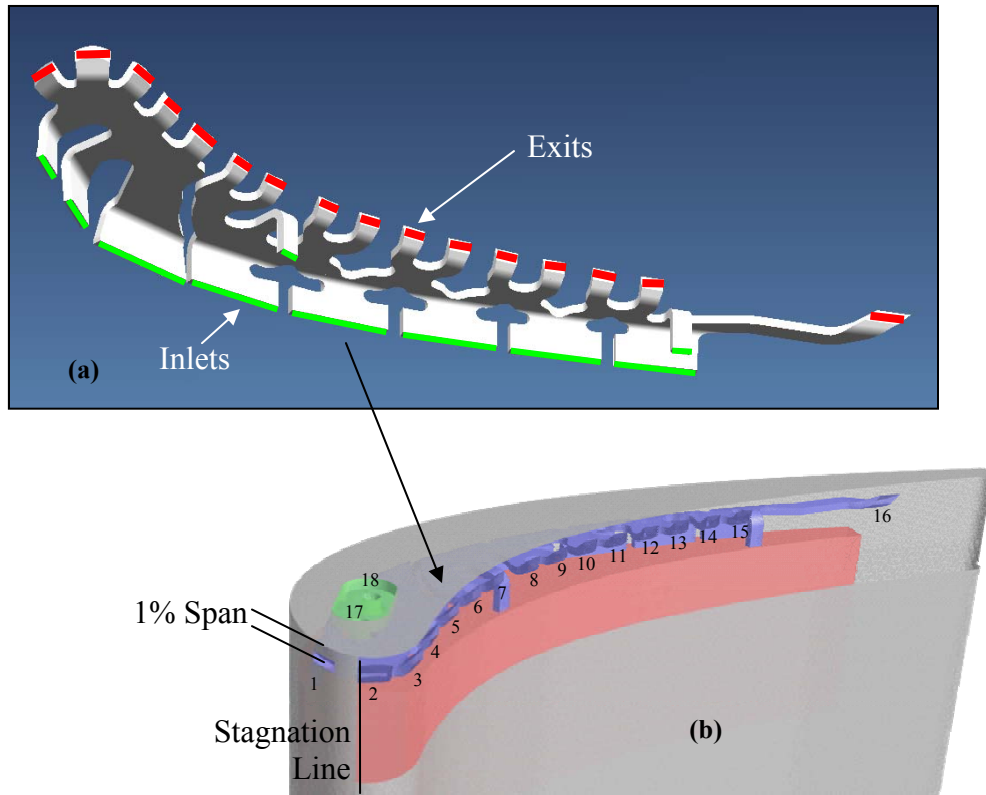


Figure 4.4. Microcircuit tip geometry passage layout (a) and hole locations on blade tip (b).

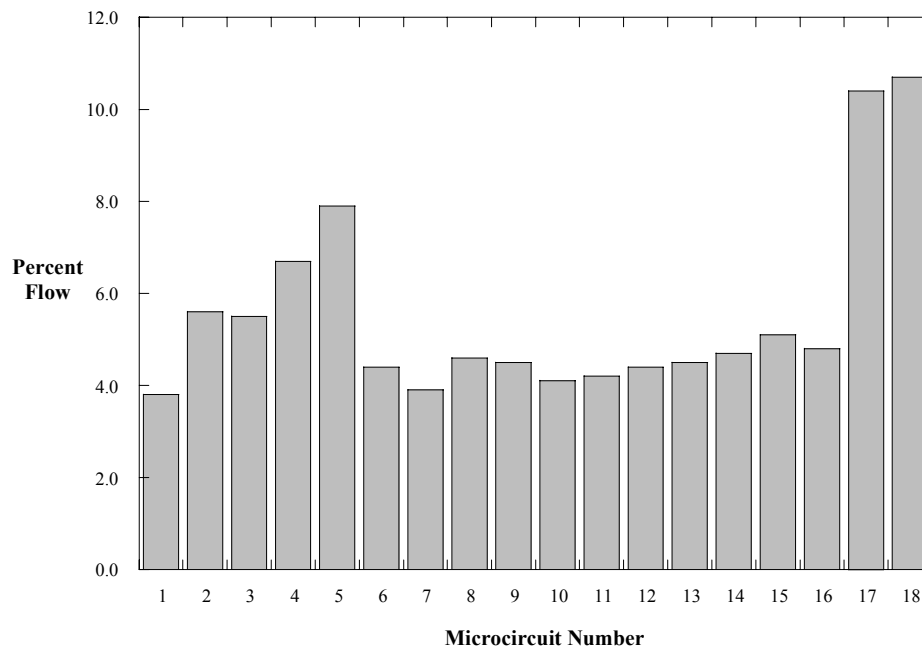


Figure 4.5. Relative coolant flow through each of the microcircuit holes (1-16) and the dirt purge holes (17-18) for typical cases .

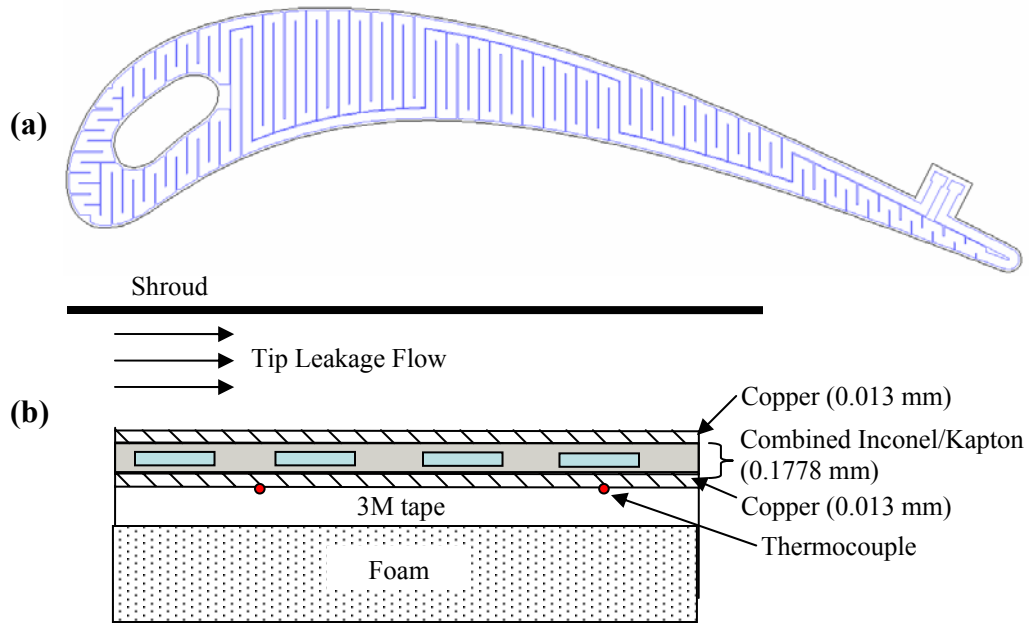


Figure 4.6. Main tip heat transfer surface showing serpentine passages (a) and detail of main tip heater as placed on the blade surface (b).

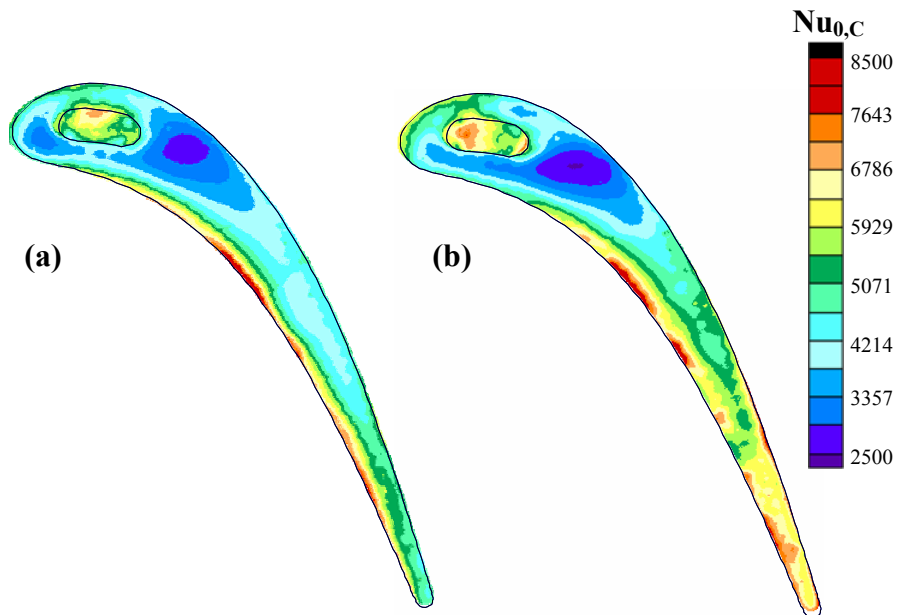


Figure 4.7. Baseline Nusselt number contour plots for the small (a) and large (b) tip gap heights.

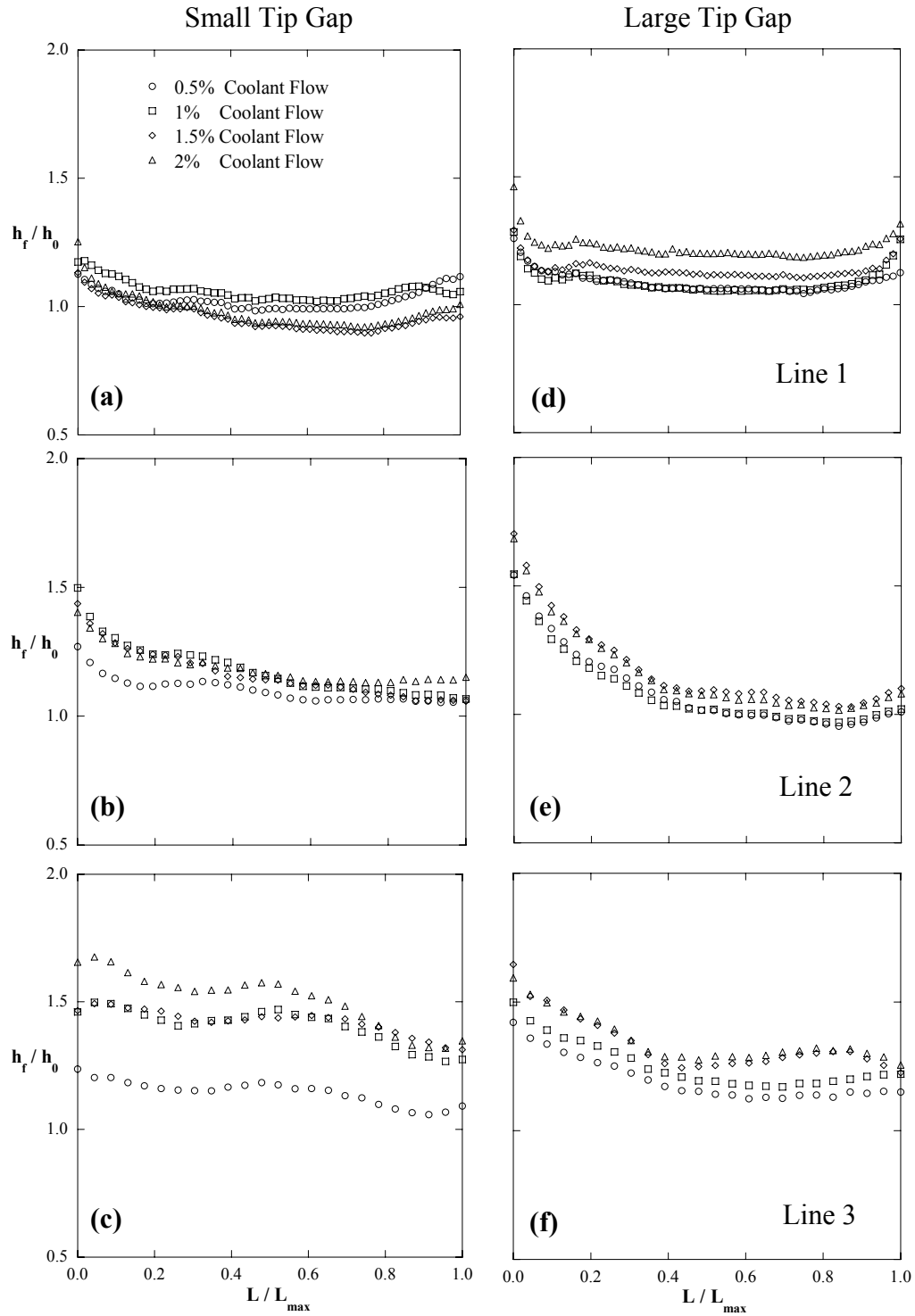


Figure 4.8. Heat transfer augmentation shown on path line plots for both tip gaps at all blowing ratios tested at lines 1, 2, and 3.

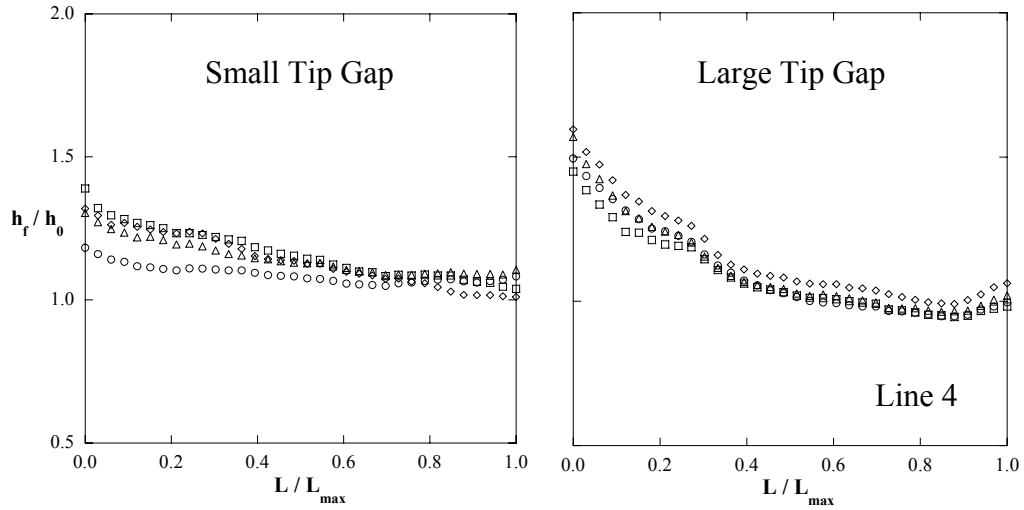


Figure 4.9. Heat transfer augmentation shown on path line 4 for both tip gaps.

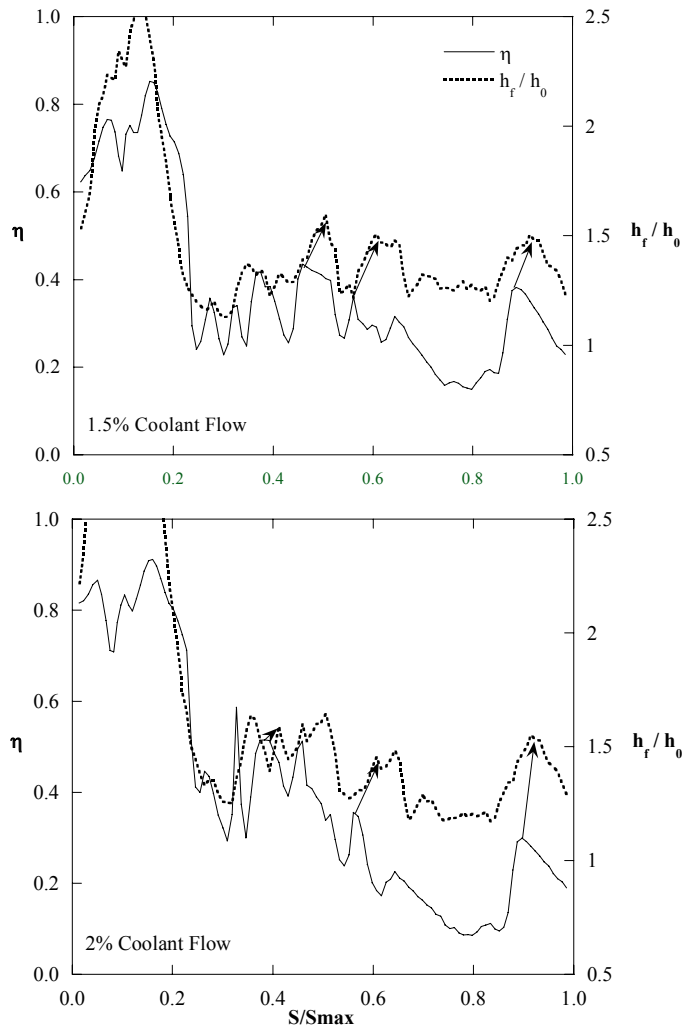


Figure 4.10. Adiabatic effectiveness and heat transfer augmentation taken at the pressure-side line showing the difference in peak locations.

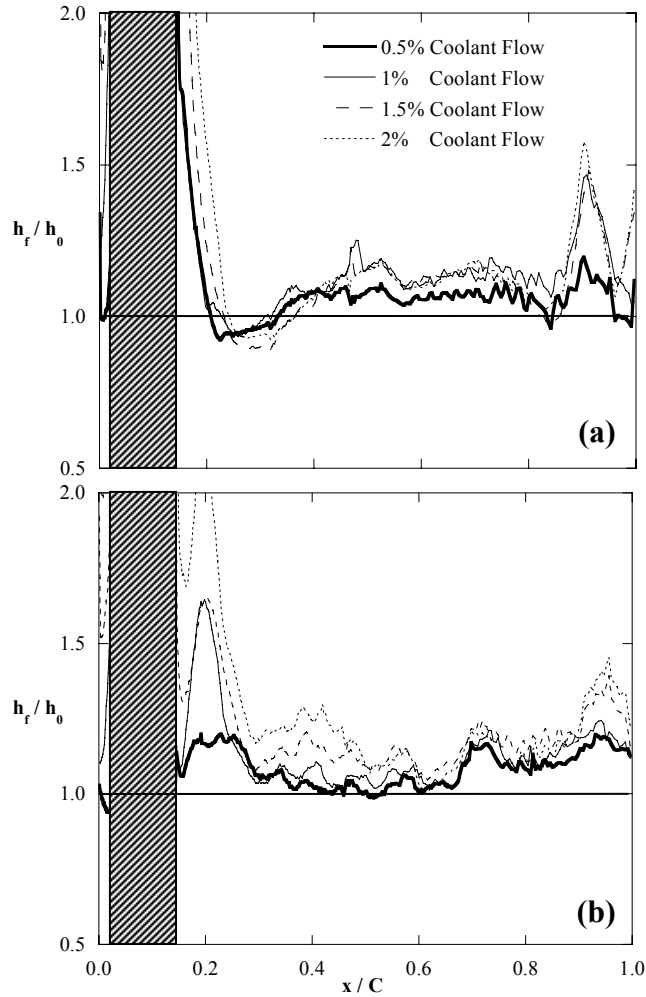


Figure 4.11 Heat transfer augmentation taken at the camber line for the small tip gap (a) and large tip gap (b).

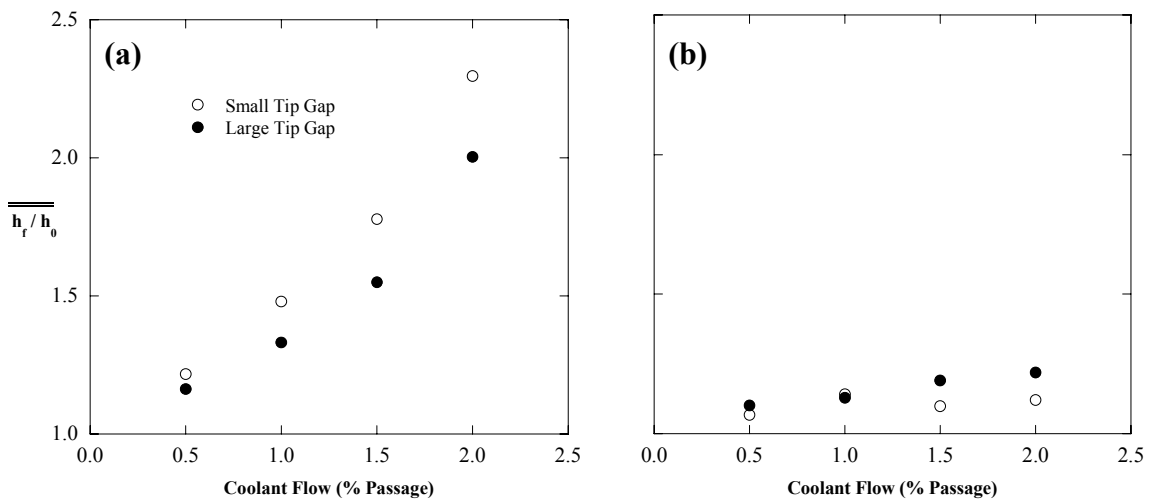


Figure 4.12. Area-averaged heat transfer augmentation with blowing for the small and large tip gaps for the entire blade surface (a) and the last 70% (b).

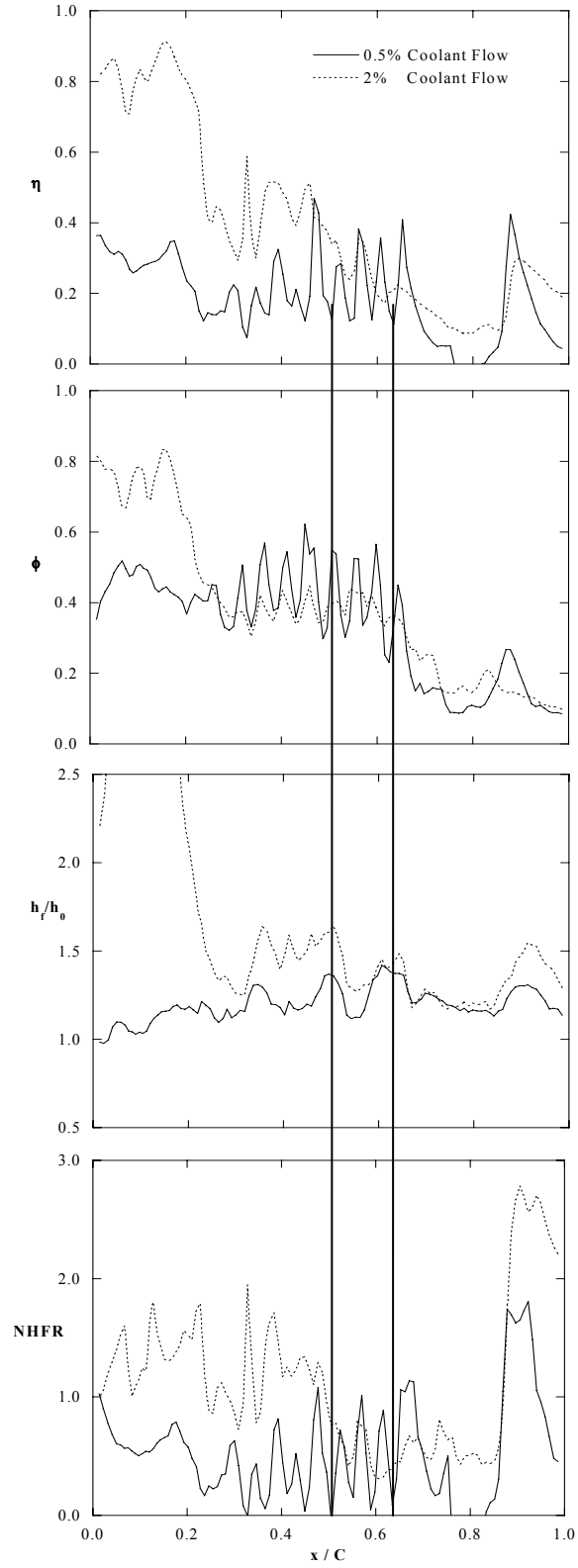


Figure 4.13. Lines showing areas of low NHFR.

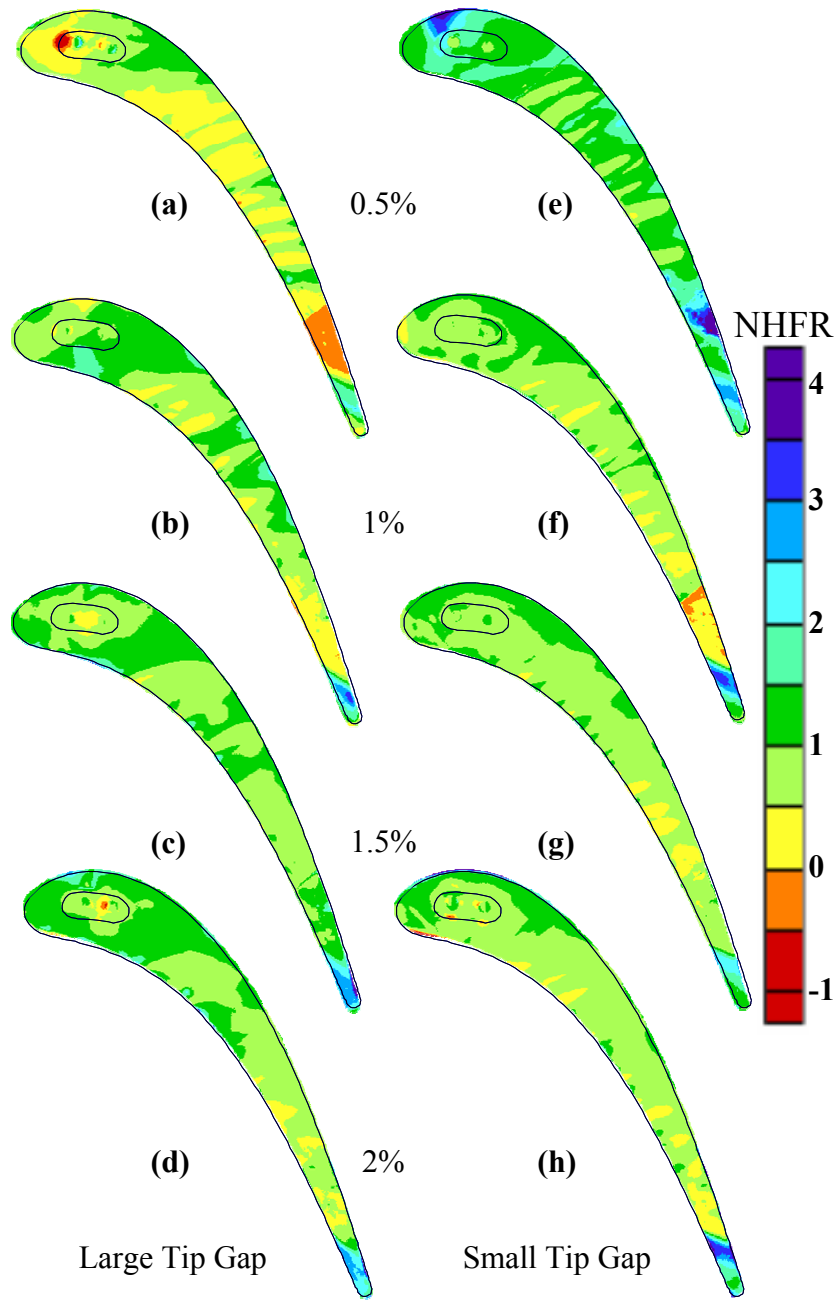


Figure 4.14. NHFR for both tip gaps at all coolant flows tested.

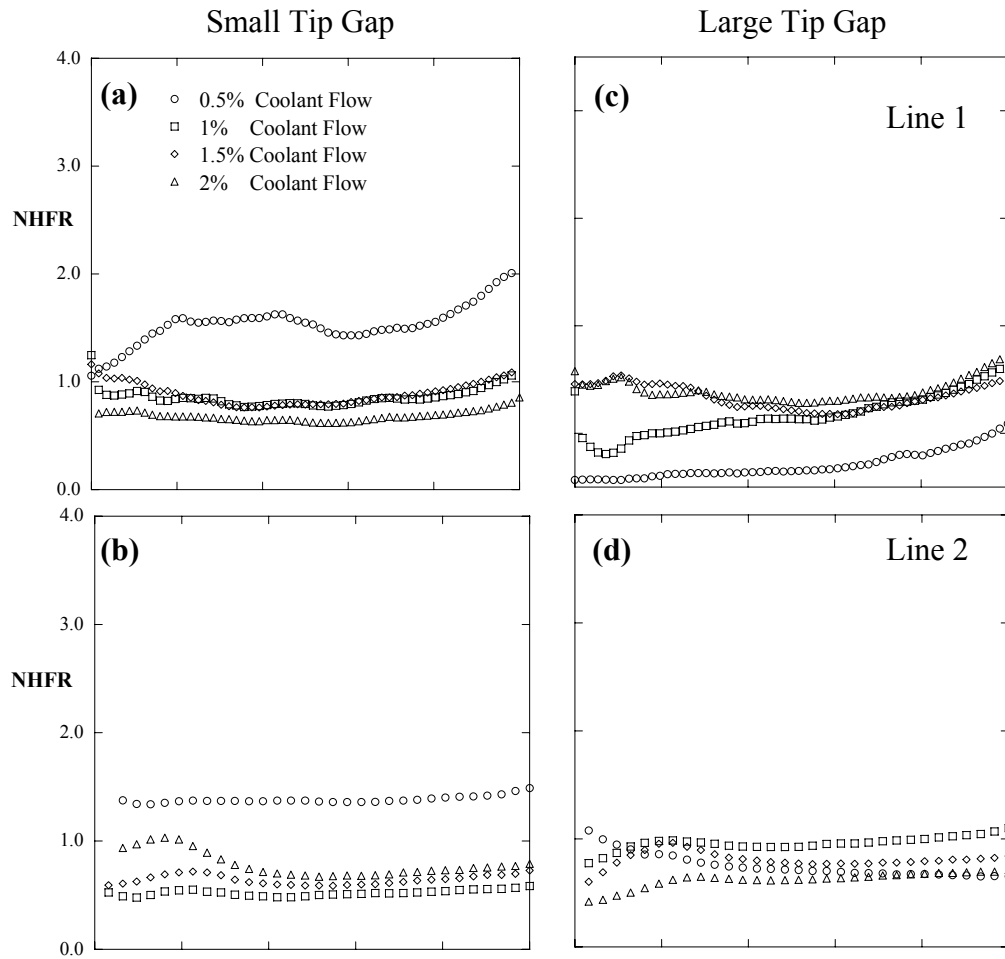


Figure 4.15 NHFR shown on path line plots for both tip gaps at all blowing ratios tested at lines 1 and 2.

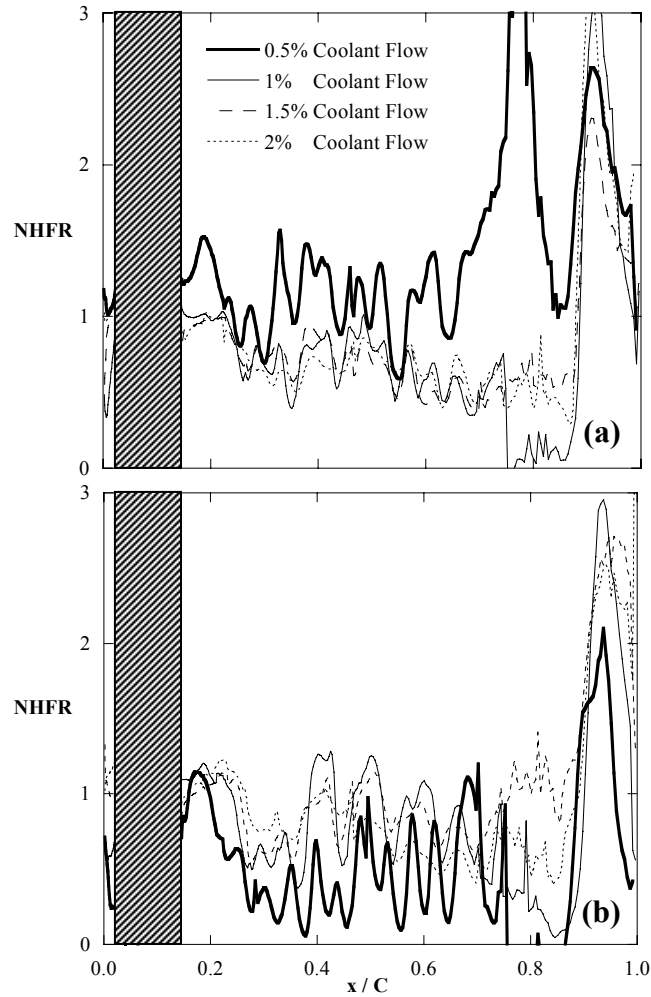


Figure 4.16. NHFR along the camber lines for the small (a) and large (b) tip gaps.

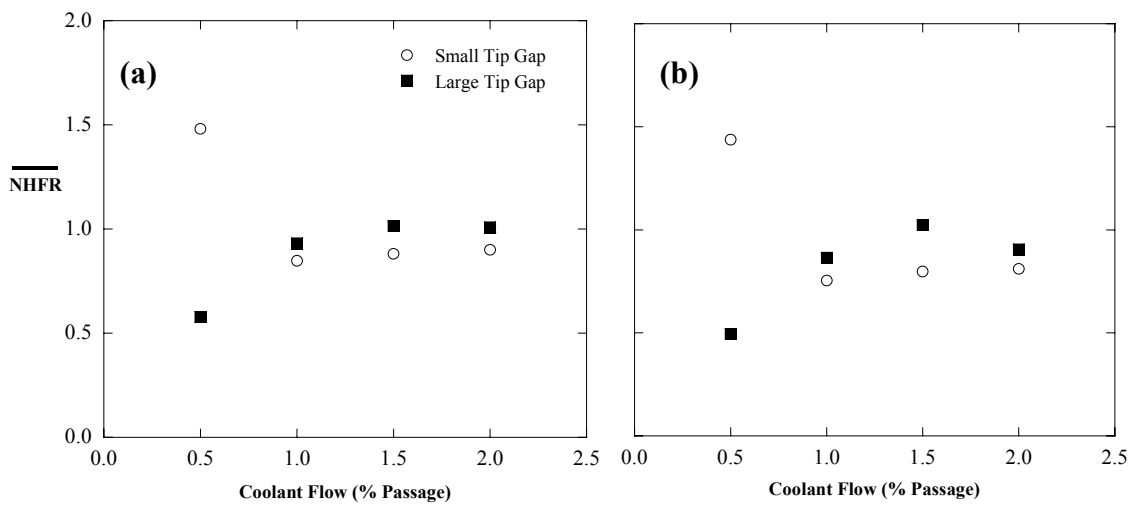


Figure 4.17. Area-averaged NHFR for the blade for the large and small tip gap over the entire blade surface (a) and the last 70% (b).

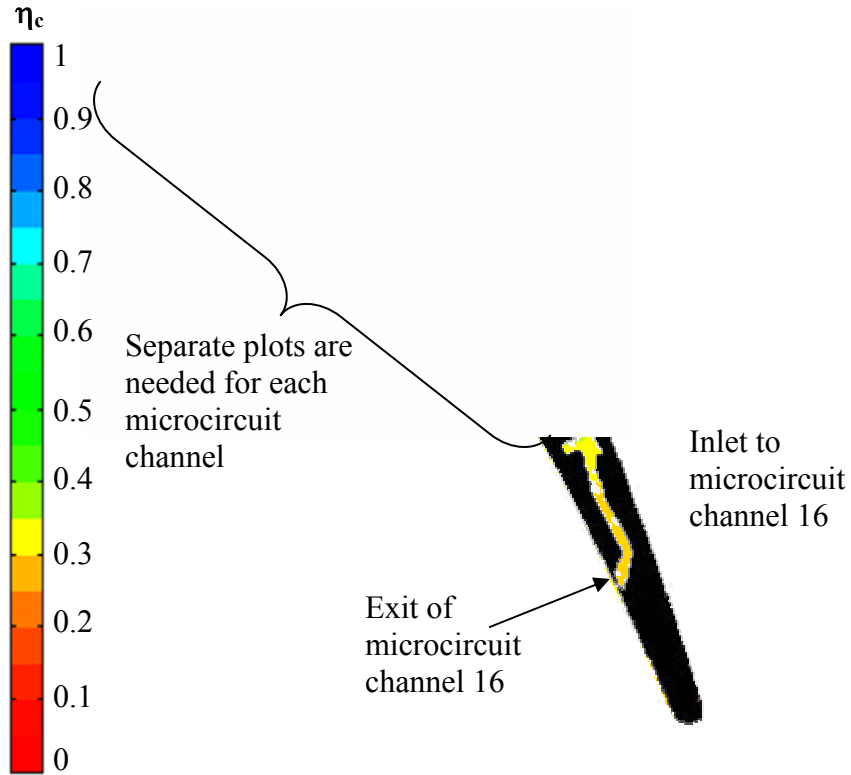


Figure 4.18. Example of methodology for finding microcircuit internal efficiency, shown here for the large tip gap, 0.5% coolant flow case.

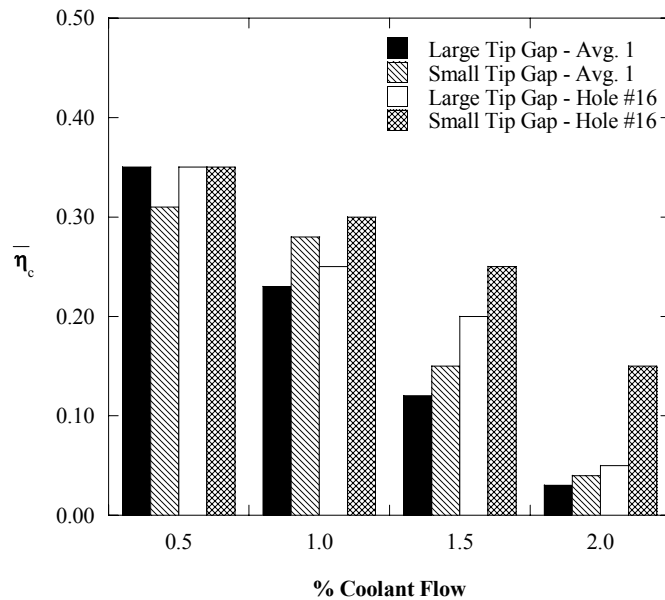


Figure 4.19. Microcircuit efficiency for all blowing ratios tested and both tip gaps.

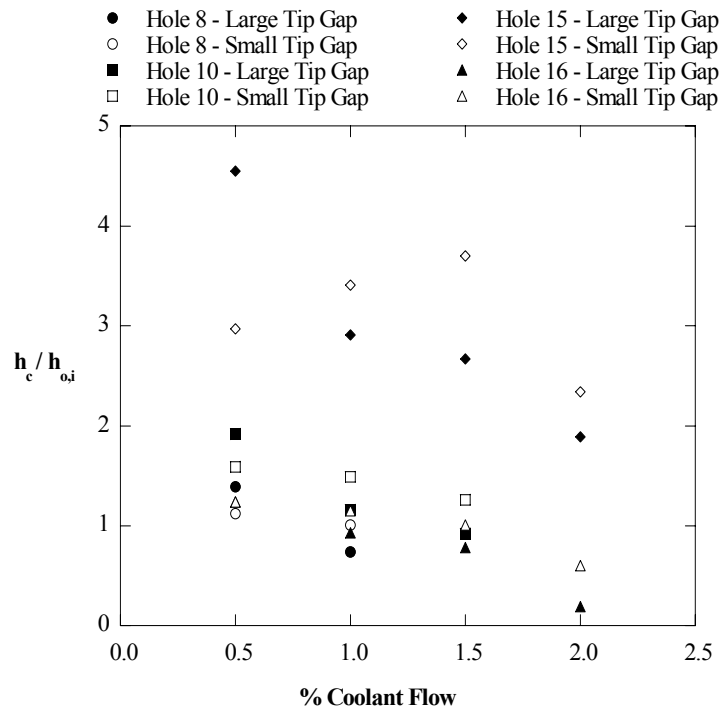


Figure 4.20. Internal heat transfer augmentation with microcircuit design shown for channels 8, 10, 15, and 16.

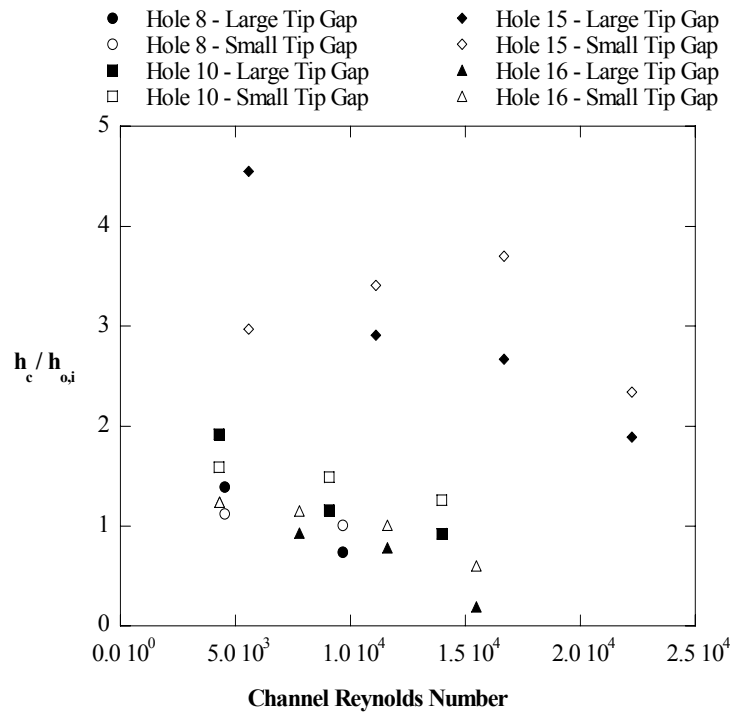


Figure 4.21. Internal heat transfer augmentation with microcircuit design plotted as a function of channel Reynolds number based on hydraulic diameter.

Appendix A: Introduction

The gas turbine engine, such as that shown in Figure A.1 is an extremely complex machine that requires many parts to perfectly operate in order to perform as designed. The turbine section, which has been pointed out in Figure A.1, is a small part of the engine, but is arguably the most studied. Research concerning the turbine has included aerodynamic shape, manufacturing methods, materials, stress and strain analysis, and heat transfer. Heat transfer studies encompass a variety of subjects ranging from computational simulations to large scale experiments such as presented in this thesis. The reason behind the thorough investigation into the turbine is because it defines the limits of the overall engine performance characteristics. With a higher combustion temperature, the power output of the turbine would be higher; however, the blade material would deteriorate quicker.

A.1 Thesis Overview

This thesis has already presented four papers documenting the film-cooling and heat transfer associated with several cooling schemes for the turbine blade tip. The first paper provided results for a simple hole injection geometry and studied the effects of blowing directly into the tip region. The second and third papers showed results from pressure side cooling schemes representing two feasible hole manufacturing techniques: EDM and laser drilling. The fourth paper reported the heat transfer associated with a novel microcircuit design for cooling the tip region which uses both internal convective cooling and external film-cooling. Some of the data has built upon the research of Couch [1] while most of the data is completely new.

The remainder of this document presents additional analysis for the studies that have been conducted and reported in the previous papers. Appendix B discusses the methods used for analyzing the experimental data as well as benchmarking and repeatability tests that were performed. The uncertainty associated with each of the measurements is also described. Appendices C through E present additional analysis that further support the topics and statements already discussed in the papers. A comparison

between the three types of tip cooling discussed in the last three papers is presented in Appendix F. Concluding remarks and recommendations for future work are discussed in Appendix G.

A.2 References

- [1] Couch, E., *Measurements of Cooling Effectiveness Along the Tip of a Turbine Blade*, Master's Thesis, Virginia Polytechnic Institute and State University, Blacksburg, VA, 2003

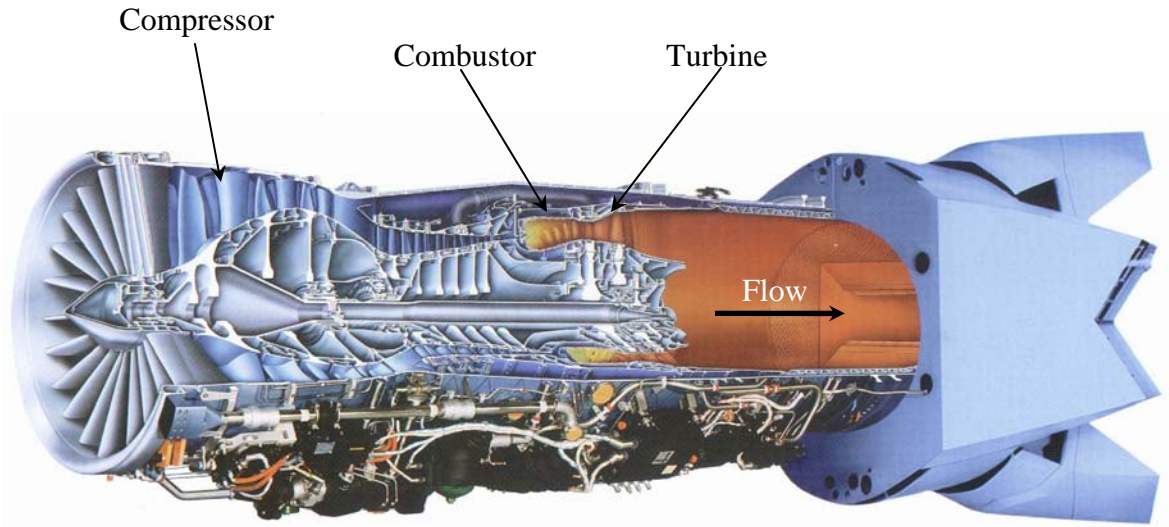


Figure A.1 Pratt & Whitney's F-119 turbo fan engine used to power the F-22 fighter.

Appendix B: Data Analysis Methods

This appendix describes the method used to analyze blade images taken with the infrared camera. Because previous experiments had been performed on the test section used for these experiments, the benchmarking cases are presented here as well as repeatability experiments performed for validation of results. Finally, the uncertainty calculations are presented for the measured variables discussed in the preceding papers.

B.1 Description of Infrared Image Analysis

The method used to combine the infrared (IR) images to make one continuous contour plot of the tip is described in this section. As discussed in the papers, contours of data along the tip of the test blade were obtained through four separate images that were calibrated independently. Through the use of an in-house MATLAB program and markers placed on the tip surface, these four separate images were mapped to make one uniform blade contour. The contouring program used a numbering scheme as shown in Figure B.1. The program then averaged each of the four sections, so that only one set of values remained at each image location. The marker locations, shown in Figure B.2, were used to map each of the images to the blade co-ordinate system, where the origin is the stagnation point.

This method positioned the blade sections together, forming one uniform contour. Because the marker locations were sometimes difficult to locate, this initial blade contour would sometimes have slight imperfections. In order to correct this, graphical user interaction was used to compare the blade image contour to the known blade outline. This comparison insured that each blade contour would be of the correct size. This is demonstrated in Figure B.3, where the initial IR images are brought into MATLAB (Figure B.3a) and mapped to the blade co-ordinate system (Figure B.3b). As this figure shows, there are slight imperfections in the mapping of the leading edge portion of the blade. The user then corrects these imperfections, and the blade is mapped to the correct shape and angle, as shown in Figure B.3c. Every tip contour presented in this thesis was

mapped using this technique. The MATLAB program used has been provided at the end of this appendix for reference.

B.2 Benchmarking and Repeatability of Experimental Results

The facility and some test geometries used for this thesis were the same as used by Couch [1]. Benchmarking tests were performed with blowing from the dirt purge holes to compare adiabatic effectiveness results between experimentalists. These two results are shown in Figure B.4. Overall, the tests show excellent agreement. The coolant levels and spreading show the same trends at each coolant flow case.

Repeatability of results presented in the papers was performed for each type of measurement. Although Couch [1] had performed repeatability tests for adiabatic effectiveness measurements, and current results have been benchmarked to his results, independent repeatability tests were performed for the other tip blowing configurations. Figure B.5 shows the repeatability test performed on the laser hole geometry at a large tip gap with 0.47% total coolant flow. As shown with the benchmarking tests, there is very good agreement between the two tests. Similar coolant levels and spreading are found for the entire surface.

Repeatability of tip heat transfer measurements were performed for blowing from the dirt purge holes at a small tip gap. This test was performed to verify repeatability of heat transfer measurements and to verify that the measurements were independent of the supplied heat flux. As discussed in the papers, all heat transfer measurements were made with a constant heat flux of $q'' = 3700 \text{ W/m}^2$ supplied to the tip surface. A repeatability test was performed with $q'' = 2500 \text{ W/m}^2$ to verify the results. Shown in Figure B.6, the heat transfer augmentation contours match very well. Because there are relatively few contour levels on the plots, quantitative comparisons were made for these results and are shown in Figure B.7. This figure compares the two cases by looking at the data along the camber line. Immediately around the dirt purge holes there is some discrepancy between the two tests. As was discussed in the papers, there are high current concentration gradients around the dirt purge holes due to cut-outs in the foil heater. At the higher heat flux case, this results in higher gradients and therefore higher heat transfer augmentation.

For the rest of the blade chord shown, the results show good agreement. At $x/L = 0.5$, the difference is on the order of 5%, which is within the uncertainty.

Repeatability measurements were also conducted for the internal heat transfer coefficients measured for the microcircuit channels. For this test, it was also desired to verify a uniformity of the coolant within the passages, which was expected because of the high channel turbulence, as mentioned in the paper. To do this, the exit thermocouples were moved for some of the passages before making the repeatability measurements, as demonstrated in Figure B.8. The repeatability results are shown in Figure B.9 in the form of internal convective effectiveness. All of the results are within uncertainty. The bold microcircuit channels (6, 11, 15) had the exit thermocouple placement changed, and verified that the passage has a uniform thermal field. This was expected because the channel Reynolds number ranged from 4300 to over 19,000 for total coolant flow rates of 0.5% and 2.0%, respectively.

B.3 Uncertainty Calculations

Uncertainty calculations were made for measurements of adiabatic effectiveness, external tip heat transfer, and internal convective effectiveness.

Adiabatic effectiveness

$$\eta = \frac{T_{\infty} - T_{AW}}{T_{\infty} - T_c}$$

Variable	Value	Precision	Bias	Total	Units
η	1	-	-	0.026	-
T_{aw}	27.91	0.058	0.4	0.404	C
T_{∞}	50.70	0.1	0.2	0.224	C
T_c	27.90	0.1	0.2	0.224	C

Variable	Value	Precision	Bias	Total	Units
η	0.2	-	-	0.025	-
T_{aw}	46.14	0.058	0.4	0.404	C
T_{∞}	50.70	0.1	0.2	0.224	C
T_c	27.90	0.1	0.2	0.224	C

External tip heat transfer

$$Nu = \frac{h t}{k}; \quad h = \frac{Q}{A(T_s - T_{\infty})}; \quad Q = Q_{tot} - Q_{rad} = \frac{V^2}{R} - \epsilon\sigma(T_s^4 - T_{\infty}^4)$$

Variable	Value	Precision	Bias	Total	Units
Q	74.5			3.92	Watts
V	2.244	0.00206	0.00309	0.004	Volts
R	1		0.001	0.001	Ω
ϵ	0.96		0.02	0.020	-
σ	5.67E-08			0.000	W/m^2K^4
T_{∞}	294.75	0.1	0.2	0.224	K
T_s	316.46	0.058	0.4	0.404	K
h	131.38			7.87	W/m^2K
A	0.02612		0.0005	0.001	m^2
T_{∞}	21.6	0.1	0.2	0.224	C
T_s	43.31	0.058	0.4	0.404	C
Nu	44.96			2.69	-
t	0.009		1.27E-05	0.000	m

Variable	Value	Precision	Bias	Total	Units
Q	62.53			2.68	Watts
V	2.057	0.00206	0.00309	0.004	Volts
R	1		0.001	0.001	Ω
ε	0.96		0.02	0.020	-
σ	5.67E-08			0.000	W/m ² K ⁴
T _∞	295.25	0.1	0.2	0.224	K
T _s	300.15	0.058	0.4	0.404	K
h	488.56			47.00	W/m ² K
A	0.02612		0.0005	0.001	m ²
T _∞	22.1	0.1	0.2	0.224	C
T _s	27	0.058	0.4	0.404	C
Nu	55.73			5.37	-
t	0.003		1.27E-05	0.000	m

Internal convective effectiveness

$$\eta_c = \frac{T_{c,o} - T_{c,i}}{T_m - T_{c,i}}$$

Variable	Value	Precision	Bias	Total	Units
η_c	1	-	-	0.008	-
T _m	33.00	0.058	0.4	0.404	C
T _{c,o}	33.07	0.1	0.2	0.224	C
T _{c,i}	25.02	0.1	0.2	0.224	C

Variable	Value	Precision	Bias	Total	Units
η_c	0.15	-	-	0.028	-
T _m	35.69	0.058	0.4	0.404	C
T _{c,o}	26.62	0.1	0.2	0.224	C
T _{c,i}	25.02	0.1	0.2	0.224	C

B.4 Nomenclature

A	= area of blade tip surface
C	= true blade chord
h_f	= film heat transfer coefficient
h_0	= baseline heat transfer coefficient
q''	= constant heat flux supplied to blade tip surface heaters
R	= resistance of precision resistor
t	= tip gap height
T	= temperature
V	= voltage across precision resistor used to determine heater current
x	= distance along blade chord
X	= blade co-ordinate system
Y	= blade co-ordinate system

Subscripts

aw	= adiabatic wall temperatures
c,o	= coolant conditions at exit to microcircuit passage
c,I	= coolant conditions at inlet to blade supply chamber
m	= blade surface temperatures measured with the alumina model
∞	= free-stream conditions as measured 1 chord upstream of the test section

Greek

ε	= emissivity of the blade tip surface
σ	= radiation constant
η	= adiabatic effectiveness
η_c	= convective effectiveness

B.5 References

- [1] Couch, E., *Measurements of Cooling Effectiveness Along the Tip of a Turbine Blade*, Master's Thesis, Virginia Polytechnic Institute and State University, Blacksburg, VA, 2003

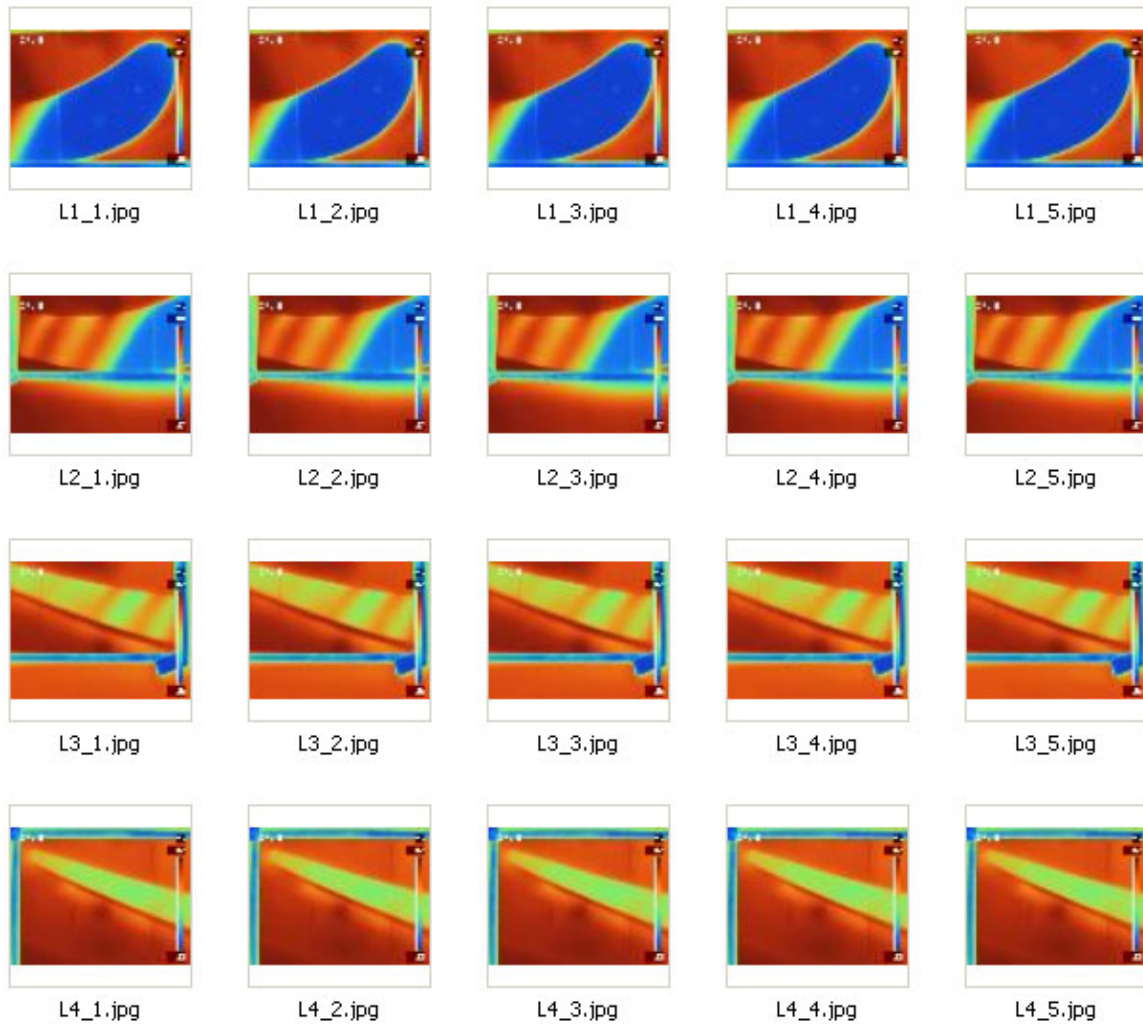


Figure B.1 Image numbering scheme used in MATLAB contouring program.

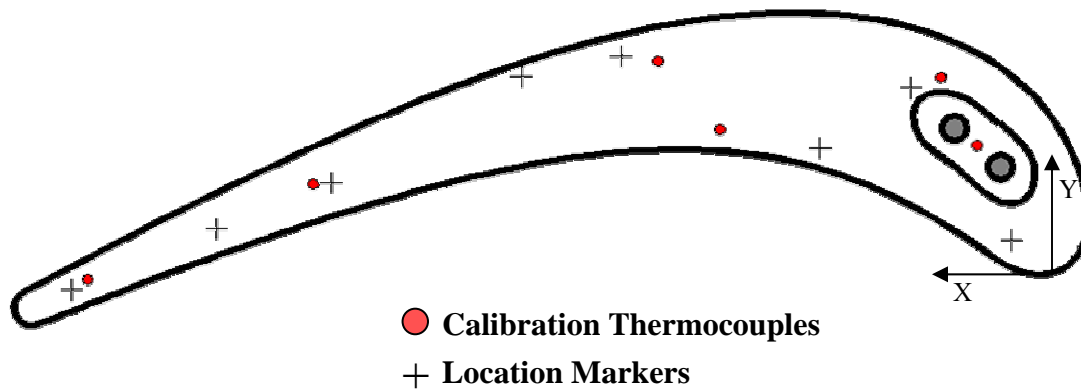


Figure B.2 Location of calibration thermocouples and markers on the test tips.

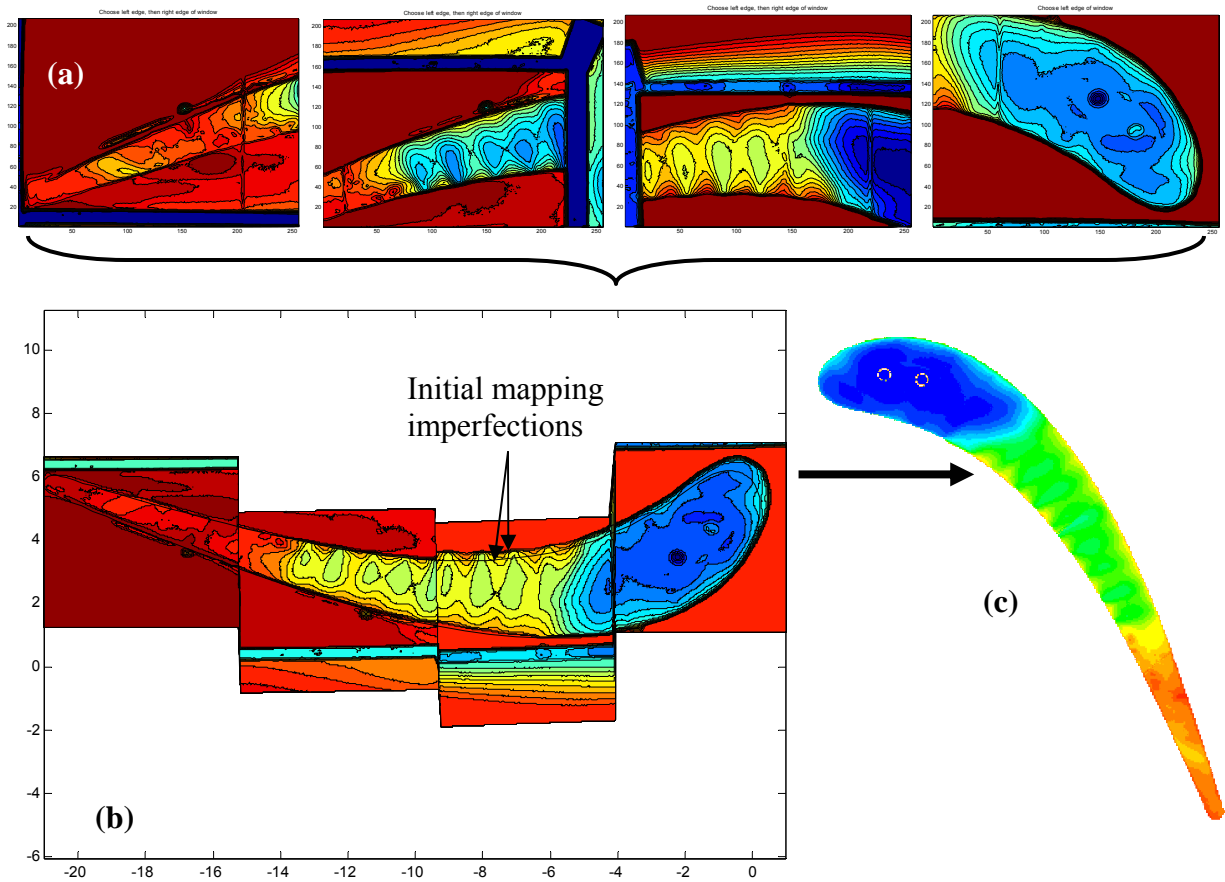


Figure B.3 Visualization of mapping sequence. Infrared images are loaded into MATLAB (a) and mapped to the blade co-ordinate system (b). User interaction corrects the imperfections and the blade contour is mapped correctly (c).

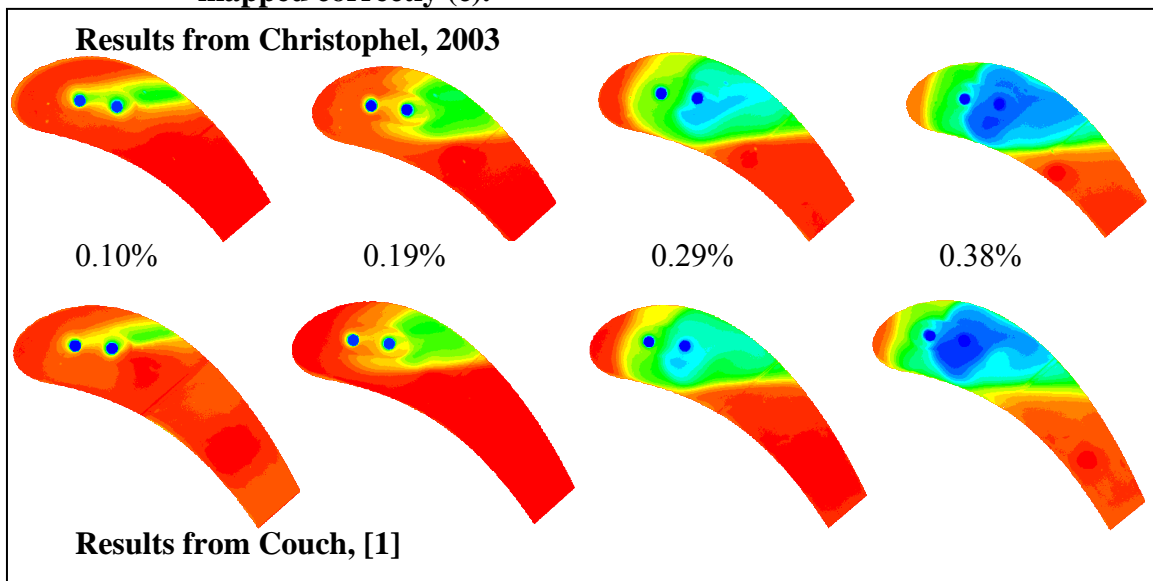


Figure B.4 Benchmarking tests for blowing from the dirt purge holes at the large tip gap at four coolant flow conditions.

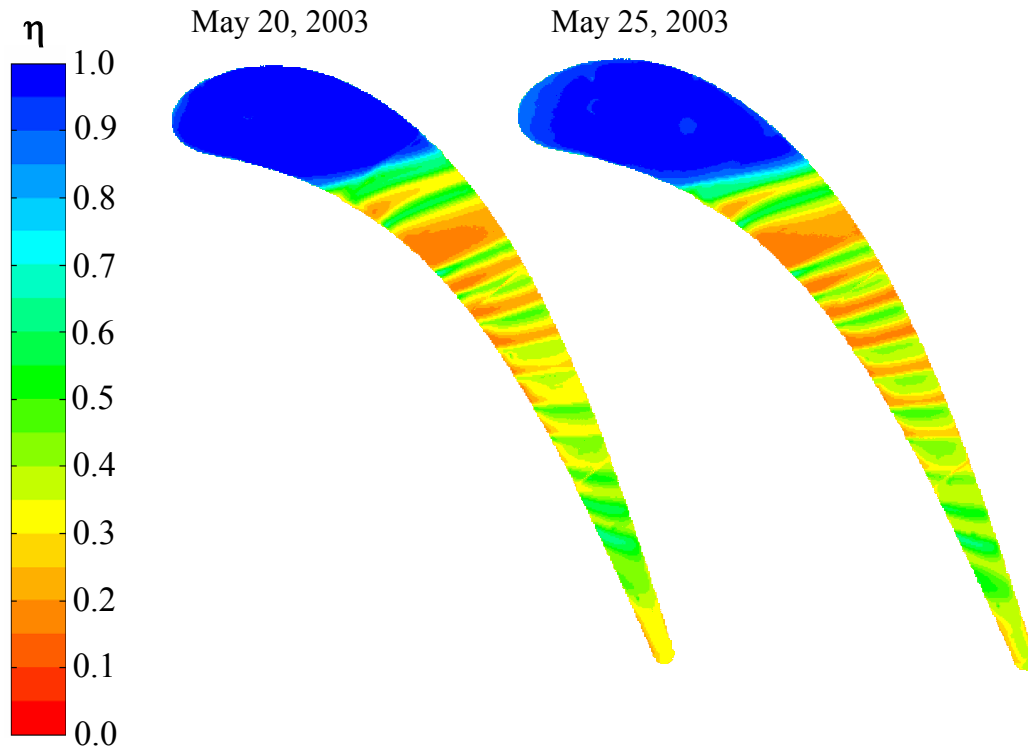


Figure B.5 Repeatability test for the laser hole geometry at the small tip gap with 0.47% total coolant flow.

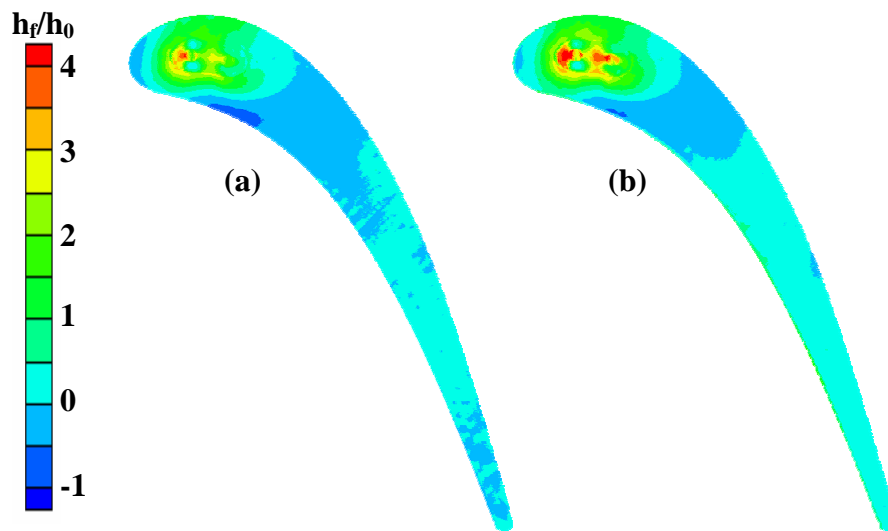


Figure B.6 Heat transfer augmentation for the dirt purge small tip gap at 0.19% total coolant flow with a heat flux of 2500 W/m² (a) and 3700 W/m² (b).

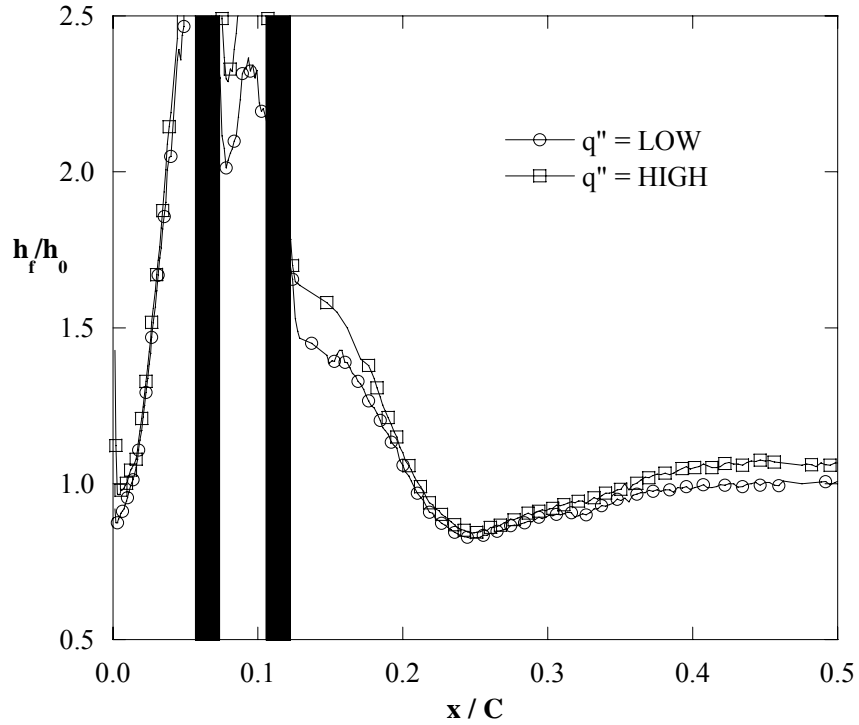


Figure B.7. Heat transfer augmentation along the camber line for the low ($q'' = 2500 \text{ W/m}^2$) and high ($q'' = 3700 \text{ W/m}^2$) dirt purge cases with 0.19% coolant flow.

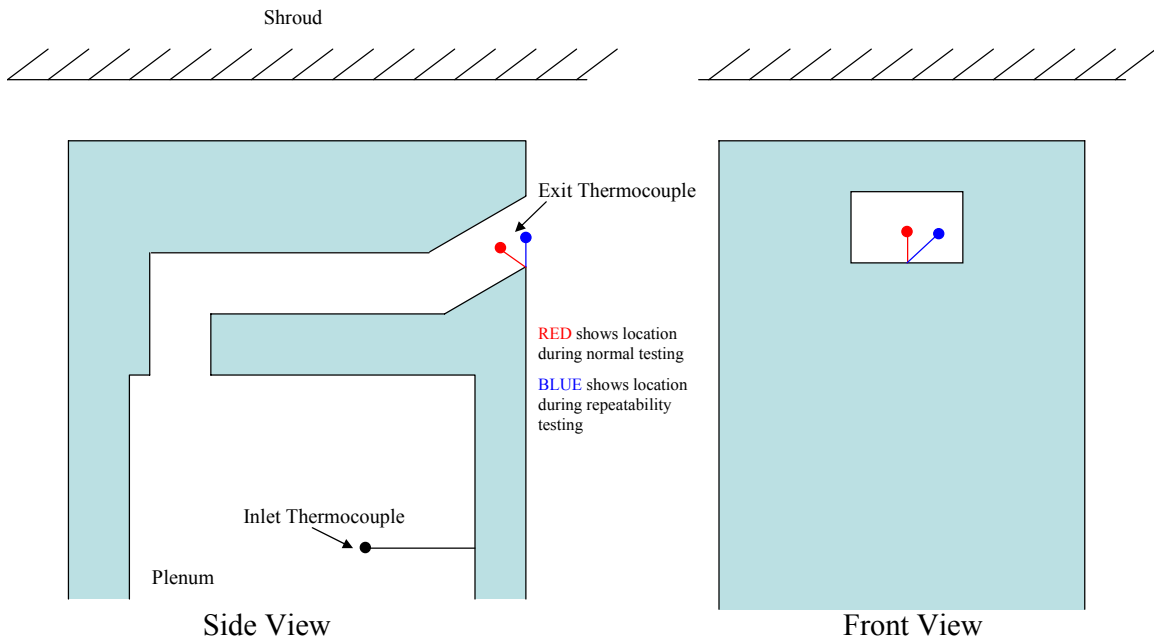


Figure B.8 Description of test performed to verify uniform thermal field within microcircuit passages and repeatability of internal heat transfer measurements.

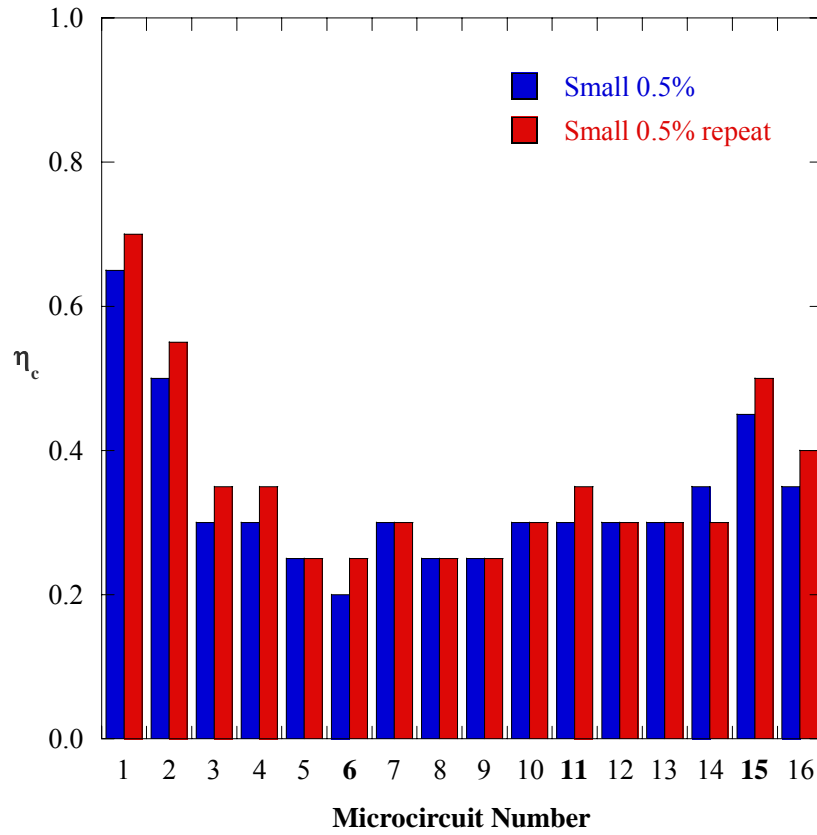


Figure B.9 Repeatability test for internal channel efficiency also verified uniform thermal field. The microcircuit numbers in bold (6, 11, 15) had the thermocouples moved as shown in Figure B.8.

MATLAB code used for tip data analysis:

```
%-----Jesse Christophel-----
load L1_1; load L1_2; load L1_3; load L1_4; load L1_5;
load L2_1; load L2_2; load L2_3; load L2_4; load L2_5;
load L3_1; load L3_2; load L3_3; load L3_4; load L3_5;
load L4_1; load L4_2; load L4_3; load L4_4; load L4_5;
L1 = 0.2*(L1_1 + L1_2 + L1_3 + L1_4 + L1_5);
L2 = 0.2*(L2_1 + L2_2 + L2_3 + L2_4 + L2_5);
L3 = 0.2*(L3_1 + L3_2 + L3_3 + L3_4 + L3_5);
L4 = 0.2*(L4_1 + L4_2 + L4_3 + L4_4 + L4_5);

marker = load('Markers.txt');
marker_indices = load('MarkerValues.txt');
x1_spacing = abs((marker(2,2) - marker(1,2))/(marker_indices(2,2) -
marker_indices(1,2)));
y1_spacing = abs((marker(2,3) - marker(1,3))/(marker_indices(2,3) -
marker_indices(1,3)));
x2_spacing = abs((marker(4,2) - marker(3,2))/(marker_indices(4,2) -
marker_indices(3,2)));
y2_spacing = abs((marker(4,3) - marker(3,3))/(marker_indices(4,3) -
marker_indices(3,3)));
x3_spacing = abs((marker(6,2) - marker(5,2))/(marker_indices(6,2) -
marker_indices(5,2)));
y3_spacing = abs((marker(6,3) - marker(5,3))/(marker_indices(6,3) -
marker_indices(5,3)));
x4_spacing = abs((marker(8,2) - marker(7,2))/(marker_indices(8,2) -
marker_indices(7,2)));
y4_spacing = abs((marker(8,3) - marker(7,3))/(marker_indices(8,3) -
marker_indices(7,3)));
x_spacing = .25*(x1_spacing + x2_spacing + x3_spacing + x4_spacing);
y_spacing = .25*(y1_spacing + y2_spacing + y3_spacing + y4_spacing);
x1_spacing = x_spacing;
x2_spacing = x_spacing;
x3_spacing = x_spacing;
x4_spacing = x_spacing;
y1_spacing = y_spacing;
y2_spacing = y_spacing;
y3_spacing = y_spacing;
y4_spacing = y_spacing;

contourf(L1, 20);
title('Choose left edge of window');
[x1_i, y1_i] = ginput(1);
close;
x1_i = fix(x1_i);
L1 = L1(:, x1_i:length(L1(1,:)));
contourf(L2, 20);
title('Choose left edge, then right edge of window');
[x2_i, y2_i] = ginput(2);
close;
x2_i = fix(x2_i);
L2 = L2(:, x2_i(1):x2_i(2));
contourf(L3, 20);
title('Choose left edge, then right edge of window');
[x3_i, y3_i] = ginput(2);
close;
x3_i = fix(x3_i);
L3 = L3(:, x3_i(1):x3_i(2));
contourf(L4, 20);
title('Choose left edge, then right edge of window');
[x4_i, y4_i] = ginput(2);
close;
x4_i = fix(x4_i);
```

```

L4 = L4(:, x4_i(1):x4_i(2));

X0 = fix(marker(1,2)/x1_spacing + marker_indices(1,2) - x1_i);
Y0 = fix(marker_indices(1,3) - marker(1,3)/y1_spacing);
X1_max = (length(L1(1,:)) - X0)*x1_spacing;
X1_min = -X0*x1_spacing;
Y1_max = (length(L1(:,1)) - Y0)*y1_spacing;
Y1_min = -Y0*y1_spacing;
X2_max = -marker(3,2) + (-marker_indices(3,2) + x2_i(2))*x2_spacing;
X2_min = -(marker(4,2) + (marker_indices(4,2) - x2_i(1))*x2_spacing);
Y2_max = marker(3,3) + (length(L2(:,1)) - marker_indices(3,3))*y2_spacing;
Y2_min = marker(3,3) - marker_indices(3,3)*y2_spacing;
X3_max = -marker(5,2) + (-marker_indices(5,2) + x3_i(2))*x3_spacing;
X3_min = -(marker(6,2) + (marker_indices(6,2) - x3_i(1))*x3_spacing);
Y3_max = marker(5,3) + (length(L3(:,1)) - marker_indices(5,3))*y3_spacing;
Y3_min = marker(5,3) - marker_indices(5,3)*y3_spacing;
X4_max = -marker(7,2) + (-marker_indices(7,2) + x4_i(2))*x4_spacing;
X4_min = -(marker(8,2) + (marker_indices(8,2) - x4_i(1))*x4_spacing);
Y4_max = marker(7,3) + (length(L4(:,1)) - marker_indices(7,3))*y4_spacing;
Y4_min = marker(7,3) - marker_indices(7,3)*y4_spacing;
X_min = X4_min;
X_max = X1_max;
Y_min = Y1_min;
Y_max = Y1_max;
L = [L4(:, :) L3(:, fix((X4_max - X3_min)/x3_spacing):length(L3(1,:)))
L2(:, fix((X3_max - X2_min)/x2_spacing)-8:length(L2(1,:)))
L1(:, fix((X2_max - X1_min)/x1_spacing)+8:length(L1(1,:)))];
L = flipud(L);

contourf(L, 20); axis equal;
[ddx no] = ginput(3);
close;

X = linspace(X_min, X_max, length(L(1,:)));
Y = linspace(Y_min, Y_max, 207);
XX = repmat(X, 207, 1);
YY = repmat(Y, 1, length(L(1,:)));

R_b_suc = load('SuctionCoordsRotated.txt');
R_b_pre = load('PressureCoordsRotated.txt');
R_b_suc = sortrows(R_b_suc, 1);
R_b_pre = sortrows(R_b_pre, 1);
a = 0*pi/180;
R_b_suc(:, 1) = R_b_suc(:, 1). *cos(a) + R_b_suc(:, 2). *sin(a);
R_b_suc(:, 2) = -R_b_suc(:, 1). *sin(a) + R_b_suc(:, 2). *cos(a);
R_b_pre(:, 1) = R_b_pre(:, 1). *cos(a) + R_b_pre(:, 2). *sin(a);
R_b_pre(:, 2) = -R_b_pre(:, 1). *sin(a) + R_b_pre(:, 2). *cos(a);
R_b_suc(:, 2) = R_b_suc(:, 2) + (256-1.5*Y0)*y1_spacing;
R_b_pre(:, 2) = R_b_pre(:, 2) + (256-1.5*Y0)*y1_spacing;

figure(2); contourf(XX, YY, L, 20); axis equal; hold on;
plot(R_b_suc(:, 1), R_b_suc(:, 2), 'k', R_b_pre(:, 1), R_b_pre(:, 2), 'k');
[dy_x, dy] = ginput(16);
close;
factor1 = (dy(16) - dy(14))/(dy(15) - dy(13));
factor2 = (dy(12) - dy(10))/(dy(11) - dy(9));
factor3 = (dy(8) - dy(6))/(dy(7) - dy(5));
factor4 = (dy(4) - dy(2))/(dy(3) - dy(1));
YY(:, 1:floor(ddx(1))) = YY(:, 1:floor(ddx(1)))*factor4;
YY(:, ceil(ddx(1)):floor(ddx(2))) =
YY(:, ceil(ddx(1)):floor(ddx(2)))*factor3;

```

```

YY(:, ceil(ddx(2)): floor(ddx(3))) =
YY(:, ceil(ddx(2)): floor(ddx(3)))*factor2;
YY(:, ceil(ddx(3)): end) = YY(:, ceil(ddx(3)): end)*factor1;

figure(2); contourf(XX,YY,L,20); axis equal; hold on;
plot(R_b_suc(:,1),R_b_suc(:,2),'k',R_b_pre(:,1),R_b_pre(:,2),'k');
[dy_x, dy] = ginput(8);
close;
dy1 = dy(8) - dy(7);
dy2 = dy(6) - dy(5);
dy3 = dy(4) - dy(3);
dy4 = dy(2) - dy(1);
YY(:, 1: floor(ddx(1))) = YY(:, 1: floor(ddx(1))) + dy4;
YY(:, ceil(ddx(1)): floor(ddx(2))) = YY(:, ceil(ddx(1)): floor(ddx(2))) +
dy3;
YY(:, ceil(ddx(2)): floor(ddx(3))) = YY(:, ceil(ddx(2)): floor(ddx(3))) +
dy2;
YY(:, ceil(ddx(3)): end) = YY(:, ceil(ddx(3)): end) + dy1;

figure(2); contourf(XX,YY,L,20); axis equal; hold on;
plot(R_b_suc(:,1),R_b_suc(:,2),'k',R_b_pre(:,1),R_b_pre(:,2),'k');

X = linspace(X_min,X_max,length(L(1,:)));
Y = linspace(Y_min,Y_max,207);
XX = repmat(X,207,1);
YY = repmat(Y,1,length(L(1,:)));
YY(:, 1: floor(ddx(1))) = YY(:, 1: floor(ddx(1)))*factor4;
YY(:, ceil(ddx(1)): floor(ddx(2))) =
YY(:, ceil(ddx(1)): floor(ddx(2)))*factor3;
YY(:, ceil(ddx(2)): floor(ddx(3))) =
YY(:, ceil(ddx(2)): floor(ddx(3)))*factor2;
YY(:, ceil(ddx(3)): end) = YY(:, ceil(ddx(3)): end)*factor1;
YY(:, 1: floor(ddx(1))) = YY(:, 1: floor(ddx(1))) + 5.0269-5.5659;
YY(:, ceil(ddx(1)): floor(ddx(2))) = YY(:, ceil(ddx(1)): floor(ddx(2))) +
3.6356-3.4557;
YY(:, ceil(ddx(2)): floor(ddx(3))) = YY(:, ceil(ddx(2)): floor(ddx(3))) +
3.4014-3.3789;
YY(:, ceil(ddx(3)): end) = YY(:, ceil(ddx(3)): end) + dy1;

%TWO
alpha = -0.5;
a = alpha*pi/180;
XX(:, ceil(ddx(2)): floor(ddx(3))) =
XX(:, ceil(ddx(2)): floor(ddx(3))).*cos(a) +
YY(:, ceil(ddx(2)): floor(ddx(3))).*sin(a);% - 12*cos(a);
YY(:, ceil(ddx(2)): floor(ddx(3))) = -
XX(:, ceil(ddx(2)): floor(ddx(3))).*sin(a) +
YY(:, ceil(ddx(2)): floor(ddx(3))).*cos(a);% - 3*sin(a);

%THREE
alpha = -1.0;
a = alpha*pi/180;
XX(:, ceil(ddx(1)): floor(ddx(2))) =
XX(:, ceil(ddx(1)): floor(ddx(2))).*cos(a) +
YY(:, ceil(ddx(1)): floor(ddx(2))).*sin(a);% - 12*cos(a);
YY(:, ceil(ddx(1)): floor(ddx(2))) = -
XX(:, ceil(ddx(1)): floor(ddx(2))).*sin(a) +
YY(:, ceil(ddx(1)): floor(ddx(2))).*cos(a);% - 3*sin(a);

%FOUR
alpha = 1.0;
a = alpha*pi/180;
XX(:, 1: floor(ddx(1))) = XX(:, 1: floor(ddx(1))).*cos(a) +
YY(:, 1: floor(ddx(1))).*sin(a);% - 12*cos(a);

```

```

YY(:, 1: floor(ddx(1))) = -XX(:, 1: floor(ddx(1))). *sin(a) +
YY(:, 1: floor(ddx(1))). *cos(a); % - 3*sin(a);

figure(3); contourf(XX, YY, L, 20); axis equal; hold on;
plot(R_b_suc(:, 1), R_b_suc(:, 2), 'k', R_b_pre(:, 1), R_b_pre(:, 2), 'k');
X_limit_blade = find(X>=R_b_suc(1, 1) & X<=R_b_suc(end, 1));
blade_suction = spline(R_b_suc(:, 1), R_b_suc(:, 2));
blade_pressure = spline(R_b_pre(:, 1), R_b_pre(:, 2));
L(:, 1: X_limit_blade(1)-1) = NaN;
L(:, X_limit_blade(end)+1: end) = NaN;
grid_suc = ppval (blade_suction, X(X_limit_blade));
grid_pre = ppval (blade_pressure, X(X_limit_blade));
for i=1:length(X_limit_blade)
    ColInd = X_limit_blade(i);
    YInd = find(YY(:, ColInd) <= grid_suc(i) | YY(:, ColInd) >=
grid_pre(i));
    if length(YInd)>0
        L(YInd, ColInd) = NaN;
    end
end
alpha = 180+49.66905;
a = alpha*pi/180;
XXX = XX.*cos(a) + YY.*sin(a);
YYY = -XX.*sin(a) + YY.*cos(a);
contourf(XXX, YYY, L, 20); axis equal;
[Cx Cy] = ginput(2);

Radius = .1969;
Centers = [Cx(1) Cy(1); Cx(2) Cy(2)];
for i = 1:length(Centers)
    Dist = sqrt((XXX-Centers(i, 1)).^2 + (YYY-Centers(i, 2)).^2);
    Index = find(Dist <= Radius);
    L(Index) = NaN;
end
ze = find(L==0);
L(ze) = NaN;
L = L - 273.15;
N = (46.7 - L)./(46.7 - 24);

N(:, 1: floor(ddx(2))) = (47.2 - L(:, 1: floor(ddx(2))))./(47.2 - 26);
N(:, ceil(ddx(2)): end) = (46.2 - L(:, ceil(ddx(2)): end))./(46.2 - 25.0);

Radius = .1969;
Centers = [Cx(1) Cy(1); Cx(2) Cy(2)];
for i = 1:length(Centers)
    Dist = sqrt((XXX-Centers(i, 1)).^2 + (YYY-Centers(i, 2)).^2);
    Index = find(Dist <= Radius);
    N(Index) = 1;
end
C0 = [255 0 0]/255; C1 = [255 43 0]/255; C2 = [255 85 0]/255; C3 = [255
128 0]/255; C4 = [255 170 0]/255; C5 = [255 212 0]/255; C6 = [255 255
0]/255; C7 = [191 255 0]/255; C8 = [128 255 0]/255; C9 = [64 255
0]/255; C10 = [0 255 0]/255; C11 = [0 255 64]/255; C12 = [0 255
128]/255; C13 = [0 255 191]/255; C14 = [0 255 255]/255; C15 = [0 204
255]/255; C16 = [0 153 255]/255; C17 = [0 102 255]/255; C18 = [0 51
255]/255; C19 = [0 0 255]/255; m = [C0; C1; C2; C3; C4; C5; C6; C7; C8;
C9; C10; C11; C12; C13; C14; C15; C16; C17; C18; C19];
figure(8);
[c, ch, cf] = contourf(XXX, YYY, N, 20);
set(ch, 'LineStyle', 'none');
axi = [0 1]; caxis(axi); colormap(m); colorbar; axis equal; axis off;

```

Appendix C: Additional Analysis for Dirt Purge Results

Results presented in the dirt purge paper mark trends seen in the adiabatic effectiveness and tip heat transfer coefficients. Also, these two measurements were combined to show the net heat flux reduction (NHFR) that dirt purge blowing provided the blade tip. This appendix presents additional analysis that was performed on the dirt purge cases that were not presented in the paper. This deals mainly with the heat transfer results because additional work on the adiabatic effectiveness has been performed by Couch [1].

C.1 Discussion of Additional Data

Contours of heat transfer augmentation with dirt purge blowing are shown in Figure C.1. These results show how much the dirt purge blowing affects the heat transfer in the area immediately surrounding the dirt purge cavity. As the coolant flow is increased from 0.10% to 0.38%, the heat transfer augmentation in the leading edge is increased for both the small and large tip gaps. Heat transfer augmentation along the downstream 70% of the blade is not affected by blowing ratio, and is generally around a value of one. This shows that the heat transfer in this region is not affected by the dirt purge blowing, which is consistent with the adiabatic effectiveness results presented by Couch [1].

Generally, the large tip gap has lower heat transfer augmentations around the dirt purge holes than the small tip gap. Also, the large tip gap shows a trend beginning at the 0.19% coolant flow case that is not seen at the small tip gap. This is the appearance of a streak of high heat transfer augmentation on the downstream side of the second dirt purge hole. As was shown in the paper, the first dirt purge hole is swept downstream and is split by the jet exiting the second dirt purge hole. The flow that is diverted to the downstream side tends to form vortices, which cause high heat transfer. These were predicted computationally, as shown in the paper, and are verified by the contour plots shown here.

Experimental results for the dirt purge blowing have also been compared along the pressure side of the tip. This line was first presented in the paper titled “Hole Shapes – Part 2.” Comparisons at this line for the adiabatic effectiveness, heat transfer augmentation, and NHFR are shown in Figures C.2, C.3, and C.4, respectively.

The adiabatic effectiveness results (Figure C.2) show that at the small tip gap, the film cooling is spreading all the way to the pressure side for the 0.19%, 0.29%, and 0.38% coolant flows at $x/C = 0.1$. At the higher flow rates, the covered area also extends over a large portion of the pressure side. For the large tip gap, the film-cooling does not reach the pressure side at the 0.10% and 0.19% coolant flow rates. At the higher two flow rates, however, the coolant begins to reach the pressure side, but is never as effective as the small tip gap. Downstream of $x/C = 0.35$, none of the cases tested show film-cooling present along the pressure side.

The heat transfer augmentations along the pressure-side line (Figure C.3) show that the heat transfer increases in the leading edge ($0 < x/C < 0.2$) with increased blowing for both gap heights. The small tip gap especially shows increasing peaks at $x/C = 0.1$ with each increase in coolant flow. Downstream of $x/C = 0.2$, for the small tip gap, the heat transfer levels out to a value of one, which means that the dirt purge blowing has no effect on the heat transfer in this region. For the large tip gap, the heat transfer along the pressure side is not affected until the coolant flow reaches 0.29%. Also, the heat transfer augmentations for the large tip gap are not as severe as with the small tip gap.

NHFR values along the pressure-side line (Figure C.4) show that the NHFR is increased with blowing for both tip gaps, and that the small tip gap has higher NHFR values than the large tip gap. For the small tip gap, the NHFR is unaffected by the dirt purge blowing downstream of $x/C = 0.35$, whereas for the large tip gap, the NHFR is unaffected by dirt purge blowing downstream of $x/C = 0.25$.

Data taken along lines normal to the blade pressure-side curve are also shown in this appendix. The lines chosen are given in Figure C.5. The data for lines 1, 2, 3, and 4 are given for all measured variables in Figure C.6, C.7, C.8, and C.9, respectively. The trends shown in these lines verify what the camber and pressure-side lines have shown about increasing adiabatic effectiveness, heat transfer augmentation, and NHFR for increasing blowing.

C.2 Nomenclature

h_f = film heat transfer coefficient
 h_0 = baseline heat transfer coefficient
 L = distance along blade thickness taken normal to pressure side curve
NHFR = net heat flux reduction
 S = distance along pressure side curve

Greek

H = adiabatic effectiveness

Subscripts

max = denotes maximum value

C.3 References

- [1] Couch, E., *Measurements of Cooling Effectiveness Along the Tip of a Turbine Blade*, Master's Thesis, Virginia Polytechnic Institute and State University, Blacksburg, VA, 2003

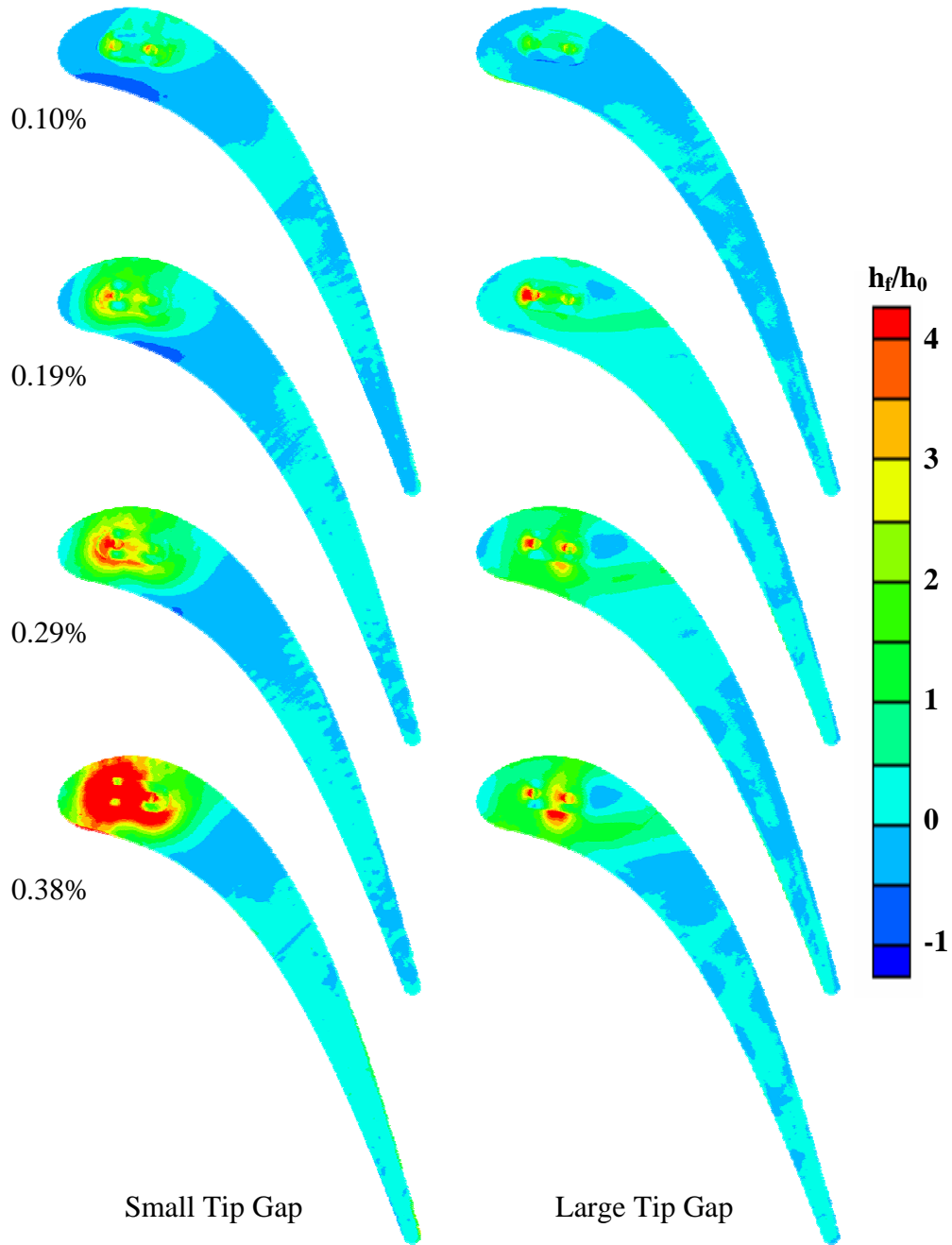


Figure C.1 Contours of heat transfer augmentation for all dirt purge cases at the small tip gap (left) and large tip gap (right).

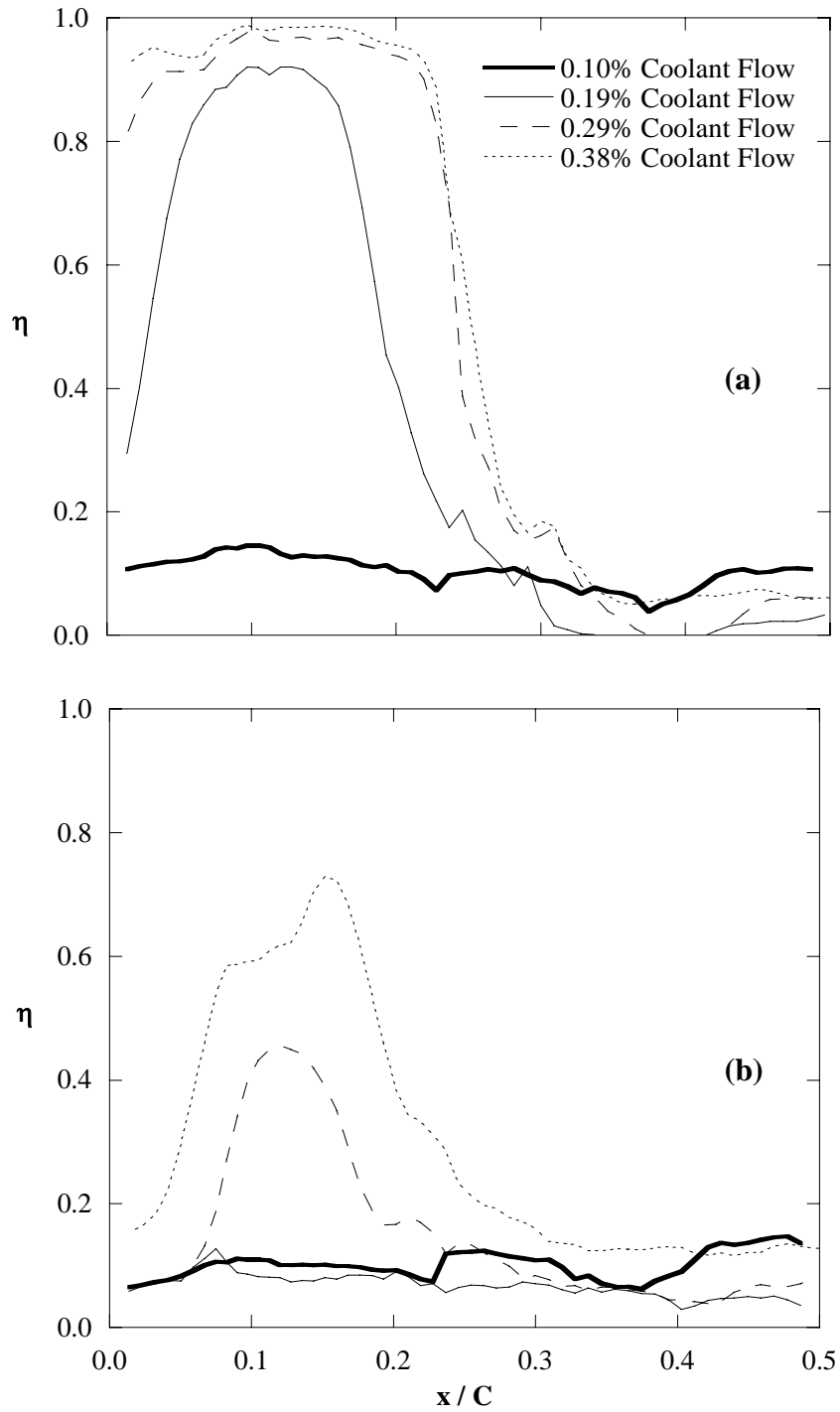


Figure C.2 Adiabatic effectiveness along the pressure-side line for the small tip gap (a) and large tip gap (b).

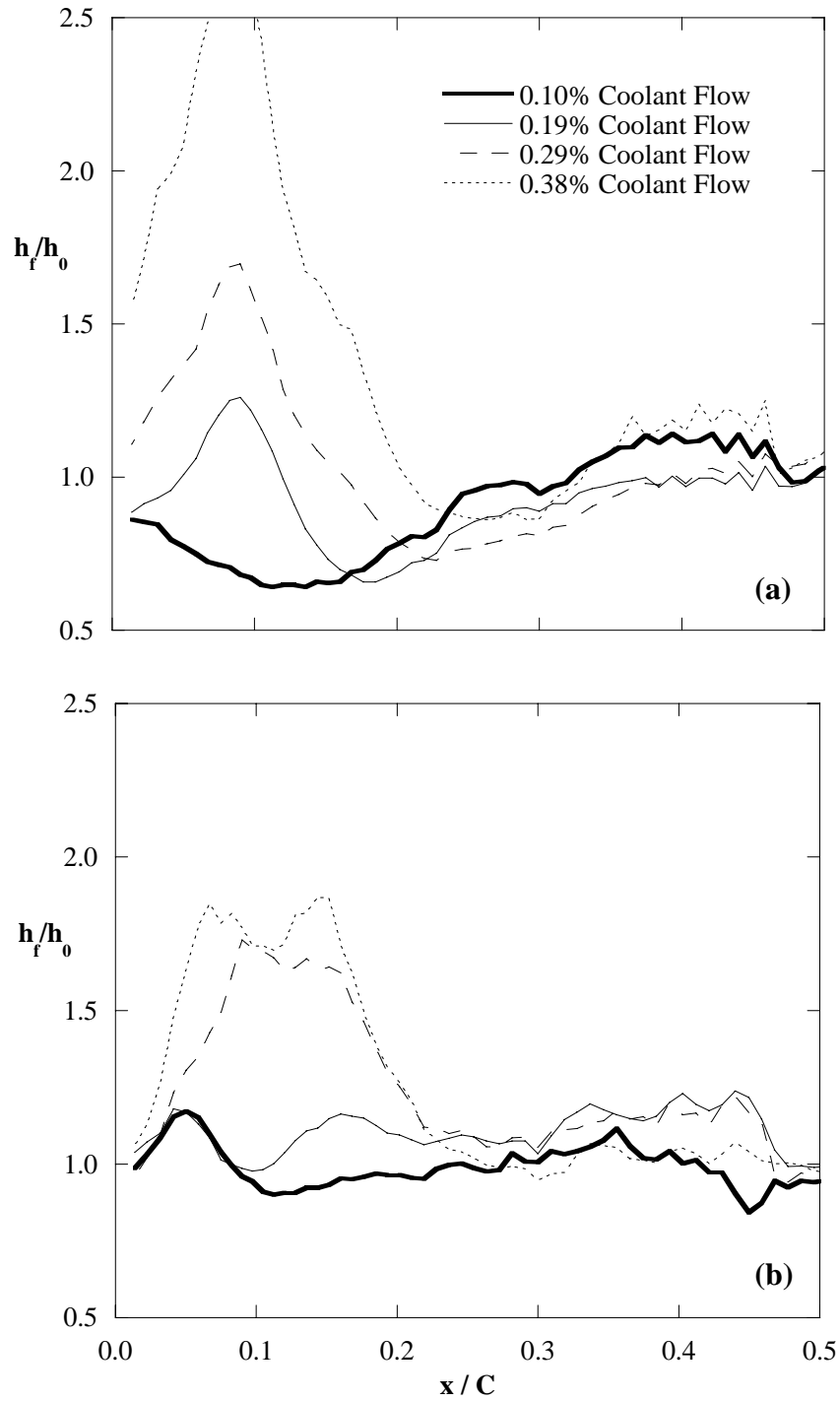


Figure C.3 Heat transfer augmentation taken along the pressure side line for all dirt purge cases at the small tip gap (a) and large tip gap (b).

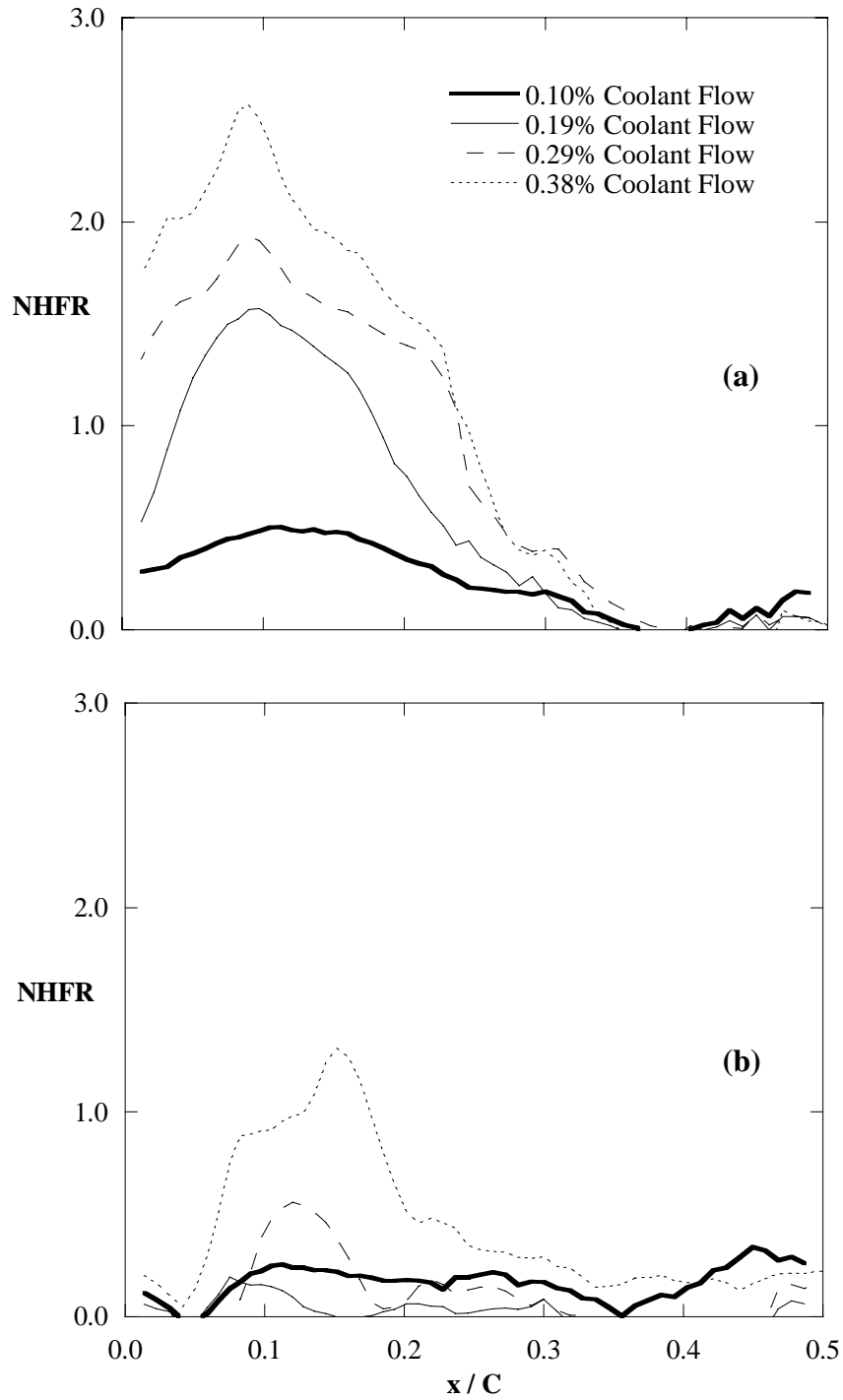


Figure C.4 NHR along the pressure-side line for the small tip gap (a) and large tip gap (b).

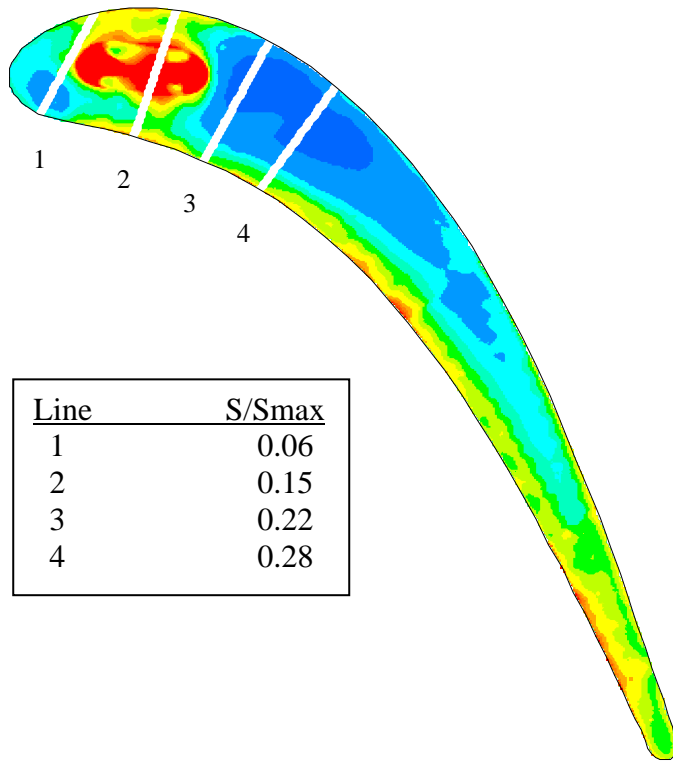


Figure C.5 Line positions used for dirt purge analysis. All lines taken normal to the blade pressure-side curve.

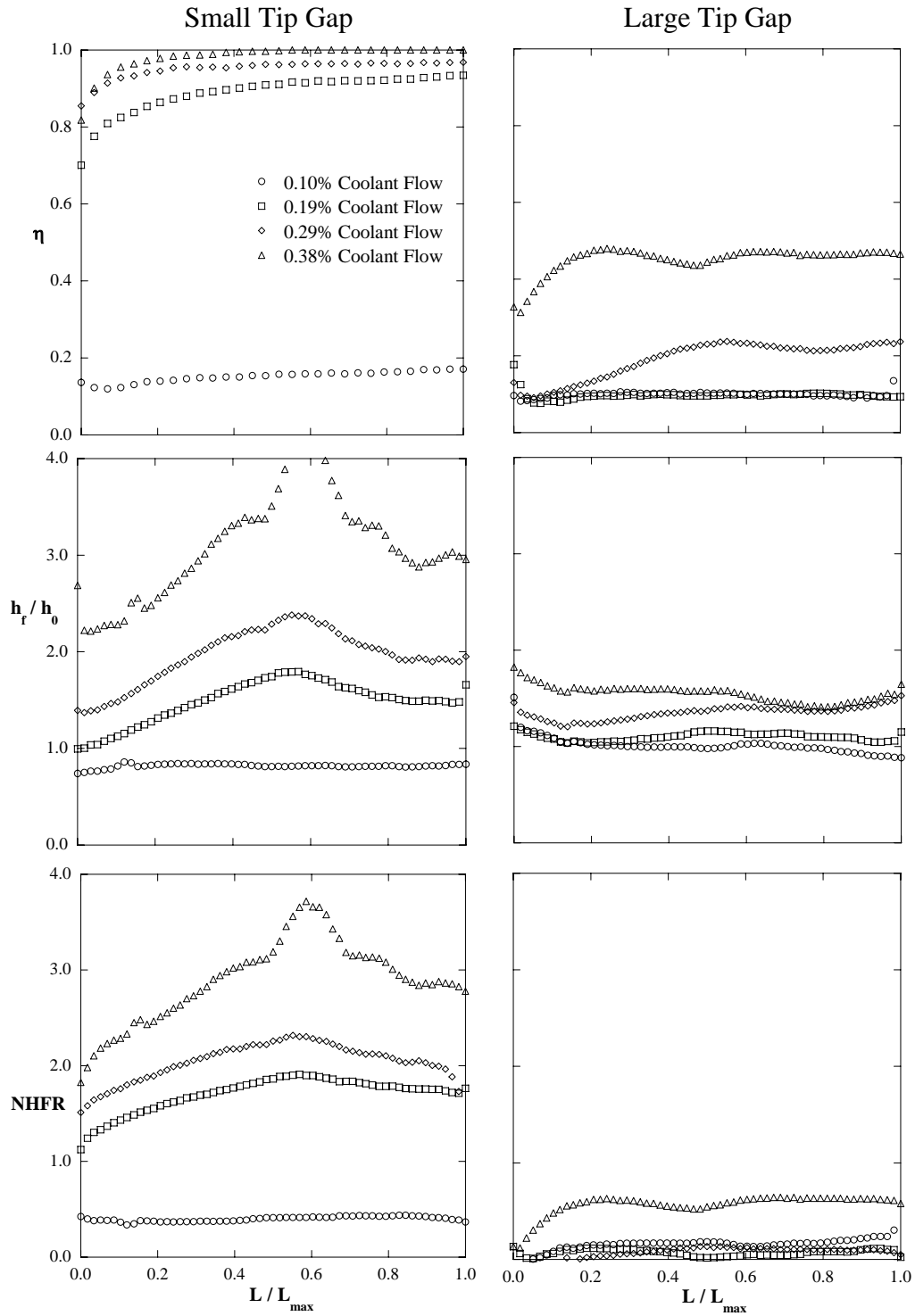


Figure C.6 Adiabatic effectiveness, heat transfer augmentation, and NHFR at line position 1 for the small (left) and large (right) tip gaps.

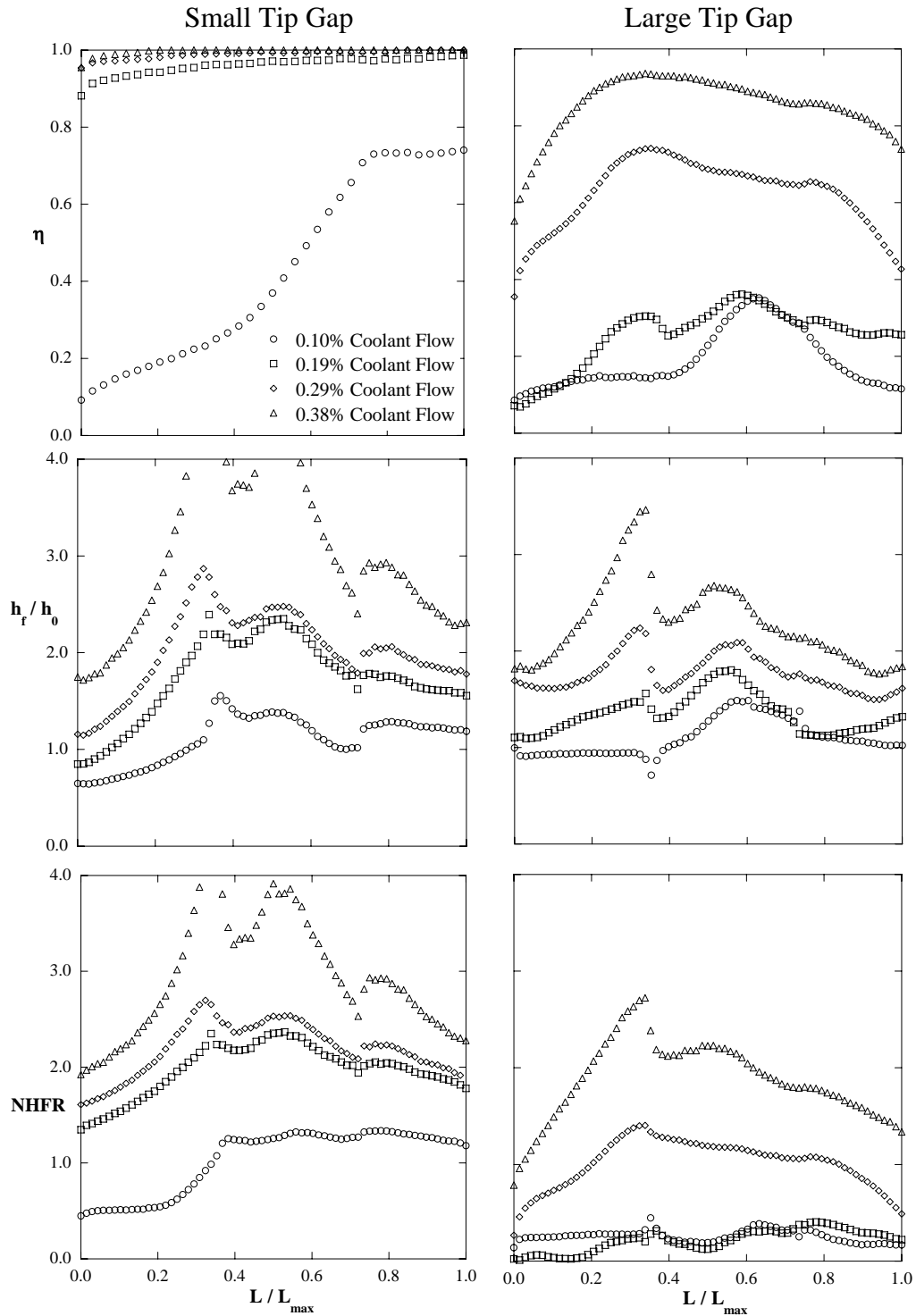


Figure C.7 Adiabatic effectiveness, heat transfer augmentation, and NHFR at line position 2 for the small (left) and large (right) tip gaps.

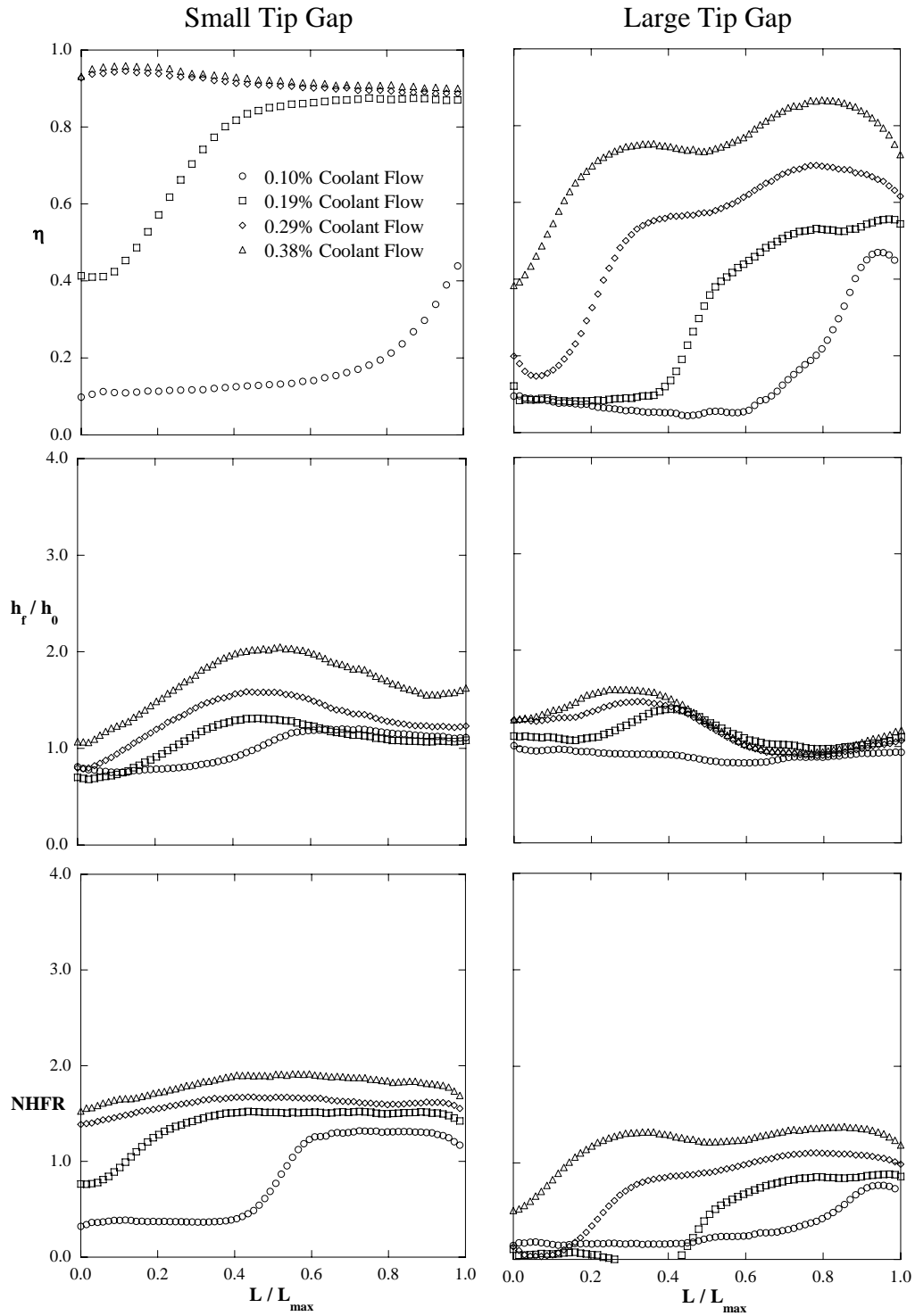


Figure C.8 Adiabatic effectiveness, heat transfer augmentation, and NHFR at line position 3 for the small (left) and large (right) tip gaps.

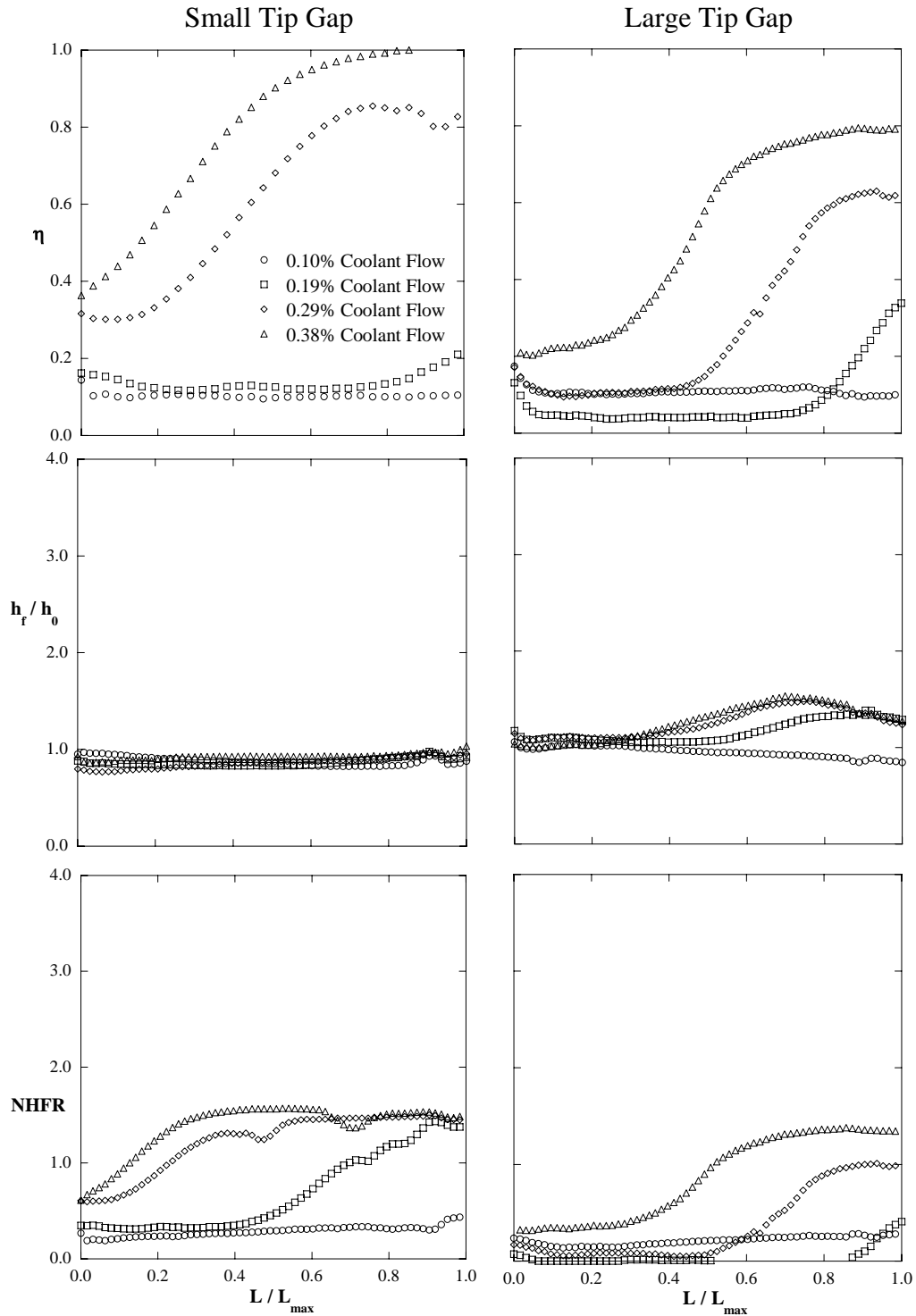


Figure C.9 Adiabatic effectiveness, heat transfer augmentation, and NHFR at line position 4 for the small (left) and large (right) tip gaps.

Appendix D: Additional Analysis for EDM and Laser Hole Shapes

D.1 Discussion of Additional Data

Additional analysis for the EDM and laser holes is presented in this appendix to further the assertions made in the papers. Contours of heat transfer augmentation on the blade tip for both geometries are shown in Figure D.1. These results show the differences in the heat transfer augmentation from the two geometries, which have been discussed in detail in the papers.

Figure D.2 shows the Nusselt number based on hydraulic diameter normalized by the fully developed correlation discussed in the paper. These ratios are shown at the three line positions described in the paper. The baseline values are shown for comparison purposes. Generally, both the EDM and laser geometries cause increased heat transfer relative to the baseline case in the entry region.

Data taken along the pressure-side of the tip is also shown in this appendix for both geometries and tip gaps at coolant flow rates of 0.58% and 1.0%. The adiabatic effectiveness results are shown in Figure D.3. For the EDM cases, the 1.0% coolant flow shows higher effectiveness values in the region between $0 < x/C < 0.3$, which is the region affected by the dirt purge blowing. Downstream of this region, both the large and small tip gaps show slightly increased effectiveness for the increased coolant flow. The laser cases also show significantly higher effectiveness values in the dirt purge affected region for higher cooling. Downstream of this region, the large tip gap shows higher values for the lower coolant flow whereas the opposite is true at the small tip gap.

The heat transfer along the pressure-side line is shown in Figure D.4. For both geometries and both gap heights, the heat transfer increases with blowing. NHFR along the pressure-side line is shown in Figure D.5. For the EDM holes, the NHFR tends to increase with blowing, especially at the large tip gap. For the laser holes, however, the large tip gap shows decreasing NHFR along the pressure-side line for increased coolant flow, whereas the small tip gap shows increased NHFR for increased blowing.

D.2 Nomenclature

h_f = film heat transfer coefficient

h_0 = baseline heat transfer coefficient

NHFR = net heat flux reduction

Nu = Nusselt number based on the hydraulic diameter of the tip gap

Nu_{fd} = fully developed Nusselt number correlation

Greek

η = adiabatic effectiveness

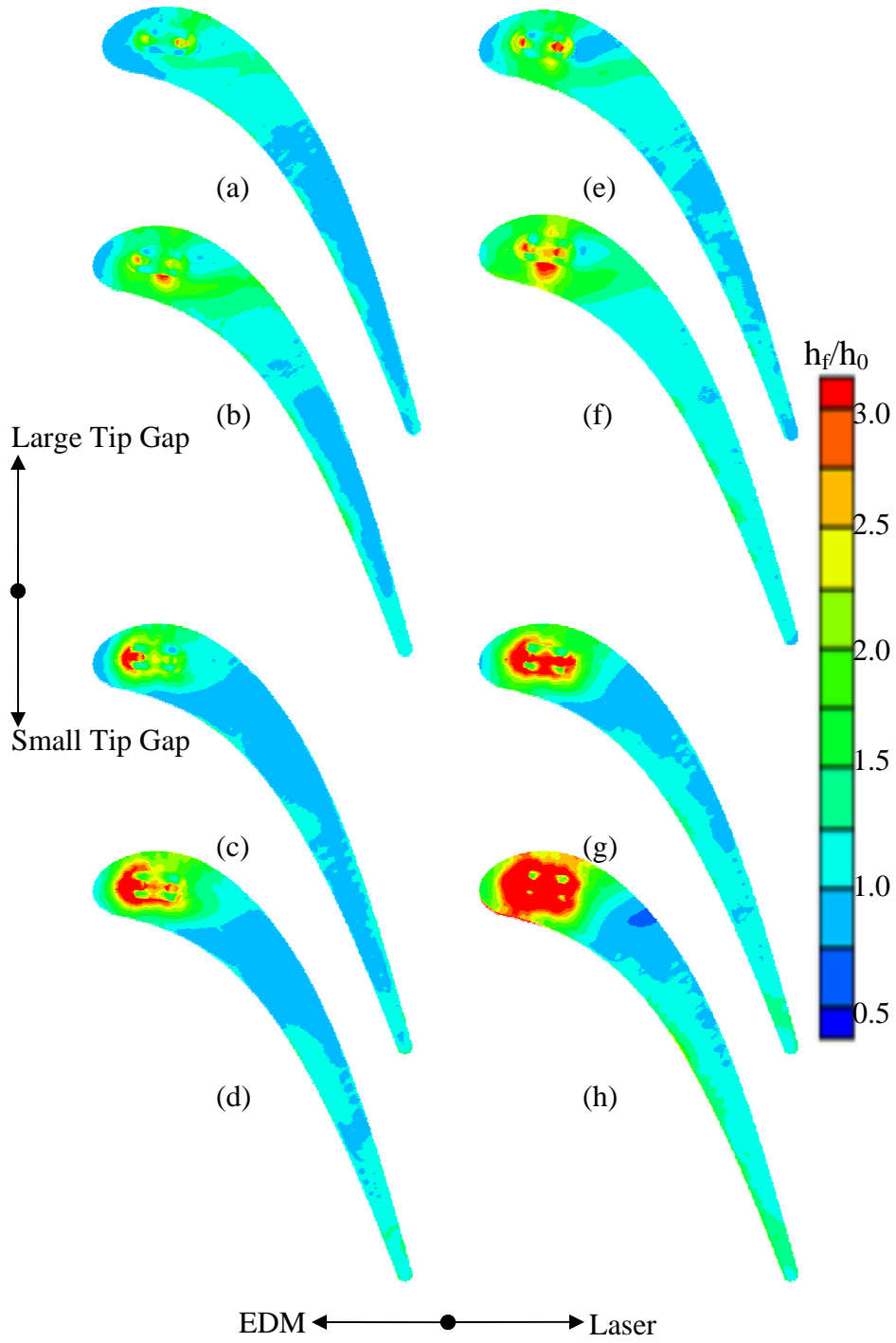


Figure D.1 Heat transfer augmentation contours for the EDM and laser holes at both tip gaps and blowing ratios tested.

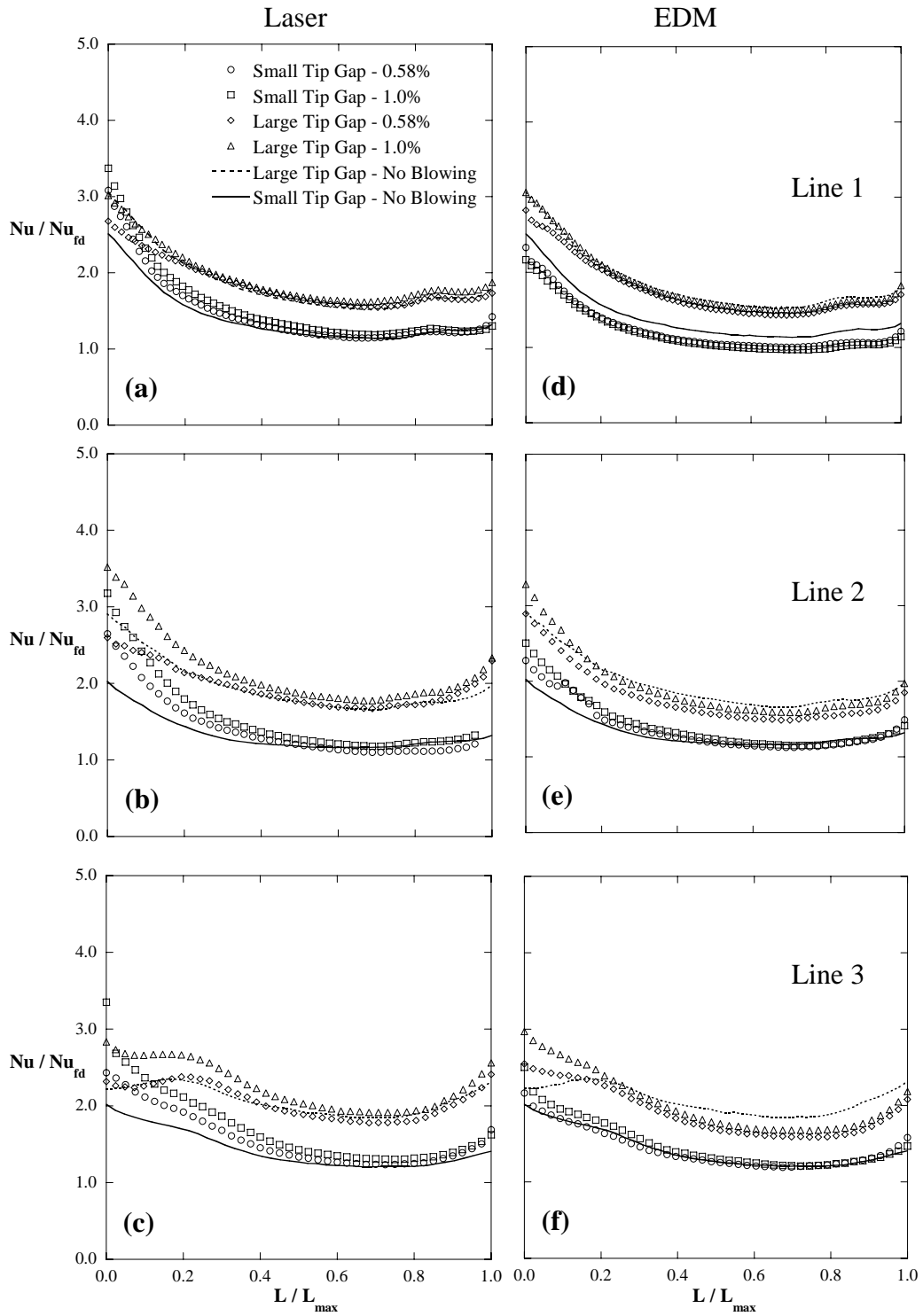


Figure D.2 Nu/Nu_0 for path lines 2, 3, and 4 as described in the third paper.

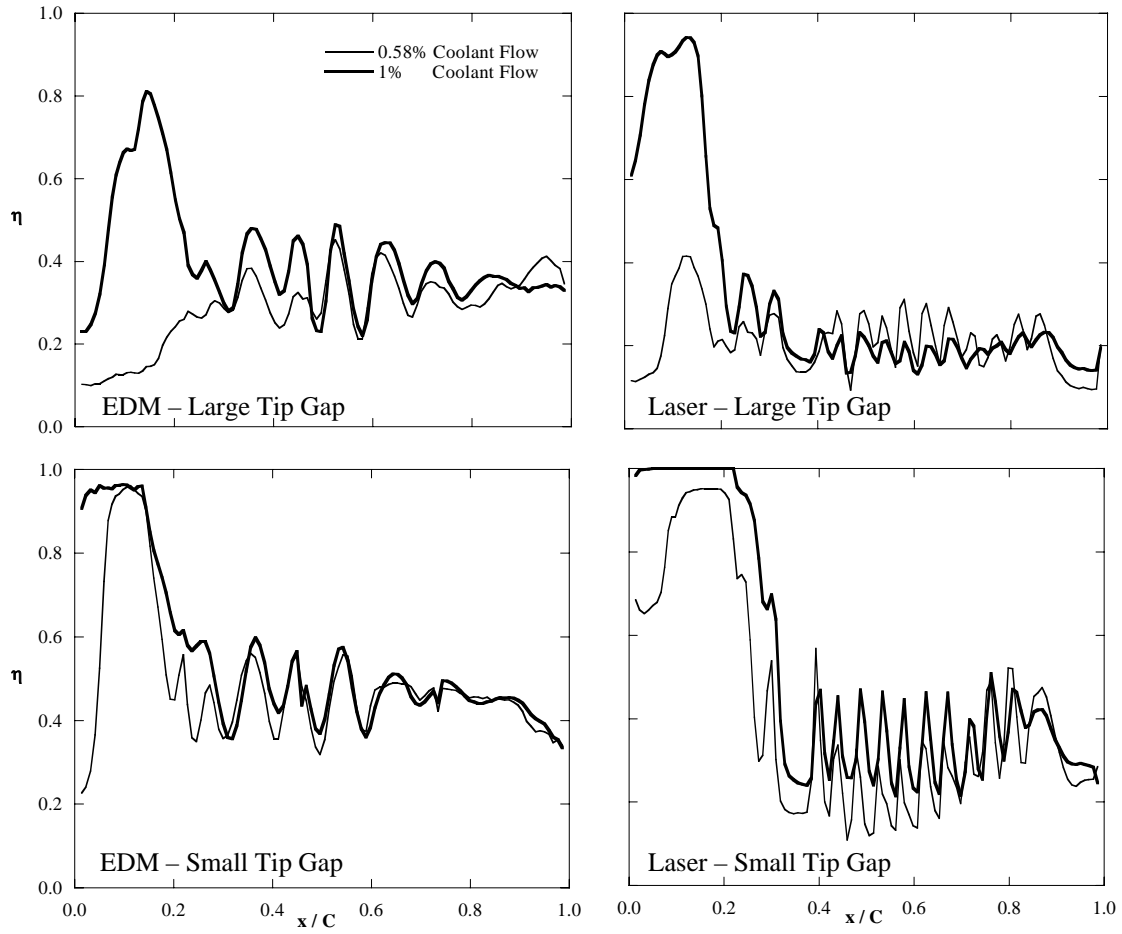


Figure D.3 Adiabatic effectiveness along the pressure-side line for the EDM and laser holes at both tip gaps and blowing ratios tested.

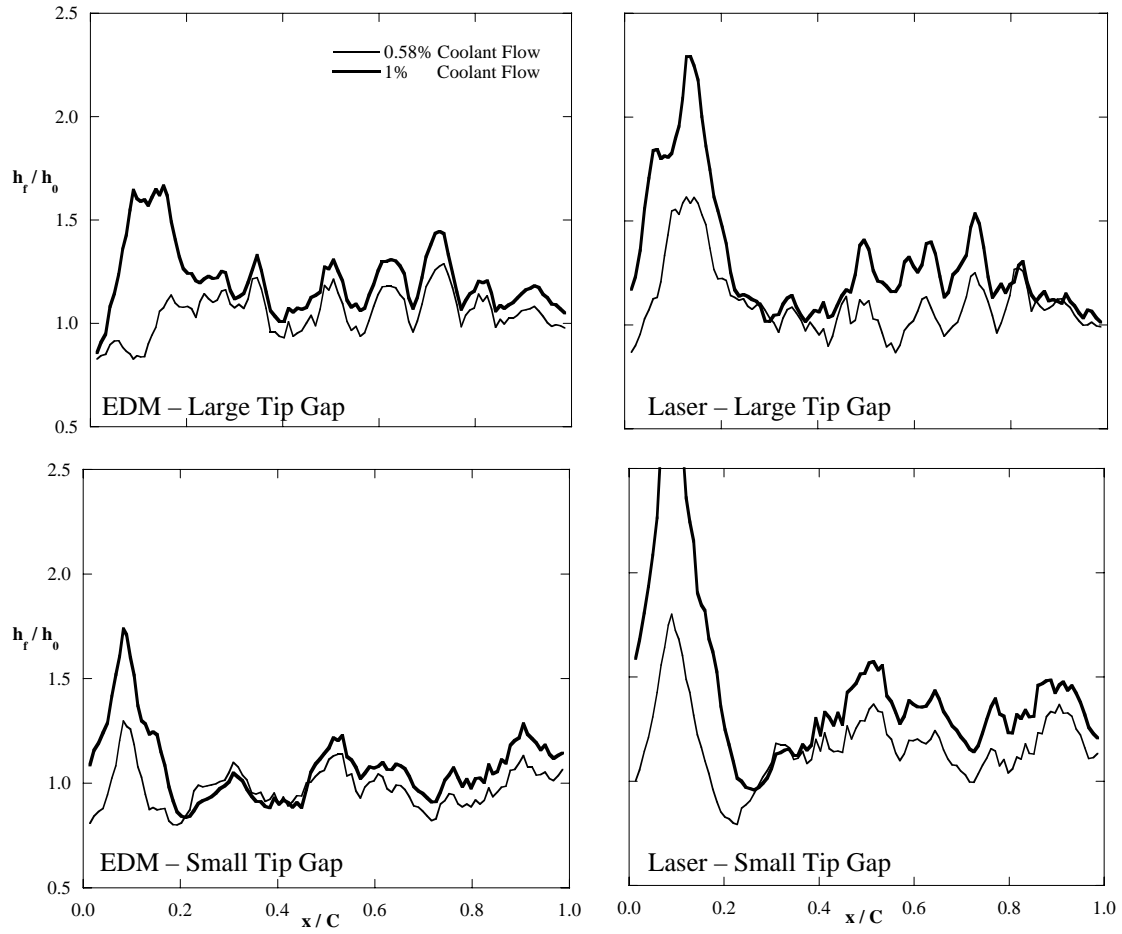


Figure D.4 Heat transfer augmentation along the pressure-side line for the EDM and laser holes at both tip gaps and blowing ratios tested.

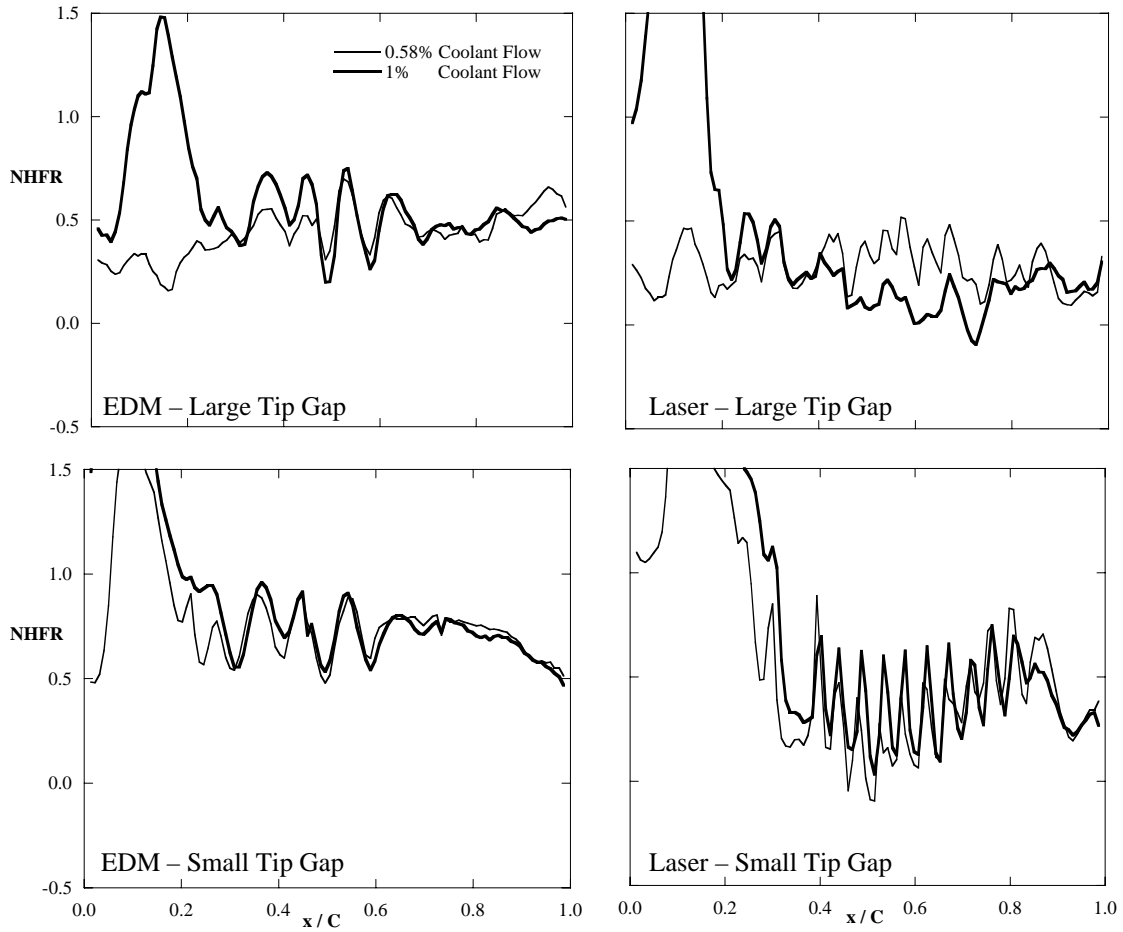


Figure D.5 NHFR along the pressure-side line for the EDM and laser holes at both tip gaps and blowing ratios tested.

Appendix E:

Additional Analysis for Microcircuit Results

Additional analysis to support the assertions made in the microcircuit paper are given in this appendix. Generally, this will focus on the external tip heat transfer and internal convective effectiveness results because further analysis has already been performed on the adiabatic effectiveness and cooling effectiveness by Couch [1].

E.1 Discussion of Additional Data

Contour plots of heat transfer augmentation along the blade tip are shown in Figure E.1. These results show increasing heat transfer, especially in the dirt purge region, as coolant flow is increased. Also, the small tip gap has higher heat transfer augmentation than the large tip gap.

Data taken along the pressure-side line of the blade tip is presented in Figures E.2 and E.3 for the small and large tip gap, respectively. These figures show that at the small tip gap, there is relatively little difference in effectiveness levels with increased coolant. At the large tip gap, however, the results generally show increasing effectiveness levels for increased coolant.

The cooling effectiveness results along the pressure-side line are shown in Figures E.4 and E.5 for the small and large tip gap, respectively. The small tip gap shows increasing effectiveness levels for increased coolant. For the large tip gap, increased effectiveness levels are shown between $0 < x/C < 0.3$ and $0.7 < x/C < 1$ for increased coolant. However, for the mid-chord region, the lowest coolant flow shows equally effective values when compared to the higher coolant cases.

Heat transfer augmentation along the pressure-side line is shown in Figures E.6 and E.7 for the small and large tip gap, respectively. Both gap heights show increased heat transfer with increased coolant flow, especially in the dirt purge region ($0 < x/C < 0.3$).

NHFR values along the pressure-side line are shown in Figures E.8 and E.9 for the small and large tip gap, respectively. For the small tip gap, the NHFR is generally

higher at the 0.5% coolant flow case, and the higher flow cases show little difference. For the large tip gap, the NHFR appears to increase with increasing coolant flow.

Figures E.10 – E.13 show comparisons along the blade pressure-side line between the adiabatic effectiveness and heat transfer augmentation for each of the blowing ratios at the large tip gap. Figures E.14 – E.17 show these same comparisons along the camber line of the blade. One of these cases was pointed out in the paper to show the difference between the location of the peak adiabatic effectiveness and peak heat transfer augmentation. All cases are shown here for the large tip gap to show how the film-cooling and heat transfer are related at each of the blowing ratios and how the difference in peak locations is magnified at the pressure-side location.

A complete list of the internal convective effectiveness values for each of the cases tested is given in Table E.1. Also, the geometric properties for each of the channels are given in Table E.2.

E.2 Nomenclature

A_c	= cross-sectional area of microcircuit passage
C	= true blade chord
D_h	= hydraulic diameter of microcircuit passage
h_f	= film heat transfer coefficient
h_0	= baseline heat transfer coefficient
L	= length of microcircuit passage
NHFR	= net heat flux reduction
x	= distance along blade chord

Greek

η	= adiabatic effectiveness
ϕ	= cooling effectiveness
η_c	= convective effectiveness

E.3 References

- [1] Couch, E., *Measurements of Cooling Effectiveness Along the Tip of a Turbine Blade*, Master's Thesis, Virginia Polytechnic Institute and State University, Blacksburg, VA, 2003

Table E.1 Microcircuit Channel Convective Effectiveness Values

	Large Tip Gap					Small Tip Gap				
	0.5%	1.0%	1.5%	2.0%		0.5%	1.0%	1.5%	2.0%	0.5% repeat
MC 1	0.85	0.9	1	1		0.65	1	1	1	0.7
MC 2	0.65	0.4	0.4	0.55		0.5	1	1	1	0.55
MC 3	0.35	0.25	0.2	0.05		0.3	0.95	0.95	0.85	0.35
MC 4	0.3	0.1	0.15	0		0.3	0.95	0.9	0.85	0.35
MC 5	0.2	0.1	0.15	0		0.25	0.9	0.85	0.8	0.25
MC 6	0.25	0.05	0	0		0.2	0.5	0.5	1	0.25
MC 7	0.3	0.2	0.05	0		0.3	0.2	0.05	0.9	0.3
MC 8	0.3	0.15	0	0		0.25	0.2	0	0	0.25
MC 9	0.3	0.2	0	0		0.25	0.25	0	0	0.25
MC 10	0.35	0.2	0.15	0		0.3	0.25	0.2	0	0.3
MC 11	0.35	0.2	0.15	0		0.3	0.25	0.05	0	0.35
MC 12	0.3	0.15	0	0		0.3	0.25	0.05	0	0.3
MC 13	0.3	0.25	0.15	0		0.3	0.25	0.2	0	0.3
MC 14	0.3	0.25	0.15	0		0.35	0.3	0.25	0	0.3
MC 15	0.6	0.4	0.35	0.25		0.45	0.45	0.45	0.3	0.5
MC 16	0.35	0.25	0.20	0.05		0.35	0.3	0.25	0.15	0.4

Table E.2 Geometric Properties of Microcircuit Channels

	L (m)	D _h (m)	A _c (cm ²)
MC 1	0.080	8.65E-03	0.98
MC 2	0.085	8.65E-03	1.00
MC 3	0.090	8.65E-03	0.98
MC 4	0.100	8.65E-03	0.98
MC 5	0.110	8.65E-03	0.98
MC 6	0.105	8.00E-03	0.65
MC 7	0.090	8.00E-03	0.65
MC 8	0.110	8.00E-03	0.65
MC 9	0.110	8.00E-03	0.65
MC 10	0.100	8.00E-03	0.65
MC 11	0.100	8.00E-03	0.65
MC 12	0.100	8.00E-03	0.65
MC 13	0.090	8.00E-03	0.65
MC 14	0.090	8.00E-03	0.65
MC 15	0.090	8.00E-03	0.65
MC 16	0.130	8.65E-03	0.95

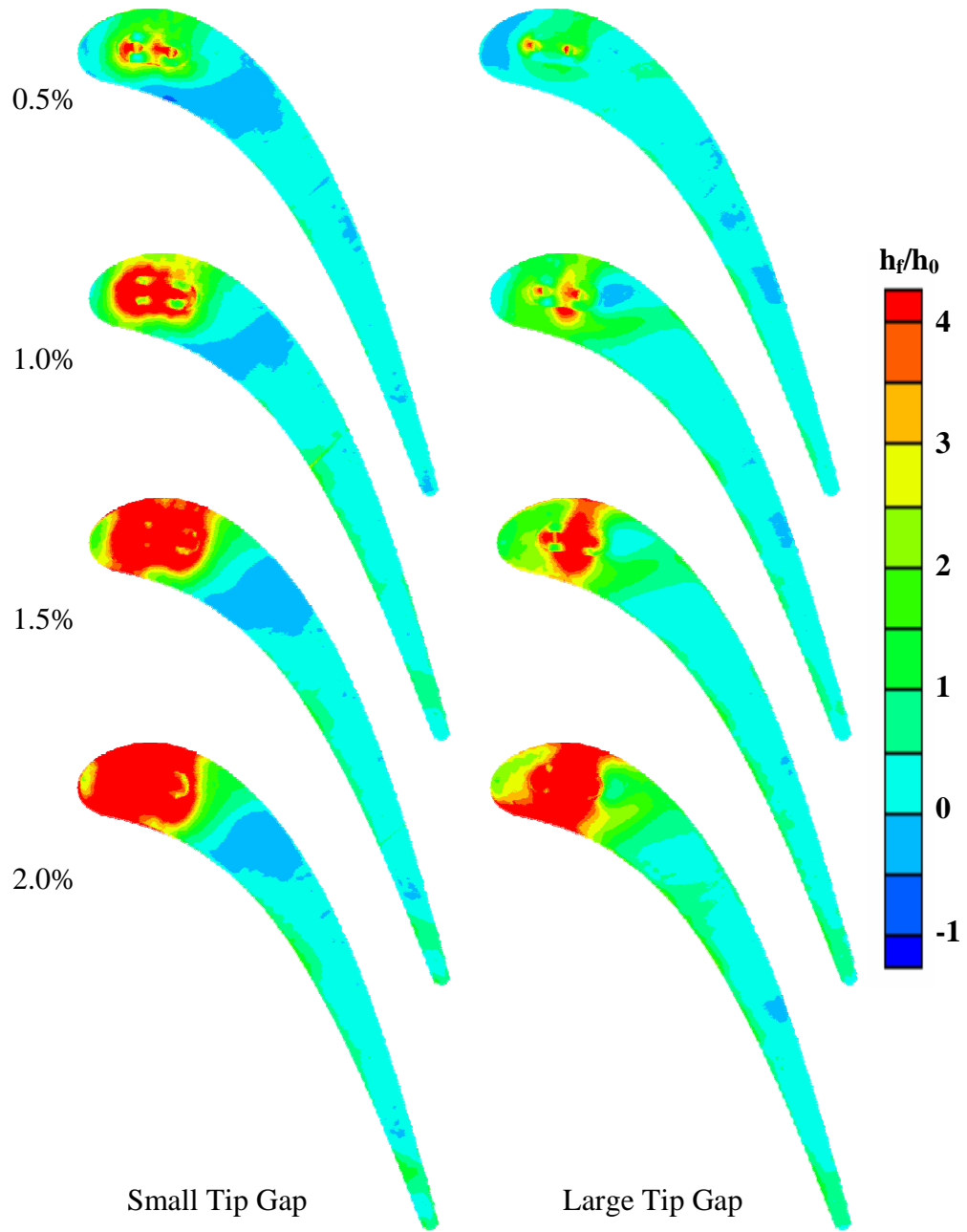


Figure E.1 Contours of heat transfer augmentation for all microcircuit cases at the small tip gap (left) and large tip gap (right).

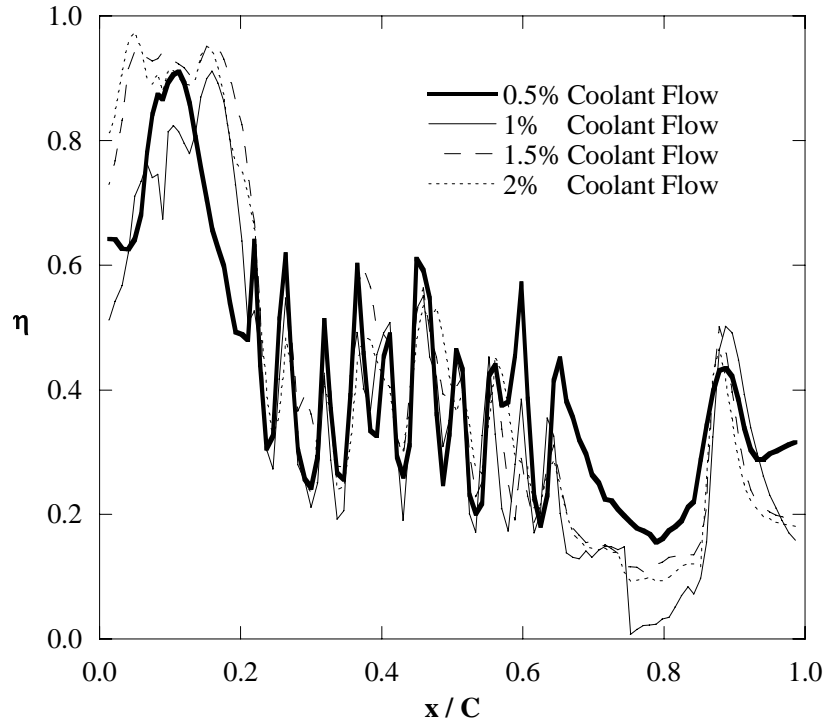


Figure E.2 Adiabatic effectiveness (η) data taken along the pressure-side line for the microcircuit small tip gap tests at all blowing ratios.

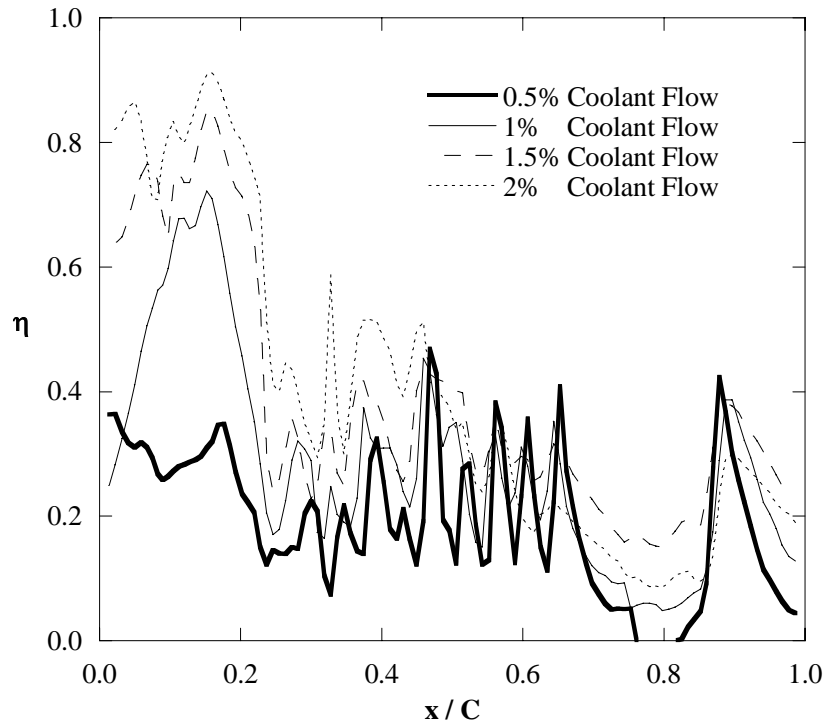


Figure E.3 Adiabatic effectiveness (η) data taken along the pressure-side line for the microcircuit large tip gap tests at all blowing ratios.

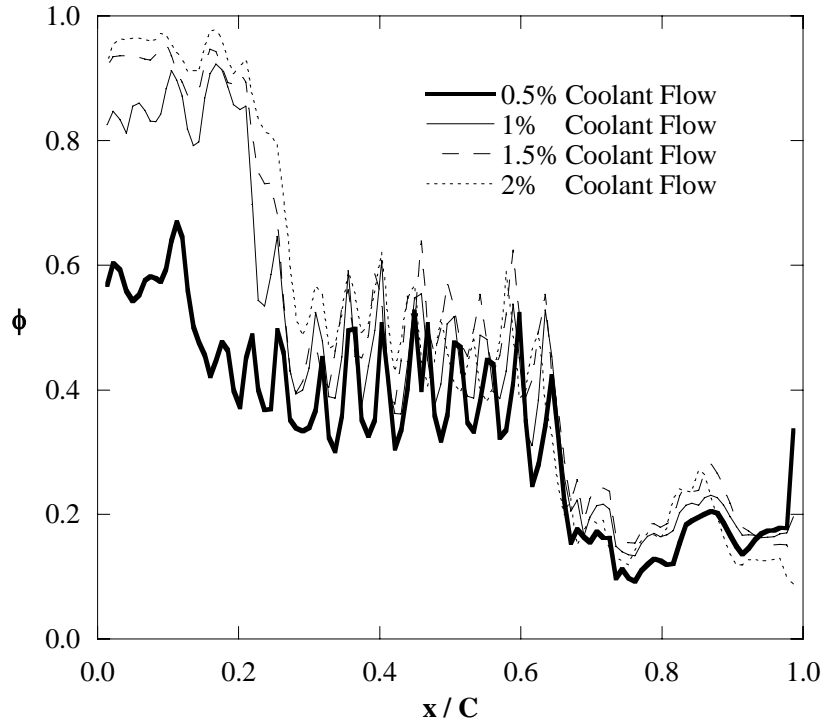


Figure E.4 Cooling effectiveness (ϕ) data taken along the pressure-side line for the microcircuit small tip gap tests at all blowing ratios.

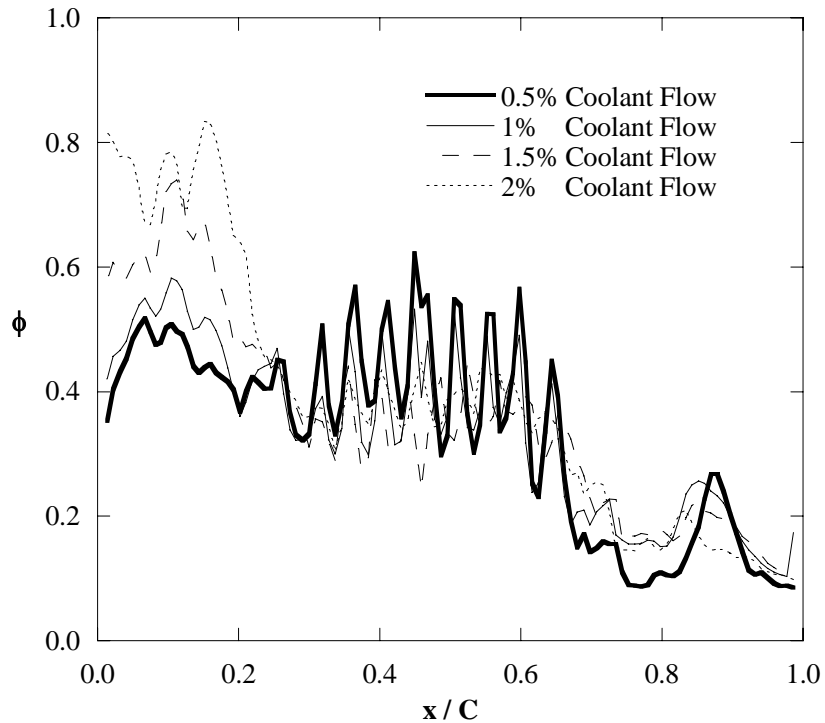


Figure E.5 Cooling effectiveness (ϕ) data taken along the pressure-side line for the microcircuit large tip gap tests at all blowing ratios.

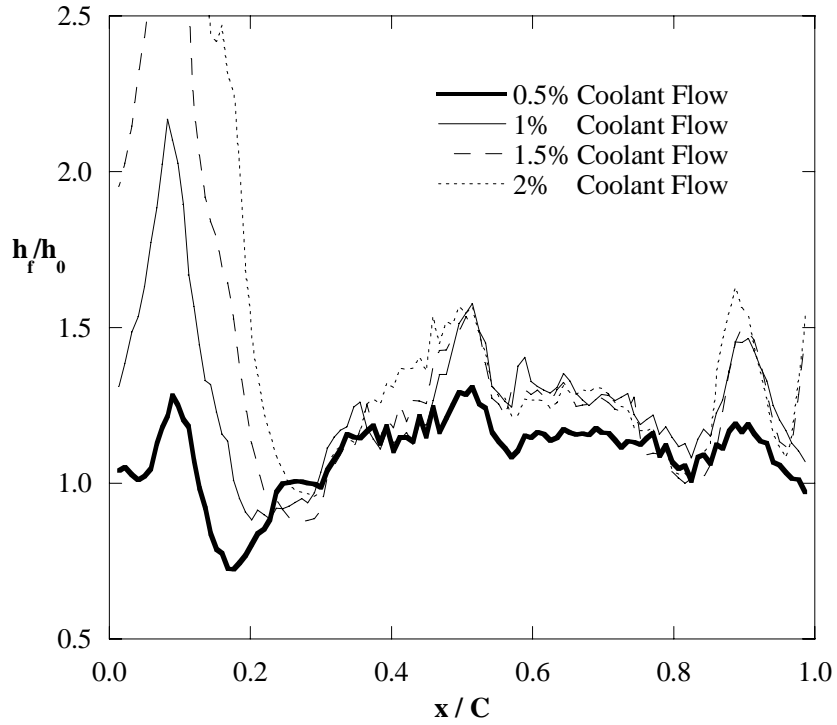


Figure E.6 Heat transfer (h_f/h_0) data taken along the pressure-side line for the microcircuit small tip gap tests at all blowing ratios.

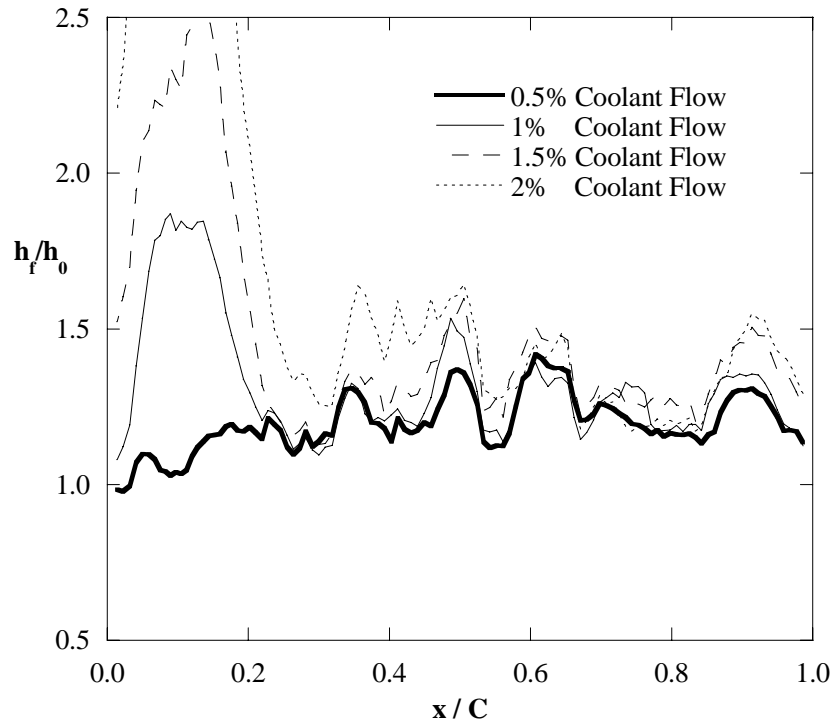


Figure E.7 Heat transfer (h_f/h_0) data taken along the pressure-side line for the microcircuit large tip gap tests at all blowing ratios.

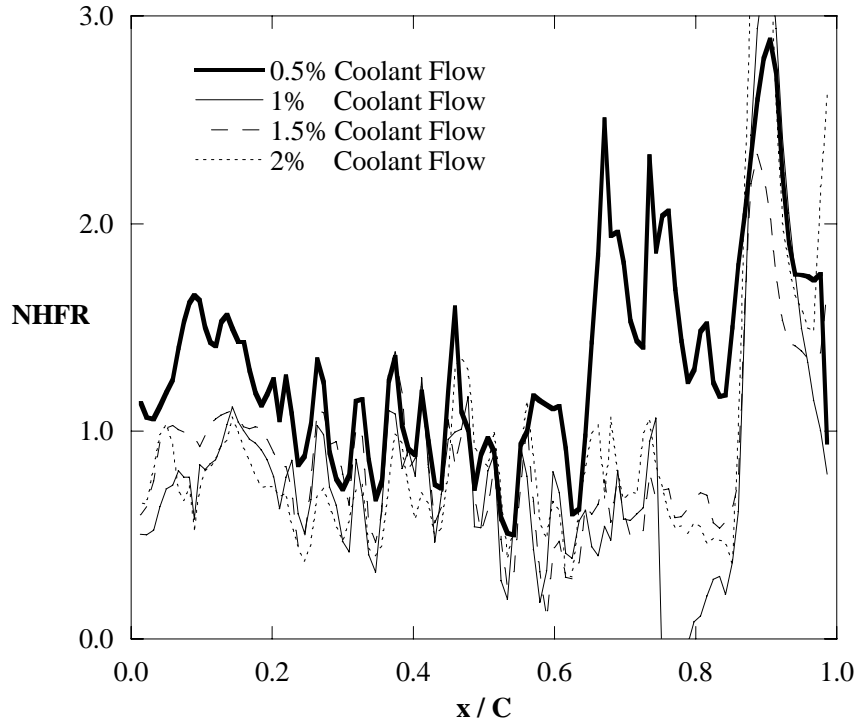


Figure E.8 NHFR data taken along the pressure-side line for the microcircuit small tip gap tests at all blowing ratios.

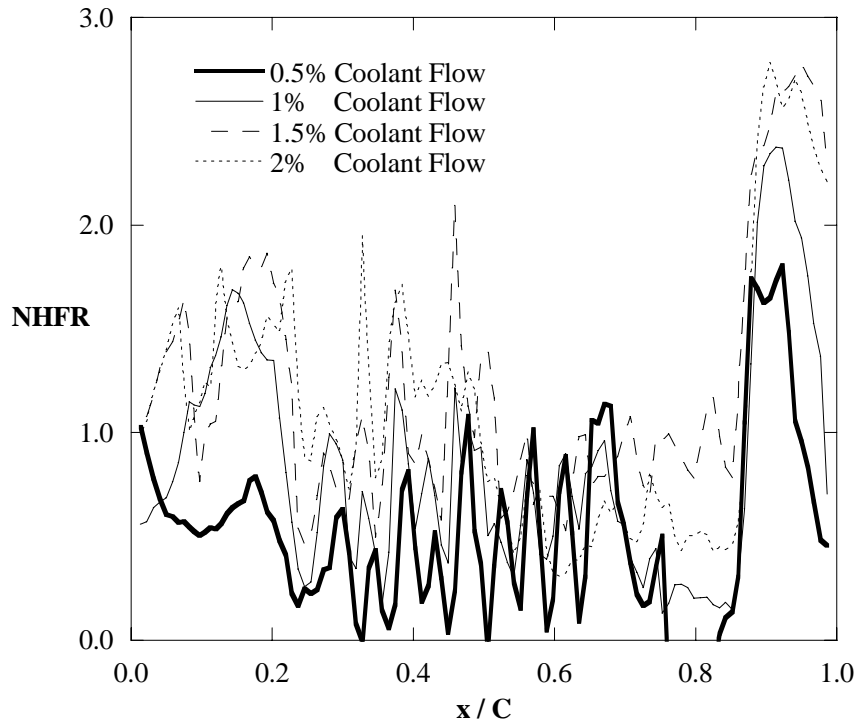


Figure E.9 NHFR data taken along the pressure-side line for the microcircuit large tip gap tests at all blowing ratios.

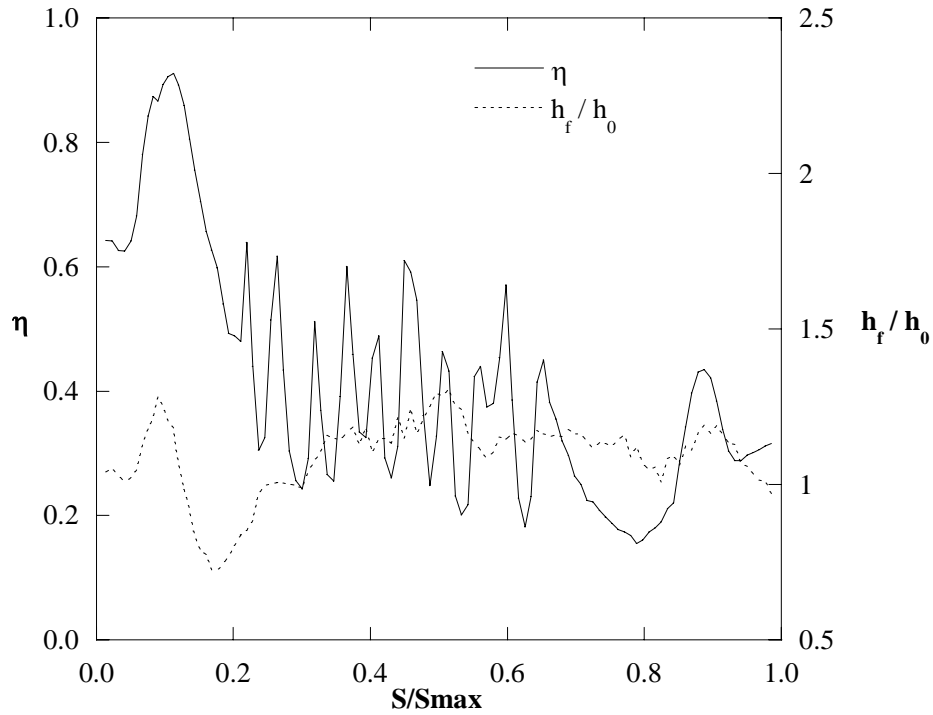


Figure E.10 Comparison of adiabatic effectiveness and heat transfer augmentation for the 0.5% coolant flow taken along the pressure-side line.

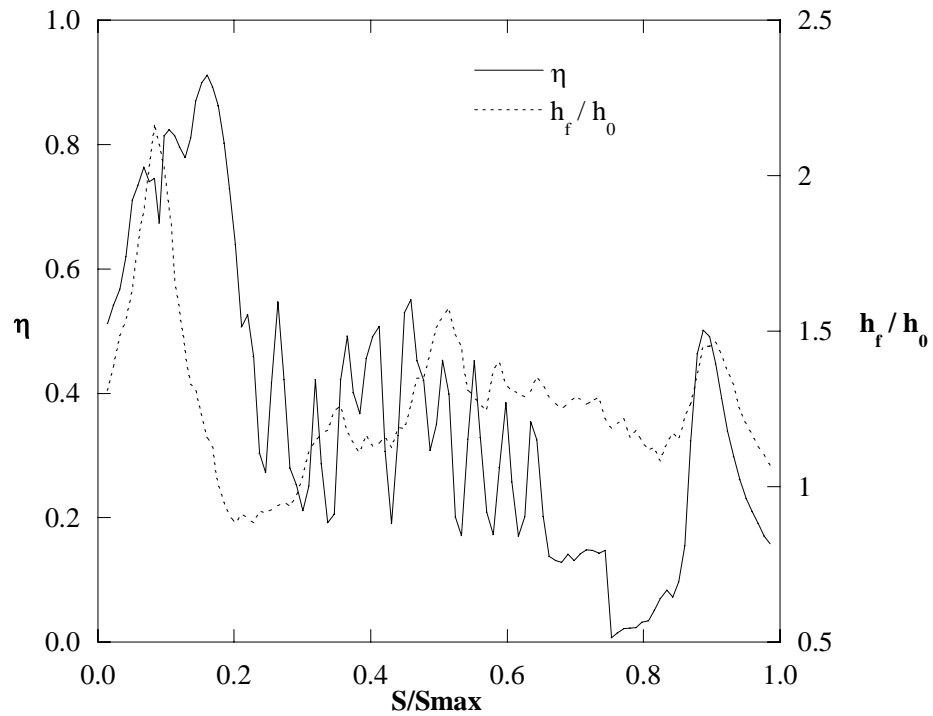


Figure E.11 Comparison of adiabatic effectiveness and heat transfer augmentation for the 1.0% coolant flow taken along the pressure-side line.

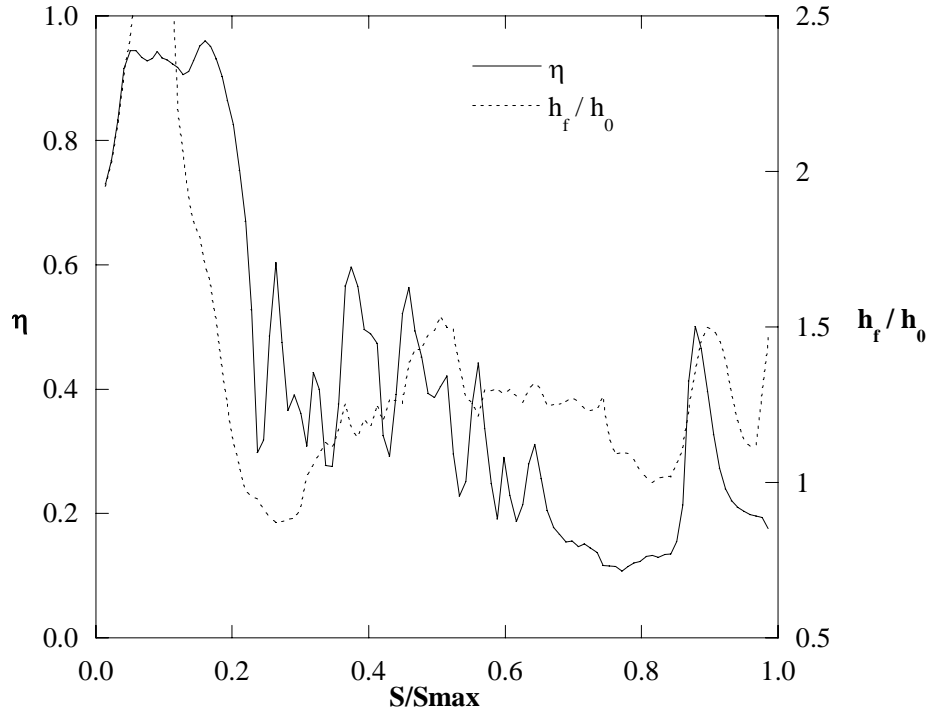


Figure E.12 Comparison of adiabatic effectiveness and heat transfer augmentation for the 1.5% coolant flow taken along the pressure-side line.

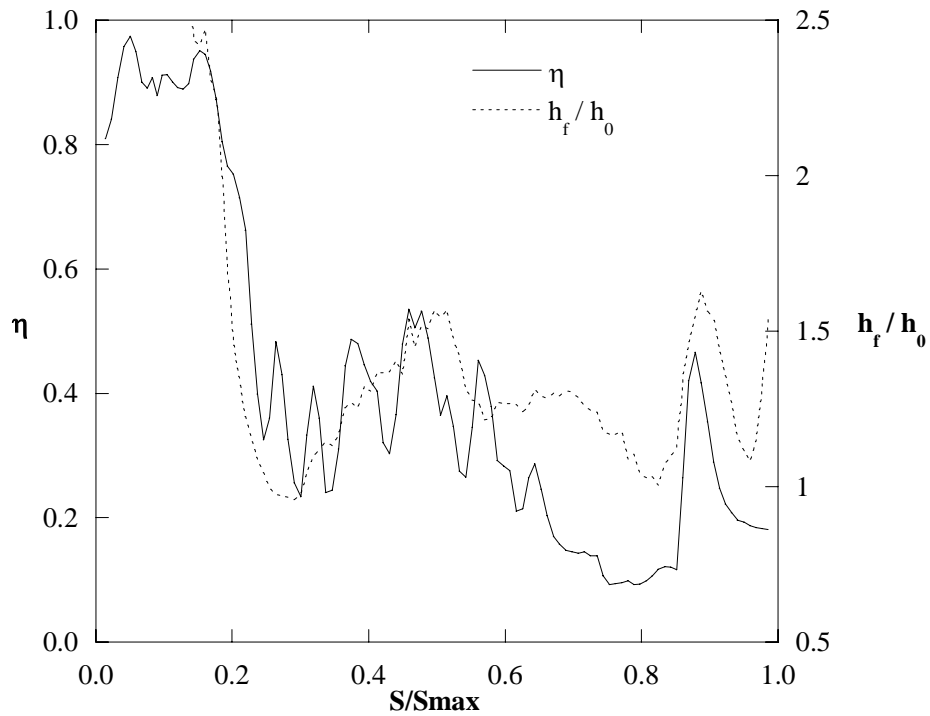


Figure E.13 Comparison of adiabatic effectiveness and heat transfer augmentation for the 2.0% coolant flow taken along the pressure-side line.

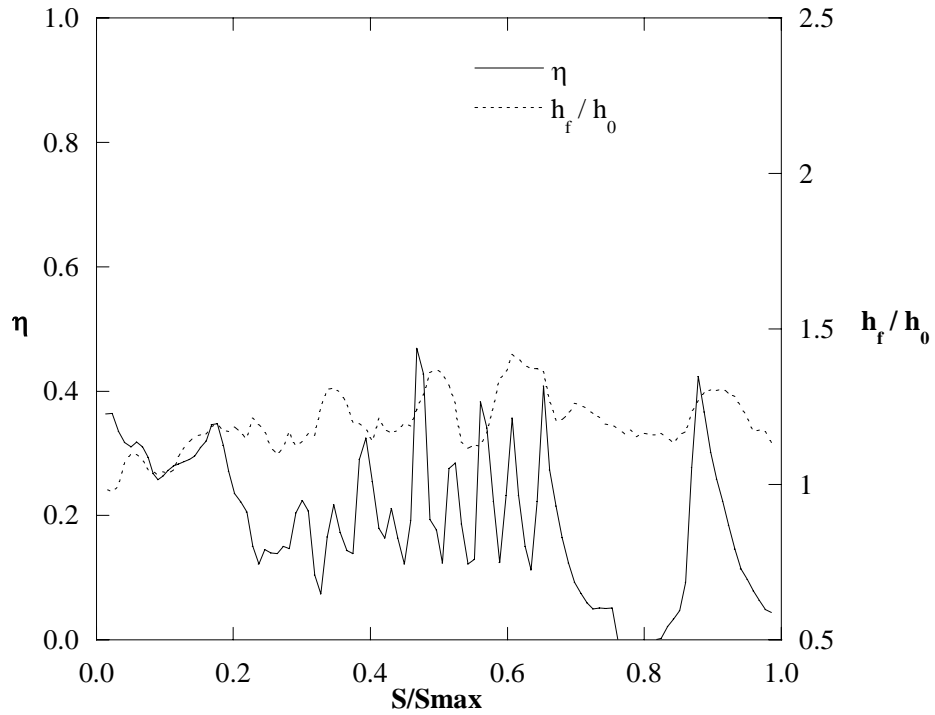


Figure E.14 Comparison of adiabatic effectiveness and heat transfer augmentation for the 0.5% coolant flow taken along the blade camber line.

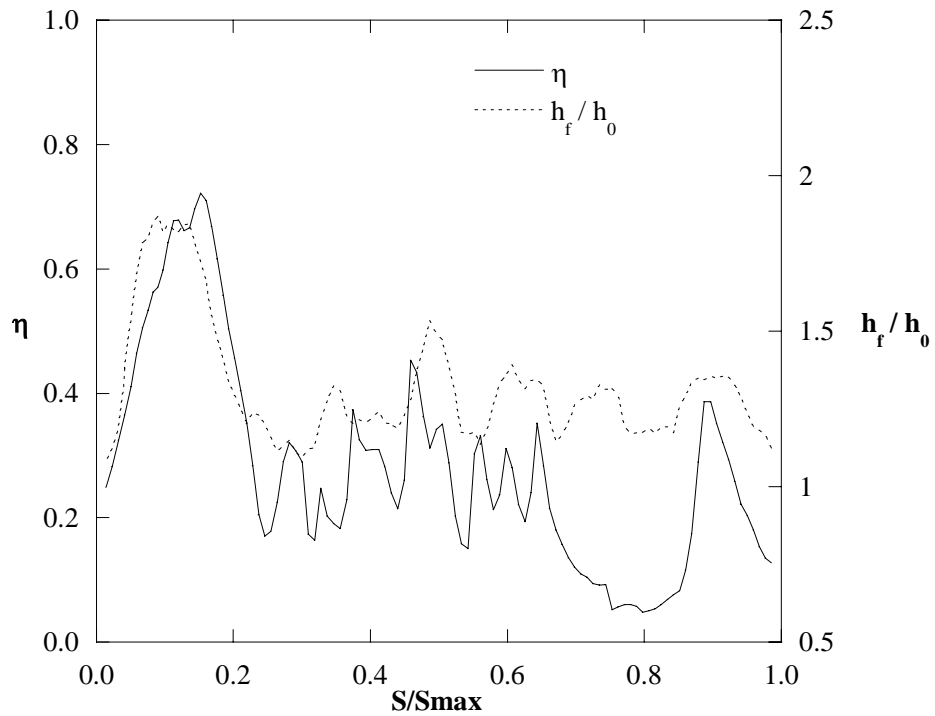


Figure E.15 Comparison of adiabatic effectiveness and heat transfer augmentation for the 1.0% coolant flow taken along the blade camber line.

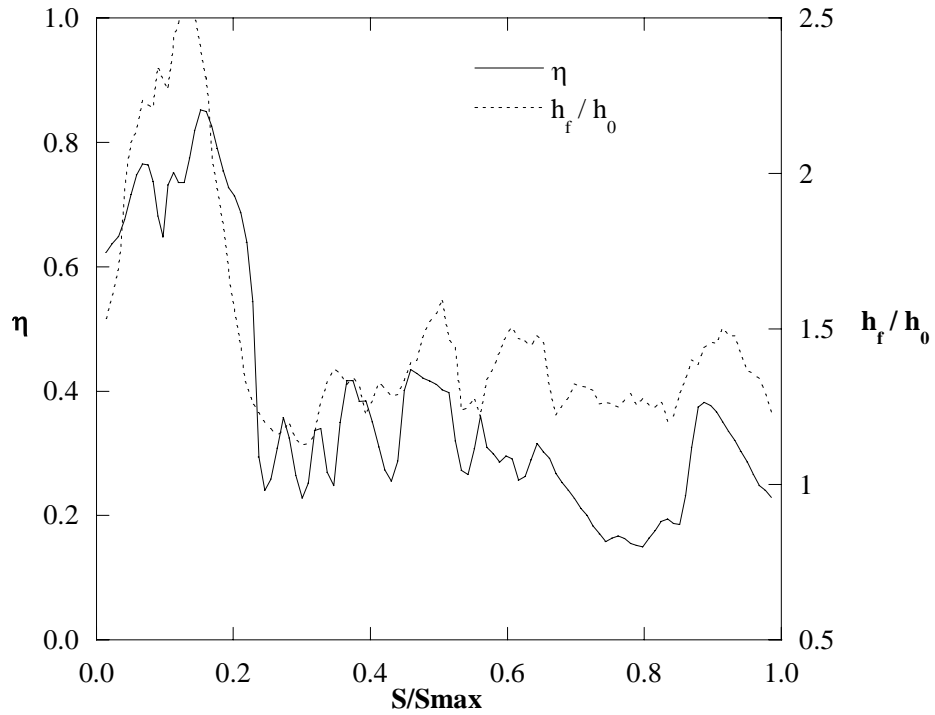


Figure E.16 Comparison of adiabatic effectiveness and heat transfer augmentation for the 1.5% coolant flow taken along the blade camber line.

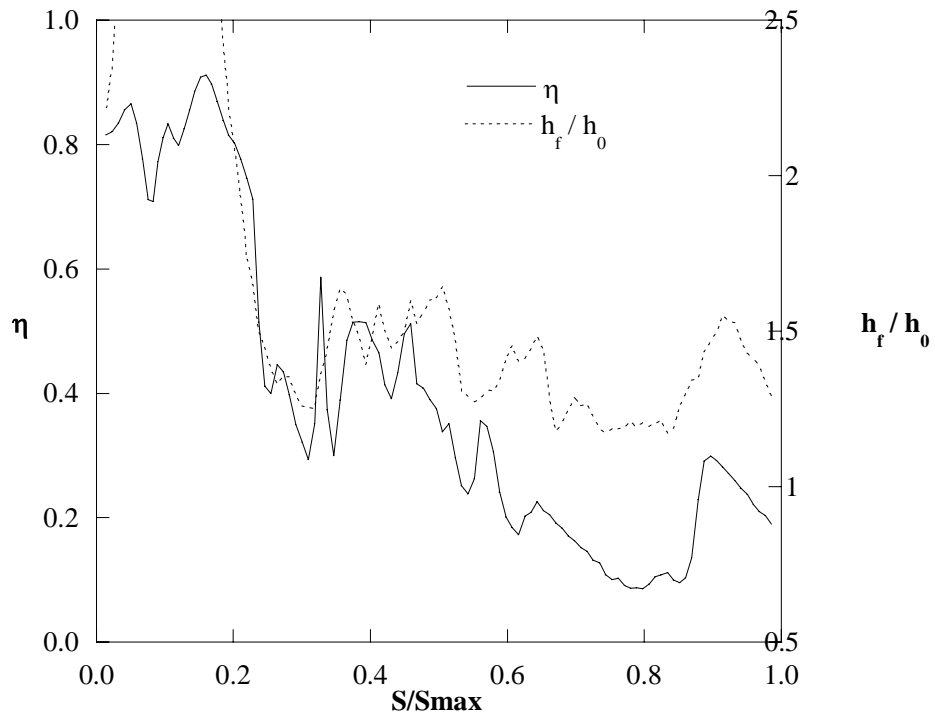


Figure E.17 Comparison of adiabatic effectiveness and heat transfer augmentation for the 2.0% coolant flow taken along the blade camber line.

Appendix F:

Comparison between EDM, Laser, and Microcircuit Designs

A comparison between the tip results due to blowing from the EDM, laser, and microcircuit film holes is presented in this appendix for a total coolant flow rate of 1.0%. While the microcircuit uses internal convection cooling as well as external film-cooling, this will serve as a direct comparison of only the film-cooling results between the geometries.

F.1 Discussion of Comparison

Figure F.1 shows the contour plots of adiabatic effectiveness, heat transfer augmentation, and NHFR for the small tip gap with 1.0% total coolant flow. These figures show that EDM holes appear to have the highest adiabatic effectiveness levels as well as the lowest heat transfer augmentation, which results in the best NHFR. Figure F.2 shows the contour plots of adiabatic effectiveness, heat transfer augmentation, and NHFR for the large tip gap with 1.0% total coolant flow. The results at the large tip gap also show that the EDM has higher effectiveness values and lower heat transfer augmentation, however the microcircuit holes appear to give the highest NHFR.

To quantify these comparisons, data has been taken along both the camber line and pressure-side line of the blade tip. Figure F.3 and Figure F.4 show the adiabatic effectiveness for each of the geometries for the small and large tip gap, respectively. Figure F.5 and Figure F.6 show the heat transfer augmentation for each of the geometries for the small and large tip gap, respectively. Figure F.7 and Figure F.8 show the NHFR for each of the geometries for the small and large tip gap, respectively. All of these plots are taken from the camber line and verify the trends seen in the contour plots.

Comparisons at the pressure-side line are shown in Figure F.9 and Figure F.10 for the adiabatic effectiveness for the small and large tip gap, respectively. Figure F.11 and Figure F.12 show the heat transfer augmentation for the small and large tip gap, respectively. Figure F.13 and Figure F.14 show the NHFR for the small and large tip gap, respectively.

Area-averaged results for the adiabatic effectiveness are shown in Figure F.15 for each of the geometries over the entire tip area (Figure F.15a) and for the last 70% of the blade (Figure F.15b). The second area-average was taken so that only results from film-hole blowing would be considered. Area-averaged results for the heat transfer augmentation are shown for all geometries over the entire tip surface in Figure F.16a and over the last 70% in Figure F.16b. Area-averaged results of NHFR for all geometries are shown for the entire tip area in Figure F.17a and for the last 70% in Figure F.17b. The microcircuit results of the cooling effectiveness are also shown averaged over the entire tip area in Figure F.18a and over the last 70% in Figure F.18b.

F.2 Nomenclature

C = true blade chord
NHFR = net heat flux reduction
 h_f = film heat transfer coefficient
 h_0 = baseline heat transfer coefficient
 x = distance along blade chord

Greek

η = adiabatic effectiveness
 ϕ = cooling effectiveness

Superscripts

 = denotes area-averaged value

F.3 References

- [1] Couch, E., *Measurements of Cooling Effectiveness Along the Tip of a Turbine Blade*, Master's Thesis, Virginia Polytechnic Institute and State University, Blacksburg, VA, 2003

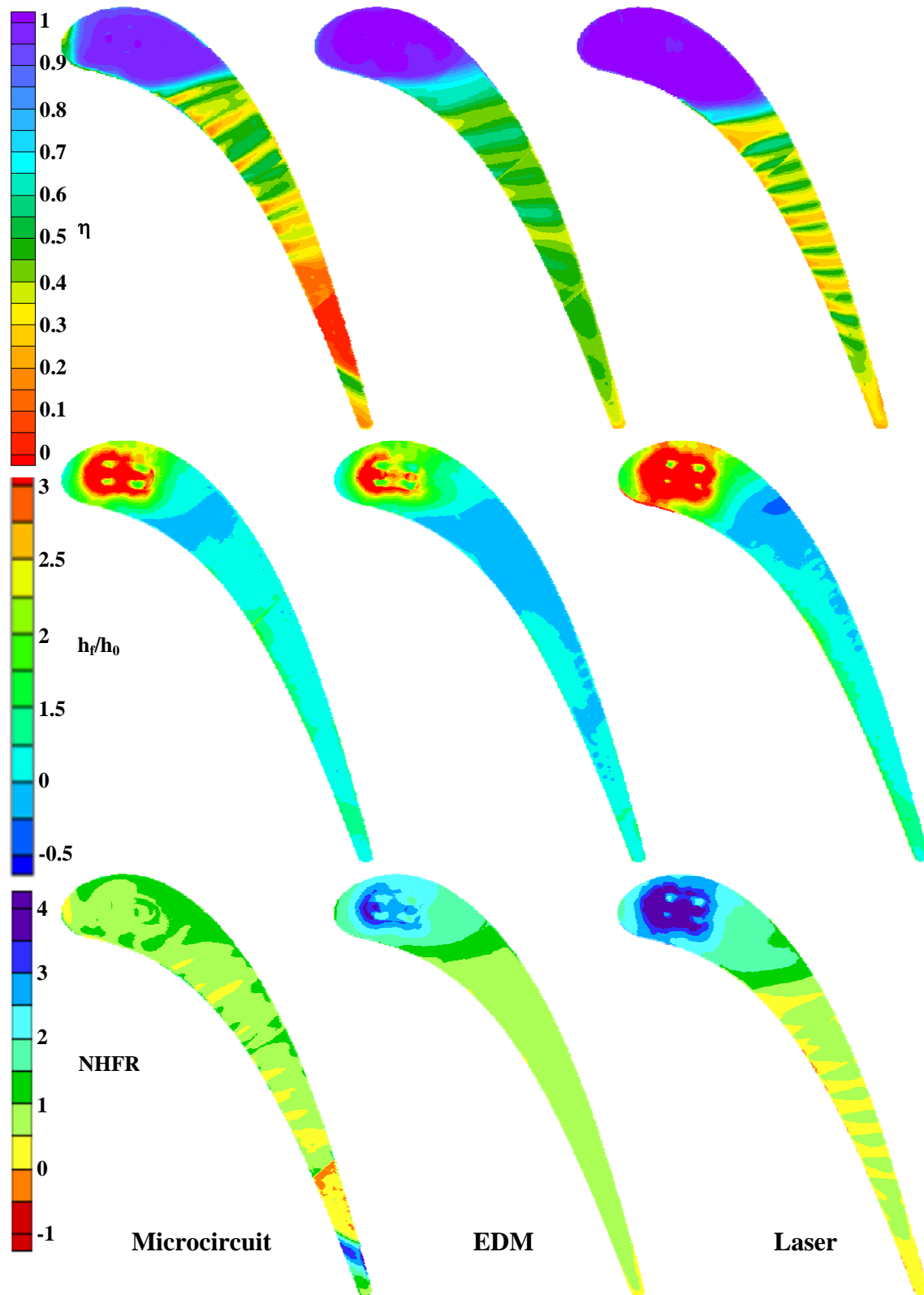


Figure F.1 Comparison between hole shapes for 1.0% coolant flow at the small tip gap.

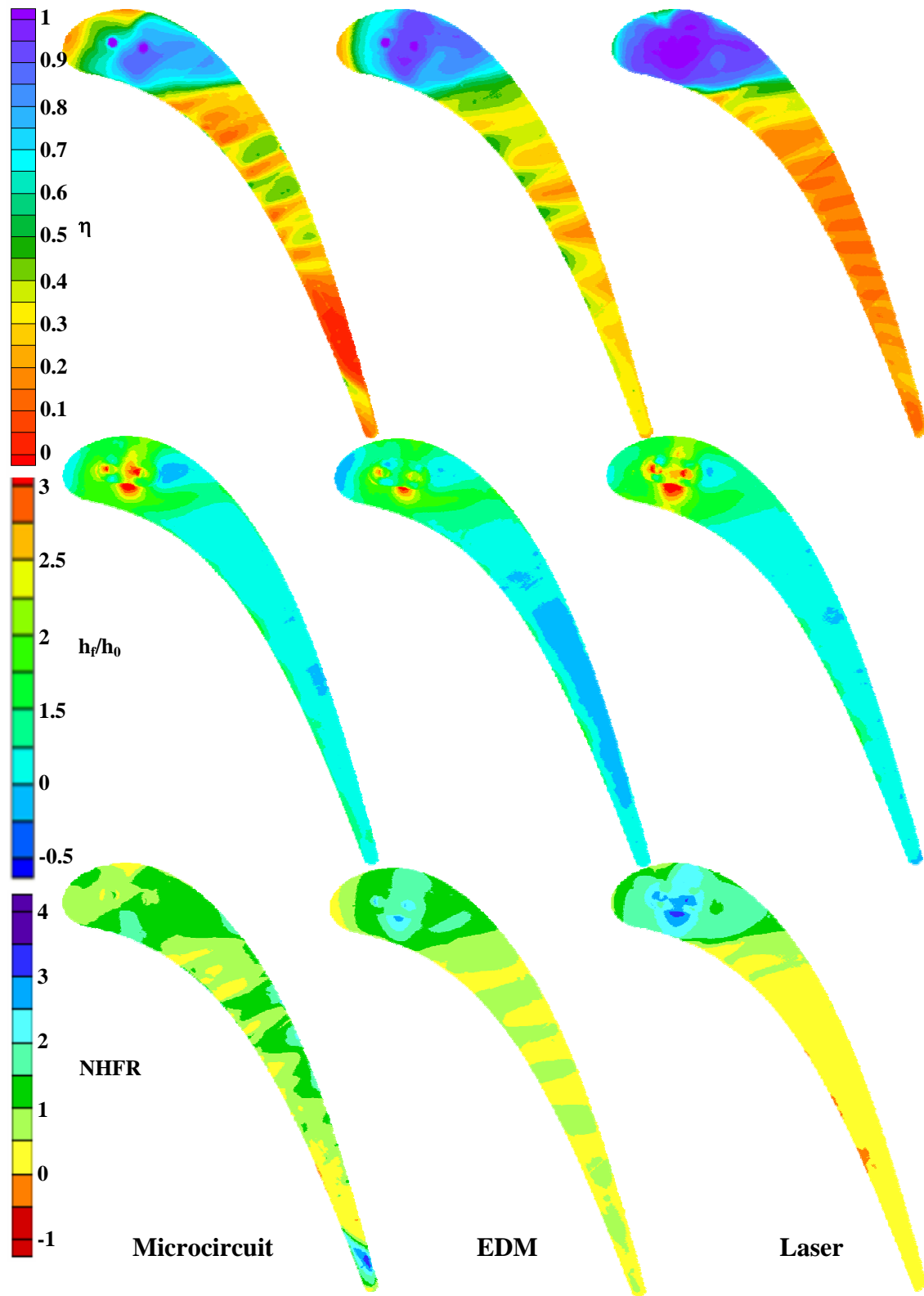


Figure F.2 Comparison between hole shapes for 1.0% coolant flow at the large tip gap.

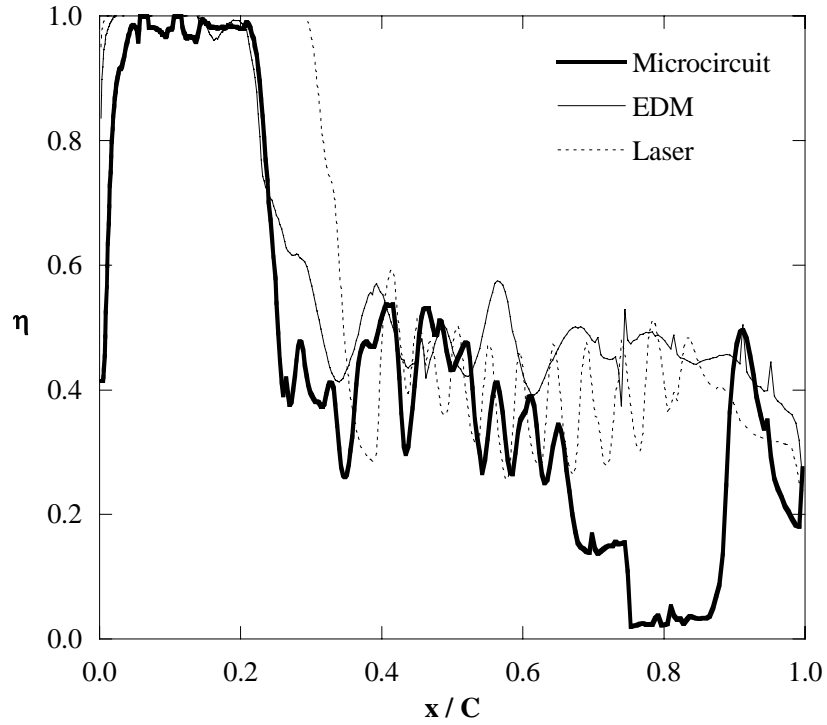


Figure F.3 Adiabatic effectiveness (η) taken along the camber line for the 1.0% coolant flow comparison at the small tip gap.

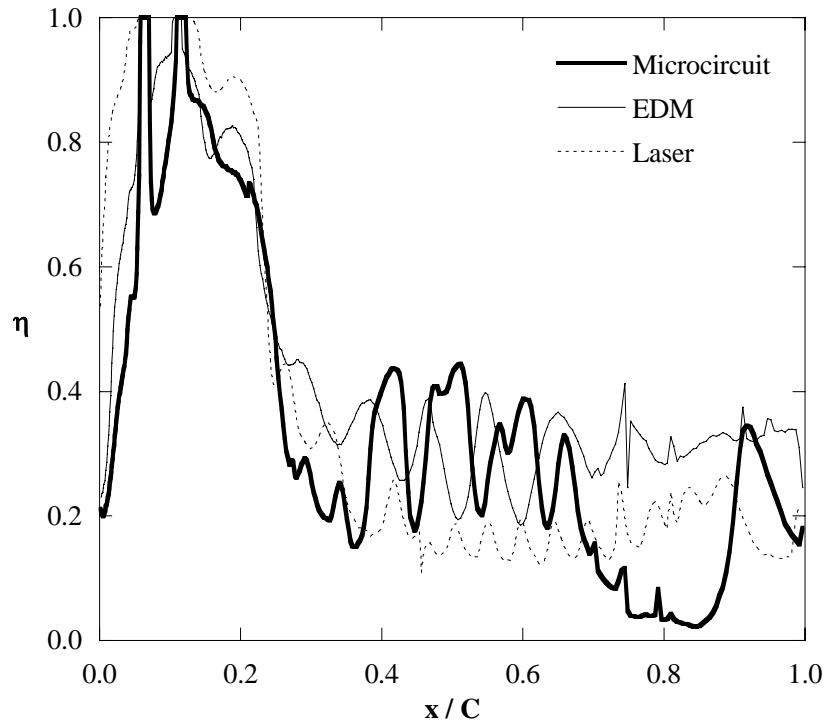


Figure F.4 Adiabatic effectiveness (η) taken along the camber line for the 1.0% coolant flow comparison at the large tip gap.

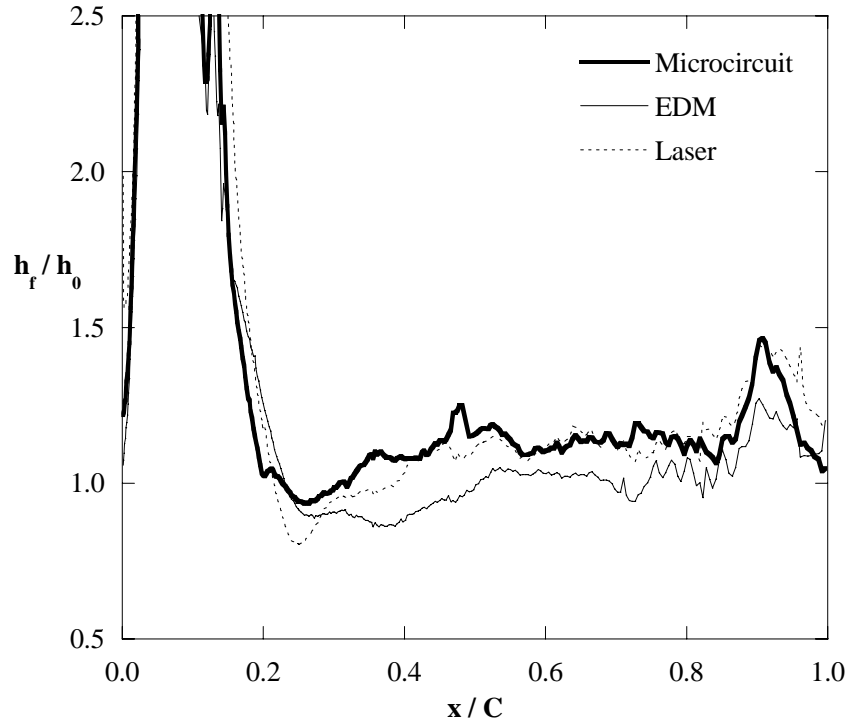


Figure F.5 Heat transfer augmentation (h_f/h_0) taken along the camber line for the 1.0% coolant flow comparison at the small tip gap.

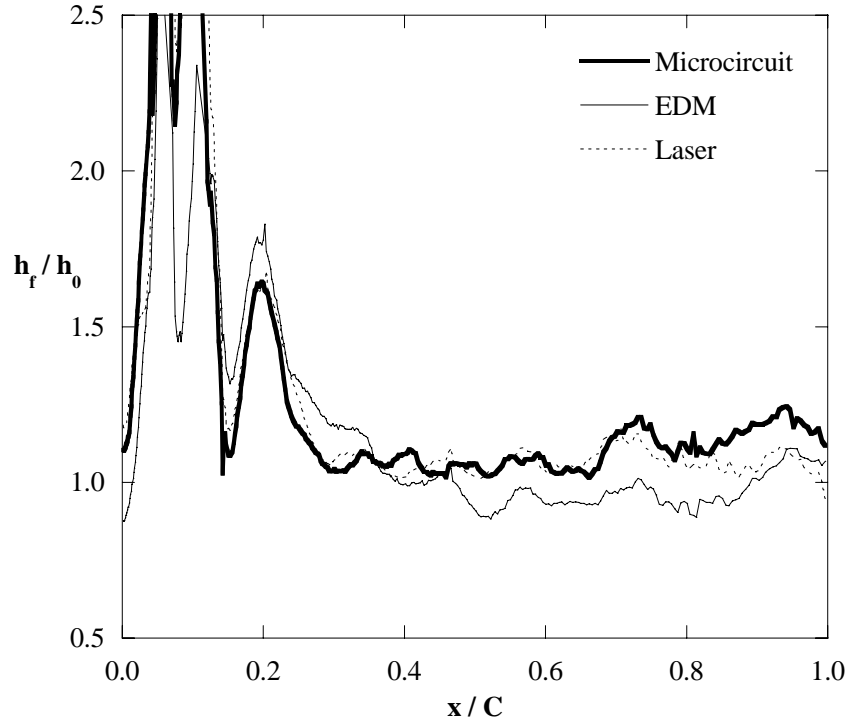


Figure F.6 Heat transfer augmentation (h_f/h_0) taken along the camber line for the 1.0% coolant flow comparison at the large tip gap.

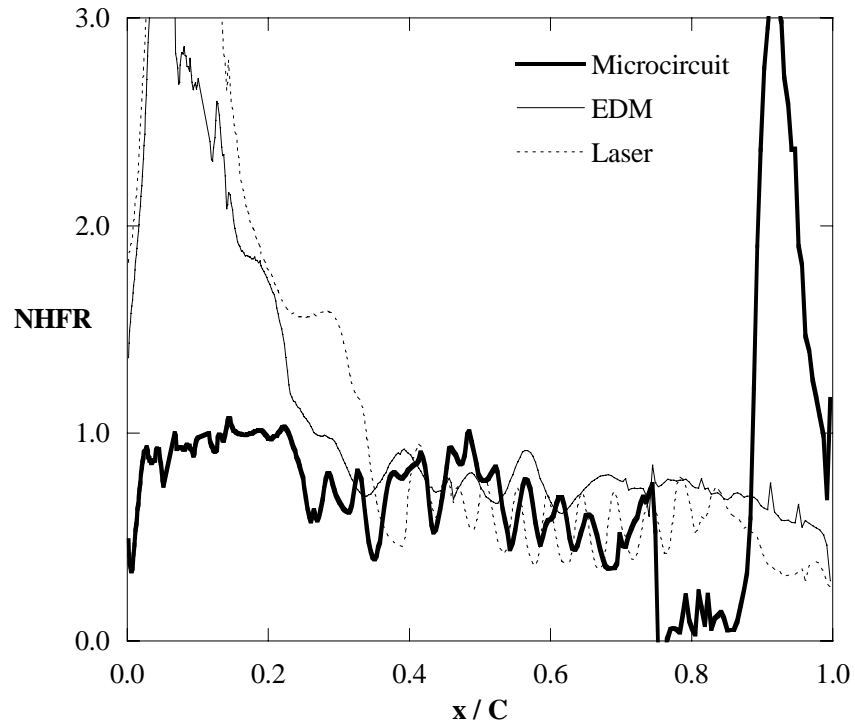


Figure F.7 NHFR along the camber line for the 1.0% coolant flow comparison at the small tip gap.

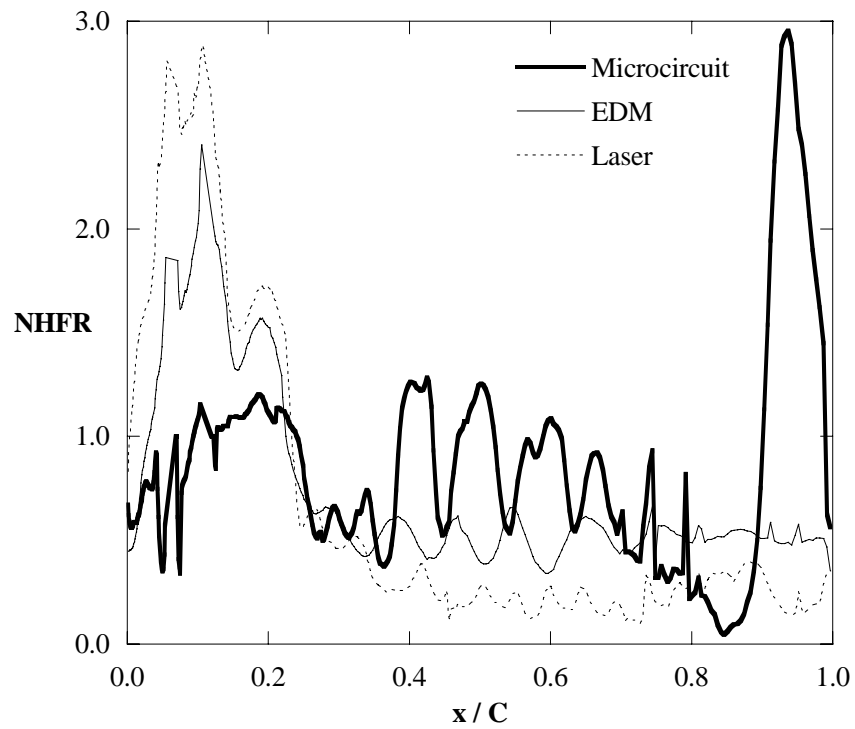


Figure F.8 NHFR along the camber line for the 1.0% coolant flow comparison at the large tip gap.

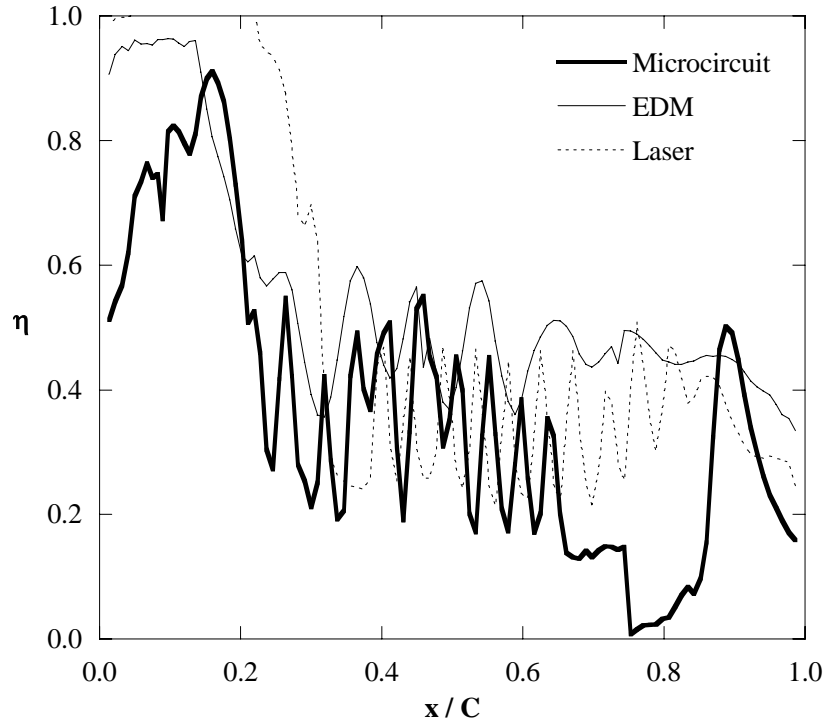


Figure F.9 Adiabatic effectiveness (η) taken along the pressure-side line for the 1.0% coolant flow comparison at the small tip gap.

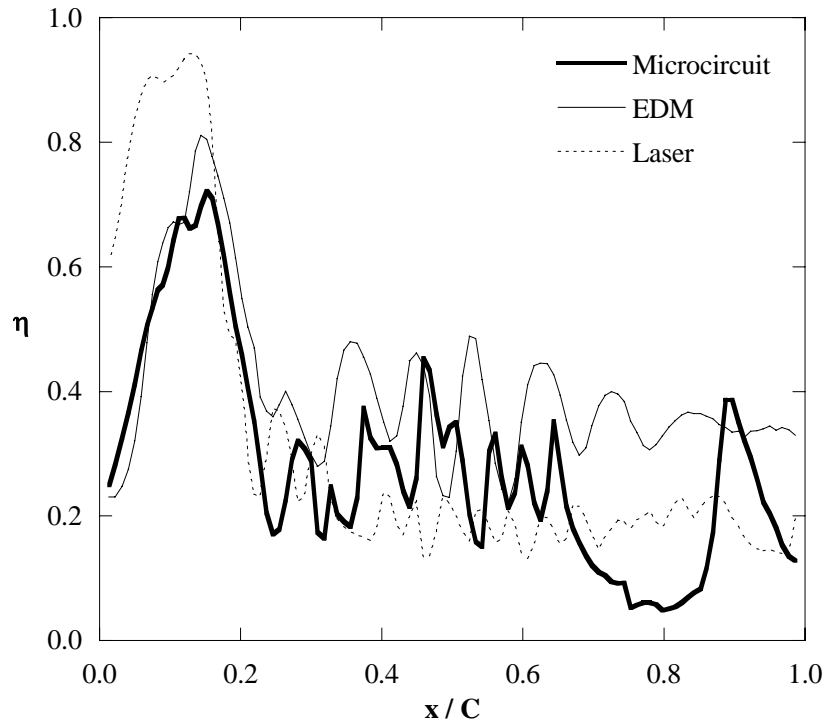


Figure F.10 Adiabatic effectiveness (η) taken along the camber line for the 1.0% coolant flow comparison at the large tip gap.

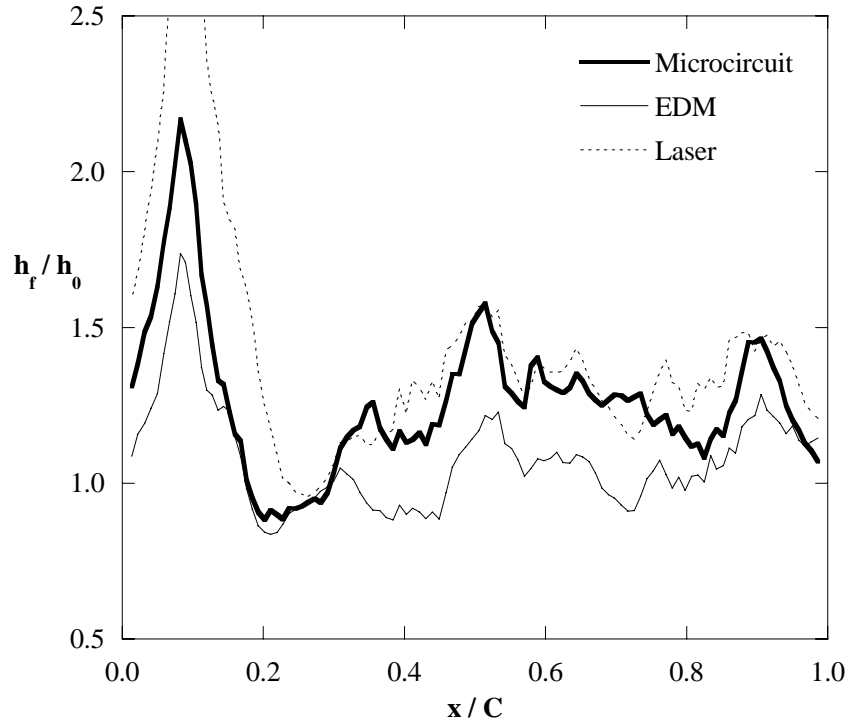


Figure F.11 Heat transfer augmentation (h_f/h_0) taken along the camber line for the 1.0% coolant flow comparison at the small tip gap.

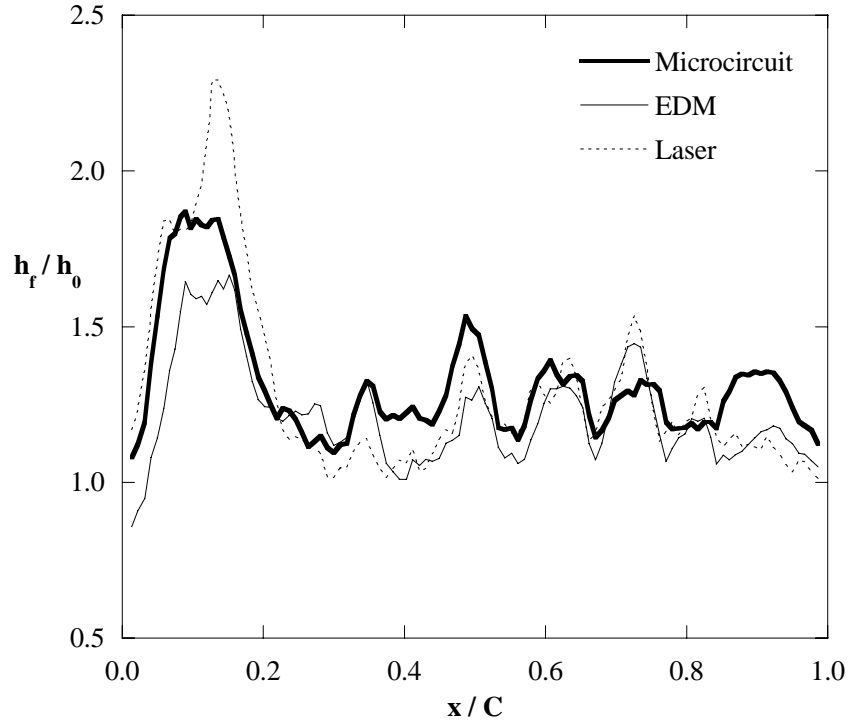


Figure F.12 Heat transfer augmentation (h_f/h_0) taken along the camber line for the 1.0% coolant flow comparison at the large tip gap.

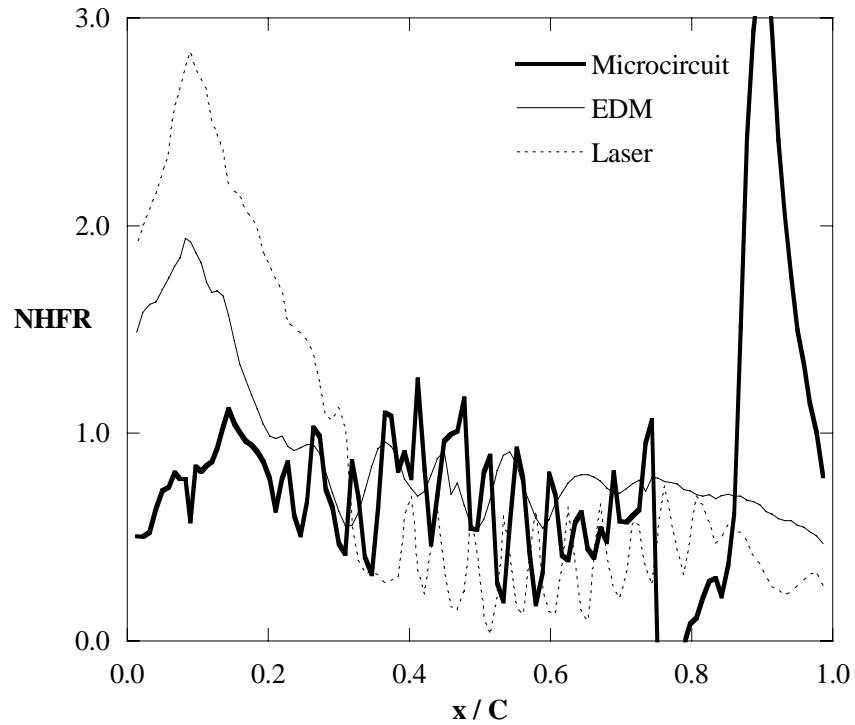


Figure F.13 NHFR along the camber line for the 1.0% coolant flow comparison at the small tip gap.

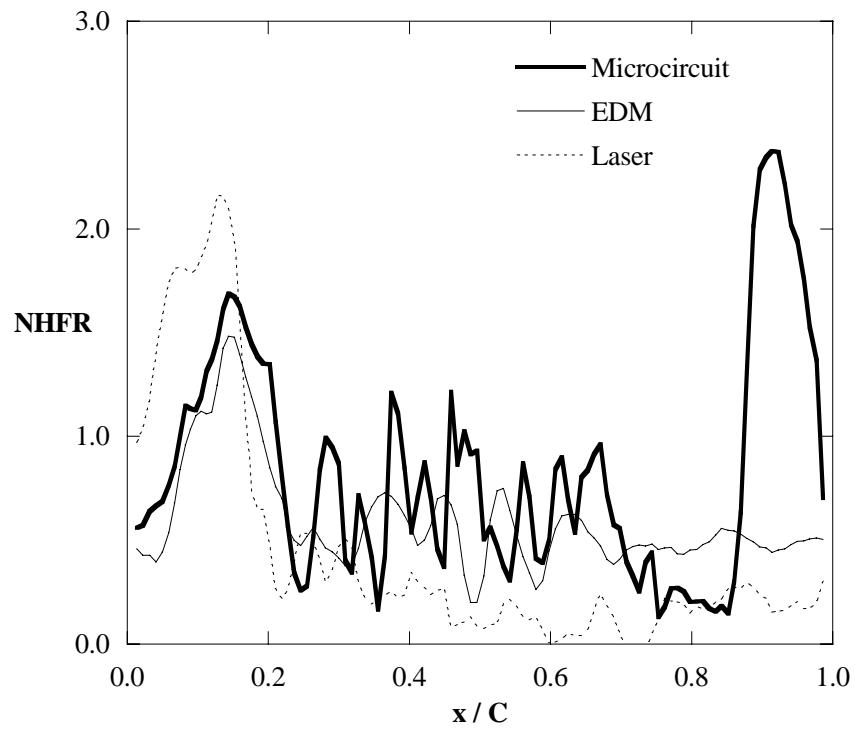


Figure F.14 NHFR along the camber line for the 1.0% coolant flow comparison at the large tip gap.

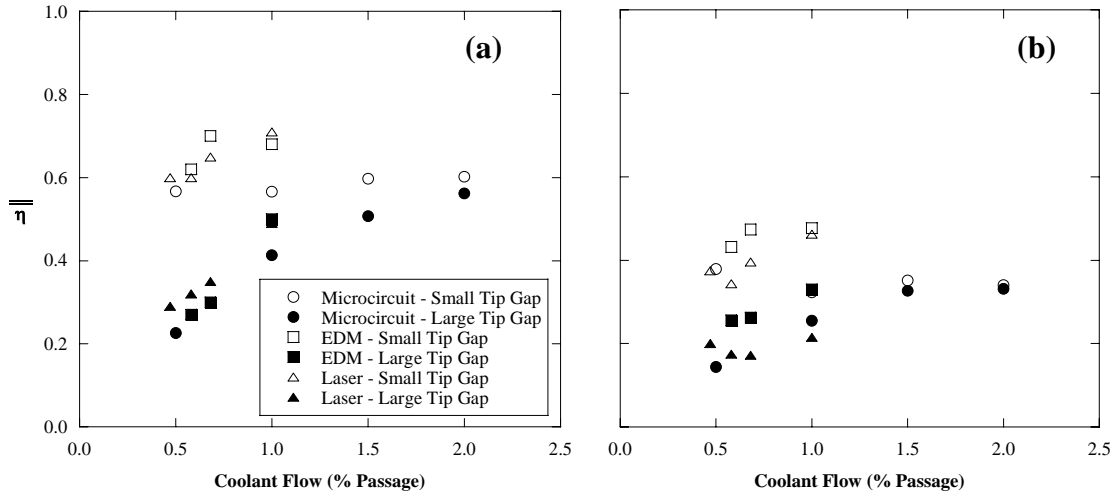


Figure F.15 Area-averaged adiabatic effectiveness levels over the entire tip (a) and the last 70% (b) for all geometries and tip gaps tested.

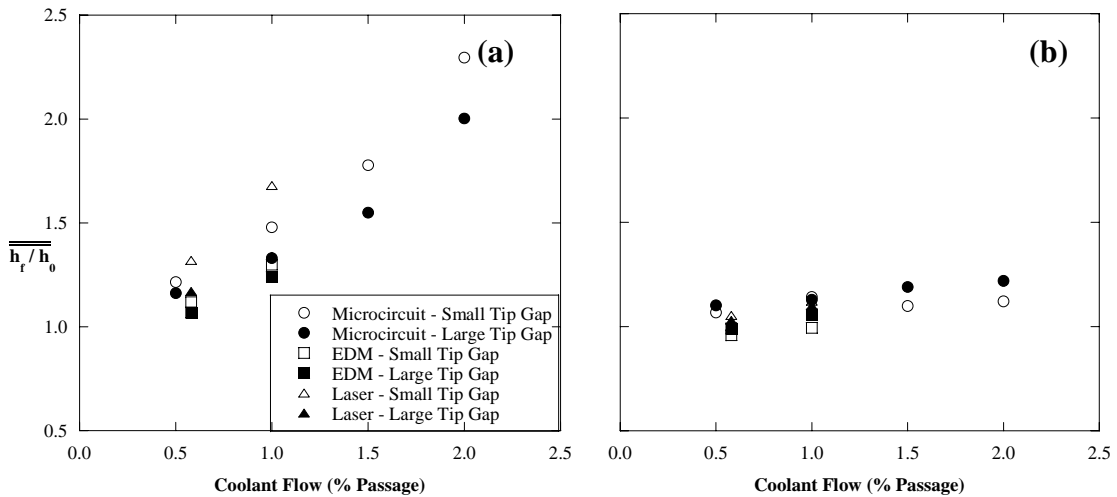


Figure F.16 Area-averaged heat transfer augmentation over the entire tip (a) and the last 70% (b) for all geometries and tip gaps tested.

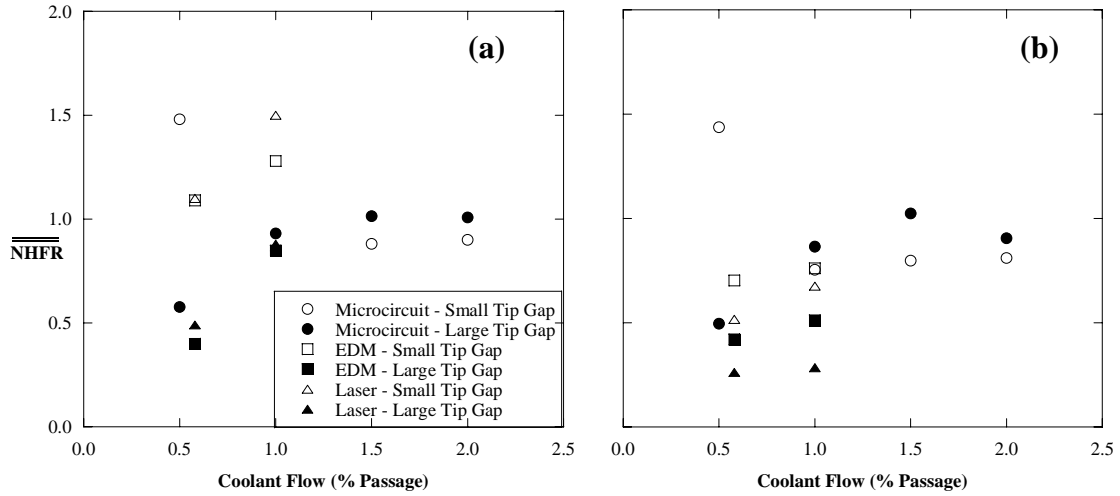


Figure F.17 Area-averaged NHFR over the entire tip (a) and the last 70% (b) for all geometries and tip gaps tested.

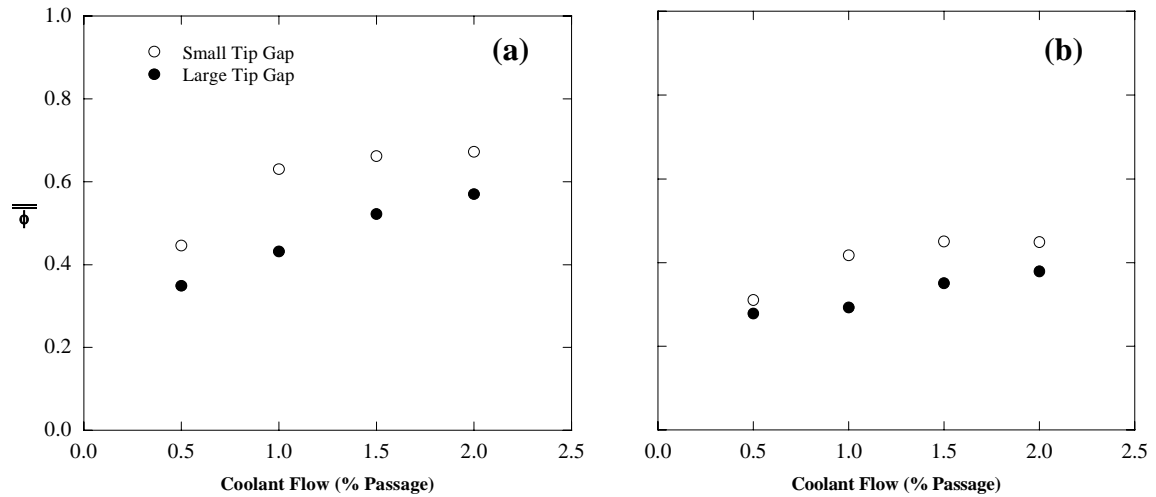


Figure F.18 Area-averaged cooling effectiveness over the entire tip (a) and the last 70% (b) for the microcircuit holes.

Appendix G: Summary and Recommendations for Future Work

This thesis reviews an extensive experimental study of different cooling schemes for the tip of a turbine blade. The results are presented in four different journal papers, three of which are currently under review. The first paper discusses heat transfer measurements along the tip as well as adiabatic film-effectiveness results obtained by Couch [1], and combines the two to calculate net heat flux reduction (NHFR). The second paper discusses the differences between a basic EDM and laser hole shape design and how effectively these geometries can provide film-cooling to the tip of a turbine blade. The heat transfer associated with the EDM and laser holes was discussed in the third paper, which also built upon the second paper by providing the NHFR results for these two hole shapes. The fourth paper presents the external tip heat transfer and internal convective effectiveness of a novel microcircuit design for cooling the tip of a turbine blade. This design was previously analyzed by Couch [1], whose results were compiled with the current studies to provide the NHFR for the microcircuit geometry. This appendix summarizes the conclusions made from each of these papers and offers recommendations for future work.

G.1 Overview of Results

Adiabatic effectiveness tests were conducted for the EDM and laser holes. The contour plots showed that the EDM holes provided tip cooling that was much more spread-out than with the laser holes. Data taken along the blade camber and pressure-side lines verified this by showing severe peaks and valleys for the laser hole cases. When comparing the area-averaged results over the entire blade, the laser holes showed higher effectiveness values than the EDM for some cases. This was due to the higher dirt purge flow for the laser holes relative to the EDM holes for the same overall coolant flow rate. To make a more direct comparison, area-averages were made over the last 70% of the blade, thereby avoiding the dirt purge affected area. These results showed higher effectiveness values for the EDM holes when compared to the laser holes. For a typical case, the mass flux ratios exiting the EDM holes were very similar to that of the laser

holes. In spite of these similar mass flux ratios, the EDM holes still showed higher effectiveness levels. This is due to the spreading of the EDM hole jets resulting from the low exiting momentum of the jets, which allows the coolant trajectory to remain attached to the blade surface. The laser jets had relatively higher exiting momentum and separated off of the blade surface, causing mixing to occur between the coolant and mainstream fluids. Both the EDM and laser jets were swept significantly downstream along the pressure side before crossing the tip gap.

Heat transfer measurements were made for a blade tip with no blowing, dirt purge blowing only, and with additional pressure side holes representing the EDM, laser, and microcircuit geometries. The baseline (no blowing) cases showed trends that agreed with what has been presented in the open literature on tip heat transfer. A region of low heat transfer was shown to be present near the thickest portion of the blade. Also, a region of high heat transfer occurred along the pressure side of the tip, representing a separation region at the entry to the tip gap. Baseline cases showed that the tip heat transfer increased with gap height. A relationship has been presented that relates the heat transfer augmentation on a flat blade tip over fully developed duct flow to the geometric properties of the blade. The baseline results of this study as well as other studies showed good agreement with this relationship.

Heat transfer measurements for the dirt purge only tests showed high heat transfer augmentations along the leading edge region. Heat transfer was only affected in the first 30% of the blade with the dirt purge blowing. The results showed that increasing the coolant flow (in-turn, the blowing ratio) caused increases in heat transfer. Also, the large tip gap had higher heat transfer values than the small tip gap. The large tip gap showed a trend at the higher blowing ratios of vortices forming along the downstream side of the second dirt purge hole. These vortices were verified by CFD predictions, and tend to cause high heat transfer.

Heat transfer measurements for the EDM hole geometry showed that the EDM holes can actually reduce the tip heat transfer in some areas when compared to the baseline case. Heat transfer measurements for the laser hole geometry, however, showed that the laser holes cause increased heat transfer from the baseline case. Both geometries

showed increased heat transfer with increased blowing, as well as higher heat transfer values for a larger tip gap.

Tip heat transfer measurements for the microcircuit geometry showed increased heat transfer when blowing was present. Similar to the other geometries tested, increasing the coolant flow caused increased heat transfer, and the large tip gap showed higher heat transfer values than the small tip gap.

Internal convective effectiveness results for the microcircuit passages showed that for lower coolant flow rates, the microcircuit passages cause increased heat transfer when compared to a fully developed rectangular duct. As the coolant flow rate is increased, the heat transfer augmentation of the passage is lowered, so that for very high flow rates, the microcircuit passage actually reduces the heat transfer from that of a fully developed rectangular duct.

Overall, the results of this thesis allow for the comparison of four separate methods for cooling the entire tip of a turbine blade. While the dirt purge, EDM, and laser holes use only film-cooling, the microcircuit uses a combination of film-cooling and internal convection cooling. These studies show that when only film-cooling is used to cool a blade tip, the shaped holes provide the best protection. When including the internal convective cooling used in the microcircuit design along with film cooling, the combination results in the higher overall blade protection compared to film-cooling alone.

G.2 Recommendations for Future Work

By studying the tip heat transfer along the tip of a turbine blade, expanded holes have been shown to reduce the tip heat transfer compared to non-expanded holes, while also increasing the coolant spreading. Also, the internal passages of the microcircuit design have proven to be effective, especially at lower coolant flow rates. This presents a good trade-off between cooling schemes because at lower flow rates, the film-cooling along the tip is diminished, especially at larger tip gaps.

It is recommended that two modifications to the microcircuit design be studied. The first modification would be to remove the last microcircuit passage. The trailing edge could then have expanded film-cooling holes placed along the pressure side of the

blade, which have been shown to provide effective tip protection. The second modification would take the existing microcircuit passage design and utilize expanded hole exits. This design would allow for adequate tip cooling by way of the microcircuit at low flow rates, and by way of the film-cooling at higher flow rates. This second modification presents a significant problem for manufacturing, and may not be feasible for some time. Variations on the coolant injection angle could be tested as well as the microcircuit channel area. This would allow the design to control the amount of coolant exiting at specific portions of the tip.

G.3 References

- [1] Couch, E., *Measurements of Cooling Effectiveness Along the Tip of a Turbine Blade*, Master's Thesis, Virginia Polytechnic Institute and State University, Blacksburg, VA, 2003

Vita

Jesse Christophel was born on August 14th, 1980 in Harrisonburg, VA to John and M.J. Christophel and has one older brother, Jared. When Jesse was 2 years old, his family moved to a 73 acre farm at the foot of the Blue Ridge Mountains just outside of Elkton, VA. During high school, Jesse lettered in cross-country and tennis, and was the trumpet soloist for his high school marching band.

Working on the farm during weekends and over the summers, Jesse was intrigued by the machinery and mechanisms with which he worked. He chose to attend Virginia Tech majoring in mechanical engineering in August of 1998. He enrolled in the B.S. M.S. program at Virginia Tech in January of 2002 and graduated Magna Cum Laude with his Bachelors in mechanical engineering in May of 2002. In June of 2002 he was married to the beautiful Kimberly Mason of Martinsville, VA. Jesse successfully defended his master's thesis on September 19th, 2003, and will begin work in the Durability group of Pratt & Whitney in East Hartford, CT.